Single-photon detectors integrated in quantum photonic circuits

Single-photon detectors integrated in quantum photonic circuits

PROEFSCHRIFT

ter verkrijging van de graad van doctor aan de Technische Universiteit Eindhoven, op gezag van de rector magnificus, prof.dr.ir. F.P.T. Baaijens, voor een commissie aangewezen door het College voor Promoties, in het openbaar te verdedigen op dinsdag 16 oktober 2018 om 16.00 uur

door

Giulia Enrica Digeronimo

geboren te Catania, Italië

Dit proefschrift is goedgekeurd door de promotoren:

voorzitter:	prof.dr.ir. G.M.W. Kroesen
1e promotor:	prof.dr. A. Fiore
co-promotor:	dr. R. Leoni (National Research Council)
Leden:	prof.dr. R.H. Hadfield (University of Glasgow)
	dr. J.J.G.M. van der Tol
	prof.dr.ir. D. van Thourhout (Universiteit Gent)
	dr. R.W. van der Heijden

Het onderzoek of ontwerp dat in dit proefschrift wordt beschreven is uitgevoerd in overeenstemming met de TU/e Gedragscode Wetenschapsbeoefening

A catalogue record is available from the Eindhoven University of Technology library
ISBN: 978-90-386-4589-6

Single-photon detectors integrated in quantum photonic circuits
By Giulia Enrica Digeronimo

The work described in this thesis has been carried in the group of Photonics and Semiconductor Nanophysics, at the Department of Applied Physics of the Eindhoven University of Technology, The Netherlands.

This research is financially supported by the European Commission, Initial Training Network PICQUE (No. 608062), by the Dutch Technology Foundation STW, Applied Science Division of NWO, the Technology Program of the Ministry of Economic Affairs under projects No. 10380, 12662 and by NanoNextNL, a micro and nanotechnology program of the Dutch Ministry of Economic Affairs, Agriculture and Innovation (EL&I) and 130 partners.

Printed by Gildeprint

Summary

Single-photon detectors integrated in quantum photonic circuits

Photons have emerged as a promising approach for quantum information processing (QIP). However it is very challenging to implement quantum processing functionalities on a large scale with bulk optics due to the extreme stability requirements and large coupling losses. In order to scale photonic QIP to more complex functionalities, quantum photonic integrated circuits (QPICs) are required. A fully-functional QPIC requires all the key quantum optical components, such as single-photon sources, passive circuit elements and single-photon detectors, integrated on a single chip.

GaAs is a favourable material in order to integrate many QPIC elements, from excellent single-photon sources to high-performance single-photon detectors. Semiconductor quantum dots (QDs) have been shown to be nearly ideal sources of non-classical light that can be efficiently routed into nanophotonic circuits. On the other side, superconducting single-photon detectors (SSPDs) combine high quantum efficiency, low dark count rates, and ultra-fast response making them promising candidates for QIP.

Despite the impressive progress made in the development of these components at the single unit level, and in the improvement of their individual performance, the efficient integration of these devices on the same chip remains a significant technological challenge that has to be addressed in order to exploit the real power of integrated quantum photonics.

In this thesis, the prototype architectures of multi-functional QPICs are presented, with an emphasis on the integration of photon sources and detectors. Several key quantum optical components have been integrated on the same chip and their functionality and coupling successfully tested. Particularly, photons, generated by excited InAs quantum dots (QDs), have been routed through ridge waveguides and filtered on-chip to a single excitonic line using photonic crystal (PhC) cavities. On the detector side, SSPDs patterned on top of suspended nanobeam (SNB) have achieved record device quantum efficiency on GaAs and have been integrated with QD sources, enabling the on-chip time-resolved measurement of their emitted photons. Furthermore two electrically independent detectors, integrated on top of the same nanobeam, have shown to be a very compact autocorrelator system for on-chip second-order correlation function $g^{(2)}(\tau)$ measurements.

The first chapter illustrates the state-of-the-art of QIP and QPIC with a particular focus on the GaAs platform. Different tuning strategies of the QDs emission and also of the cavity modes are compared, as well as different types of single photon detectors with a special attention to SSPDs and their performance parameters.

Chapter 2 covers the experimental methods used for the realization of these QPICs.

Chapter 3 is dedicated to the design and fabrication of the SSPDs, including the study of the optimized parameters used for the sputtering of the NbN films.
In Chapter 4 the differences between the standard process used for the fabrication of PhC structures and the low-temperature (LT) process optimized for the SSPDs integration are highlighted. The technological issues are analysed and solved when possible, showing that the LT fabrication process has the capability to preserve high performance for each component of a QPIC demonstrator (including InAs QDs sources, SSPDs on SNB and PhC filters). A fabrication attempt of a second QPIC demonstrator (including also a p-i-n diode for Stark control of the QDs emission and a nano-opto-electro-mechanical PhC cavity) is also presented in this chapter together with the preliminary characterization of each component of the circuit.
In Chapter 5 the performance of SNB SSPDs are presented. The SSPDs presents a device quantum efficiency (DQE) of 28% at λ=1310nm in transverse-electric (TE) polarization, polarization-independent behaviour and a jitter of 127±8ps. Patterning the nanowire on top of a SNB, instead of a standard ridge waveguide, did not improve the DQE as much as estimated, however a new record for the DQE on GaAs platform has been established. Moreover a SNB autocorrelator system, composed of two electrically-independent SSPDs on top of a suspended nanobeam, is presented in this chapter. The system does not present any static or dynamic crosstalk, showing that it is possible to perform a HBT experiment on chip. This result, combined with the small jitter, shows how the SNB autocorrelator system is suitable for the on-chip characterization of single-photon emitters.
In the first part of Chapter 6, different designs of PhCC-PhCWG systems, used as filters of single excitonic QDs lines, are experimentally tested. The design with in-line coupling and two holes in the barrier presents all the required parameters for an efficient filtering action: free spectral range $\geq$ 60nm, quality factor Q=1000 and transmission of 23%.
In the second part of the chapter, the functionality of the QPIC demonstrator is investigated by testing the coupling between the three main components (SSPDs, QDs, PhC filters). The SSPDs and QDs coupling is tested using the SSPDs for on-chip time-resolved photoluminescence (PL) measurements of the QDs emission. From the PL spectra a strong dependence of the rise time τ_r as a function of the excitation power level, attributed to an Auger-mediated interband relaxation process, is observed, as well as a spontaneous emission lifetime τ_d = 0.94ns. The capability to isolate and transmit a single excitonic line through the filter proves the QDs-filter coupling.
In the last chapter the results are summarised and considerations about the realization of a fully-functional QPIC are made.

Table of Contents

Glossary of symbols and acronyms

Symbol	Description
A	Absorptance
A_d	Detector active area
A_l	Laser spot area
a	Lattice constant
c	Speed of light in vacuum
e^-	Electron
E	Energy density
f	Detector frequency
$g^{(2)}(\tau)$	Second-order correlation function
h	Planck constant
I_b	Bias current
I_c	Critical current
k	Light wave vector
k_z	Vertical component of **k**

$\mathbf{k}_{\parallel}$	In-plane component of **k**
L	Waveguide length
L_k	Kinetic inductance
l	Wire length
n	Refractive index
N_c	Number of counts
N_Φ	Number of photons incident on the detector
P	Power
P_{dep}	Deposition pressure
ph	Phonon
r	Position vector
r	Holes radius
R	Reflectance at the waveguide facet
R_L	Load resistance
R_n	Normal resistance
t	Thickness of the film
T	Transmission
T_c	Critical current
ΔT_c	Width of superconducting-normal transition
t_{heat}	Heating time
T_{dep}	Deposition temperature
T_{set}	Set temperature
w	Wire width
α	Propagation loss
α_{TE}	Modal absorption coefficient for TE mode
α_{TM}	Modal absorption coefficient for TM mode
ε	Dielectric permittivity
η_c	Coupling efficiency
η_i	Internal quantum efficiency
λ	Light wavelength
Φ	Gas flow
ρ_{rms}	Root mean square roughness
τ	Total time constant of a SSPD
τ_D	Dead time
τ_d	Decay time
τ_e	Time constant for the supercurrent recovery in SSPD
τ_{fall}	Time constant for the supercurrent decay in SSPD
τ_r	Rise time
ω	Frequency

Acronym	Description
AFM	Atomic force microscope
AS	Antisymmetric
BS	Beam splitter
BSS	Beam step size
CMOS	Complementary metal-oxide semiconductor
CNT	Carbon nanotube
CW	Continuous wave
DBR	Distributed glass reflector
DC	Direct current
DCR	Dark count rate
DOI	Diamond on insulator
DQE	Device quantum efficiency
EBL	Electron beam lithography
FP	Fabry-Perot
FSR	Free spectral range
FWHM	Full width half maximum
HBT	Hanbury Brown-Twiss
HSQ	Hydrogen Silsequioxane
ICP	Inductively-coupled plasma
IR	Infrared
IRF	Instrument response function
IV	Current-Voltage
LED	Light-emitting diode
LN	Lithium niobate
LOQC	Linear optics quantum computation
LT	Low temperature
MBE	Molecular beam epitaxy
MEMS	Micro-electromechanical system
MMI	Multimode interferometer
MOSFET	Metal-oxide-semiconductor field-effect transistor
NA	Numerical aperture
NOEMS	Nano-opto-electro-mechanical system
NV	Nitrogen vacancy
PC	Photon Counts
PECVD	Plasma enhanced chemical vapour deposition
PhC	Photonic crystal
PhCC	Photonic crystal cavity
PhCWG	Photonic crystal waveguide
PL	Photoluminescence
PMT	Photomultiplier tube
PS	Phase shifter

PSD	Position sensitive detector
PVD	Physical vapour deposition
Q	Quality factor
QCSE	Quantum confined Stark effect
QD	Quantum Dot
QE	Quantum efficiency
QEC	Quantum error correction
QIP	Quantum information processing
QKD	Quantum key distribution
QPIC	Quantum photonic integrated circuit
RF	Radiofrequency
RIE	Reactive ion etching
RWG	Ridge waveguide
S	Symmetric
SDE	System detection efficiency
SE	Spectroscopic ellipsometry
SEM	Scanning electron microscopy
SiN	Silicon nitride (Si_3N_4)
SiV	Silicon vacancy
SFWM	Spontaneous four-wave mixing
SNB	Suspended nanobeam
SOI	Silicon on insulator
SP	Single photon
SPAD	Single photon avalanche diode
SPD	Single photon detector
SSPD	Superconducting single photon detector
T	Transition
TE	Transverse Electric
TEM	Transmission electron microscope
TES	Transition edge sensor
TM	Transverse Magnetic
TR	Time resolved
UV	Ultra-violet
V	Mode volume
VAP	Vortex-antivortex pair
WG	Waveguide

Chapter 1

Introduction

"... it seems that the laws of physics present no barrier to reducing the size of computers until bits are the size of atoms, and quantum behaviour holds sway."
Richard P. Feynman (1985)

1.1 Quantum information processing (QIP)

In a world overwhelmed by increasing amounts of data, finding new ways to store and process information has become a necessity. Conventional silicon-based electronics has experienced rapid and steady growth, thanks to the progressive miniaturization of its basic component, the transistor, but that trend cannot continue indefinitely. Indeed, it is stated by Moore's law[1] that the number of electronic components integrated in a chip doubles every 18 months. However, after 50 years, the law has arrived to saturation and within 3 years the expected lower limit in terms of transistor size (7 nm) will be reached[2]. Therefore, the chip industry is exploring different paths in order to find the next revolutionary technology that will allow further increasing the computing power. One possibility is the use of quantum technology.
In a classical device, information is stored and manipulated in binary form: the elementary components (bits) have two states, each of which encodes the binary 0 or 1. To move beyond the binary system, one can exploit the laws of quantum mechanics. A quantum-mechanical object with two state at its disposal can occupy either of those two states, but also an arbitrary combination (superposition) of the two. This result in infinitely many quantum states that a single quantum bit (qubit) can take; together with another property of quantum mechanics, entanglement, it allows for a much more powerful information platform than is possible with conventional components.
Quantum information processing (QIP) uses qubits as its basic information units. To be useful for QIP, a qubit needs to be both isolated from its environment and tightly controllable, which places stringent requirements on its physical realization. A number of qubit types have been proposed and experimentally realized that satisfy at least some of these criteria, and tremendous progress has been made over the past decade in improving the figures of merit, such as the coherence time. Superconducting circuits, trapped atoms,

colour centres, Majorana fermions and photons are some of the possible physical candidates for QIP applications[3].
Photons are exceptionally attractive for QIP, since they combine low decoherence rate and high propagation speed[4]. Moreover the information can be encoded as qubit choosing between a large number of degrees of freedom of the light such as polarization, spatial or temporal modes, frequency and angular momentum.
In the following, an overview of the potential applications of photonic QIP is given, including quantum communication, simulation and computing.

1.1.1 Quantum communication

Quantum communication is the use of quantum mechanics for transferring qubits between two separate locations. One of the most important types of quantum communication is quantum key distribution (QKD) which consists of the process of sharing a secret key between two parties (usually indicated as Alice and Bob) so that an eavesdropper (usually called Eve) has no possibility to learn the key`s value even intercepting all the communication between Alice and Bob. This is guaranteed by the laws of quantum mechanics. If Alice sends quantum bits to Bob, an eavesdropping attempt by Eve will produce a change in the qubits state that Alice and Bob will notice. The idea of QKD was first proposed in early 80s with a protocol for secure communication (BB84)[5].
Practical implementations of QKD using photons as qubit faces several challenges including efficient single-photon sources and detectors at telecom wavelengths which limit the distance and bit exchange rate of QKD protocols[6]. Also channel losses create the need to realize the quantum repeaters for distribution of the signal through the lossy channel creates practical restrictions for QKD implementation[7]. In 2015 QKD over a distance of 300 km has been demonstrated on an optical fibre system [8].
Recently (2017), two entangled photons sent from a satellite to two ground stations, for total distance of 2400 km, were observed maintaining the entanglement, laying the groundwork for future intercontinental quantum key distribution experiments[9]. Moreover, later the same year, the BB84 protocol was successfully implemented over the satellite links and the two ground stations[10].

1.1.2 Quantum simulation

The idea of quantum simulation was first proposed by Feynman[11]. Quantum simulators offer an environment that exploits another quantum system obeying the same rules of quantum mechanics as the system to be simulated, but it is easier to measure. In this way, the inability of the classical computers to simulate the behaviour of quantum systems can be overcome. For instance, calculating the ground state energies of many-body systems

becomes exponentially harder by using the classical supercomputers as the number of particles increases whilst it gets only polynomially difficult for a simulating quantum system[12]. To date quantum simulators have been realized in a variety of platforms including trapped ions, atoms, superconducting circuits and photons[13]. Recently, boson sampling experiments have been used to prove the validity of photonic quantum simulation[14]. The boson samplers are photonic circuits (Fig. 1.1) consisting of a nested network of interferometers that couple *m* photonic modes fed by a number *n* of indistinguishable single photons. The probability that *n* single photons are detected at *n* output ports of the system can be calculated by evaluating the permanent of the matrix that describes the unitary transformation of the circuit. If the circuit is realized in such a way that the input-output transformation is characterized by a uniformly random matrix, then calculating the transition probability has been shown to belong to a class of computationally hard problems[15]. The direct measurements of the outcome from a physical boson sampler will give the solution of the computationally hard problem much faster than any classical machine. Even though the boson sampling problem does not have practical application in itself, it could serve as a demonstration of "quantum supremacy"[16].

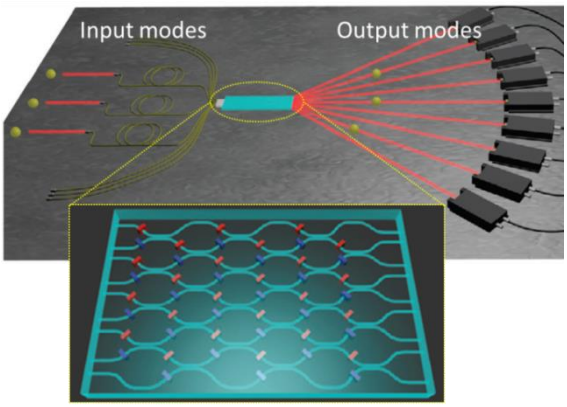

Fig. 1.1 Sketch of a boson sampling circuits, in which the interferometers with 9 inputs/outputs ports are integrated in a glass chip. Reprinted from [17].

1.1.3 Quantum computing

In a quantum computer the bits are replaced with qubits, therefore data are encoded in a superposition of 0 and 1 and not in a well-defined state as classical bits. This property gives the quantum computers a powerful advantage due to their inherent parallelism for solving certain type of problems (for example the algorithm of the factorization of a number), where the quantum computer performs exponentially faster than its classical counterpart[18]. This does not necessarily mean that quantum computers are going to be

faster than classical ones for all problems, but they are indeed more powerful for particular applications or algorithms where their inherent computational parallelism is an advantage.

However, there is a dangerous flaw to this increase in computational power. In fact, the qubits need to interact strongly with one another, and with the external inputs for control, and outputs for detection, but nothing else. This leads to the quantum conflict: balancing just enough control and coupling, while preserving quantum coherence.

Fortunately, it has been shown that with quantum error correction (QEC) it is possible to perform fault-tolerant quantum computing[19].The essential idea in QEC is to encode information in subsystems of a larger physical space that are immune to noise. In fact, since real physical qubits suffer from decoherence, QEC can be used to define fault-tolerant logical qubits, employing multiple physical qubits to get redundancy. All this suggests that for building a quantum computer the following requirements are necessary:

- a physical qubit that is well isolated from the environment and is capable of being addressed and coupled to more than one extra qubit in a controllable manner,
- a fault-tolerant architecture supporting reliable logical qubits,
- universal gates, initialization, and measurement of logical qubits.

A physical quantum computer satisfying all three of these requirements is still an outstanding challenge. Several platforms have been proposed for the realization of quantum computers[3] and which one is the most suitable is still an open question. However, physical qubits in trapped-ion and superconducting systems have reached the point where errors are at or below the threshold[20,21], and networks of 4–9 superconducting qubits with individual control and readout have been used to show concepts of error correction[22]. These networks, with a number of physical qubits below 10, are very far from the estimated 50[23] and 100[24] physical qubits required in order to guarantee computational power that can be never replicated on a classical machine.

However, during these recent years, the race to the first scalable quantum computer has seen a strong competition between the major computing companies, enabling huge steps forward.

While a first attempt to commercialize a quantum computer based on superconducting qubits was proposed by D-Wave in 2011[25], the end of the race appears approaching now with IBM and Google. First IBM (November 2017) launched “Q IBM” (Fig. 1.2 a) that works with 50 superconducting qubit[26] , and later Google (March 2018) “Bristlecone” (Fig. 1.2 b) that operates with 72 qubit also based on superconducting technology[27]. Microsoft instead has based its strategy on Majorana fermions, promising the demonstration of the first topological qubits by the end of 2018[28].

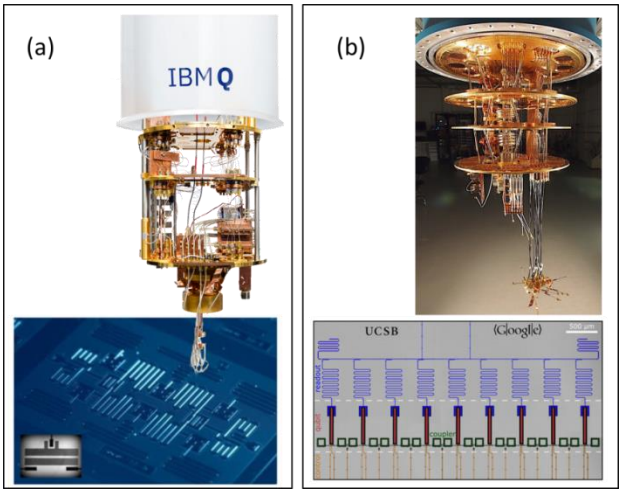

Fig. 1.2 a) Picture of the IBM Q quantum computer, below 8 qubit device and optical micrograph detail of a single qubit (in grey). b) Picture of the Google Bristelcone quantum computer, below optical micrograph of a 9 qubit device.

The photonic approach for quantum computers is attractive thanks to their low decoherence rate, high propagation speed, and large number of degrees of freedom that can be used to encode the information. The encoded quantum information can be manipulated with conventional optical elements. However, in contrast to the manipulation of single photons, deterministic two qubit quantum gates require strong nonlinear interaction between the photons and therefore are difficult to realize. Fortunately, in 2001 the concept of linear optics quantum computation (LOQC) was suggested[29]. This approach showed that scalable quantum computing is possible using only single-photon sources and detectors, and linear optical circuits such as beam splitters and phase shifters, to carry out probabilistic computation. In the past years the concept of LOQC has moved from a mathematical proof-of-possibility towards practical realization, with demonstrations of simple quantum algorithms[30] and theoretical developments that dramatically reduce the resource overhead[4]. These developments employ the ideas of cluster-state quantum computing[31], in which quantum computation consists entirely of one-qubit measurements on a particular class of entangled states (the cluster states), and have been demonstrated experimentally[4].

Currently the efforts towards photonic quantum computing are focused on high efficiency single-photon sources and detectors and chip-scale waveguide quantum circuits. Moreover the advances in photonic quantum computing are expected not only to support photonic qubits, but also to benefit other types of quantum computer hardware using photons for quantum communication between matter qubits[32].

1.2 Quantum photonic integrated circuit (QPIC)

As previously mentioned, QIP with photons is promising and already very interesting results have been achieved, especially considering cryptography. However, even the simplest photonic QIP experiments require careful interfacing of many optical elements. Therefore the implementation of quantum processing functionalities on a large scale has been very limited, due to the extreme stability requirements and large coupling losses related to bulk optics.
In order to scale photonic QIP to more complex functionalities, such as boson samplers or cluster-state quantum computers, in which few tens of photons are required, the concept of quantum integrated photonic circuits (QPICs) is introduced[34]. QPICs promise many key advantages, including scalable, easily reconfigurable architectures, small system footprint, enhanced light-matter interaction, high stability of optical elements and the interfacing with CMOS electronics, which can perform the control of optical circuits and auxiliary classical computation. However some stringent criteria are required for the realization of a QPIC: on-demand generation of high-purity quantum optical states of light, ultralow tolerance for losses and spectral mismatches, fast and high efficiency detectors.
Considering these criteria, almost every linear quantum information protocols can be realized in a QPIC containing these key components: pump sources, single- and entangled-photon sources, filters, waveguides, directional couplers, switches, quantum memories, detectors and fibre couplers. All these functionalities are challenging to implement within a single material. For this reason, several devices and small-circuits that address specific tasks have been developed in parallel for different materials. In the following each one of the main platforms (silicon-based, III-V semiconductors, diamond, others) is presented, in order to illustrate the range of opportunities offered by different materials. At the end, the progresses achieved in terms of integrating different devices are listed.

1.2.1 Silicon-based platforms

Silicon-based platforms include silica-on-silicon, silicon-on-insulator (SOI), and silicon nitride-on-silica. The first demonstrations of QPICs were made with silica-on-silicon waveguides[34]. Due to the large mode size, silica waveguides are easily interfaced with free-space optics and fibres, facilitating the first demonstrations of integrated circuits for LOQC type quantum gates[35]. Currently, SOI platform are replacing silicon-on-silicon[36], due to the higher refractive index of silicon compared to silica that allow smaller waveguide bend radius compared to that in silica waveguides. Moreover SOI platform offers two major advantages over other competing platforms: natural compatibility with

the CMOS industry, and extremely well developed fabrication techniques developed for silicon electronics and photonics.

Single-photon production on silicon chips is based on a spontaneous four-wave mixing (SFWM) process with quantum information primarily being encoded into the photon path[37].

This technique is based on the non-linear conversion of a bright pump into two correlated photons, the signal and the idler, which have a slightly different wavelength. Since the individual statistics for both the signal and idler photon numbers are Poissonian, single-photon generation requires the suppression of the probabilities for obtaining zero photons and more than one photon per pulse. The vacuum component is rejected employing the detection of one signal photon (herald) to flag the presence of the idler photon. The probabilities for two or more photons are reduced by attenuating the pump far below the level required to produce one pair on average. Standard telecom lasers can be used for pumping, but their on-chip integration will likely require heteroepitaxy or hybridization with another material[38]. However, the pump attenuation, which makes the generation process highly probabilistic, strongly reduces the applicability of these sources for large-scale quantum information processing. Moreover, the relatively narrow bandwidth of the SFWM emission in silicon complicates the pump filtering and requires a large number of highly resonant elements to achieve the desired pump extinction without affecting the signal and idler. Currently resonant attenuations of 50 dB and more can be obtained on chip[39]. After generation, photons are routed using silicon wire waveguides with sub-micron mode size, promising very large-scale integration[40]. Such waveguides, in combination with modulators can realize delay lines with small programmable fixed delay ranging from tens of ps to a few ns[41]. The telecom range photons can be detected on-chip using superconducting single-photon detectors (SSPDs)[42]. SSPDs have been integrated in silicon-based waveguides[43,44] showing great performance in term of jitter (tens of ps), efficiency (>90%) and dark count rates (<10Hz). However, it is an open question whether the operation of these detectors is compatible with non-linear sources and switching. Indeed the scattering of the high pump power outside the waveguide region cannot be easily suppressed using integrated filters, possibly resulting in spurious detector counts. At the same time, the reconfigurable elements within SOI circuits are based on the thermo-optic effect, meaning they are incompatible with the low-temperature operation stability required for the SSPDs.

1.2.2 Diamond-based platforms

Diamond has long been known as a material with exceptional mechanical, thermal and optical properties but difficult to synthesize and process. Thanks to recent developments on the fabrication techniques[45], diamond has emerged as a competitive platform for realizing highly functional QPICs[46]. The main advantage, that this material brings, is the

possibility to choose between hundreds of mid-gap defects (colour centres), some of which constitute outstanding quantum systems.

Mainly, two types of diamond platforms are in use. Bulk single-crystal diamond chips are preferred in situations where colour centres with superior properties are desired, although they are very difficult to process. Diamond-on-insulator (DOI) chips, in which polycrystalline diamond films[47] or crystalline diamond membranes[48] are grown on insulator substrate, making them a fabrication-friendly alternative.

Between the colour centres, two are of particular interest for QIP applications: nitrogen-vacancy (NV)[49] and silicon-vacancy (SiV)[50].

NV centres have their own electronic structure that can be optically addressed. Indeed optical read-out of the electronic spin state at room temperature has been demonstrated in early studies[51]. Moreover, they possess unrivalled electron spin coherence time, that coupled with the nuclear spins of diamonds, has allowed the demonstration of storage of quantum information[52] , quantum error correction[53] and coherent transfer of quantum information from a photon to a nuclear spin[54]. These functionalities make the NV centre a fully functional quantum memory and a register for fault-tolerant QIP.

However these experiments were limited by the low efficiency with which single-photons are collected from an NV centre in a bulk crystal[55], due to the presence of the phonon sideband.

Therefore improving the collection efficiency of single-photons is required in order to produce valid NV centre single-photon sources. Major improvements have been observed via the integration into photonic structures (e.g. waveguides, cavities, pillars)[56,57]; however it is still remain an large engineering challenge to position the NV centre at a location of intense optical field.

SiV centres possess lifetime-limited optical transitions with no spectral diffusion[58] and very small inhomogeneous linewidths[59]. Therefore they can be potentially used for scalable on-demand generation of indistinguishable single photons without need for frequency tuning[60]. Although, also in this case, the quantum efficiency is quite low and can be partially improved with integration of the colour centres into photonic structures[61]. Moreover the SiV electronic spin has a much shorter coherence time than that of the NV centre, and requires substantial magnetic field for optical addressing[62].

Diamond waveguide structures, based on total internal reflection, naturally provide an integrated highly efficient interface for colour centre manipulation and fluorescence collection. Free-standing photonic crystal cavities have been realized in diamond membranes grown on sacrificial substrate[63]. Moreover, NbN-based SSPDs, with good performance, have been fabricated on polycrystalline diamond surface grown via chemical vapour deposition on a silica-on silicon wafer[64].

The unique and diverse functionalities of colour centres, combined with the possibility of integration with the other above mentioned photonic components, could open the avenue for the integrated deterministic generation and manipulation of quantum information[46], that contrast with the inherently probabilistic operation of linear QPICs.

1.2.3 III-V semiconductor-based platforms

The use of III-V materials, especially GaAs and InP compounds, is very promising for QPICs, compared to other platforms.

Indeed, well-developed semiconductor laser technology allows on-chip integration of highly tunable pump sources with electrical injection[65]. Three-dimensional confinement of both electrons and holes in heterostructures gives rise to quantum dots (QDs) which potentially provide on-demand single-photon generation across the NIR range with near unity internal efficiency[66]. The on-demand emission of QDs constitutes a significant advantage over heralded single-photon sources realized with nonlinear parametric processes, although it requires cryogenic temperatures. Efficient photon collection is achieved mainly using integrated photonic crystal (PhC) structures, which allow over 98% coupling efficiency for QDs[67].

The combination of a diode junction and an embedded quantum dot has led to the demonstration of an electrically driven entangled-photon source[68] of quality sufficient to perform quantum teleportation[69]. Furthermore, the capability to manipulate the spin of electrons and holes populating the dot levels opens new avenues to spin-dependent propagation directions of single photons, in schemes that deviate from the original LOQC proposals[70].

Along with the availability of active quantum sources, III-V materials are characterized by a non-zero electro-optic coefficient. The use of electro-optic effects for the realization of phase-shifters[71] is particularly important, because allows the reconfiguration of these elements without interfering with the low-temperature optimum operation conditions of QDs sources and SSPDs.

Currently, GaAs is the most developed III-V photonic platform for quantum applications in terms of single quantum circuit elements[72]. GaAs has a high refractive index, allowing high density integration and strong light confinement in GaAs/AlGaAs waveguides. Moreover, SSPDs have been integrated on top of GaAs waveguides[73].

While each circuit element has been successfully developed on the III-V platform, the integration and control of these elements for producing large-scale QPICs is a big technological challenge. Indeed, photon indistinguishability between different QDs requires complicated system for tuning[74], larger linear losses in III-V based waveguides compared to Si-based waveguides limit the achievable circuit complexities and the detectors quantum efficiency has to be strongly improved in order to reach the near-unity efficiency. Additionally, in order to apply QDs for deterministic QIP, significant suppression of the decoherence mechanisms in QDs is needed.

1.2.4 Other platforms

Basic integrated quantum photonic functionalities have been demonstrated also in other material systems.
Lithium niobate (LN) is employed for integrated quantum optics since long time[75], therefore fabrication techniques are well developed. Single-photon sources, based on parametric processes on LN waveguides, have been used to generate high quality correlated photon pair[76]. Moreover fast electro-optic modulation[77] has been achieved in on-chip LN waveguides. However, LN devices are often large in size, and the experiments are mostly limited to quantum communication-related functionalities[78].
Silicon carbide (SiC) is a high bandgap group IV material, which, like diamond, offers a wide variety of colour centres. In contrast to diamond, fabrication techniques for SiC structures are better developed [79]. These colour centres can serve as bright and stable single-photon sources[80] and optically addressable spin qubits with coherence times approaching milliseconds[81]. The research on SiC colour centres is in its relatively early stages, as well as the implementation on this material of other components such as SSPDs.
Glass-based circuits, which can be patterned via femtosecond laser writing[82], offer a versatile way to prototype complex linear circuits made of several directional couplers. These can be controlled in polarization and along three-dimensions. They have been employed in first boson sampling circuits[83] and their subsequent verification protocols[14]. The integration of standard QPIC components such as single-photon sources and detectors as well as the control electronics is still an unresolved issue. Additionally, relatively small refractive index contrast in the waveguides prevents high density integration. Nonetheless, silicate glass circuits obtained by direct writing feature fast production, high fabrication tolerance, and great design flexibility.

1.2.5 Integration

While the development of single quantum photonic devices is very intense across many material platforms, the efficient integration of these devices on the same chip is required in order to exploit the real power of integrated quantum photonics.
A qualitative comparison of the different platforms, based on the degree of integration reported in literature, is shown in Tab. 1.1. Each platform is represented by a different colour and each line in the table corresponds to the integrated devices demonstrated within a single chip.
Si and $LiNbO_3$ display a high degree of integration, given their long history of development as photonic materials. However the diamond technology, in these later years, has developed so much that a chip containing almost all the required components has been realized[84]. In fact the single-photon emission from electrically-driven intrinsic carbon

nanotubes (CNTs) has been employed to prove on-chip generation, guiding and detection of single photons.

But, perhaps, only the III-V materials currently offer the entire range of required on-chip devices ranging from a pump laser to single-photon detectors. However, no system up to date demonstrates on-chip integration of all components.

Due to the strong requirements imposed on materials and great variety of devices needed to implement in a highly functional QPICs, one new approach based on heterogeneous integration is emerging lately. Indeed, optically[85] and electrically[86] pumped InAs/GaAs quantum dot lasers have been demonstrated by direct growth on Si substrates. Single-photon sources based on III-V QDs have been implemented on Si, using different techniques: from bonding of a GaAs chip containing QDs onto a silicon photonic chip containing single-qubit circuitry[87] to probe-based manipulation to integrate QDs into SiN waveguides[88] and onto MEMS[82]. Diamond micro waveguides containing single NV centres, used as single photon-sources, have been hybridized onto silicon chips [89].

A hybrid approach has also been utilized to increase SSPD fabrication yield, by bonding SiN membranes with pre-characterized superconducting nanowires to silicon and AlN waveguides[90].

Device hybridization is attractive to demonstrate high quality individual devices with high fabrication yield, but is a slow, costly and therefore less desirable procedure for industry-scale production. Composite wafers can be obtained by wafer bonding, but the resulting devices suffer from lack of uniformity and yield.

	Source Pump	Photon Source	Passive circuitry	Active circuitry	Photon Detector
SOI [91]		SFWM	WG, MMI	TOPS	
SOI [43]			WG, DC		NbN wire
Si_3N_4 [92]		SFWM	WG, DC	TOPS	
Si_3N_4 [44]			WG, DC		NbTiN wire
Diamond [84]	ED	CNT	WG, DC		NbN wire
InP [93]	SOA		WG, MMI	EOPM	
GaAs [94]		QD	WG		NbN wire
GaAs [95]*	ED	QD	WG, MMI		
$LiNbO_3$ [76]		SPDC	WG, DC	EOPM	
$LiNbO_3$ [96]			WG		NbN wire

Tab. 1.1 State-of-the-art integration of quantum photonic devices in on-chip circuits. Each plattform is differentiate by a colour.
CNT- carbon nanotube, DC- directional coupler, ED – electrically driven, EOPM – electro-optic phase modulator, MMI - multimode interference coupler, QD - quantum dot, SFWM – spontaneous four-wave mixing, SOA – semiconductor optical amplifier, SPDC – spontaneous parametric down conversion, TOPS – thermo-optic phase shifter, WG – waveguide.
* the integration with WG and MMI has been demostrated later with respect to the cited paper.

Heteroepitaxy may still be the preferred route towards achieving fully-functional QPICs, and so far only III-V compounds appear to cover the full range of required components. Therefore they appear a promising candidate for highly dense and functional QPICs in the long term.

Indeed for this work the platform chosen for the realization of the QPIC is GaAs. Fig. 1.3 shows a sketch of a prototypical QPIC based on a GaAs platform, where the generation, the manipulation, and the detection of single photons are carried out within a single chip. In order to erase the energy mismatch between multiple resonators and quantum dots, each cavity-emitter node is equipped with a dot-tuning and a cavity-tuning mechanism. These mechanisms are essential to overcome the initial energy detuning between remote sources and to produce indistinguishable single photons.

The generated single photons can be transferred to low-loss waveguides (WGs) via mode couplers. Linear optical components such as beam splitters (BSs) and phase shifters (PSs) can be designed to implement probabilistic logic gates for LOQC computation.

Lastly, waveguide-coupled superconducting single-photon detectors can be employed to convert the optical signal into electrical pulses.

In the following paragraphs, the two active components (single-photon sources and detectors) of this prototypical QPIC are going to be detailed introduced.

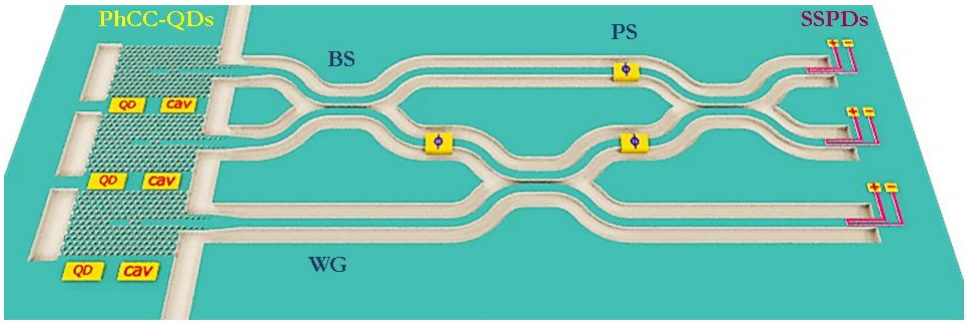

Fig. 1.3 Prototype of a GaAs-based QPIC. Single photons generated in PhC cavities are transferred to waveguides (WGs). A reconfigurable network of splitters (BSs) and phase shifters (PSs) allows the linear manipulation of the quantum states of the light and - in the example reported here- the realization of a probabilistic CNOT gate. A set of SSPDs generates electrical signals by single-photons absorption. Courtesy of Dr. M. Petruzzella.

1.3 Single-photon source

Semiconductor quantum dots have been shown to be nearly ideal sources of non-classical light that can be efficiently routed into nanophotonic circuits. As previously explained QDs offer the advantage of much higher efficiency and easier filtering of the pump beam, compared to other integrated single-photon sources such as the ones used in Si-based or LN platforms. Moreover, approaches to reproducibly control the exciton and cavity energy on-chip, have been developed, in order to produce indistinguishable single photons.
In the following, the QDs are firstly presented, then the PhC cavities, and finally two approaches to tune QDs and cavities.

1.3.1 Quantum dots

When a semiconductor material layer is embedded in a semiconductor with a higher bandgap a potential well for the charge carriers is formed. If the dimension of the well is smaller than de Broglie wavelength of the charge carriers, quantum mechanical effects start to govern the physics of the structure. In this situation the energy of the system is quantized and according to the dimensionality of the confinement different structures can form (for 1D, 2D and 3D confinements, quantum wells, quantum wires and quantum dots, respectively). In the case of 3D confinement the density of the states will show a delta function behaviour similar to an atom.
Employing a molecular beam epitaxy (MBE) system, layers of lattice-mismatched semiconductor materials are deposited on top of each other, in order to create QDs[97] embedded in the semiconductor layer. The lattice mismatch creates strain which leads to the formation of self-assembled 3D islands (Fig. 1.4 a inset), this technique of QDs growth is known as Stranski-Krastanov[98]. For this work, a layer of InAs is deposited on top of GaAs, with a lattice mismatch of 7%. The creation of small InAs islands is energetically favourable, but the nucleation process is purely random with no control over the spatial position of the dot, unless prepatterning of the surface is used, resulting in site-controlled QDs[99]. Dots grown using this technique have diameters in the range of 10-30 nm and heights varying from 1 to 10 nm. As a final step, the dots are typically capped with GaAs to limit the effects of oxidation and non-radiative channels from the presence of surface states. For quantum optics experiments it is crucial to control the dot density in order to isolate single dot lines. This can be achieved by carefully tuning the temperature and the nucleation rate during the growth. In this way it is possible to grow dots with density below 5-10 QDs per μm^2, as for the samples used for this work[100] (Fig 1.4 a).

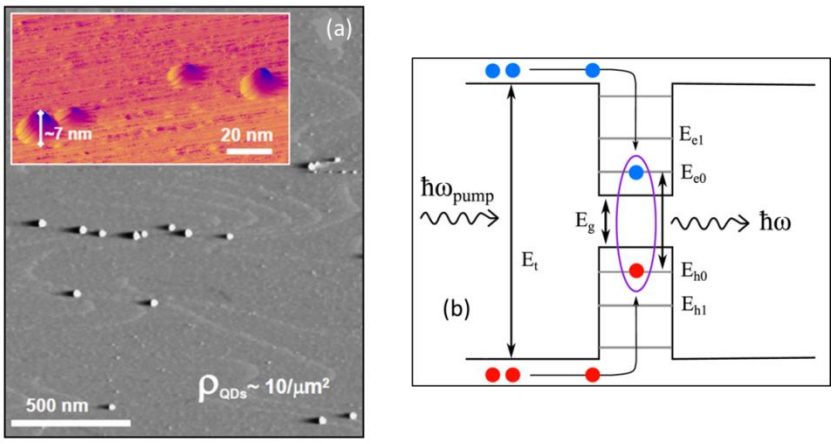

Fig. 1.4 a) Atomic Force Microscope image of low-density self-assembled InAs QDs on GaAs. Inset: detail of the dimension of a self-assembled QDs (courtesy of Dr. T.Xia). b) Typical energy diagram of the QD heterostructures, where the pumped electron recombines with the hole in valance band and emits a photon with a frequency equal to the difference in energy levels.

As indicated in the energy diagram of a typical QDs (Fig. 1.4 b), an electron can be excited and brought to the conduction band leaving an available state in the valence band. It is usually convenient to consider the valence band as having a hole instead of missing an electron. The interaction of an electron and a hole creates a bound state which is called an exciton. Generation of an electron-hole pair can be achieved electrically or optically (for example by pumping the electron by an off-resonant laser to a higher energy state which decays quickly to the excited state). When an electron from the conduction band recombines with a hole in the valence band emits a single photon (with the same frequency as the energy of the exciton). The observation of sharp atomic-like (single QD) lines (with linewidth < 200 μeV) can be achieved only at low temperatures (< 50K) since at higher temperatures the linewidth broadening of the QDs increases due to their increased interaction rates with the phonons, which makes the observation of the sharp QD lines impossible[101]. A linewidth smaller than 1meV is indeed necessary in order to isolate the emission of a single excitons from the one of biexcitons or multi-exciton complexes, which would spoil the photon statistics. Moreover, QDs emit photons with a specific polarization, due to a dominant quantization axis along the growth direction [001]. The polarization of the emitted photon lies in the plane perpendicular to the [001] crystallographic direction and couples with the transverse electric (TE) polarized modes of a PhC cavity[97].

The QDs used for this work have low-temperature emission wavelengths between 1200-1300 nm and linewidths between 20-180 μeV.

1.3.2 Photonic crystal cavities

Cavities are important for two reasons: to increase the collection efficiency from single emitters and to produce indistinguishable single photons. The need of a photonic structure to maximize the number of collected photons arises from the low coupling efficiency ("spontaneous emission coupling factor") from a QD to the mode of a standard waveguide. Moreover, any scattering event with phonons limits the coherence properties of quantum dots and thereby reduces the indistinguishability[97]. In order to reduce the decoherence, two approaches can be applied. In one approach the exciton can be forced to emit faster before the occurrence of scattering processes. In this case the acceleration of the spontaneous emission can be obtained through the Purcell effect by positioning the emitter inside a resonant cavity[102]. In the other approach the dot can be excited using a resonant laser to limit the influence of the fluctuating carriers produced by the non-resonant excitation (resonance fluorescence method)[103].

For the prototype QPIC proposed in this work (Fig 1.3) the integration of emitters with cavities is the followed approach to reduce the QDs decoherence. In particular photonic crystal cavities (PhCCs) have been chosen for light confinement.

Photonic crystals are structures where the refractive index of the dielectric is modulated periodically[104]. In a strong analogy with the electronic potential produced by the regular arrangements of nuclei in a crystalline solid, a periodic modulation of the dielectric constant over a sub-wavelength scale can originate bandgaps for photons.

The dielectric permittivity (ε) of a PhC has a discrete translation symmetry and can be written as $\boldsymbol{\varepsilon(r+R) = \varepsilon(r)}$, for every position of the space r and with $R = n_x a_x + n_y a_y + n_z a_z$ (n_i are integers and a_i the basis vectors of the lattice). The solutions of the Maxwell's equations in this lattice are eigenfunctions of the form:

$$\mathbf{E_k(r)} = \mathbf{u_k(r)}\, e^{i\mathbf{kr}} \qquad (1.1)$$

where k is known as Bloch wave-vector and spans over the first Brillouin zone of the reciprocal space. The expression of the electric field differs from a plane wave due to the periodic part of the Bloch function $\mathbf{u_k(r)}$, which inherits the symmetry of the crystal, $\mathbf{u_k(r) = u_k(r+R)}$.

In this way it is possible to construct a band diagram which provides the dispersion relation $\omega(\mathbf{k})$ between the frequency and the wave vector. For each $\mathbf{k}$ the range of accepted frequencies can be extracted from this band diagram. Depending on the parameters of the lattice (refractive index, lattice constant, etc.), there might be a range of frequencies where the light cannot propagate within the crystal. These frequencies are called photonic bandgaps. An example of band diagram calculations is shown in Fig. 1.5 a.

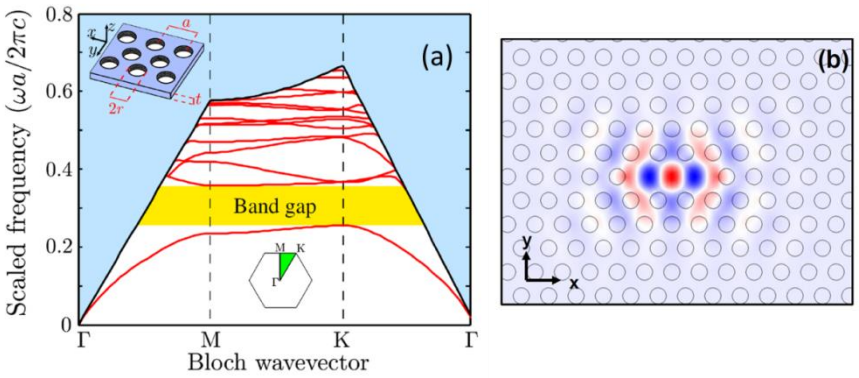

Fig. 1.5 a) Calculated band diagram of a triangular PhC made of holes etched in a GaAs slab for the TE-like mode. The blue shading shows the continuum of radiation inside the light cone and the yellow area indicates the photonic bandgap[104]. The inset shows the high symmetry points of the first Brillouin zone. b) Simulated Y-component of the electric field for a L3 PhC cavity[104].

The refractive index periodicity can exist in 1, 2 and 3 dimensions, however only 2D PhC slab[105] are going to be considered in this work. They consist of a thin semiconductor membrane, where an array of holes has been drilled, surrounded by a cladding of lower refractive index (n_{clad}), such as air. One of the main advantages of these structures is that they can be engineered for in-plane coupling to a circuit, which is essential for the realization of QPICs.

In a PhCC slab, light is confined in the plane due to the Bragg reflection of the photonic crystal and in the vertical direction z by total internal reflection. However, decomposing the **k** vector in vertical component (k_z) and in-plane component ($\mathbf{k}_\parallel$), modes with small in-plane component (from the Snell's law: $\mathbf{k}_\parallel < n_{clad}\omega/c$) exist inside the light-cone and form a loss radiation channel outside the plane of the membrane. These modes are called leaky modes.

By introducing defects in the crystal structure of a photonic bandgap material (for example by removing some holes in a slab PhC), localized modes (with frequencies within the photonic bandgap) will be allowed to exist in that defect while forbidden to propagate within the crystal (Fig. 1.5 b). In this way it is possible to create optical confinement to realize waveguides (PhCWGs) or cavities (PhCCs).

While in a standard 2D waveguides two kinds of modes are supported: the electric transverse (TE) modes (electric field polarized in the plane of the membrane) and transverse magnetic (TM) modes (magnetic field polarized in the plane of the membrane). In a PhCWG only the TE modes propagates, due to the absence of a TM photonic bandgap. Therefore, since QDs have a preferential polarization that perfectly couples with the TE modes, the emitted photons will propagate in a PhCWG only in TE polarization.

Two important figure of merit of a PhCC to determine the interaction with the QDs are the mode volume (V) of the cavity and the quality factor (Q). The quality factor is defined as the ratio between the total energy stored in the cavity (ω) and the total energy loss rate (κ)

considering both radiation into light cone and fabrication imperfection. The ratio Q/V is used to determine the Purcell-enhancement of an emitter positioned in the field maximum, matched in frequency and polarization with the cavity mode, as follow[106]:

$$F_P = \frac{3}{4\pi^2}\left(\frac{\lambda}{n}\right)^3 \frac{Q}{V}. \qquad (1.2)$$

1.3.3 Quantum dot tuning

An efficient coupling of QDs with PhCCs is crucial for the implementation of quantum architectures that need single-photon sources with high quantum efficiency, coherence and reproducibility. Unfortunately spatial and spectral matching between these two components is not easy to achieve. A qualitative estimation for a low-Q (1000) cavity gives probability of spectral resonance of 10%, which drastically decreases considering higher-Q cavities.

Additionally, as already mentioned, the energy of the QD excitonic states is not exactly the same for different QDs, since they have slightly different shapes, sizes and chemical compositions, due to the stochastic nature of their nucleation process. The energy broadening associated with this physical inhomogeneity can span up to 20 meV, or even more for distant dots. Therefore the capability to independently govern the energy of cavities and emitters is of fundamental importance for any QPI application.

The emitter-cavity spatial matching has been addressed with different techniques such as prepatterning of the substrate, resulting in site-controlled QDs[99] or patterning of a proper PhCC around a quantum emitter previously characterized in position and spectrum with microscopic techniques[107]. Also for the emitter-cavity spectral matching different techniques have been developed and few of the most relevant for tuning post-processing the QDs emission energy are going to be presented in the following.

One of the easiest techniques to implement is the thermal tuning. Both the cavity modes and the QDs emission can be tuned by changing the temperature of their environment. Due to the thermo-optics effect the electronic bandgap of the semiconductor is modified by the temperature variation with a consequent modification of the exciton energy[108]. The average QD emission tuning rate is of 0.35nm/K[109]. The sample can be heated up by heaters inside the cryostat or by the opto-thermal method with a power-tunable laser focused on the device. However tuning through thermal heating presents several drawbacks: small tunability range below 9K, QDs tunability not independent from the one of the cavity, incompatibility with other QPIC components such as superconducting detectors.

Other explored techniques for QDs tuning are: magnetic field[110], strain[111], optical Stark effect[112], free carrier injection[113]. However all these tuning methods could either strongly affect the other components of the QPIC or do not guarantee independent tunability of QDs and cavities.

Instead, electric field tuning, specifically using Stark diodes, appears to be the most promising in terms of independent tunability and compatibility. Since the QD emission is determined by its discrete energy levels, an external electric field can be used to modify in a perturbative manner the permanent QD dipole, therefore shifting the excitonic energy. The energy shift due to the applied electric field is known as quantum confined Stark effect (QCSE).
The implementation of the QCSE can be achieved by integrating the quantum emitter inside the intrinsic region of a semiconductor heterojunction like a p-i-n diode. The band bending provided by the electric field across the junction is responsible for the energy tuning and in principle high tuning range and ultrafast modulation can be obtained[114]. By sandwiching
the QD with thin AlGaAs barriers to reduce the tunnelling effect of carrier across the bias-induce triangular potential, a giant Stark tuning of about 30 nm can be obtained for multiple excitonic complexes inside a single QD under biases up to 300 kV/cm[115]. The spontaneous emission enhancement of single QDs tuned in resonance with a PhCC by means of electric field in diode structures was reported by several groups[116-118]. In this work the tentative implementation of diodes for Stark tuning in a QPIC is presented in Chap. 4.3.

1.3.4 Photonic crystal cavities tuning

The quality factor and the resonant wavelength of a photonic crystal cavity are extremely sensitive to the configuration of the periodic hole pattern. In fact, small random variations (order of few nanometres) in the positions and radii of the PhC holes, arising from the unavoidable imperfections in the fabrication process, can drastically alter the optical properties of a PhCC. In particular, this fabrication uncertainty is translated into a dispersion of the resonant wavelengths of ≈10nm for nominally identical cavities, without taking into account the variation over different fabrication runs. Designs to mitigate the effect of disorder on the Q-factor have been proposed[119], as well as lithographic tuning[120], which consists in making several copies of a cavity with varying lattice constant, expecting that one of them has the desired nominal parameters. Nevertheless, the cavity wavelength can fluctuate during time by ageing effects and oxidation[121], therefore also in this case a post-processing control is a necessary tool for the realization of a reliable single-photon source.
Also in this case several tuning technique have been explored over the years. Some techniques such as oxidation[122] or deposition of dielectric layers[123] are not reversible methods. Others, such as near-field probes[124] or fluid infiltration[125], cannot be used for tuning at cryogenic temperatures. Adsorption of gasses[126] can be used to change the refractive index. The adsorption process can be actively controlled by inputting a certain amount of Xe or Ne through an external tank inside the cryostat and the heating of a laser

be used to restore the energy of the cavity to its initial value. However, it is questionable whether the gas-based methods can offer a reproducible and continuous control for wavelength tuning.

Methods based on optical nonlinear effects, such as thermal tuning or free-carriers injection, can be used for QDs tuning as well as for cavity tuning. However, this implies that they cannot provide an independent control of the two components.

Nano-opto-electro-mechanical systems (NOEMSs) have been employed in a number of ways to reconfigure the wavelength and the mode profile of a cavity[127]. For example near-field probe techniques have been employed via electromechanical actuation of a dielectric tip integrated on a chip with the PhCC[128,129]. Although these methods allow a controllable red-shift lying in the nanometre range, the Q-factor can be strongly affected by the additional losses introduced by the perturbation.

Electromechanical systems have been also adopted to re-configure discrete parts of a photonic crystal cavity. For example, 1D PhC nanobeam can be separated in two parts along the axial direction, with the possibility to tune the gap in between[130], or varying the out-of-plane[131] or in-plane[132] position of the beam. In general, since the field maximum is located in the air region, these cavities cannot be employed to enhance the emission of quantum dots located in the semiconductor region.

A more convenient approach, which ensures both a high tunability and high field intensity at the dot location, is based on coupled photonic crystal cavities, which have been coupled both laterally[133] and vertically[134]. In this thesis, this last approach has been considered for cavity tuning, and the tentative implementation within a QPIC including superconducting detectors is presented in Chap. 4.3.

The vertical coupling of two photonic crystal cavities is realized using two thin parallel membranes and modifying the distance between them electromechanically (Fig. 1.6 a). The idea, theoretically proposed by Notomi et al.[135], allows widely tunable PhCCs with low Q losses and with the possibility of embedding QDs in the membrane. The basic principle of operation of a double-membrane NOEMS relies in the alteration of the effective refractive index in a 2D PhCC. If two identical parallel membranes are brought at small distances such that the evanescent tail of each guided mode penetrates the other slab, they form a coupled system. The mode energy splits and results in two decoupled modes delocalized over the two membranes. These modes are called symmetric (S) and anti-symmetric (AS) from the profile of their electric field (Fig. 1.6 b). When the inter-membrane distance (d) is changed, a change in the cavities coupling occurs and the two modes, S and AS, change frequency. The frequency tuning as function of the inter-membrane separation is shown in Fig. 1.6 c.

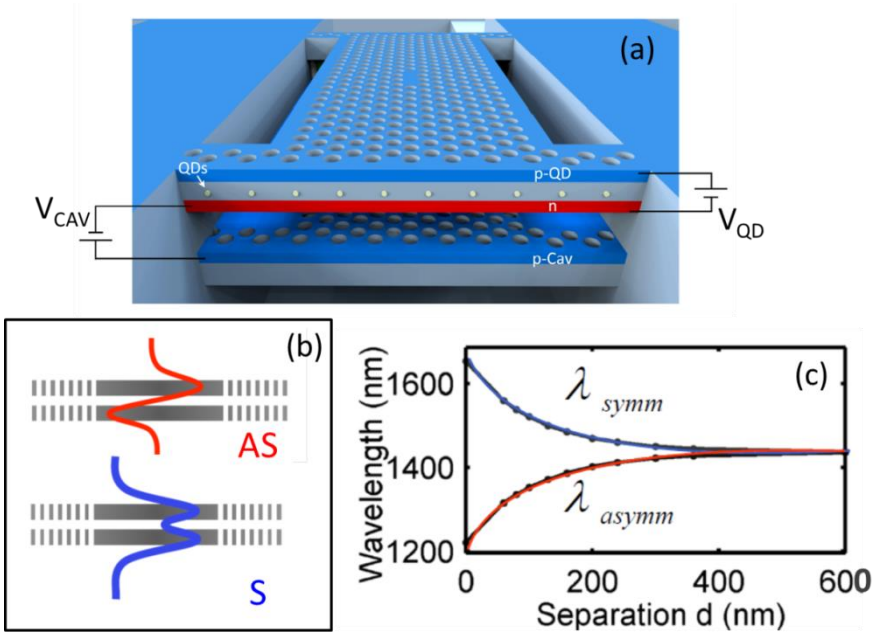

Fig. 1.6 a) Sketch of the double-membrane NOEMS device, including the top p-i-n diode for QD tuning and the bottom n-i-p diode for the cavity actuation[74]. b) Sketch of the antisymmetric (AS) and symmetric modes electric field profiles. c) Simulations of the PhCC mode tuning as a function of the intermembrane separation d[134].

The displacement of the slabs can be achieved electromechanically using an electrostatic actuator. The electrostatic force is obtained from the separation of charges across an insulating material through metallic contacts (a capacitor). A p-i-n junction operated in reverse bias behaves very similarly to a charged capacitor. The accumulation of electrons and holes in the p and n doped regions respectively, results in an attractive force which displaces the two semiconductor slabs. When the bias is removed the original position is restored thanks to the elasticity of the semiconductor.

This double-membrane NOEMS together with the QD p-i-n diode allowed the realization of a working cavity-emitter node, like the one shown in Fig. 1.3. By independently controlling the Stark voltage applied to the emitters and the distance between the two PhC slabs, the tuning of the on-chip cavity-emitter node has been demonstrated, showing a large Purcell enhancement of a QD transition[74]. Moreover the on-chip implementation of such cavity-emitter nodes with ridge waveguides and 50:50 beam splitters has been proved[136]. Therefore the integration of such components with superconducting single-photon detectors, would be the final step toward the realization of a fully-working QPIC on monolithic platform like the one proposed in Fig. 1.3.

1.4 Single-photon detector (SPD)

The other key component of a quantum integrated photonic circuit is the single-photon detector (SPD). An SPD typically produces an electrical signal after absorption of a photon. The main figures of merit characterizing an SPD are the spectral range, the dark count rate, the detection efficiency, the dead time, the timing jitter and the photon number resolution capability.
The spectral range is the interval of wavelengths to which the detector is sensitive. A dark count is a detection event not triggered by the absorption of a photon in the wavelength range of interest. The dark count rate (DCR) is the number of such false detection events recorded in one second. The detection efficiency is the efficiency with which a photon triggers a detection event. The dead time is the time interval that the detector needs to reset in order to be able to detect the next photon. The timing jitter is the variation in the time span between the photon absorption and the appearance of a voltage pulse at the output, which sets the timing resolution. The photon number resolution capability is the ability of a detector to distinguish how many photons are simultaneously absorbed.
In the ideal case, a perfect single photon detector provides unitary detection efficiency and jitter, dead time and DCR that are equal to zero.
The SPD can be classified in two main groups, based on the material where photon absorption takes place: semiconducting ones, including photo-multiplier tubes (PMTs) and single-photon avalanche detectors (SPAD), and superconducting ones, including transition-edge sensors (TESs) and superconducting single-photon detectors (SSPDs).

Photomultiplier tube (PMT)

The PMT was the first reported device able to detect single-photons[137, 138]. A PMT consist of a vacuum chamber containing an anode, several dynodes and a photocathode made of a low work function material, typically a semiconductor (e.g. GaAs). When a photon strikes the photocathode it extracts an electron that is accelerated toward the first dynode and provokes emission of secondary electrons upon impact. The consecutive impact of the latter on other dynodes multiplies the number of electrons that will eventually fall on the anode. Due to the avalanche-like mechanism, the electron flow to the anode results in a measurable current. The choice for the photocathode material not only determines the spectral range to which the PMT is sensitive, but can also make the PMT sensitive to the photon number. Indeed, if the photocathode is chosen such that the energy carried by two photons is required to eject the primary photon, the PMT can be used as a two-photon detector. The detection efficiency of a typical PMT is $\sim$ 40% at λ=500nm, but only $\sim$ 2% at the wavelength interesting for telecommunication applications, λ=1550nm. Moreover they are not suitable for integration.

Single-photon avalanche diode (SPAD)

The SPAD is an avalanche photodiode running in the so-called "Geiger" mode. In this mode, a reverse bias voltage larger than the breakdown voltage is applied to the diode. When a photon is absorbed, an electron-hole pair is created. The electric field is such to accelerate the electron and generate an avalanche of electrons through impact ionization with lattice atoms. In this condition, the flow of electrons results in a macroscopic and self-sustaining current that indicates the absorption of a single-photon. In order to give the detector the possibility to reset, the external circuit is designed to quench the avalanche process.

The choice of the semiconductor material determines the spectral sensitivity of the SPAD. For example, InGaAs SPADs have a spectral cut-off for absorption at λ=1652nm, therefore suitable for telecommunication applications. InGaAs SPAD typically have detection efficiency of 15% and few tens of Hz of DCR[139], although different combinations of efficiency and DCRs are also possible. However they supply for the relatively low efficiency and high DCR, with very low jitter (<0.1ns) and dead time (~10ns), which for gated-devices can go even lower arriving to a record count rate of 1.5GHz[140], although suitable only for limited applications (e.g. QKD). Moreover, as well as for the PMTs, they do not require cryogenic temperature to operate, but, differently than PMT, they are in principle suitable for on-chip integration, as it has been proved for CMOS circuits[141], but not yet for InGaAs SPADs.

Transition-edge sensor (TES)

The TES is a thermal detector that measures the energy of an optical pulse. It consists of a thin superconducting film deposited on an insulating substrate. The substrate is kept at a base temperature that is chosen in such a way to maintain the film at its transition between the superconducting and the normal state, where the film resistance strongly depends on temperature. In this condition, the absorption of a photon causes a small variation in the film temperature which corresponds in a measurable change of film resistance. The selected base temperature prevents the fast cooling down of the electrons via the substrate, however a negative electro-thermal feedback allows the device to reset for a new photo-detection.

The TES has photon number resolving capabilities due to its working principle. Indeed, the absorption of more than one photon results in a consistently higher change in film resistance.

The spectral sensitivity can be tuned with the choice of the anti-reflection coating deposited on the thin film or with the use of a cavity designed for certain wavelengths. At telecom wavelength a detector efficiency of 90% with very low DCR has been achieved for these detectors[142]. However they are characterized by a long dead time (max. count rate 0.1 MHz) and large jitter (100ns), moreover they require an operational temperature

of 100mK. Due to the slow response TESs are unsuited for high-speed QIP, but are suitable for photonic integration how it has been demonstrated[143].
The perfect compromise, between high speed, high efficiency, not too low operational temperature and on-chip integrability, is represented by SSPDs. Indeed, for the detector component of the proposed QPIC (Fig. 1.3), this kind of SPD is the one chosen.

1.4.1 Superconducting single-photon detectors (SSPD)

The concept of SSPD was first proposed and demonstrated in 2001 by Golt'sman et. al.[42] The first proposed structure was based on 5 nm-thick and 200 nm-wide NbN nanowire, that was later modified towards narrower wires (100nm) folded into a meander (Fig. 1.7 b) to increase the active interaction area with the incoming photons. When such wires are kept well below the critical temperature Tc of the chosen superconducting film and biased just below its critical current Ic the absorption of a photon can be registered.
The first suggested working mechanism was the hotspot model[42,144], later refined in 2005[145]. This model is schematized in Fig. 1.7 a.

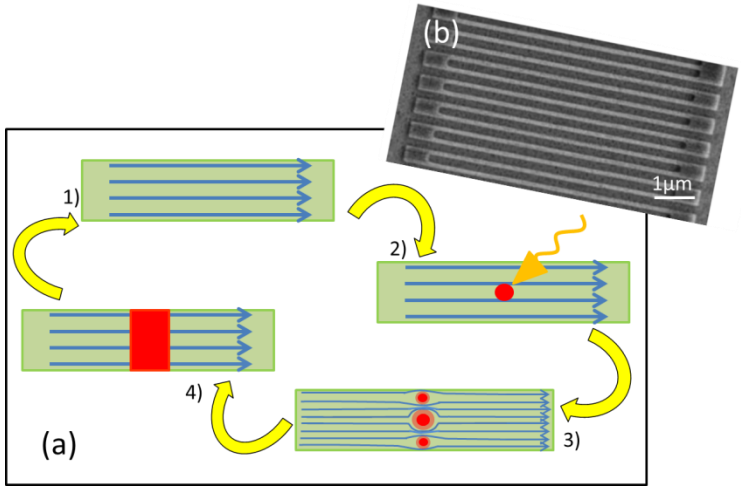

Fig. 1.7 a) Schematic of the hotspot model: 1. the wire is biased with bias current close to its critical current, 2. a photon is absorbed in the wire and creates an hotspot (red spot), 3. the supercurrent is forced to flow along the periphery of the hotspot, the local current density in these areas becomes higher than the critical current creating resistive regions, 4. a resistive belt across the wire is formed. b) SEM image of a meander SSPD.

When an incident photon with energy of hν is absorbed, it breaks a Cooper pair in the wire, this creates a highly energetic quasi-particle. During the relaxation process, this quasi-particle breaks new pairs successively by inelastic electron-electron (e^- - e^-) scattering, causing an avalanche of quasi-electrons from other broken Cooper pairs. The formation of hot-electrons can cause the creation of a resistive region called 'hotspot' in the wire. When the energy of the quasi-electrons becomes close to the superconducting

bandgap energy, the quasi-electrons start to recombine and the interaction of the quasi-electrons with the phonons (e^- - ph interaction) dominates over e^- - e^- interaction, therefore the energy of the quasi-particle is dissipated as heat in the material. The photon-induced hotspot is in the scale of few tens of nanometres in diameter depending on the incident photon energy. Therefore, the hotspot is not enough by itself to make the whole section of the wire resistive. Due to the formation of the hotspot, however, the current avoids the resistive region and is expelled to the side-walks (Fig. 1.7 a step 3). This current redistribution can trigger the transition to the normal state across the entire wire, according to the original hot-spot model, (Fig. 1.7 a step 4). This transition from superconducting to normal state is detected as a voltage pulse. The hotspot model is very intuitive and can explain the detection of high energy photons (UV and visible range). For less energetic photons (NIR range) the model suggests a sharp spectral cut-off in the detection efficiency; however a monotonous decrease as function of the photons wavelength has been experimentally observed [145].

Therefore the model was refined in 2005. Unlike the hotspot model which assumes that all quasi-particles are concentrated in a small cylinder around the hotspot (where the photon is absorbed), the refined hotspot model considers the diffusion of non-equilibrium quasiparticles from the photon absorption spot, in the still superconducting neighbourhood across the wire. The formation of a resistive state due to the redistribution of the supercurrent can also occur without the formation of a normal region. This model manage to correctly predict the wavelength of the knee-like point ($\lambda_{cut\text{-}off}$) after which the monotonous decrease starts, however it still fails to describe the behaviour for higher wavelengths (Fig. 1.8 a).

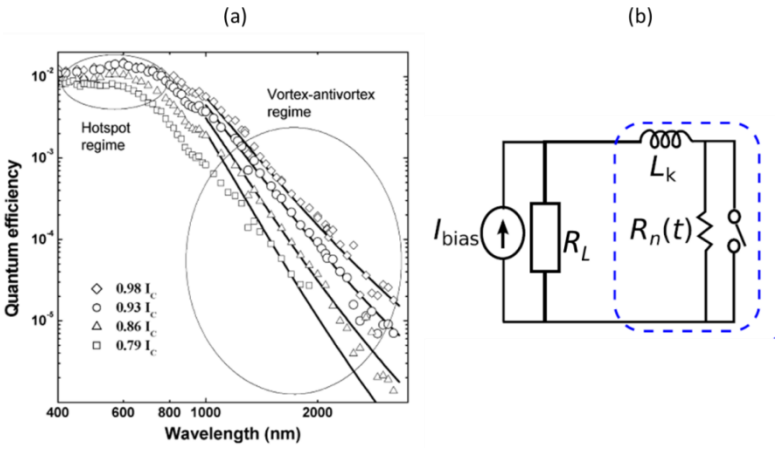

Fig. 1.8 a) Spectral dependence of the SSPDs. While the detection of the high-energy photons is explained by hotspot mechanism, detection at long wavelengths is explained by vortex-antivortex pair or vortex unbinding mechanisms[146]. b) A simple electrical equivalent circuit of a SSPD. L_k is the kinetic inductance of the nanowire and R_n is the hotspot resistance. The SSPD is current biased at I_{bias}. Opening and closing the switch simulates the absorption of a photon. An output pulse is measured acrossthe load resistance R_L.

A possible cause of the slow roll-off for the detection efficiency was first put forward by Semenov et al. in 2008[146], suggesting vortex-assisted detection events. When a photon with wavelength beyond $\lambda_{cut\text{-}off}$ is absorbed, the perturbation of the superconducting state is not enough to trigger a detection event but can enhance the probability for thermal activation of a vortex-antivortex pair (VAP) unbinding. Then, under the effect of the Lorentz force, the vortex and antivortex are dragged toward opposite wire edges. During their motion, the vortex and antivortex dissipate energy giving rise to a detection event. The VAP unbinding is not the only mechanism proposed to explain the slow roll-off in the detection efficiency. The other suggested vortex mechanisms, the one for which the photon absorption lowers the potential barrier for the vortexes to enter the nanowires[147] is energetically the most favourable. An experimental test reported by Renema et al. in 2014[148] suggests how the combination between quasi-particle diffusion and vortex unbinding is the key to explain the detection mechanism of the SSPDs.
If the mechanism that creates the resistive region in the nanowires is still under debate, what happens after that it is very clear.
In fact, an SSPD can be considered as a switch in parallel with a high resistor (R_n) and connected in series to a kinetic inductance L_k (Fig. 1.8 b). When the SSPD is in the superconducting state, the switch is closed and the supercurrent flows through it without encountering any resistance. As soon as the transition to the normal state takes place, the switch opens and the current, which keeps on flowing through the device, encounters the resistance R_n. Due to Joule heating, the dimension of the normal section tends to increase. This process is counteracted by the electro-thermal feedback[149]. Since R_n is much higher than the load resistance ($R_L = 50\Omega$), the current will be diverted toward the branch parallel to the SSPD giving rise to a measurable voltage pulse. In this way, the current through the SSPD decreases with a time constant $\tau_{fall} = L_k/[50\Omega+R_n]$ so that the device can cool down and recover for the next detection event. Once the SSPD is again superconducting, the current will recover with a time constant $\tau_e = L_k/50\Omega$. Therefore the total time constant is $\tau = \tau_{fall} + \tau_e$. However, considering $R_n >> 50\Omega$, the total time constant τ can be approximated to the only τ_e component. The time required to the wire to recover 95% of its bias value is around $3\tau_e$ and it is called dead time[149]. The dead time together with other performance parameters of an SSPD are going to be discussed in more detail in the following.

1.4.2 SSPD performance parameters

Since the first demonstration of a NbN based SSPD in 2001[42] the field developed and matured to the point that SSPDs are now a commercially available product. Significant technological progress has been made in the subsequent years in order to produce SSPDs with the best possible performance; however there are still few limitations (relatively long dead time, fabrication yield, and low operation temperature) that can be addressed in order to make them the best solution in terms of SPD.

Quantum efficiency (QE)

QE is the probability that an incident photon generates a measurable signal. Throughout this thesis, the quantum efficiency is referred as percentage, with a maximum QE corresponding to 100 %. There are two sub-definitions of the QE such as the device quantum efficiency (DQE) and the system quantum efficiency (SQE).
The DQE is an intrinsic property of the detector which is directly related with the material and the geometry. It is defined as the probability that the detector clicks when a photon is incident on its active area. It is equal to the product of the absorptance (A) and the internal quantum efficiency (η_i) defined as the probability of forming a voltage output upon absorption of a photon:

$$DQE = A \cdot \eta_i \qquad (1.3)$$

This value does not include any possible losses that occur before the photon arrives to the detector active region. Therefore, for fibre-based or free-space experiments, another efficiency definition is used: the SQE. SQE is the probability that the detector clicks if a photon is incident at the input of the detection system (e.g. input fibre, microscope objective, etc.). It is equal to the product of the DQE and the coupling efficiency (η_c) of the light to the device:

$$SQE = DQE \cdot \eta_c \qquad (1.4)$$

The coupling efficiency comprises any loss between the input and the detector. In this work, in which the detectors are integrated on top of GaAs waveguides, it is fundamental to experimentally estimate η_c such to derive the DQE. If the photon source is outside of the integrated chip, the η_c has to takes into account the loss between the input fibre and the waveguide, due to facet reflection and mode overlap, other than the waveguide losses. However if the source is integrated in the same chip, the coupling efficiency is reduced only to the waveguide losses; therefore the concept of SQE is basically not relevant anymore. Since in this thesis all the photonic components are integrated in the same chip, the DQE is the only interesting parameter and has been calculated as follows:

$$DQE = \frac{N_c}{N_\Phi} \qquad (1.5)$$

where N_c is the number of counts, calculated as difference between the photon counts and the dark counts, and N_Φ the number of photons incident on the detectors. If an external photon source is used, such as a laser, N_Φ can be calculated as follow:

$$N_\Phi = \frac{P\lambda}{hc} \cdot \eta_c \qquad (1.6)$$

the laser power P corrected by the coupling efficiency, divided by the photon energy hc/λ. Moreover, for measurements with top coupling excitation through a microscope objective, N_Φ has been multiplied by the ratio A_d/A_l, where A_d is the detector active area (wire width + pitch for the wire length) and A_l is the laser spot area. In this way, considering the consistent difference between those two areas, all the photons not falling within the detector active area have been excluded.

The value of QE depends on the bias current I_b and it increases exponentially with I_b at low currents, due to the increasing internal quantum efficiency, until it reaches a saturation, corresponding to unity internal efficiency for the best detectors[150]. Indeed, for higher currents it is more likely that the hot-spot produced by photon absorption results in a transition to the resistive state. In order to operate the detector with a high efficiency, it is very common to bias a detector as close as possible to the critical current, even though also the DCR is higher.

The quantum efficiency of the SSPDs can be optimized, bringing the three component η_c, A and η_i as close as possible to unity. For example, in the case of an external photon source, the coupling efficiency η_c was increased at the very beginning introducing the meander design[151], that has a bigger active area to interact with the impinging photons, rather than one single nanowire. More recently η_c has been further improved using an optical self-alignment mechanism between the fibre tip and the SSPD meander, with a precision of 3μm that allowed obtaining a SQE of 93%[152].

The absorptance A is limited by the ultrathin thickness of the superconducting film. The calculated theoretical limits for a 5nm thick film are for example 30% on sapphire[153] and 10% on GaAs[154]. In order to address this limitation, optical cavities or waveguides are used to enhance the absorptance.

The use of optical cavities helps to maintain the photons of a selected wavelength trapped inside the cavity until they are absorbed by the detectors. Meander SSPDs inside optical cavities have been demonstrated, achieving 93% of SQE with WSi[152] films and 80% of SQE with NbN films[155]. Currently the major companies selling SSPDs use optical cavities in their systems.

The absorption efficiency can be also enhanced by exploiting the waveguide geometry where the travelling wave is evanescently coupled to the detector. The waveguide SSPD approach benefits from the high modal absorption of the guided mode that allows unity absorptance with waveguide lengths of a few tens of micrometers. The maximum efficiency has been reported on NbN nanowires patterned on Si waveguide and with a DQE that reaches the 91 % at the maximum bias current[43]. Waveguide SSPDs have been demonstrated on SiN using NbTiN wires[44] and WSi wires[156], on GaAs[73] using NbN wires and on diamond using NbN wires[64]. Moreover NbTiN wires have been integrated on top of Si nanobeam cavity reaching a DQE of the 96%[157]. To date this has been the only attempt to fabricate SSPDs on top of suspended waveguides similar to the ones presented in Chap. 5.

The internal quantum efficiency η_i depends on several factors. Among those, the wire width, the film thickness, the wavelength of the impinging photons and the choice of superconducting thin film were shown to be relevant. The η_i can be improved with wires of width ~30nm[158] or by reducing the superconducting film thickness[159]. The reduction of wire width, as well as the reduction of film thickness, decreases the wire volume where the energy of the absorbed photon is deposited. Therefore, given a fixed photon wavelength, the narrower (or thinner) wire will be more responsive than a wider (or thicker) wire because the perturbation of superconductivity that follows a photon absorption has higher probability of resulting in a detection event. For the same reason and for a fixed wire dimension, η_i can be increased by employing photons of shorter wavelengths since, a higher energy will be deposited in the same wire volume.

A similar approach can be used to understand why certain superconducting materials have higher η_i than others. Amorphous materials, such as WSi[152] or MoSi[160], that have lower superconducting bandgap compared to the standard niobium-based materials, have been demonstrated to approach almost unity η_i. Indeed, given a photon with certain energy, its absorption will break a number of Cooper pairs that depends on the ratio between photon energy and superconducting gap. Therefore in a low-gap material the number of quasi-particles created after photon absorption is higher and so the transition from superconducting to normal state is favoured. The efficiencies reached with those materials, even at low values of bias current, are higher than the ones achieved for Nb-based materials, however it has to be considered that low bandgap also means low critical temperature. In fact, to achieve the highest efficiencies, WSi detectors need to be operated at temperature below 1K, this requires special cooling mechanisms. Instead the Nb-based detectors work well at temperatures of 2-3 K, which can be reached with liquid He or with pulse-tube coolers.

An important aspect that often limits the η_i of the SSPDs is the film quality. In fact, it has been reported that the increase in meander active area, which is usually pursued to improve the coupling efficiency, leads to suppression of critical current[161]. Such reduction in I_c has been attributed to the presence of isolated point-like defects with reduced critical current, named constrictions[162]. In the case in which the SSPD presents a constriction, its final I_c will be limited to the I_c value of the constriction, therefore limiting the maximum efficiency. In addition, only that point-like defect will respond to incoming light efficiently since it will be the only one in the wire to be biased close to the wire I_c. The origin of these inhomogeneities is still object of debate, probably it is related to variation in the wire width, the crystal structure or the thickness of the film. An indication that variations in the crystal structure could be the reasons behind the film inhomogeneities, is the fact that in amorphous materials this problem is much less present. One way to limit the effect of the inhomogeneities on the η_i is the use of shorter wires[163].

Finally it has to be noted that the inhomogeneities problem is not only limiting the detector quantum efficiency but also the fabrication yield. Indeed, due to their stochastic behaviour, two nominally identical devices present different I_c values and therefore

different detection efficiencies. This is the reason why hybrid methods of bonding SiN membranes with pre-characterized superconducting nanowires to silicon and AlN waveguides have been developed[87].

Dark counts rate (DCR)

A dark count is defined as a false detection event occurring in the dark condition of the experimental set-up, i.e. without intentional optical input. A dark count can be distinguished into intrinsic and extrinsic. The extrinsic DCR is caused by the absorption of infrared photons produced by the black body radiation of the environment in which the experiment is carried out. Those can be reduced and eventually completely suppressed by introducing cold filters.
The intrinsic DCR is due to thermal fluctuations which produce a switching to the resistive state without photon absorption. While the DCR increases with the I_b, it can be decreased by lowering the operating temperature of the detector. Even though the DCR is lower at low temperatures, the intrinsic DCR does not vanish and stays finite at $I_b \sim I_c$. The cause for the intrinsic DCR is still object of debate, but it is presumably related to vortices entering the nanowires, either as unbinding of vortex-antivortex pairs or by the lowering of the barrier potential for vortex entry. However, a reduction of DCR was achieved also through several theoretical and technological improvements. For example, a deeper understanding of the current crowding[164] combined with the employment of new optimized designs which minimize this phenomenon[165] revealed that the choice of detector geometry influences the dark count rate.

Dead time

As already mentioned the dead time is the time needed to the detector to recover the bias current in the wires, such that it is ready to register the arrival of another photon. Therefore the SSPDs are blind to photons within this time period. The dead time is calculated from the detection pulse (Fig. 1.9 a), in which it is possible to distinguish a fast rising part due to the photon detection (few ps) and a decay part that correspond to the recovery of the current (tens of ns). In Fig. 1.9 a) the time constant τ_e related to the exponential decay is indicated, together with the dead time $\tau_D = 3\tau_e$. As said in par. 1.4.1, $\tau_e = L_k/R_L$ therefore at fixed $R_L = 50\Omega$, the time constant is imposed by the kinetic inductance L_k and it depends on the superconducting film and on the wire geometry.
The dead time limits the maximum count rate of the detector the frequency $f = 1/\tau_D$. Therefore, to speed up the device, τ_D needs to be decreased. There are two ways to reduce the time constant: decreasing L_k by reducing the total length of the wire or increasing the impedance seen by the detector[166]. The reduction of the wire length may limit the area of the meander and that decreases the coupling efficiency or for the waveguide detectors the absorptance decreases and leads to a lower detection efficiency. Both decreasing the length and increasing the resistance, on the other hand, might lead to 'latching'[167]. The

latching occurs when the recovery of the current in the nanowire is faster than the full re-establishment of the superconducting state. Thus, the current recovers and flows back through the detector before its resistance has dropped to zero and due to the corresponding Joule heating, it cannot recover back to the superconducting phase. Therefore in order to avoid the latching L_k and R_L needs to be carefully determined[166,168]. Since L_k is inherent to the superconducting film, different superconducting materials have different L_k. Indeed, for example, even if the amorphous materials (WSi, MoSi) have shown outstanding quantum efficiencies, on the other hand they are slower than Nb-based detector. Even applying a multi-pixel SSPD approach[169], in order to overcome the speed limitation, to date the maximum reached count rates have been 50MHz for amorphous materials[160] and 800MHz for Nb-based one[43]. Therefore the GHz regime, desirable for QIP applications, has not yet been achieved.

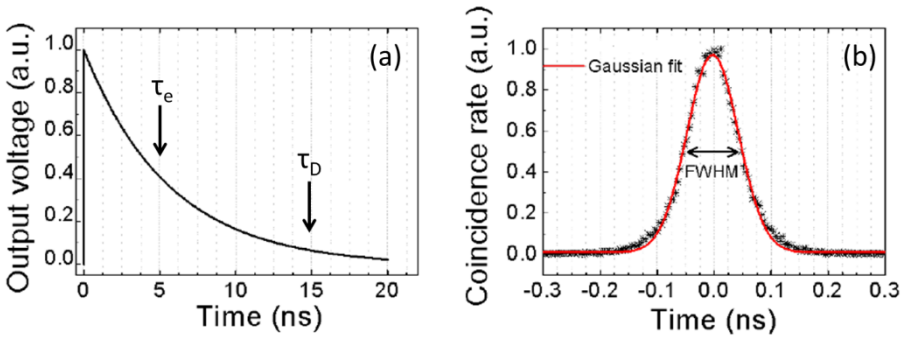

Fig. 1.9 a) Simulated pulse shape of a NbN SSPD, the dead time τ_D and the time constant of the exponential decay τ_e are indicated with arrows. b) measured jitter of a waveguide SSPD, the data is fit by using Gaussian (red) function.

Jitter

The jitter (or timing resolution) is the timing accuracy of registering a photon, namely the uncertainty in the delay between the photon absorption and the output pulse. While semiconductor SPDs have a non-Gaussian distribution for jitter, SSPDs show a Gaussian-like jitter[170] (Fig. 1.9 b). Similarly to the dead time, SSPDs made with amorphous superconducting materials have higher jitter compared to Nb-based ones. In fact, NbN SSPDs have been reported with jitter as low as 18 ps[171], while for WSi or MoSi have been reported values slightly above 100ps[152,160]. Low jitter is demanded in fast lifetime measurements using time correlated single-photon counting since the temporal resolution is determined by that value[172].

Owing to the fast response (few ns) and low jitter (<50 ps), which are very appealing for high-speed quantum photonic information processing, SSPDs outperform the other SPD technologies in the near-infrared.

1.5 Scope of the thesis

As discussed in par. 1.2.3, GaAs represents a promising material platform to realize many QPIC elements, from SP sources that manifest excellent figure of merits (purity, indistinguishability, brightness) to high-performance single-photon detectors. However, despite the impressive progress made in the development of these components at the single unit level, and in the improvement of their individual performances, the efficient integration of these devices on the same chip is required in order to exploit the real power of integrated quantum photonics. As shown in par. 1.2.5 to date a fully-functional QPIC has not been proved in any platform.
Following the prototype architecture of the fully integrated photonic quantum circuit proposed in Fig. 1.3, in this work other two, slightly simpler but still fully-functional, QPICs are proposed.

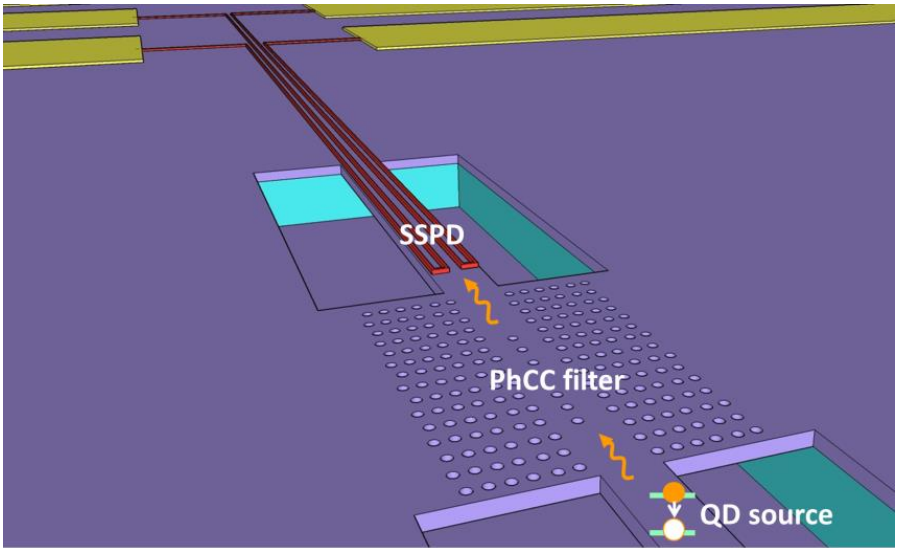

Fig. 1.10 Sketch of the proposed QPIC on single-membrane GaAs platform. Single photons are produced via spontaneous emission of excitons in QDs, efficiently funnelled in waveguides, filtered by a PhCC and detected by SSPDs on top of SNB.

The first QPIC (Fig. 1.10) is realized on a single-membrane GaAs platform with embedded InAs QDs and on which photonic crystal waveguides (PhCWGs) and cavities (PhCCs) are fabricated and SSPDs are patterned on top of suspended nanobeams (SNBs). Thanks to the addition of PhCCs and PhCWGs, the emission from one or several QDs can be filtered on-chip, so that single photons originating from a single excitonic line are funnelled to circuits and then measured. The superconductive nanowires are integrated on top of a SNB instead of a ridge waveguide since shorter lengths are sufficient to reach high absorption, due to the tighter field confinement[173]. This is expected to reduce the

role of wire inhomogeneities and increase the efficiency. Moreover it is possible to place two electrically-independent detectors on top of the SNB, such that the same guided mode is probed by the two SSPDs[172]. The autocorrelators together with the PhC filters would, for example, allow performing a Hanbury-Brow-Twiss (HBT) experiment[174] completely on-chip, which would be a meaningful validation of a fully-functional QPIC.
However, as already mentioned in par. 1.3.3, without a control on the energy of the QDs emission and cavity mode, the resonance between these two components is based only on probability, therefore without a concrete possibility of scalability to QPIC applications. The introduction of independent tuning systems for each one of these two components instead allowed to demonstrate the cavity-emitter node (Fig. 1.3) for on-demand single-photon emission, as mentioned in par. 1.3.4.
Therefore the second proposed QPIC demonstrator (Fig. 1.11) is based on a double-membrane GaAs platform with embedded InAs QDs and doped layers for the fabrication of p-i-n diodes used for the Stark control of the QDs emission (par. 1.3.3) and for the actuation of the NOEMS photonic crystal cavities (par. 1.3.4). Of course as for the first proposed QPIC, SSPDs are patterned on top of SNBs, in order to detect on-chip the single-photon emission coming from the cavity-emitter node.

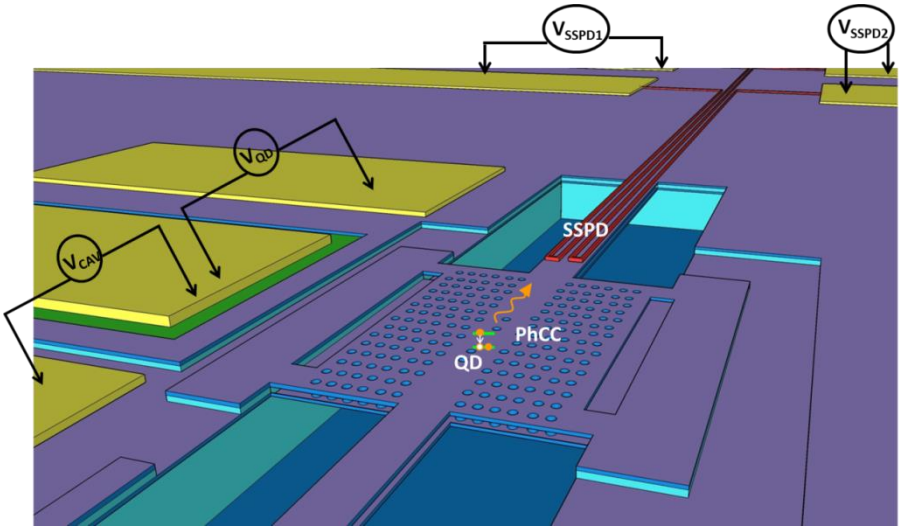

Fig. 1.11 Sketch of the proposed QPIC on double-membrane GaAs platform. The QD emission energy is controlled by Stark effect using the p-i-n diode biased with voltage V_{QD}. The modes of the double-membrane cavity are brought in resonance with the QD emission, actuating the NOEMS through the n-i-p diode using voltage V_{CAV}. The photon emitted by the cavity-emitter node is funneled through the PhC waveguide to the system of two electrically indipendent SSPDs biased with different voltage V_{SSPD1} and V_{SSPD2}. The two SSPDs can perform HBT measurements on-chip in order to prove the single-photon nature of the emitted photon.

The integration of all these different functionalities on the same platform shows significant technological challenges that are going to be addressed in the next chapters. Chap.2 covers the experimental methods used for the realization of these QPICs.

Chap. 3 is dedicated to the design and fabrication of the SSPDs, including the deposition of the NbN film.
Chap.4 explores the low-temperature fabrication process, which allows the integration of the different components of the above mentioned circuits. In this chapter, the differences, between the standard process used for the fabrication of PhC structures and the one optimized for the SSPDs integration, are highlighted; the technological issues analysed and solved when possible. A fabrication attempt of the more complex QPIC of Fig. 1.11 is also presented in this chapter together with the preliminary characterization of each component of the circuit.
The performance of the SSPDs patterned on top of the SNB are presented in Chap.5.
The QPIC realized following Fig. 1.10 is fully-characterized in Chap. 6. Particularly the filtering functionality of the system PhCWG-PhCC-PhCWG is explained and experimentally tested. Moreover the interaction between each component of the circuit is presented.
Finally in Chap. 7 the results are summarised and considerations about the realization of a fully-functional QPIC are made.

References

[1] G.E. Moore, “Cramming More Components onto Integrated Circuits”, *Electronics*, **38** pp. 114–117, 1965.

[2] https://www.technologyreview.com/s/601441/moores-law-is-dead-now-what/

[3] T.D. Ladd, F. Jelezko, R. Laflamme, Y. Nakamura, C. Monroe, J.L. O’Brien, "Quantum computers", *Nature*, **464** pp. 45–53, 2010.

[4] J.L. O`Brien, “Optical quantum computing”, *Science*, **318** pp. 1567–1570, 2007.

[5] C.H. Bennett, G. Brassard, “Quantum cryptography: Public key distribution and coin tossing”, *Proceedings of IEEE International Conference on Computers, Systems and Signal Processing*, **175** pp. 8, 1984.

[6] G. Brassard, N. Lutkenhaus, T. Mor, B.C. Sanders, “Limitations on practical quantum cryptography” *Physical Review Letters*, **85** pp. 1330, 2000.

[7] H. Takesue, S.W. Nam, Q. Zhang, R.H. Hadfield, T. Honjo, K. Tamaki, Y. Yamamoto, “Quantum key distribution over a 40dB channel loss using superconducting single photon detectors”, *Nature Photonics*, **1** pp. 343, 2007.

[8] H. Shibata, K. Shimizu, H. Takesue, and Y. Tokura, “Superconducting nanowire single-photon detector with ultralow dark count rate using cold optical filters”, *Applied Physics Express*, **6** pp. 072801, 2013.

[9] J. Yin, Y. Cao, Y.-H. Li, S.-K. Liao, L. Zhang, J.-G. Ren, W.-Q. Cai, W.-Y. Liu, B. Li, et al., “ Satellite-based entanglement distribution over 1200 kilometers”, *Science* , **365** pp. 1140-1144, 2017.

[10] S.K. Liao, W.Q. Cai, J. Handsteiner, B. Liu, J. Yin, L. Zhang, D. Rauch, M. Fink, J.G. Ren, W.Y. Liu,et al., "Satellite-Relayed Intercontinental Quantum Network", *Physical Review Letters*, **120** pp. 030501, 2018.

[11] R. P. Feynman, “Simulating physics with computers”, *International Journal of Theoretical Physics*, **21** pp. 467, 1982.

[12] M. Georgescu, S. Ashhab, Franco Nori, “Quantum Simulation”, *arXiv:1308.6253v3*, 2014.

[13] A. Aspuru-Guzik, P. Walther, “Photonic quantum simulators” *Nature Physics*, **8** pp. 285, 2012.

[14] M. Bentivegna, N. Spagnolo, C. Vitelli, F. Flamini, N. Viggianiello, L. Latmiral, P. Mataloni, D. J. Brod, E. F. Galvão, A. Crespi, R. Ramponi, R. Osellame, F. Sciarrino, "Experimental scattershot boson sampling", *Science Advance* **, 1** pp. 1400255, 2015.

[15] Scott Aaronson, Alex Arkhipov. "The computational complexity of linear optics", *Proceedings of the forty-third annual ACM symposium on Theory of computing*, pp. 333–342, 2011.

[16] L. Latmiral, "Reaching quantum supremacy with a boson sampling experiment", *arXiv:1511.08161v2*, 2015.

[17] N. Spagnolo, C. Vitelli, M. Bentivegna, D. J. Brod, A. Crespi, F. Flamini, S. Giacomini, G. Milani, R. Ramponi, P. Mataloni, R. Osellame, E.F. Galva, F. Sciarrino, "Experimental validation of photonic boson sampling", *Nature Photonics* ,**8** pp. 615–620, 2014.

[18] P. W. Shor, "Polynomial-Time Algorithms for Prime Factorization and Discrete Logarithms on a Quantum Computer", *Society for Industrial and Applied Mathematics Review*, **41** pp. 303-332, 1999.
[19] J. Preskill, "Fault-tolerant quantum computation", *arXiv:9712048v1*, 1997.

[20] R. Barends, J. Kelly, A. Megrant, A. Veitia, D. Sank, E. Jeffrey, T.C. White, J. Mutus, A. G. Fowler, B. Campbell, Y. Chen, Z. Chen, B. Chiaro, A. Dunsworth, C. Neill, P. O'Malley, P. Roushan, A. Vainsencher, J. Wenner, A.N. Korotkov, A.N. Cleland, J.M. Martinis, "Superconducting quantum circuits at the surface code threshold for fault tolerance", *Nature* , **508** pp. 500–503, 2014.

[21] T.P. Harty, D.T.C. Allcock, C.J. Ballance, L. Guidoni, H.A. Janacek, N.M. Linke, D.N. Stacey, D.M. Lucas, "High-Fidelity Preparation, Gates, Memory, and Readout of a Trapped-Ion Quantum Bit", *Physics Review Letters*, **113** pp. 220501, 2014.

[22] J. Kelly, R. Barends, A.G. Fowler, A. Megrant, E. Jeffrey, T.C. White, D. Sank, J.Y. Mutus, B. Campbell, Y. Chen, Z. Chen, B. Chiaro, A. Dunsworth, I.-C. Hoi, C. Neill, P.J.J. O'Malley, C. Quintana, P. Roushan, A. Vainsencher, J. Wenner, A. N. Cleland, J.M. Martinis, "State preservation by repetitive error detection in a superconducting quantum circuit", *Nature* , **519** pp. 66–69, 2015.

[23] C. Neill, P. Roushan, K. Kechedzhi, S. Boixo, S.V. Isakov, V. Smelyanskiy, R. Barends, B. Burkett, Y. Chen, Z. Chen, B. Chiaro, A. Dunsworth, A. Fowler, B. Foxen, R. Graff, E. Jeffrey, J. Kelly, E. Lucero, A. Megrant, J. Mutus, M. Neeley, C. Quintana, D. Sank, A. Vainsencher, J. Wenner, T.C. White, H. Neven, J.M. Martinis, "A blueprint for demonstrating quantum supremacy with superconducting qubits", *arXiv:1709.06678v1*, 2017.

[24] J.M Gambetta, J.M. Chow, M. Steffen, "Building logical qubits in a superconducting quantum computing system", *NPJ Quantum Information*, **3**:2, 2017.

[25] M.W. Johnson, M.H.S. Amin, S. Gildert, T. Lanting, F. Hamze, N. Dickson, R. Harris A.J. Berkley, J. Johansson, P. Bunyk, E.M. Chapple, C. Enderud, J.P. Hilton, K. Karimi, E. Ladizinsky, N. Ladizinsky, T. Oh, I. Perminov, C. Rich, M.C. Thom, E. Tolkacheva, C.J.S. Truncik, S. Uchaikin, J. Wang, B. Wilson, G. Rose, "Quantum annealing with manufactured spins", *Nature*, **473** pp. 194–198, 2011.

[26] https://www.research.ibm.com/ibm-q/

[27] https://ai.googleblog.com/2018/03/a-preview-of-bristlecone-googles-new.html

[28] https://www.microsoft.com/en-us/quantum/

[29] E. Knill, R. Laflamme, G.J. Milburn, "A scheme for efficient quantum computation with linear optics", *Nature*, **409** pp. 46–52, 2001.

[30] A. Politi, J.F.C. Matthews, J.L. O'Brien, "Shor's quantum factoring algorithm on a photonic chip", *Science*, **325** pp. 1221, 2009.

[31] R. Raussendorf, H.J. Briegel, "A one-way quantum computer", *Physics Review Letters*, **86** pp. 5188–5191, 2001.

[32] H.J. Kimble, "The quantum internet", Nature, 453 pp. 1023-1030, 2008.

[33] J.L. O`Brien, A. Fusawa, J. Vuckovic, "Photonic quantum technologies", *Nature Physics*, 3 pp. 687-695, 2009.

[34] A. Politi, J. Matthews, M.G. Thompson, J.L. O'Brien, "Integrated Quantum Photonics", *IEEE Journal of Selected Topics in Quantum Electronics*, **15** pp. 1673–1684, 2009.

[35] A. Politi, M.J. Cryan, J.G. Rarity, S. Yu, J.L. O'Brien, "Silica-on-Silicon Waveguide Quantum Circuits", *Science*, **320** pp. 646–649, 2008.

[36] J.W. Silverstone, D. Bonneau, J.L. O'Brien, M.G. Thompson, "Silicon Quantum Photonics", *IEEE Journal of Selected Topics in Quantum Electronics*, **22** pp. 1–13, 2016.

[37] J.W. Silverstone, D. Bonneau, K. Ohira, N. Suzuki, H. Yoshida, N. Iizuka, M. Ezaki, C. M. Natarajan, M.G. Tanner, R.H. Hadfield, V. Zwiller, G.D. Marshall, J.G. Rarity, J.L. O'Brien, M.G. Thompson, "On-chip quantum interference between silicon photon-pair sources", *Nature Photonics*, **8** pp. 104–108, 2014.

[38] D. Liang, J. E. Bowers, "Recent progress in lasers on silicon", *Nature Photonics*, **4** pp. 511–517, 2010.

[39] N.C. Harris, D. Grassani, A. Simbula, M. Pant, M. Galli, T. Baehr-Jones, M. Hochberg, D. Englund, D. Bajoni, C. Galland, "Integrated Source of Spectrally Filtered Correlated Photons for Large-Scale Quantum Photonic Systems", *Physics Review X*, **4** pp. 41047, 2014.

[40] D.J. Lockwood, L. Pavesi, *Silicon Photonics II*, Topics in Applied Physics (Springer-Verlag), **119**, 2011.

[41] J. Xie, L. Zhou, Z. Li, J. Wang, J. Chen, "Seven-bit reconfigurable optical true time delay line based on silicon integration", *Optics Express*, **22** pp. 22707, 2014.

[42] G.N. Gol'tsman, O. Okunev, G. Chulkova, A. Lipatov, A. Semenov, K. Smirnov, B. Voronov, A. Dzardanov, C. Williams, R. Sobolewski, "Picosecond superconducting single-photon optical detector", *Applied Physics Letters*, **79** pp. 705–707, 2001.

[43] W.H.P. Pernice, C. Schuck, O. Minaeva, M. Li, G.N. Goltsman, A.V. Sergienko H.X. Thang, "High-speed and high-efficiency travelling wave single-photon detectors embedded in nanophotonic circuits", *Nature Communications*, **3** pp. 1325, 2012.

[44] C. Shunck, W.H.P. Pernice, H.X. Thang, "Waveguide integrated low noise NbTiN nanowire single-photon detectors with milli-Hz dark count rate", *Scientific Reports*, **3** pp. 1893, 2013.

[45] P. Rath, S. Ummethala, C. Nebel, W.H.P. Pernice, "Diamond as a material for monolithically integrated optical and optomechanical devices", *Physics Status Solidi*, **212** pp. 2385–2399, 2015.

[46] T. Schröder, S.L. Mouradian, J. Zheng, M.E. Trusheim, M. Walsh, E.H. Chen, L. Li, I. Bayn, D. Englund, "Quantum nanophotonics in diamond", *Journal of Optics Society America B*, **33** pp. B65, 2016.

[47] P. Rath, N. Gruhler, S. Khasminskaya, C. Nebel, C. Wild, W.H.P. Pernice, "Waferscale nanophotonic circuits made from diamond-on-insulator substrates", *Optics Express*, **21** pp. 11031, 2013.

[48] B.J.M. Hausmann, B. Shields, Q. Quan, P. Maletinsky, M. McCutcheon, J.T. Choy, T.M. Babinec, A. Kubanek, A. Yacoby, M.D. Lukin, M. Lončar, "Integrated diamond networks for quantum nanophotonics", *Nano Letters*, **12** pp. 1578–1582, 2012.

[49] M.W. Doherty, N.B. Manson, P. Delaney, F. Jelezko, J. Wrachtrup, L.C.L. Hollenberg, "The nitrogen-vacancy colour centre in diamond", *Physics Reports*, **528** pp. 1–45, 2013.

[50] R.E. Evans, A. Sipahigil, D.D. Sukachev, A.S. Zibrov, M.D. Lukin, "Narrow-Linewidth Homogeneous Optical Emitters in Diamond Nanostructures via Silicon Ion Implantation", *Physics Review Applied*, **5** pp. 44010, 2016.

[51] P. Tamarat, T. Gaebel, J.R. Rabeau, M. Khan, A.D. Greentree, H. Wilson, L.C.L. Hollenberg, S. Prawer, P. Hemmer, F. Jelezko, J. Wrachtrup, "Stark shift control of single optical centers in diamond", *Physics Review Letters*, **97** pp. 083002, 2006.

[52] P.C. Maurer, G. Kucsko, C. Latta, L. Jiang, N.Y. Yao, S.D. Bennett, F. Pastawski, D. Hunger, N. Chisholm, M. Markham, D.J. Twitchen, J.I. Cirac, M.D. Lukin, "Room-Temperature Quantum Bit Memory Exceeding One Second", *Science*, **336** pp. 1283–1286, 2012.

[53] T.H. Taminiau, J. Cramer, T. van der Sar, V.V Dobrovitski, R. Hanson, "Universal control and error correction in multi-qubit spin registers in diamond", *Nature Nanotechnology*, **9** pp. 171–176, 2014.

[54] S. Yang, Y. Wang, D.D.B. Rao, T. Hien Tran, A.S. Momenzadeh, M. Markham, D.J. Twitchen, P. Wang, W. Yang, R. Stöhr, P. Neumann, H. Kosaka, J. Wrachtrup, "High-fidelity transfer and storage of photon states in a single nuclear spin", *Nature Photonics*, **10** pp. 507–511, 2016.

[55] A. Beveratos, R. Brouri, T. Gacoin, J.P. Poizat, P. Grangier, "Nonclassical radiation from diamond nanocrystals", *Physics Review A*, **64** pp. 061802, 2001.

[56] M.W. McCutcheon, M. Loncar, "Design of a silicon nitride photonic crystal nanocavity with a quality factor of one million for coupling to a diamond nanocrystal", *Optics Express*, **16** pp. 19136, 2008.

[57] T.M. Babinec, B.J.M. Hausmann, M. Khan, Y. Zhang, J.R. Maze, P.R. Hemmer, M. Lončar, "A diamond nanowire single-photon source", *Nature Nanotechnology*, **5** pp. 195-199, 2010.

[58] L.J. Rogers, K.D. Jahnke, T. Teraji, L. Marseglia, C. Müller, B. Naydenov, H. Schauffert, C. Kranz, J. Isoya, L.P. McGuinness, F. Jelezko, "Multiple intrinsically identical single-photon emitters in the solid state", *Nature Communications*, **5** pp. 4739, 2014.

[59] R.E. Evans, A. Sipahigil, D.D. Sukachev, A.S. Zibrov, M.D. Lukin, "Narrow-Linewidth Homogeneous Optical Emitters in Diamond Nanostructures via Silicon Ion Implantation", *Physics Review Applied*, **5** pp. 44010, 2016.

[60] A. Sipahigil, K.D. Jahnke, L.J. Rogers, T. Teraji, J. Isoya, A. S. Zibrov, F. Jelezko, M.D. Lukin, "Indistinguishable Photons from Separated Silicon-Vacancy Centres in Diamond", *Physics Review Letters*, **113** pp. 113602, 2014.

[61] J. Riedrich-Möller, S. Pezzagna, J. Meijer, C. Pauly, F. Mücklich, M. Markham, A.M. Edmonds, C. Becher, "Nanoimplantation and Purcell enhancement of single nitrogen-vacancy centers in photonic crystal cavities in diamond", *Applied Physics Letters*, **106** pp. 221103, 2015.

[62] L.J. Rogers, K.D. Jahnke, M.H. Metsch, A. Sipahigil, J.M. Binder, T. Teraji, H. Sumiya, J. Isoya, M.D. Lukin, P. Hemmer, F. Jelezko, "All-Optical Initialization, Readout, and Coherent Preparation of Single Silicon-Vacancy Spins in Diamon", *Physics Review Letters*, **113** pp. 263602, 2014.

[63] J. Riedrich-Möller, L. Kipfstuhl, C. Hepp, E. Neu, C. Pauly, F. Mücklich, A. Baur, M. Wandt, S. Wolff, M. Fischer, S. Gsell, M. Schreck, C. Becher, "One- and two-dimensional photonic crystal microcavities in single crystal diamond", *Nature Nanotechnology*, **7** pp. 69–74, 2011.

[64] P. Rath, O. Kahl, S. Ferrari, F. Sproll, G. Lewes-Malandrakis, D. Brink, K. Ilin, M. Siegel, C. Nebel, W. Pernice, "Superconducting single-photon detectors integrated with diamond nanophotonic circuits", *Light: Science & Applications*, **4** pp. 338, 2015.

[65] F. Boitier, A. Orieux, C. Autebert, A. Lemaître, E. Galopin, C. Manquest, C. Sirtori, I. Favero, G. Leo, S. Ducci, "Electrically Injected Photon-Pair Source at Room Temperature", *Physics Review Letters*, **112** pp. 183901, 2014.

[66] A. J. Shields, "Semiconductor quantum light sources", *Nature Photonics*, **1** pp. 215, 2007.

[67] M. Arcari, I. Söllner, A. Javadi, S. Lindskov Hansen, S. Mahmoodian, J. Liu, H. Thyrrestrup, E.H. Lee, J.D. Song, S. Stobbe, P. Lodahl, "Near-Unity Coupling Efficiency of a Quantum Emitter to a Photonic Crystal Waveguide", *Physics Review Letters*, **113** pp. 1–5, 2014.

[68] C.L. Salter, R.M. Stevenson, I. Farrer, C.A. Nicoll, D.A. Ritchie, A.J. Shields, "An entangled-lightemitting diode", *Nature*, **465** pp.594–597, 2010.

[69] J. Nilsson, R.M. Stevenson, K.H.A. Chan, J. Skiba-Szymanska, M. Lucamarini, M.B. Ward, A.J. Bennett, C.L. Salter, I. Farrer, D.A. Ritchie, A.J. Shields, "Quantum teleportation using a lightemitting diode", *Nature Photonics*, **7** pp. 311–315, 2013.

[70] A.B. Young, A.C.T. Thijssen, D.M. Beggs, P. Androvitsaneas, L. Kuipers, J.G. Rarity, S. Hughes, R. Oulton, "Polarization Engineering in Photonic Crystal Waveguides for Spin-Photon Entanglers", *Physics Review Letters*, **115** pp. 153901, 2015.

[71] J. Wang, A. Santamato, P. Jiang, D. Bonneau, E. Engin, J.W. Silverstone, M. Lermer, J. Beetz, M. Kamp, S. Hoefling, M.G. Tanner, C.M. Natarajan, R.H. Hadfield, S.N. Dorenbos, V. Zwiller, J.L. O'Brien, M.G. Thompson, "Gallium arsenide (GaAs) quantum photonic waveguide circuits", *Optics Communications*, **327** pp. 49-55, 2014.

[72] C.P. Dietrich, A. Fiore, M.G. Thompson, M. Kamp, S. Höfling, "GaAs integrated quantum photonics: Towards compact and multi-functional quantum photonic integrated circuits", *Laser & Photonics Review*, 2016.

[73] J. Sprengers, A. Gaggero, D. Sahin, S. Jahanmirinejad, G. Frucci, F. Mattioli, R. Leoni, J. Beetz, M. Lermer, M. Kamp, S. Hofling, A. Fiore, "Waveguide superconducting single-

photon detectors for integrated quantum photonic circuits", *Applied Physics Letters*, **99** pp. 181110, 2011.

[74] M. Petruzzella, T. Xia, F. Pagliano, S. Birindelli, L. Midolo, Z. Zobenica, L.H. Li, E.H. Linfield, A. Fiore, "Fully tuneable, Purcell-enhanced solid-state quantum emitters", *Applied Physics Letters*, **107** pp. 1411109, 2015.

[75] S. Tanzilli, A. Martin, F. Kaiser, M. P. de Micheli, O. Alibart, D.B. Ostrowsky, "On the genesis and evolution of integrated quantum optics", *Laser Photonics Review*, **6** pp. 115–143, 2012.

[76] H. Jin, F.M. Liu, P. Xu, J.L. Xia, M.L. Zhong, Y. Yuan, J.W. Zhou, Y.X. Gong, W. Wang, S.N. Zhu, "On-Chip Generation and Manipulation of Entangled Photons Based on Reconfigurable Lithium-Niobate Waveguide Circuits", *Physics Review Letters*, **113** pp. 103601, 2014.

[77] D. Bonneau, M. Lobino, P. Jiang, C.M. Natarajan, M.G. Tanner, R.H. Hadfield, S.N. Dorenbos, V. Zwiller, M.G. Thompson, J.L. O'Brien, "Fast path and polarization manipulation of telecom wavelength single photons in lithium niobate waveguide devices", *Physics Review Letters*, **108** pp. 1–5, 2012.

[78] O. Alibart, V. D'Auria, M. De Micheli, F. Doutre, F. Kaiser, L. Labonté, T. Lunghi, É. Picholle, S. Tanzilli, "Quantum photonics at telecom wavelengths based on lithium niobate waveguides", *arXiv:1608.01100*, 2016.

[79] S. Castelletto, L. Rosa, B.C. Johnson, "Silicon Carbide for Novel Quantum Technology Devices", *Advanced Silicon Carbide Devices and Processing*, pp. 221–247, 2015.

[80] B. Lienhard, T. Schröder, S. Mouradian, F. Dolde, T.T. Tran, I. Aharonovich, D. Englund, "Bright and photostable single-photon emitter in silicon carbide" *Optica*, **3** pp. 768, 2016.

[81] W.F. Koehl, B.B. Buckley, F.J. Heremans, G. Calusine, D.D. Awschalom, "Room temperature coherent control of defect spin qubits in silicon carbid", *Nature*, **479** pp. 84–87, 2011.

[82] R. Osellame, S. Taccheo, M. Marangoni, R. Ramponi, P. Laporta, D. Polli, S. De Silvestri, G. Cerullo, "Femtosecond writing of active optical waveguides with astigmatically shaped beams", *Journal of the Optical Society of America B*, 20 pp. 1559-1567, 2003.

[83] A. Crespi, R. Osellame, R. Ramponi, D.J. Brod, E.F. Galvão, N. Spagnolo, C. Vitelli, E. Maiorino, P. Mataloni, F. Sciarrino, "Integrated multimode interferometers with arbitrary designs for photonic boson sampling", *Nature Photonics*, **7** pp. 545–549, 2013.

[84] S. Khasminskaya, F. Pyatkov, K. Słowik, S. Ferrari, O. Kahl, V. Kovalyuk, P. Rath, A. Vetter, F. Hennrich, M.M. Kappes, G. Gol'Tsman, A. Korneev, C. Rockstuhl, R. Krupke, W. H.P. Pernice, "Fully integrated quantum photonic circuit with an electrically driven light source", *Nature Photonic*, 10 pp. 227, 2016.

[85] Y. Wan, Q. Li, A.Y. Liu, A.C. Gossard, J.E. Bowers, E.L. Hu, K.M. Lau, "Optically pumped 1.3μm room-temperature InAs quantum-dot micro-disk lasers directly grown on (001) silicon", *Optics Letters*, **41** pp. 1664, 2016.

[86] S. Chen, W. Li, J. Wu, Q. Jiang, M. Tang, S. Shutts, S.N. Elliott, A. Sobiesierski, A.J. Seeds, I. Ross, P.M. Smowton, H. Liu, "Electrically pumped continuous-wave III–V quantum dot lasers on silicon", *Nature Photonic*, **10** pp. 307–311, 2016.

[87] E. Murray, D.J.P. Ellis, T. Meany, F.F. Floether, J.P. Lee, J.P. Griffiths, G.A.C. Jones, I. Farrer, D.A. Ritchie, A.J. Bennett, A.J. Shields, "Quantum photonics hybrid integration platform", *Applied Physics Letters*, **107** pp. 171108, 2015.

[88] I.E. Zadeh, A.W. Elshaari, K.D. Jöns, A. Fognini, D. Dalacu, P.J. Poole, M.E. Reimer, V. Zwiller, "Deterministic Integration of Single Photon Sources in Silicon Based Photonic Circuits", *Nano Letters*, **16** pp. 2289–2294, 2016.

[89] L. Li, T. Schröder, E.H. Chen, M. Walsh, I. Bayn, J. Goldstein, O. Gaathon, M.E. Trusheim, M. Lu, J. Mower, M. Cotlet, M.L. Markham, D.J. Twitchen, D. Englund, "Coherent spin control of a nanocavity-enhanced qubit in diamond", *Nature Communications*, **6** pp. 6173, 2015.

[90] F. Najafi, J. Mower, N.C. Harris, F. Bellei, A. Dane, C. Lee, X. Hu, P. Kharel, F. Marsili, S. Assefa, K.K. Berggren, D. Englund, "On-chip detection of non-classical light by scalable integration of singlephoton detectors", *Nature Communications***, 6** pp. 5873, 2015.

[91] J. Wang, D. Bonneau, M. Villa, J. W. Silverstone, R. Santagati, S. Miki, T. Yamashita, M. Fujiwara, M. Sasaki, H. Terai, M.G. Tanner, C.M. Natarajan, R.H. Hadfield, J.L. O'Brien, M.G. Thompson, "Chip-to-chip quantum photonic interconnect by path-polarization interconversion", *Optica*, **3** pp. 407, 2016.

[92] C. Xiong, X. Zhang, A. Mahendra, J. He, D.Y. Choi, C.J. Chae, D. Marpaung, A. Leinse, R.G. Heideman, M. Hoekman, C.G.H. Roeloffzen, R.M. Oldenbeuving, P.W.L. van Dijk, C. Taddei, P.H.W. Leong, B.J. Eggleton, "Compact and reconfigurable silicon nitride time-bin entanglement circuit", *Optica*, **2** pp. 724, 2015.

[93] P. Sibson, C. Erven, M. Godfrey, S. Miki, T. Yamashita, M. Fujiwara, M. Sasaki, H. Terai, M.G. Tanner, C.M. Natarajan, R.H. Hadfield, J.L. O'Brien, M.G. Thompson, "Chip-based Quantum Key Distribution", *Nature Communications*, **8** pp. 13984, 2017.

[94] G. Reithmaier, M. Kaniber, F. Flassig, S. Lichtmannecker, K. Müller, A. Andrejew, J. Vučković, R. Gross, J.J. Finley, "On-Chip Generation, Routing, and Detection of Resonance Fluorescence", *Nano Letters*, **15** pp. 5208–5213, 2015.

[95] M. Petruzzella, F.M. Pagliano, Ž. Zobenica, S. Birindelli, M. Cotrufo, F.W.M. van Otten, R.W. van der Heijden, A. Fiore, "Electrically driven quantum light emission in electromechanically tuneable photonic crystal cavities", *Applied Physics Letters*, **111** pp. 251101, 2017.

[96] M.G. Tanner, L.S.E. Alvarez, W. Jiang, R.J. Warburton, Z.H. Barber, R.H. Hadfield, "A superconducting nanowire single photon detector on lithium niobate", *Nanotechnology*, **23** pp. 505201, 2012.

[97] M. Radulaski, K.A. Fischer, J. Vuckovic, "Nonclassical Light Generation from III-V and Group-IV Solid-State Cavity Quantum Systems", *arXiv:1701.03039v1*, 2017.

[98] J.E. Prieto, I. Markov, "Stranski–Krastanov mechanism of growth and the effect of misfit sign on quantum dots nucleation", *Surface Science*, **664** pp. 172-184, 2017.

[99] P. Gallo, M. Felici, B. Dwir, K.A. Atlasov, K.F. Karlsson, A. Rudra, A. Mohan, G. Biasiol, L. Sorba, E. Kapon, "Integration of site-controlled pyramidal quantum dots and photonic crystal membrane cavities", *Applied Physics Letters*, **92** pp. 263101, 2008.

[100] B. Alloing, C. Zinoni, V. Zwiller, L.H. Li, C. Monat, M. Gobet, G. Buchs, A. Fiore, E. Pelucchi, and E. Kapon. "Growth and characterization of single quantum dots emitting at 1300 nm" *Applied Physics Letters*, **86** pp.101908, 2005.

[101] M. Bayer, A. Forchel, "Temperature dependence of the homogeneous linewidth in InGaAs/GaAs self-assembled quantum dots" *Physical Review B*, **65** pp. 041308, 2002.

[102] E.M. Purcell, "Spontaneous emission probabilities at radio frequencies", *Physical Review*, **69** pp. 681, 1946.

[103] A. Muller, E.B. Flagg, P. Bianucci, X.Y. Wang, D.G. Deppe, W. Ma, J. Zhang, G.J. Salamo, M. Xiao, C.K. Shih, "Resonance Fluorescence from a Coherently Driven Semiconductor Quantum Dot in a Cavity", *Physics Review Letters*, **99** pp. 187402, 2006.

[104] J.D. Joannopoulos, S.G. Johnson, J.N. Winn, R.D. Meade, "Photonic Crystal Molding the Flow of Light", *3rd ed. Princeton University Press: Princeton*, NJ, USA, 2008.

[105] T. F. Krauss, R.M. De la Rue, S. Brand, "Two-dimensional photonic bandgap structures operating at near-infrared wavelengths" *Nature*, **383** pp. 699. 1996.

[106] Rodney Loudon, "The quantum theory of light" *OUP Oxford*, 2000.

[107] A. Badolato, K. Hennessy, M. Atatüre, J. Dreiser, E. Hu, P.M. Petroff, A. Imamoglu, "Deterministic Coupling of Single Quantum Dots to Single Nanocavity Modes", *Science*, **308** pp. 1158–1161, 2005.

[108] G. Ghosh, “Temperature dispersion of refractive indices in semiconductors”, *Journal of Applied Physics*, **79** pp. 9388, 1996.

[109] B. Wild, R. Ferrini, R. Houdré, M. Mulot, S. Anand, and C.J.M. Smith., “Temperature tuning of the optical properties of planar photonic crystal microcavities”, *Applied Physics Letters*, **84** pp.846, 2004.

[110] R.M. Stevenson, R.J. Young, P. Atkinson, K. Cooper, D.A. Ritchie, A.J. Shields, “A semiconductor source of triggered entangled photon pairs”, *Nature* , **439** pp. 179–182, 2006.

[111] S. Seidl, M. Kroner, A. Högele, K. Karraib, R.J. Warburton, A. Badolato, P.M. Petrof, “Effect of uniaxial stress on excitons in a self-assembled quantum dot”, *Applied Physics Letters*, **88** pp. 203113, 2006.

[112] T. Unold, K. Mueller, C. Lienau, T. Elsaesser, A.D. Wieck, “Optical Stark Effect in a Quantum Dot: Ultrafast Control of Single Exciton Polarizations”, *Physics Review Letters*, **92** pp. 157401, 2004.

[113] F. Raineri, C. Cojocaru, R. Raj, P. Monnier, A. Levenson, C. Seassal, “Tuning a two-dimensional photonic crystal resonance via optical carrier injection” *Optics Letters*, **30** pp. 64–66, 2005.

[114] T. Miyazawa, T. Nakaoka, T. Usuki, J. Tatebayashi, Y. Arakawa, S. Hirose, K. Takemoto, M. Takatsu, N. Yokoyama, “Electric field modulation of exciton recombination in InAs/GaAs quantum dots emitting at 1.3μm”, *Journal of Applied Physics*, **104** pp. 013504, 2008.

[115] A.J. Bennett, R.B. Patel, J. Skiba-Szymanska, C.A. Nicoll, I. Farrer, D.A. Ritchie, A.J. Shields, “Giant Stark effect in the emission of single semiconductor quantum dots” *Applied Physics Letters*, 97 pp. 031104, 2010.

[116] M. Francardi, L. Balet, A. Gerardino, N. Chauvin, D. Bitauld, L.H. Li, B. Alloing, A. Fiore, “ Enhanced spontaneous emission in a photonic-crystal light-emitting diode”, *Applied Physics Letters*, 93 pp. 143102, 2008.

[117] A. Laucht, F. Hofbauer, N. Hauke, J. Angele, S. Stobbe, M. Kaniber, G. Böhm, P. Lodahl, M-C Amann, J.J. Finley, “Electrical control of spontaneous emission and strong coupling for a single quantum dot”, *New Journal of Physics*, **11** pp. 023034, 2009.

[118] G. Shambat, B. Ellis, J. Petykiewicz, A. Majumdar, M. Mayer, T. Sarmiento, J. Vuckovic, J. Harris, E. Haller, “Electrically driven photonic crystal nanocavity devices” *Advanced Photonics Congress 2012 OSA*, 2012.

[119] M. Minkov, V. Savona, “Automated optimization of photonic crystal slab cavities”, *Scientific Reports*, **4** pp. 5124, 2014.

[120] O. Painter, A. Husain, A.T. Scherer, P.T. Lee, I.H. Kim, J.D. O'Brien, P.D. Dapkus, "Lithography tuning of a two-dimensional photonic crystal laser array", *IEEE Photonics Technology Letters*, **12** pp. 1126–1128, 2000.

[121] L. Balet, M. Francardi, A. Gerardino, N. Chauvin, B. Alloing, C. Zinoni, C. Monat, L.H. Li, N. Le Thomas, R. Houdré, A. Fiore, "Enhanced spontaneous emission rate from single InAs quantum dots in a photonic crystal nanocavity at telecom wavelengths", *Applied Physics Letters*, **91** pp. 123115, 2007.

[122] F. Intonti, N. Caselli, S. Vignolini, F. Riboli, S. Kumar, A. Rastelli, O.G. Schmidt, M. Francardi, A. Gerardino, L. Balet, L.H. Li, A. Fiore, M. Gurioli, "Mode tuning of photonic crystal nanocavities by photoinduced non-thermal oxidation", *Applied Physics Letters*, **100** pp. 033116, 2012.

[123] S. Schartner, S. Kalchmair, A.M. Andrews, P. Klang, W. Schrenk, G. Strasser, "Post-fabrication fine-tuning of photonic crystal quantum well infrared photodetectors", *Applied Physics Letters*, **94** pp. 231117, 2009.

[124] A.F. Koenderink, M. Kafesaki, B.C. Buchler, V. Sandoghdar, "Controlling the Resonance of a Photonic Crystal Microcavity by a Near-Field Probe", ", *Physics Review Letters*, **95** pp. 153904, 2005.

[125] D. Psaltis, S.R. Quake, C. Yang. "Developing optofluidic technology through the fusion of microfluidics and optics", *Nature*, **442** pp. 381–386, 2006.

[126] S. Mosor, J. Hendrickson, B.C. Richards, J. Sweet, G. Khitrova, H.M. Gibbs, T. Yoshie, A. Scherer, B. Shchekin, D.G. Deppe, "Scanning a photonic crystal slab nanocavity by condensation of xenon", *Applied Physics Letters*, **87** pp. 141105, 2005.

[127] H. Du, F.S. Chau, G. Zhou, "Mechanically-Tunable Photonic Devices with On-Chip Integrated MEMS/NEMS Actuators", *Micromachines*, **7** pp. 69, 2016.

[128] X. Chew, G. Zhou, H. Yu, F.S. Chau, J. Deng, Y.C. Loke, X. Tang, "An in-plane nano-mechanics approach to achieve reversible resonance control of photonic crystal nanocavities", *Optics Express*, **18** pp. 22232–22244, 2010.

[129] A. Hakansson, H. Miyazaki, "Inverse Design of Microelectromechanically Controlled Scattering Optical Elements", *Japanese Journal of Applied Physics*, **46** pp. 011104, 2007.

[130] P. Shi, H. Du, F.S. Chau, G. Zhou, J. Deng, "Tuning the quality factor of split nanobeam cavity by nanoelectromechanical systems", *Optics Express*, **23** pp. 19338–19347, 2015.

[131] T. Lin, X. Zhang, Y. Zou, F.S. Chau, J. Deng, G. Zhou, "Out-of-plane nano-electro-mechanical tuning of the Fano resonance in photonic crystal split-beam nanocavity", *Applied Physics Letters*, **107** pp. 153107, 2015.

[132] T. Lin, F. Tian, P. Shi, F.S. Chau, G. Zhou, X. Tang, J. Deng, "Design of mechanically-tunable photonic crystal split-beam nanocavity", *Optics Letters*, **40** pp. 3504–3507, 2015.

[133] H. Du, X. Zhang, J. Deng, Y. Zhao, F.S. Chau, G. Zhou, "Lateral shearing optical gradient force in coupled nanobeam photonic crystal cavities", *Applied Physics Letters*, **108** pp. 171102, 2016.

[134] L. Midolo, F. Pagliano, T.B. Hoang, T. Xia, F.W.M. van Otten, L.H. Li, E.H. Linfield, M. Lermer, S. Hofling, A. Fiore, "Spontaneous emission control of single quantum dots by electromechanical tuning of a photonic crystal cavity", *Applied Physics Letters*, **101** pp. 091106, 2012.

[135] M. Notomi, H. Taniyama, S. Mitsugi, E. Kuramochi, "Optomechanical wavelength and energy conversion in high-q double-layer cavities of photonic crystal slabs", *Physical Review Letters*, **97** pp. 023903, 2006.

[136] M. Petruzzella, S. Birindelli, F.M. Pagliano, D. Pellegrino, Ž. Zobenica, S. Fattah Poor, F.W.M. van Otten, L.H. Li, E.H. Linfield, A. Fiore, "Tuneable Waveguide-Coupled cavity-dot node", in review, 2018.

[137] R.H. Hadfield, "Single-photon detectors for optical quantum information applications",
Nature Photonics, **3** pp. 696, 2009.

[138] M.D. Eisaman, J. Fan, A. Migdall, S.V. Polyakov, "Single-photon sources and detectors", *Review of Scientific Instruments*, **82** pp. 071101, 2011.

[139] MPD website. http://www.micro-photon-devices.com/Products/SPAD-by-Wavelength/
900nm-1700nm/InGaAs-InP.

[140] N. Namekata, S. Adachi, and S. Inoue. "1.5 GHz single-photon detection at telecommunication wavelengths using sinusoidally gated InGaAs/InP avalanche photodiode" *Optics Express*, **17** pp. 6275, 2009.

[141] S. Tisa, A. Tosi, F. Zappa, "Fully-integrated CMOS single photon counter", *Optics Express*, **15** pp. 2873, 2007.

[142] A.E. Lita, A.J. Miller, S.W. Nam, "Counting near-infrared single-photons with 95% efficiency", *Optics Express*, **16** pp. 3032, 2008.

[143] B. Calkins, P. L. Mennea, A.E. Lita, B.J. Metcalf, W.S. Kolthammer, A.L. Linares, J.B. Spring, P.C. Humphreys, R.P. Mirin, J.C. Gates, P.G.R. Smith, I.A. Walmsley, T. Gerrits, S.W. Nam, "High quantum-efficiency photon-number-resolving detector for photonic on-chip information processing", *Optics Express*, **21** pp. 22657-22670, 2013.

[144] A.D. Semenov, G.N. Goltsman, A.A. Korneev, “Quantum detection by current carrying superconducting film”, *Physica C: Superconductivity*, **351** pp. 349–356, 2001.

[145] A. Semenov, A. Engel, H.-W. Huebers, M. Siegel, “Spectral cut-off in the efficiency of the resistive state formation caused by absorption of a single-photon in current-carrying superconducting nano-strips”, *The European Physical Journal B-Condensed Matter and Complex Systems*, **47** pp. 495–501, 2005.

[146] A.D. Semenov, P. Haas, H.-W. Hübers, K. Ilin, M. Siegel, A. Kirste, T. Schurig, A. Engel, “Vortex-based single-photon response in nanostructured superconducting detectors”, *Physica C: Superconductivity*, **468** pp. 627–630, 2008.

[147] L.N. Bulaevskii, M.J. Graf, C.D. Batista, V.G. Kogan, “Vortex-induced dissipation in narrow current-biased thin-film superconducting strips” *Physical Review B*, **83** pp. 144526, 2011.

[148] J.J. Renema, R. Gaudio, Q. Wang, Z. Zhou, A. Gaggero, F. Mattioli, R. Leoni, D. Sahin, M.J.A. de Dood, A. Fiore, M.P. van Exter, “Experimental Test of Theories of the Detection Mechanism in a Nanowire Superconducting Single Photon Detector”, *Physics Review Letters*, 112 pp. 117604, 2014.

[149] A.J. Kerman, J.K.W. Yang, R.J. Molnar, E.A. Dauler, K.K. Berggren, “Electrothermal feedback in superconducting nanowire single-photon detectors”, *Physical Review B*, **79** pp. 100509, 2009.

[150] K. Smirnov, A. Divochiy, Y. Vakhtomin, P. Morozov, P. Zolotov, A. Antipov, V. Seleznev, “NbN single-photon detectors with saturated dependence of quantum efficiency”,
Superconductor Science and Technology, **31** pp. 035011 ,2018.

[151] A. Verevkin, J. Zhang, Roman Sobolewski, A. Lipatov, O. Okunev, G. Chulkova, A. Korneev, K. Smirnov, G.N. Goltsman, A. Semenov, “Detection efficiency of large-active-area NbN single-photon superconducting detectors in the ultraviolet to near-infrared range” *Applied Physics Letters*, **80** pp. 4687, 2002.

[152] F. Marsili, V.B. Verma, J.A. Stern, S. Harrington, A.E. Lita, T. Gerrits, I. Vayshenker, B. Baek, M.D. Shaw, R.P. Mirin, S.W. Nam, “Detecting single infrared photons with 93% system efficiency”, *Nature Photonics*, **7** pp. 210, 2013.

[153] V. Anant, A.J. Kerman, E.A. Dauler, J.K. Yang, K.M. Rosfjord, K.K. Berggren, “Optical properties of superconducting nanowire single-photon detectors”, *Optics Express*, **16** pp. 10750–10761, 2008.

[154] A. Gaggero, S. J. Nejad, F. Marsili, F. Mattioli, R. Leoni, D. Bitauld, D. Sahin, G. J. Hamhuis, R. Nötzel, R. Sanjines, A. Fiore, “Nanowire superconducting single-photon detectors on GaAs for integrated quantum photonic applications”, *Applied Physics Letters*, **97** pp. 151108–151108, 2010.

[155] T. Yamashita, S. Miki, H. Terai, Z. Wang, “Low-filling-factor superconducting single photon detector with high system detection efficiency”, *Optics Express*, **21** pp.27177–27184, 2013.

[156] J.M. Shainline, S.M. Buckeley, N. Nader, C.M. Gentry, K.C. Cossel, J.W. Cleary, M. Popovic, N.R. Newbury, S.W. Nam, R.P. Mirini, “Room-temperature-deposited dielectrics and superconductors for integrated photonics”, *Optics Express*, **25** pp. 10325, 2017.

[157] M.K. Akhalaghi, E. Schelew, J.F. Young, “Waveguide Integrated Superconducting Single Photon Detectors Implemented as Coherent Perfect Absorbers”, *Nature Communications*, **6** pp. 9233, 2015.

[158] F. Marsili, F. Najafi, E. Dauler, F. Bellei, X. Hu, M. Csete, R.J. Molnar, K.K. Berggren, “Single-photon detectors based on ultranarrow superconducting nanowires”, *Nano Letters*, **11** pp. 2048, 2011.

[159] M. Hofherr, D. Rall, K. Ilin, M. Siegel, A. Semenov, H.-W. Hubers, N.A. Gippius, “Intrinsic detection efficiency of superconducting nanowire single-photon detectors with different thicknesses”, *Journal of Applied Physics*, **108** pp. 014507, 2010.

[160] V.B. Verma, B. Korzh, F. Bussières, R.D. Horansky, S.D. Dyer, A.E. Lita, I. Vayshenker, F. Marsili, M.D. Shaw, H. Zbinden, R.P. Mirin, S.W. Nam, “High-efficiency superconducting nanowire single-photon detectors fabricated from MoSi thin-films”, *Optics Express*, **23** pp. 33792, 2017.

[161] J.K.W. Yang, A.J. Kerman, E. Dauler, B. Cord, V. Anant, R.J. Molnar, K.K. Berggren, “Suppressed critical current in superconducting nanowire single-photon detectors with high fill-factors”, *IEEE Transactions on Applied Superconductivity*, **19** pp. 318, 2009.

[162] A.J. Kerman, E.A. Dauler, J.K.W. Yang, K.M. Rosfjord, V. Anant, K.K. Berggren, G.N. Goltsman, B.M. Voronov, “Constriction-limited detection efficiency of superconducting nanowire single-photon detectors”, *Applied Physics Letters*, **90** pp. 101110, 2007.

[163] R. Gaudio, K.P.M. op`t Hoog, Z. Zhou, D.Sahin and A. Fiore, “Inhomogeneous critical current in nanowire superconducting single-photon detectors”, *Applied Physics Letters*, **105** pp. 222602, 2014.

[164] J.R. Clem, K.K. Berggren, “Geometry-dependent critical currents in superconducting nanocircuits”, *Physics Review B*, **84** pp. 174510, 2011.

[165] M.K. Akhlaghi, H. Atikian, A. Eftekharian, M. Loncar, A.H. Majedi, “Reduced dark counts in optimized geometries for superconducting nanowire single photon detectors”, *Optics Express*, **20** pp. 23610, 2012.

[166] A.J. Kerman, E.A. Dauler, W.E. Keicher, J.K.W. Yang, K.K. Berggren, G. Goltsman, B. Voronov, "Kinetic-inductance-limited reset time of superconducting nanowire photon counters", *Applied Physics Letters*, **88** pp. 111116, 2006.

[167] J.K.W. Yang, A.J. Kerman, E.A. Dauler, V. Anant, K.M. Rosfjord, K.K. Berggren, "Modelling the electrical and thermal response of superconducting nanowire single-photon detectors", *IEEE Transactions on Applied Superconductivity*, **17** pp. 581–585, 2007.

[168] S. Jahanmirinejad, A. Fiore, "Proposal for a superconducting photon number resolving detector with large dynamic range", *Optics Express*, **20** pp. 5017–5028, 2012.

[169] M. Tarkhov, J. Claudon, J.Ph. Poizat, A. Korneev, A. Divochiy, O. Minaeva, V. Seleznev, N. Kaurova, B. Voronov, A.V. Semenov, G. Goltsman, "Ultrafast reset time of superconducting single photon detectors" *Applied Physics Letters*, **92** pp. 241112, 2008.

[170] M.J. Stevens, R.H. Hadfield, R.E. Schwall, S.W. Nam, R.P. Mirin, J.A. Gupta, "Fast lifetime measurements of infrared emitters using a low-jitter superconducting single-photon
detector", *Applied Physics Letters*, **89** pp. 031109–031109, 2006.

[171] L. You, X. Yang, Y. He, W. Zhang, D. Liu, W. Zhang, L. Zhang, L. Zhang, X. Liu, S. Chen, Z. Wang, X. Xie, "Jitter analysis of a superconducting nanowire single photon detector", *AIP Advances*, **3** pp. 072135–072135, 2013.

[172] D. Sahin, A. Gaggero, T. Ba Hoang, G. Frucci, F. Mattioli, R. Leoni, J. Beetz, M. Lermer, M. Kamp, S. Höfling, A. Fiore, "Integrated autocorrelator based on superconducting nanowires", *Optics Express*, **21** pp. 11162–11170, 2013.

[173] D. Sahin, A. Gaggero, J.W. Weber, I. Agafonov, M. A. Verheijen, F. Mattioli, J. Beetz, M. Kamp, S. Höfling, M.C.M. van de Sanden, R. Leoni, A. Fiore, "Waveguide nanowire superconducting single-photon detectors fabricated on GaAs and the study of their optical properties", *IEEE Journal of Selected Topics in Quantum Electronics*, **2** pp. 1-10, 2015.

[174] R.H. Brown and R. Twiss, "A test of a new type of stellar interferometer on sirius", *Nature*, **4541** pp. 1046–1048, 1956.

Chapter 2

Experimental methods

2.1 Quantum dots and heterostructure growth

All the wafers used for this work are composed of layers of different materials such as AlGaAs, GaAs intrinsic, p-doped, n-doped and with some layers including embedded QDs. The technique used to produce such wafers is the molecular beam epitaxy.

2.1.1 Molecular Beam Epitaxy (MBE)

MBE indicates a method for building ordered layers of materials from molecular/atom beams of different elements. A schematic illustration of the ultra-high vacuum (10^{-10} Torr) growth chamber of a typical solid source MBE machine is shown in Fig 2.1.

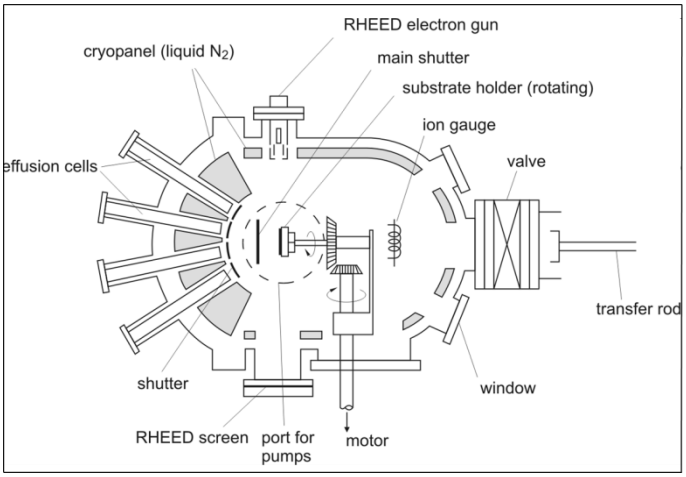

Fig. 2.1 Schematic illustration of the growth chamber of MBE[1]

The Createc SY022 MBE system at the TU/e Nanolab has a similar chamber configuration as the one shown on the schematic. Eight cells are installed in the MBE system including Ga, Al, In and As. During growth, molecular beams are generated by heating up materials in the crucibles of the effusion cell. The sample is mounted on a

molybdenum holder and fixed to an adapter connected to a rotation mechanism. In order to achieve a homogenous deposition of material over a wafer, the substrate is rotated during growth. The molecular beams can be easily switched on and off by opening or closing the shutters, this enables a rapid switching of different materials and therefore the growth of layered materials with an atomically precise interface. The sublimated elements condense on the surface of the substrate and form atomic bonds with each other. The substrate temperature plays a crucial role in the growth of the material by influencing the mobility and the desorption rate of adatoms on the surface. The substrate temperature is measured by a thermocouple placed behind the sample holder adapter. However, this is not precise enough, due to the absence of physical contact between the thermocouple and the substrate. Since the substrate temperature is essential for the epitaxy process, especially for the growth of low-density QDs, a more precise substrate temperature monitoring method is used. A calibrated kSA BandiT system[2] determines the temperature of the semiconductor substrate with a precision of 0.1°C.

2.1.2 Growth conditions

Excluding the wafers for the integration with nanomechanical structures, the growth for single membrane structures follows the design and condition described below.
The series of epitaxial layers starts with the wafer deoxidation and a first buffer layer of few hundreds nm of bare GaAs on a [001]-oriented 2" GaAs substrate. An $Al_xGa_{1-x}As$ sacrificial layer with x = 67 - 79% is then grown with a thickness of 1.5µm. The first half of the GaAs membrane is then grown with a thickness of 150 nm. The active material is embedded in the next step as a low-density layer of QDs. The InAs self-assembled quantum dots are grown with a very low growth rate (0.0023 mono layers/s) by means of a Stranski-Krastanov technique[3]. To tune the optical emission of these quantum emitters a subsequent InGaAs capping layer is deposited, an ensemble emission wavelength centred around 1300 nm at room temperature is achieved. The second half of the GaAs membrane is then grown with the same thickness as the first half.
Two specifications are crucial, in order to efficiently perform fully on-chip single-photon experiments, a low QDs density and a very low roughness of the surface. The conditions to grow low density QDs have been previously optimized using a substrate temperature of 580°C and 2 mono layers of InAs under an In background pressure of $3x10^{-9}$ Torr, this allows to achieve a density in the range of 10-30 dots/μm^2.
The roughness of the superficial layer has never been an important specification in relation to devices for sources, it plays instead a crucial role in this case of integration with detectors.
It is necessary to have a substrate's surface with very low roughness (<0.5 nm), since the internal quantum efficiency of the detector depends on the quality and uniformity of the superconducting film[4]; consequently, a rough film could produce an inefficient SSPD.

For this reason, during growth, an extra final step has been added in order to accomplish the specification on roughness. The deposition of a few atomic layers of GaAs, at 20 °C above the oxide removal temperature (585 °C) under an As flux, yields samples with a smooth surface (root mean square roughness = 0.4 nm).

2.1.3 Characterization of the wafer

Surface

The surface morphology is characterized with an atomic force microscope (AFM) Veeco Dimension 3100, working in tapping mode. AFM provides an atomic level height-resolution of the structure. In the measurement, the sample can be moved in x-y-z directions. The AFM tip is mounted to an AFM tip holder and fixed to the AFM head with the movement controlled by a piezo. A laser beam is focused to the backside of the AFM tip and is reflected to a position sensitive detector (PSD). Before scanning, the tip is brought close to the sample surface, where the force between the sample and the tip is strong. During scanning, the cantilever of the AFM tip oscillates. The amplitude and the frequency of the oscillation are kept constant during the scan by using a feedback loop to analyze the laser spot detected by the PSD and control the piezo actuator in the z direction. The AFM tips used are NT-MDT NSG10 series noncontact single crystal silicon SPM tips with Pt conductive coating and with the resonant frequency in the range of 140-390 kHz, force constant of 3.1-3.76 N/m. The cantilever length, width and thickness are 95±5 µm, 30±3 µm and 2±0.5 µm respectively[5].
The AFM images are analyzed by Gwyddion, open source statistical parametric mapping software which can perform many data visualization and data processing tasks[6]. In the following two AFM images after processing are shown, one of a standard low-density QDs single membrane wafer and one with the same structure but in which the extra final growth step to smooth the surface has been performed.

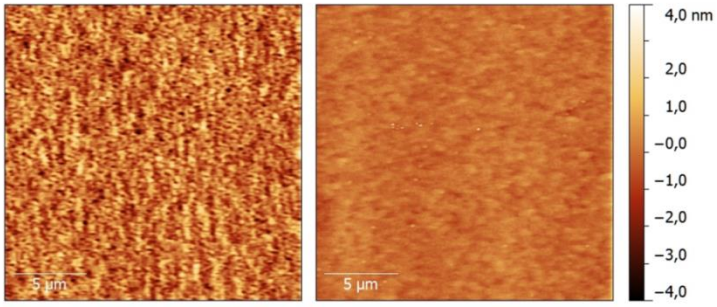

Fig. 2.2 AFM images of the surface of a low-density QDs single-membrane wafer before (left) and after (right) the smoothing final growth step

Photoluminescence

The optical characterization of the QDs emission and the cavity modes of the fabricated devices is performed by a micro-photoluminescence (mPL) setup where a He-flow cryostat able to work at temperature down to 6-9K is interfaced with an optical apparatus. The QDs in the sample can be excited by an external laser source in non-resonant, quasi-resonant or resonant configuration. The re-emitted photons are collected by the use of a near-infrared objective (100x, numerical aperture NA=0.6) and sent directly, in free space or through a single mode optical fibre, to the dispersion grating of a spectrometer (Horiba Jobin Yvon FHR 1000). The emission spectrum can be measured through the light dispersed into an InGaAs pixels array cooled at the liquid nitrogen temperature with a resolution below 200μeV. In a standard confocal mPL set-up the PL signal and the laser pump are spatially separated by using a beam splitter or a dichroic mirror. In the case of non-resonant or quasi-resonant excitation the laser filtering is commonly realized by mean of high-pass optical filters that suppress the laser component at lower wavelength. A series of high-precision piezo-motors are normally used to control the relative position between the optics and the sample in order to probe different regions of the measured device. For alignment purpose a LED can be used to illuminate the sample while the reflected image can be deflected by another beam splitter and directed to a CCD camera.

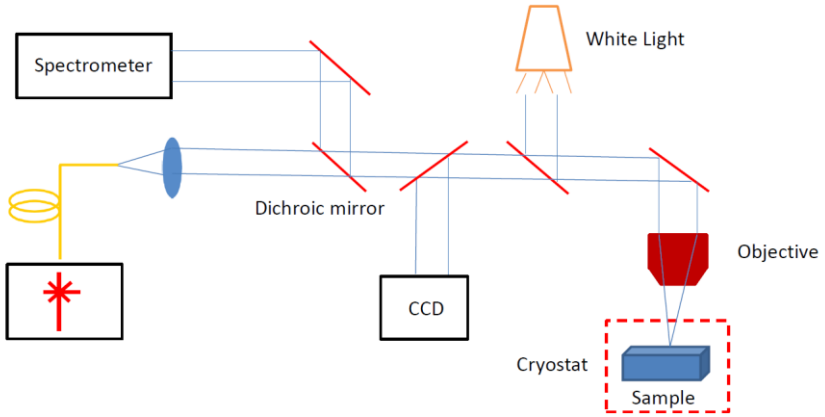

Fig. 2.3 Sketch of the micro-photoluminescence setup

In the following two examples of micro-PL spectra of the QD emission on bulk at room temperature are shown. The two spectra were measured on the same wafer but the second spectrum refers to a piece in which an extra annealing step at 400°C has been performed. Indeed the sputtering deposition of the superconducting film requires an annealing of the heterostructured wafer at around 400°C and this could produce a variation on the QDs emission spectra. The comparison shows only a small (5nm) blue shift both of ground and

first excited state and a small increase in the relative intensity of the ground state. These changes do not have consequences for the next fabrication steps.

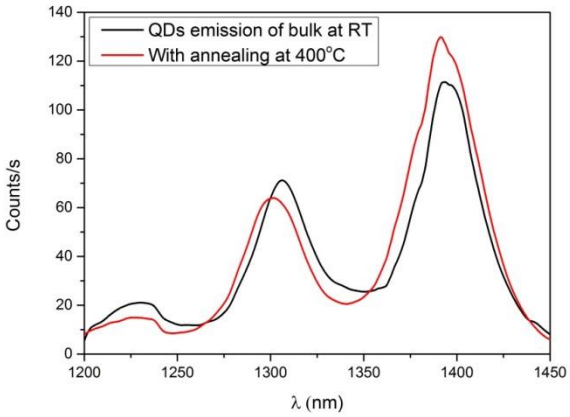

Fig. 2.4 RT PL spectra comparison of bulk QDs emission before and after annealing at 400°C

2.2 Sputter deposition of NbN films

The deposition of the superconducting thin film for SSPD fabrication has historically been performed by means of a direct current (DC) reactive magnetron sputtering [7]. In the following the sputtering technique and the process conditions used for this work are presented.

2.2.1 DC reactive magnetron sputtering

Sputtering is a non-thermal physical vapour deposition (PVD) method suitable for thin film deposition. The process is based on the energy and momentum transfer from the ionized sputtering gas to the solid target (Fig. 2.5 inset). Under a low-pressure inert gas (Ar) atmosphere, a high voltage across the anode and the cathode is applied and the plasma is created. Then, the cathode material, i.e. the target (Nb) is bombarded with the inert gas (Ar) ions and the surface atoms of the target are ejected by the highly energetic ions. The specimen on the anode (GaAs) is coated by the bombarded cathode material. The sputtering target can be either an element or a compound. Commonly, nitride and oxide compounds are deposited by introducing a reactive gas such as N_2 and O_2 into the plasma during the deposition, in this case to form niobium nitride (NbN). The sputtering process is performed in a high or ultra-high vacuum environment. There are two reasons

for that. First of all, it provides a longer mean-free path for the ejected atom. Secondly, it increases the quality of the film in terms of purity by controlling the amount of contamination. Typically a sputter system is operated below 10^{-6} Torr. In our processing, the fabrication of superconducting material is very demanding and requires the highest possible purity level. Thus, the base pressure is kept at the level of 10^{-9} Torr which is considered as an ultra-high vacuum.

For this work, a sputtering system from AJA Intern., INC., ATC 1500-F has been used to grow NbN films on different GaAs-based heterostructure. It is equipped with the reactive gasses N_2 and O_2 and with four targets as source materials and each is 2-inch in diameter.

In Fig. 2.6, the machine and the inside of the vacuum chamber with four-chimneys are shown. The different numbers identify the different components of the system.

The inlet (1) is used to introduce the N_2 into the growth chamber. N_2 flow is controlled with a flow meter. The view port (2) is mainly to look through while engaging the sample holder and retracting the “transfer-arm" to the linear, rotary stage and also to observe the plasma during the process. The colour of the plasma can be used to identify if there is any contamination in the chamber. Plasma colour with pure Ar at low-pressures is identified with its characteristic purple emission. It turns to pink-purple with N_2 while the oxygen contamination changes the colour to dark-purple. There is also a shutter inside to protect the window from being deposited. The loadlock chamber (3) is important to preserve high vacuum conditions in the main chamber while transferring the samples. There are two vacuum gauges (4) available in the system for low (convectron gauge) and high (capacitance manometer) range of pressure measurement. The bias unit (5) allows adjusting the current (voltage) biasing. The unit labelled with (6) is the temperature control unit and it is used for reading and setting a temperature value. According to the current configuration, the location of the NbN target is shown at (7), and Au, Ti and Cr are located at (8), (9) and (10), respectively.

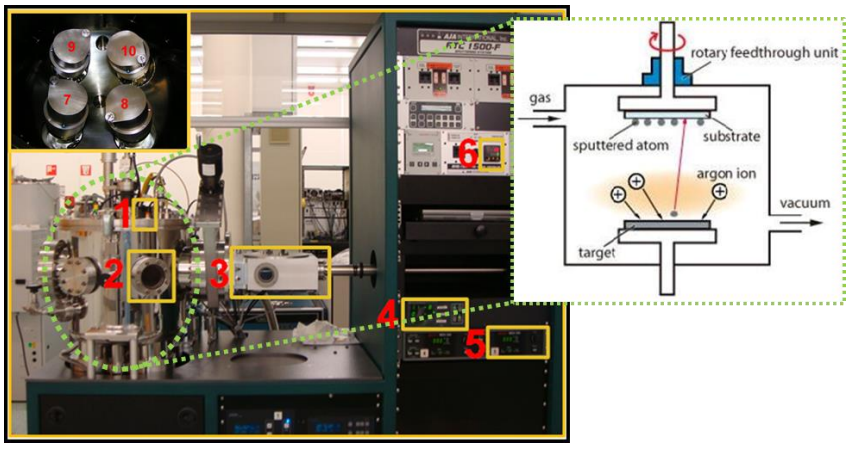

Fig. 2.5 Picture of the sputtering system used in this work to growth the NbN films. Inset: Schematic of the working system of a sputtering machine.

2.2.2 Deposition condition

A large number of variables can be tuned within a process, and even a small variation of one of the chosen parameters can produce a large difference on the quality of the produced film.

- The angle of the target and the rotation of the sample holder: these parameters are adjusted in order to obtain a uniform film thickness on the samples grown within the same batch. The angle also plays a role to convey the ions momentum to the atoms of the target, which is the highest at a right angle.
- The distance between the target and the substrate is mostly shorter for a sputter system than for the other vacuum systems. The most important reason is to eliminate the number of intermediate scatterings/collisions the ejected atom might experience during the time of flight.
- Current (voltage) supply is directly related to the energy provided to the positively charged ions which are accelerated and then eject an atom from the target material.
- The total sputtering pressure sets the amount of total particles (inert gas + reactive gas) in the chamber to form a plasma during the deposition. Sputtering process occurs mostly at low-pressure (< 5 mTorr), this has the advantage to obtain high mean-free path of the ions, which is inversely proportional to pressure. Therefore, the pressure is kept low enough to enhance the mean-free path but high enough to ignite and sustain the plasma. The pressure is adjusted automatically by the movement of a gate valve accordingly to the set pressure.
- The flow of the reactive gas N_2 determines the stoichiometry of Nb_xN_y, while an Ar flow is used to ignite the plasma and keep it stable. The flow is measured in unit of sccm (standard cubic centimetres per minute).
- The substrate temperature determines the particle dynamics at the substrate surface. At low temperatures, the mobility of the adatoms is small which may create a thickness variation along the surface. While at higher temperature the mobility is increased, arsenic evaporation from the substrate starts to be a problem, as it is going to be explained extensively in the next chapter (Chap.3.2.1). The nominal temperature can be tuned from room temperature up to 800°C. The value is read using a thermocouple located between the two infrared-lamps, located at the back side of the substrate holder. Therefore, it is expected that the temperature is lower on the sample holder and surface than the reported values. Moreover an important role on the effective temperature on the substrate is played by the working condition of the installed infrared lamps, the amount of indium used to mount the samples on the holder and the thickness of the holder that continuously changes after every mechanical polishing of its surface.

- The deposition time determines the thickness of the film, which is measured by spectroscopic ellipsometer as explained later in this chapter. The growth rate strongly depends on of the above described parameters and has been adjusted from time to time to achieve the standard thickness of ~5nm.
- The preconditioning of the chamber and sample holder determines the initial pressure inside the chamber. As already discussed the highest purity level is required and a base pressure of ultra-high vacuum (10^{-9} Torr) has to be reached. In general, high vacuum systems are built with certain equipments, such as cryogenic temperature chambers walls or seals and gaskets used between components, that easily allows the system to reach the ultra-high vacuum pressure range. However these techniques are not realisable in our setup. Therefore, other techniques are implemented to improve the vacuum of deposition chamber. A titanium (Ti) deposition cycle is used prior to each real deposition run to decrease the base pressure temporarily below $1x10^{-8}$ Torr. Ti is well known for interacting with the gasses and forms a stable product, with this method the system is temporarily conditioned by decreasing the concentration of the H_2O molecules present in the chamber. It is temporary because Ti is consumed and becomes not functional any more due to the following deposition run and a constant out-gassing within the chamber. Moreover it has been noticed, that a poor initial vacuum ($> 7x10^{-9}$ Torr) creates problems in keeping a stable plasma during the deposition and so affects negatively the quality of the film.

All these variables can be modified to optimise the desired film stoichiometry and the quality of the film. While having so many parameters brings flexibility, it may complicate the optimisation.

In addition, it is important to keep track of the erosion of the target. It is known that when the target is eroded, the effective applied power applied on the target changes and therefore the energy and the dynamics of the ejected Nb atoms do. That degrades the quality of the film. In order to avoid that, the target is operated within a voltage range of 345-360 V. The targets are ordered either from AJA Intern., INC. or from Kurt Lesker, with a dimension of 2 x 0.250 inch and purity of 99.95 %.

Last but not least, it is crucial to monitor the roughness and amount of Ti deposited on top of the sample holder (Inconel). At the beginning of every sputtering film deposition campaign the sample holder is mechanically polished, then cleaned in an ultrasonic bath with acetone first and with isopropanol after and finally baked above the growth temperature (>450°C) in order to assure the cleanness of the holder and evaporate the water molecules. The GaAs chips (~$1.5x1.5mm^2$) are attached to the sample holder by melted Indium to ensure a good and uniform thermal contact.

2.2.3 Characterization of the film

After the deposition, the superconducting NbN film is characterized by several techniques. Three specifications of the film are measured. The roughness of the surface by AFM in the same way described previously for surface characterization of the wafer after MBE growth. The thickness of the film is measured by spectroscopic ellipsometry. The critical temperature of the superconducting film by measuring the resistance of the film as function of temperature.

Thickness measurement

Thickness measurements are performed ex-situ with spectroscopic ellipsometry (SE) from J.A. Woollam Co. Inc. right after the deposition[8]. SE is a non-destructive technique and operates in a spectral range of 200-1000 nm, with an accuracy of few atomic layers. The software, CompleteEASE, is interfaced for data acquisition and analysis. The SE is a very accurate technique as it measures the changes in the polarisation of light after the reflection from a film or a multilayer. The polarization state of the light incident upon the sample may be decomposed into an *s* and a *p* component (the *s* component has the electric field oscillating perpendicular to the plane of incidence and parallel to the sample surface, and the *p* component has it oscillating parallel to the plane of incidence). The amplitudes of the *s* and *p* components of the reflectance are denoted by R_s and R_p and their ratio defines the complex reflectance:

$$\rho = \frac{R_s}{R_p} = \tan \Psi \, e^{i\Delta} \quad (2.1)$$

The polarization change is quantified by the amplitude ratio, Ψ, and the phase difference, Δ.

Since ellipsometry is measuring the ratio of two values (rather than the absolute value of either), it can be considered very accurate and reproducible, moreover the angle of incidence is chosen close to the Brewster angle to ensure maximum difference in the ratio between the two components. One weakness of ellipsometry is that the measured Ψ and Δ cannot be converted directly into the optical properties of the sample, normally a model analysis must be performed. Direct inversion of Ψ and Δ is only possible in very simple case of isotropic, homogeneous and infinitely thick film. In all other cases a layer model must be established, which considers the optical constants (refractive index) and thickness parameters of all individual layers of the sample including the correct layer sequence. Using an iterative procedure unknown optical constants and/or thickness are varied and Ψ and Δ values are calculated. The calculated Ψ and Δ values which match the experimental data best provide the optical constant and thickness parameters of the sample. For this work a purely mathematical technique, which is called Basis-spline (B-spline), is used in order to model the thin metal layer (NbN) on top of the semiconductor substrate (GaAs).

B-spline is a fitting technique of the layer without requiring any prior knowledge of the layer in interest and it provides the physical parameters of thickness and refractive indices. Once the model that best fits the experimental data has been found, the film thickness of every sample/film can be easily measured by SE and used to adjust the deposition time according to the required thickness, around 5nm for all the films used in this work.

R(T) measurement

The measure of the resistance of the film in function of the temperature (R(T)) allows one to extract the critical temperature T_c and the transition width ΔT_c. Those properties are measured with a dipstick through a four point method. The dipstick consists of a long stick carrying the sample at one of its ends and allows to cool the NbN film down to 4.2K by inserting it directly into a Liquid Helium (LHe) dewar[9]. A sketch of the system is shown in the following Fig.2.6

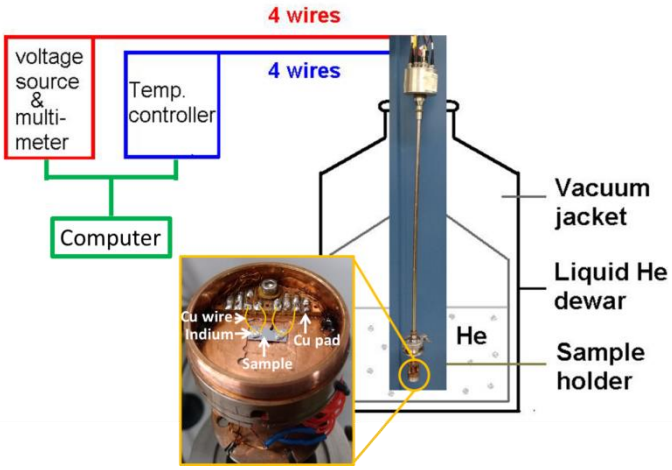

Fig. 2.6 Sketch and pictures of the R(T) measurment system. a) picture of the dipstick head

The sample, which is mounted on the dipstick head with the VGE-7031 LakeShore varnish, is connected to four copper pads via four copper wires. These copper wires are connected to other wires running along the length of the dipstick until the room temperature connections (coaxial cables). At room temperature, the coaxial cables are connected to a Keithley 2010 multimeter, a Yokogawa 7651 current source and a temperature controller LakeShore 330. The temperature is measured with a LakeShore DT-670 diode and changed by a heating resistor with a feedback loop. Both the diode and the resistance are located in the sample holder right under the sample stage. The measurements are computer-controlled with a home-written Lab-VIEW program. Once

the NbN film is inside the dewar and it reaches a temperature lower than its Tc, a fixed current is supplied to it and a temperature scan starts. During this scan the temperature is increased by a desired fixed amount and, when it is stable at the given value, the voltage drop across the NbN film is recorded through two separate contacts. The film resistance is then calculated and plotted as a function of the film temperature. By the end of the temperature scan, a graph similar to that reported in Fig. 2.8 is obtained. The parameters Tc and ΔTc are determined using the average and the difference of the temperatures corresponding to 80 % and 20 % of the average normal resistance derived following the procedure reported in ref. [9].
Typical values for a NbN film of thickness ~5nm deposited at a base temperature of 400°C are Tc ~ 10K and ΔTc ~ 0.3K. In the next chapter (Chap. 3.3) will be discussed more in detail the dependence of Tc on the deposition temperature, and its effect on the surface roughness and ultimately on the efficiency of the SSPDs.

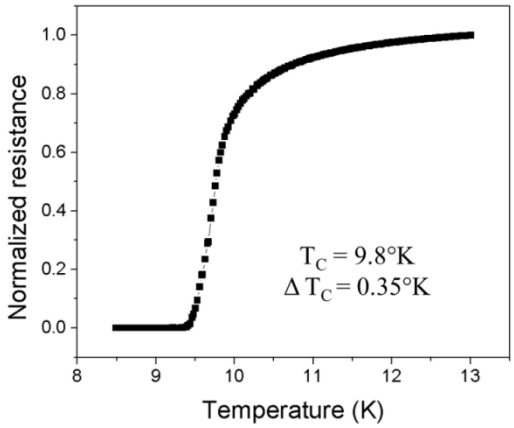

Fig. 2.7 Typical R(T) curve of a NbN film of thickness ~5nm

2.3 Post-growth processing

Once all the wanted layers have been grown and deposited on our wafer, a second phase of nanofabrication starts. The definition of metal contacts, superconducting wires, photonic crystal structures and waveguides, as well as different etchings, are optimized in order to allow the integration of the different components of the chip and performed using the following machine located in the NanoLab@TU/e cleanroom facility.

2.3.1 Optical and electronic lithography

At the core of nano-devices fabrication is the possibility to create high resolution microscopic structure with a well-defined geometry. The technique to define a geometrical pattern into a chip by using a resist, is called lithography. Two kind of lithography are used for this work: optical lithography and electron beam lithography (EBL).

Optical lithography

In photolithography the resolution of the patterned design is proportional to the wavelength of the radiation source used to illuminate a sensitive photoresist layer through small apertures in a Cr mask. Ultra-violet (UV) light achieves resolutions in the order of 0.5µm and is used for fast exposures. A photo-sensitive layer deposited on top of the desired substrate is brought in contact with the patterned mask and exposed under a high power UV lamp. All the Cr masks have been designed within Clewin4 and exported in Graphics Database System (GDS) format to be then realized in TU Delft.
In this work the optical lithography has been used to define the contact pads and to open them to make electrical contacts at the end of the process avoiding to remove the SiN (Chap.4.2.7).
In order to define the contact pads, the negative resist MaN440 from Micro Resist Tech. is spun onto the NbN film for 30s at 5000rpm with the Karl Suss RC8 spinner. After this a baking of 5min at 95°C is necessary to harden the resist giving it the right photo-sensitivity. A Suss Microtech MA6 aligner in contact mode has been used for the UV exposure where a high vacuum is created between the sensitive material and the Cr mask improving the patterning results. The sample is exposed to the UV light for a time interval of 100s. Following the exposure, the photoresist is developed with MaD332-s for 2min and 30s where the non-exposed areas are dissolved.

Electron beam lithography

Whenever a higher resolution is required, EBL has to be chosen in order to pattern structures of nanometric size. Two different EBL machine has been used for this work: RAITH150-TWO during the first half period of this research work and RAITH EBPG 5150 during the second half.
The RAITH150-TWO features a motorized X-Y-Z stage, an electron gun with acceleration voltage up to 30kV inside a scanning electron microscope column. A movable beam deflector and blanker and a pattern generator allow for the high-resolution control of the relative position between sample and electron beam. The position accuracy is controlled within 1 nm by means of laser interferometric techniques. The pattern in this case is drawn by the electron beam into the e-beam resist following the coordinates of a

series of geometrical shapes that can be specified in a dedicated software. An initial manual alignment is necessary to regulate the sample orientation, the aperture, the stigmation and the focus of the beam and the write-field mismatch. The writing-field is an imaginary square of $100x100\mu m^2$ and is the smallest unit of discretization in the raw movement of the electron beam. During the automatic patterning the stage moves from the centre of a writing-field to another. Within each writing-field the e-beam is rapidly deflected with a fine movement providing excellent resolution but between two different write-fields stitching errors < 50 nm may occur. To avoid this possibility the desired patterns must be concentrated in individual write-fields and not across them. The SEM detectors can also be used to perform overlay exposures on substrates already patterned with alignment marks. The capacity of the machine to provide an almost perfect alignment of the nanowires on top of the suspended nanobeam has been tested with very good results and a precision around 250nm. After the definition of the metal contact and alignment markers through optical lithography, a first step of EBL is performed to define the pattern of the nanowires. The sample with contact pads is covered with a high-resolution negative electron-beam resist, the HSQ (hydrogen silsesquioxane) XR-1541-6 from DOW CORNING. The sample is spun with the CONVAC ST 146 spinner for 1 minute at 4000rpm and is then baked for 2 min at 150°C and 2 min at 220°C. The sample is now ready to be loaded into the EBL writer. But before that, a thin layer of Au (~7.5nm) is evaporated on the sample edge in order to avoid the resist charging during the EBL beam focusing. The gold layer deposition is performed with the Edwards Auto 306 evaporator. An acceleration voltage of 20kV with a beam aperture slit of 15µm is used for the EBL exposure. The manual and automatic mark alignments are performed to align the design with the existing contact pads. On this system the electronic dose (C/cm^2) that the EBL has to deposit in order to expose the resist is severely affected by the sample material and the focusing on the surface during the manual alignment, meaning that for every exposure the dose has to be fine-tuned accordingly to the specific sample. After the exposure the sample is developed for 1min15s in a solution of ultra-pure water and AZ developer (4:1). A second EBL step is performed for the definition of PhCCs, SNBs and RWGs. In this case the e-beam resist is spun on top of a SiN layer previously deposited. An e-beam positive polymer resist (Zeon Corp. ZEP-520A) is spread out at around 2700rpm for 1min, as it will be discussed later in Chap.4.2.3 the spinning velocity has to be carefully calibrated in order to obtain the right thickness to allow the formation of well-defined holes of PhC during the next etching step. A baking step first for 4 min from 100°C to 150°C and then for 2 min at 200°C produces the hardening of the resist. The focusing on this resist is relatively easy and does not require the deposition of a thin metallic layer, moreover the influence of the focusing on the dose for this resist is way less critical. An acceleration voltage of 30kV with a beam aperture slit of 10µm is used for this process, and manual and automatic alignment carefully performed since in this step the alignment between nanowires and SNB is executed. After exposure the sample is developed in n-

amylacetate for 68s followed by a 52 s rinse in a MIBK:IPA(890:110) solution of methylisobutyl-ketone and isopropanol.

The RAITH EBPG 5150 is optimized for fast direct write application on sample sizes going from pieces to full wafer. It features an electron gun with acceleration voltage that is kept stable at 100kV and all the initial alignment (aperture, stigmation and focus of the beam) is automatically performed by the machine. The stage is almost fixed in all the coordinates. The X-Y plane can rotate of an angle less than 2°, meaning that when the sample is mounted on the stage the tilting of the X-Y coordinate of the sample with respect to the coordinate system of the stage cannot be more than 2°. The sample is mounted on the stage using an optical microscope in order to align the two coordinate systems as well as possible. Indeed it has been observed that whenever the alignment angle is higher than 2° it creates a mismatch between the overlay than can be larger than 500nm. The axis of the stage is also fixed, however the machine is able to effectively adjust the focusing within 50µm above and below the reference height of the stage. During the mounting of the sample is possible to check the height of the sample by means of a laser interferometric system, that exactly replicates the one inside the machine. Whenever the sample is out of the automatic focusing adjustment range, it is necessary to manually change the height of the stage using some spacers. The alignment for overlay exposure is automatically done using squared metal markers of $20x20\mu m^2$, however if the automatic procedure fails, it is always possible to proceed with a manual alignment using the SEM detectors inside the machine. This machine is not designed for imaging purpose like the previous one, but it still allows to operate manually whenever required. The writing-field dimension can be controlled by software by the user and it goes up to $500x500\mu m^2$. However the system is so fast (from 50 to 100MHz) that the thermal drift of the stage is neglectable so it is not necessary to fit a full pattern within a writing-field in order to avoid stitching errors, like for the previous system. According to the kind of structure that has to be patterned, it is possible to play with two parameters, the beam current and the beam step size (BSS). Since in this system the acceleration voltage is fixed at 100kV, it is the effective current going on the sample that as to be controlled. The range goes from 0.5nA, usually used to define small structures (below 100nm), to 100nA used for patterns of micrometric size. The BSS is the distance between the steps of the beam as it writes the pattern and basically defines the resolution. For very fine patterns a small spot size and step in between is advisable in order to make continuous well defined patterns, in this machine the minimum is 0.5nm.

This system has been used for this work to define not only the nanowires and PhC structures but the metal contact pad together with the alignment markers as well. For the metal contact, an e-beam positive polymer resist (Micro Chem 495 PMMA A11) is spun at 7000rpm for 1min and baked at 180°C for 3min Since the smallest feature of this pattern is 10µm in size and in order to speed up the exposure, the maximum current (100nA) has been used with a quite large BSS of 100nm. The resist is developed in a

solution of MIBK:IPA(890:110) for 1min and 20s and rinsed in isopropanol for the same time.
The nanowires are patterned in the same way as with the previous EBL, using a current of 1nA and a BSS of 5nm. Thanks to the autofocusing of this new machine, the deposition of the thin metallic layer in order to avoid charging has been eliminated. Moreover the autofocusing has significatively reduced the dependence of a well-defined pattern on the accuracy of the right choice for the electronic dose.
The PhCs structures are exposed with a current of 0.5nA and a BSS of 5nm, while the ridge waveguide with a current of 1nA and 10nm of BSS.

2.3.2 Metal evaporation and lift-off

Whether the metal pad definition has been done by optical lithography or EBL, after the resist development, the sample is introduced in the electron-beam evaporator FC2000 to deposit the metals. The metals are loaded in crucibles that can be selectively rotated and heated up to very high temperature by an electron beam with energy up to 15 keV. Once the metal starts to evaporate the shutter is opened allowing the migration of its atoms towards the surface of the sample mounted inside the main vacuum chamber at 10^{-7} Torr. The metal condenses then on the entire wafer forming a thin metallic layer with variable thickness. The deposition rate, and therefore the final thickness, is controlled by means of piezoelectric crystal made to resonate at their characteristic frequencies. In this work a first layer of 50nm of Ti is deposited followed by 200nm of Au. The deposited metal covers the entire sample surface and fills in the empty areas between the photoresist structures. In the lift-off phase, when the sample is kept in acetone vapour for 1h and 30 min, the photoresist dissolves allowing the lifting off of the metal. In order to ensure the complete removal of the metal in the areas outside the contact pads, the samples are kept in acetone, in the ultrasonic bath for 30s, cleaned with isopropanol and blown-dry with N_2.

2.3.3 ICP PECVD

Most of the fabrication processes rely on the use of a thin dielectric layer as an etching mask during the lithographic steps. The fabrication process for PhC structures has been previously optimized by other colleagues of the group and use a dielectric layer of SiN deposited on the substrate with the use of a PECVD machine. This kind of machine requires the use of high temperature (300°C) in order to produce a homogenous layer, the use of a low temperature process would create a non-cohesive layer unable to resist to the subsequent etching process. This is why the use of a different machine has been needed to deposit the SiN layer for this work. The ICP PECVD allows the deposition at room

temperature of a homogeneous and high quality SiN layer. An Oxford Plasmalab System 100 customized to work as an ICP PECVD machine is used for this work.
The system consists of a load-lock and a reactor chamber. The loadlock is used for sample mounting and can be easily vented or pressurized. When the pressure inside the loadlock is lower than 10^{-3} Torr, a sealed venting port opens and the sample is automatically transferred between the load-lock and the reactor chamber. The thermal contact between the sample holder and the base of the chamber is created through a small He flux (5sccm). The process starts when the pressure inside the reactor chamber is lower than 10^{-6} Torr. Mass flow controller (MFC) valves allow the injection of precursor gasses (silane SiH_4, ammonia NH_3 and oxygen O_2) with controlled ratios. The SiN layer for example is formed through the interaction of SiH_4 and NH_3.
The main difference between the PECVD and the ICP PECVD consist of the way in which the plasma is created and sustained and has strong consequences on the density of the plasma (Fig 2.8).
In a PECVD system the plasma is created by applying a voltage between two electrodes that ionize and dissociate the gas molecules. The regions between the plasma and the electrodes (sheath) present a really low electronic density and they can be modelled as the dielectric regions of a capacitor. The system can be imagined like two capacitors in series in which the plasma and the top and bottom electrode are the capacitor plates. Due to the high mobility of the electrons, the plasma can be considered like the positive electrode of the system and this allow the ions to be accelerated towards the top and bottom electrodes. The ions, accelerated toward the bottom electrode, impact on the sample surface and chemically reacts, allowing the growth of the layer. A strong RF (radio frequency) electric field of few hundreds Watts oscillating at 13.56 MHz can be also applied to enhance the ionization and dissociation of the gas molecule. Even applying a RF electric field the plasma density cannot reach the one of an ICP system that generally is two orders of magnitude higher. In the ICP the electric field is induced by an oscillating magnetic field. The top electrode is replaced by a coil in which a RF current induces an oscillating magnetic field, orthogonal to the plane of the coil. The magnetic field induces an electric field tangential to the coil turns, that is used to ionize and dissociates the gas molecules. Since the electric field is parallel to the bottom electrode, there is no capacitive coupling between the plasma and the substrate and therefore no ionic bombardment. Thanks to the radiofrequency value set at 13.56MHz, the ions reach the bottom electrode after several RF cycles so that the energy with which they impinge on the substrate is a time-average of the potential. On this system the RF is kept stable in time thanks to an automatic feedback system, in which two capacitors are used to control the impedance of the RF generator. The RF frequency is fixed, however several parameters can be changed: ICP power, RF power, total pressure inside the chamber, total and relative gas flux, substrate temperature and deposition time. All those parameters are strongly dependent on each other in order to ignite the plasma and maintain it stable. On Chap. 4.2.3 the chosen parameters to produce the SiN mask are presented together with the deposition procedure.

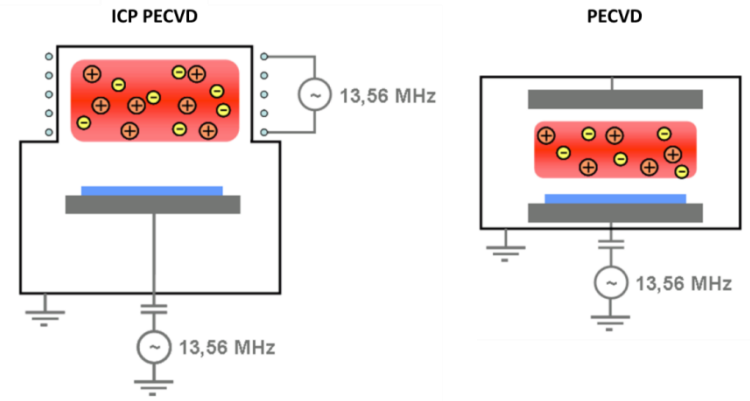

Fig. 2.8 Sketch of the working mechanism of an ICP PECVD (left) and of a PECVD (right)

2.3.4 Dry etching

Once the pattern is lithographically defined with one of previous methods, it can be transferred to the underlying SiN mask or to the GaAs substrate. The defined area can be isotropically or anisotropically etched by means of wet and dry etching techniques while the regions that should remained untouched are covered with a proper hard mask previously deposited. Among the dry etching techniques, plasma etching is the most widely used. The working system is similar to the one already described for the PECVD system (Fig. 2.10 right). The chemically reactive gases are subjected to the RF electric field at 13.56MHz to be dissociated and ionized. The high mobility electrons, created in the plasma, are accelerated towards the bottom electrode and sustain the plasma. Since the bottom electrode is electrically insulated they accumulate there forming a large negative self-bias and a static electric field pointing down in the chamber. The more massive ions in the plasma are less susceptible to the RF field but can be accelerated by the negative voltage, reach the sample with high energy and etch it by a combination of sputtering and chemical reactions. Therefore, the plasma not only provides a sufficient density of ions in the chamber but also accelerates them to achieve a strong mechanical bombardment.
To achieve the anisotropic, smooth and deep etching of nanometric features, the optimal balance between isotropic chemical reactions and uni-directional ion bombardment must be found. These two components can be controlled by changing temperature, pressure, RF power and the stoichiometric ratio of the reactive chemicals. For this work two different plasma etching machines have been used: reactive ion etching (RIE) (Oxford Pasmalab 100) and the barrel etcher (TePla 100). The RIE is based on the working principle discussed before and it has been operated at room temperature for all the dry etching steps of the process (NbN, SiN, GaAs).

A barrel etcher uses a microwave oscillating field with power in the range between 50 W and 300 W instead of a RF bias. It is a smaller and simpler machine compared to RIE and anisotropic etching is not possible. A high isotropy is accompanied by a low ion bombardment since in this case the DC self-bias cannot be created. The standard usage is with pure oxygen plasma for sample cleaning or photo-resist and e-beam resist removal.

2.3.5 Wet etching

In all the other cases where a clean and smooth isotropic etching is required or for selective removal of sacrificial layers in suspended structure fabrication a wet technique is preferred. During the wet etching the sample is immersed in a compound chemical solution capable of eroding one or multiple III/V materials. Etching rate and selectivity can be controlled by temperature and stoichiometric ratio between the chemical reactants. The etching depth is controlled by tuning the time of immersion. A de-ionized water rinse is performed after each wet etching to stop the chemical reaction at the desired point. The main solutions used during the process are HF 1% and HCl 37% concentrated.

2.4 Electro-optical measurement setups

To electrically and optically characterize the devices used in this work two setups have been used. The micro-manipulated probe station has been used only to characterize the electrical and optical properties of SSPDs. The waveguide probe station has been used not only for the electro-optical characterization of the nanobeam SSPDs, but also for the optical characterization of PhCs filter and in general for the study of the interaction between the different components of the integrated chip.

2.4.1 Micro-manipulated probe station

The micro-manipulated probe station (μ-PS) from Janis Research Co. Inc. (ST-500) has been used mainly to pre-characterize all the SSPDs produced for this work. Fig. 2.9 shows a schematic of the setup.
The cryostat has an inlet that hosts two smaller tubes inside. One of them is the vacuum line that provides a system vacuum through a turbo-molecular pump. Before cooling down, the chamber is evacuated overnight down to a pressure level of ~10^{-5}Torr. The other one is for the transfer line required to cool the sample by a continuous flow of liquid helium (L-He). The transfer line has an adjustable flow-control needle in order to regulate the L-He flow. This setup reaches a base temperature of 4.2K, measured at the sample mount. The μ-PS allows mounting the samples up to 1x1cm^2 on a removable sample holder. Therefore, this setup is very convenient to test a whole chip (in a suitable size) in

one cooling down. It is quite critical to keep the whole sample at a temperature as close to as possible to the base temperature read on the sensor. Therefore a high thermally conducting varnish from LakeShore (VGE-7031) and copper clamps are exploited for the sample mounting. The application of the varnish is very critical since the thermalisation to the sample holder is mostly provided through the varnish. Thus, the varnish is evenly distributed on the mounting holder and the sample is gently rotated over a small angular range and pressed on the sample holder in order to avoid any air gap that can play a role as an insulating layer. It has been observed that the two copper clamps are a good aid for a good thermal contact, this is why the lithography mask is designed in such a way that the samples can be mounted without touching the devices. For a good thermal contact, it is important that the holder is completely flat, if there are some scratches, the surface can be improved using polishing papers with very fine grading.

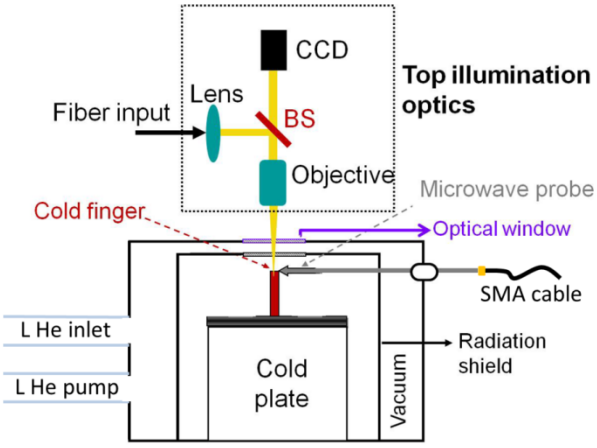

Fig. 2.9 Sketch of the μ-PS

The devices are contacted with a 50Ω, 40 GHz radio frequency (RF) micro probe (μm-probe) from GGD Industries, Inc., which is configured with a ground-signal-ground (GSG) configuration, each with a spacing of 100 μm. The probe is connected to the electrical circuit at room temperature via an SMA cable and can be translated with micro-manipulated independent X, Y, Z translation stages that have a travelling range of a few centimetres. While micro-manipulation with a large range of translation is advantageous, the room-temperature control of the μ-probe introduces some heat-transfer to the setup. Thus, even though it is possible to mount two probes for this system, to minimize the temperature only one is assembled. The cryostat has an optical window (at 300K) and a cold filter (at 25K) for a free-space coupling. The cold filter transmits only the visible and near-infrared range of the spectrum and eliminates the far-infrared portion of the blackbody radiation. The optics is mounted on computer-controlled Thorlabs X, Y, Z translational stages, each controlled with TDC-001 motion controllers. The input light

(λ=1310nm) is coupled into free space and collimated by a lens. The parallel beam encounters an iris (1.5mm diameter) and a beam splitter (45% reflection, 55% transmission) and it is then directed toward a microscope objective (NA=0.03) which focuses the beam onto the sample. The choice of the iris was dictated by the need for a uniform device illumination. The presence of the iris, indeed, reduces the numerical aperture and increases the spot diameter on the sample to ~20μm. Finally, the light reflected back from the sample, reaches the CCD camera placed above the beam splitter which, thus, provides the image of the sample in real time.
The electrical characterization of the nanowires consists of acquiring the current flowing through the device as a function of the voltage across it. Such a measurement is performed by connecting the circuit reported in Fig. 2.10 (a) to the probe and, thus, to the SSPD.

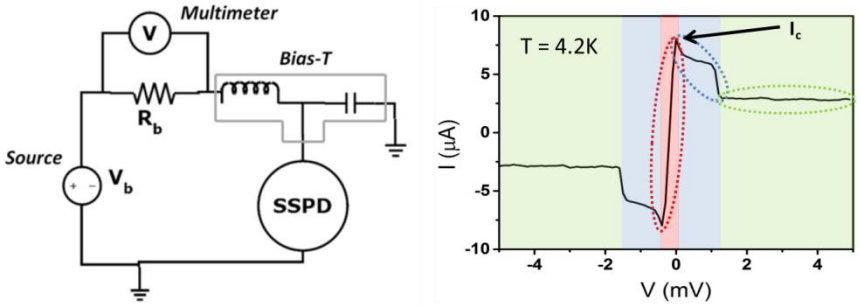

Fig. 2.10 a) Schematic of the circuit connected to the SSPD used for the electrical characterization. b) Typical IV curve of an SSPD. The coloured ovals underline the different regions of the SSPD electrical characteristic.

The voltage source Yokogawa 7651 supplies the bias voltage V_b to the SSPD through a 10Ω resistor (R_b) and the DC port of a bias-T (Mini-Circuits ZBNT-60-1W). When the RF port of the bias-T is not used, it is terminated with a 50Ω-matched cap. During the acquisition, the voltage V_b is swept and, simultaneously, the voltage drop across the resistor R_b is measured by the multimeter Agilent 34970A. The current flowing through the SSPD is then calculated and plotted as a function of V_b. The typical IV curve is reported in Fig. 2.10 (b). The IV curve in the graph reveals three main regions: the superconducting region (red oval), the relaxation-oscillation region (blue oval) and the ohmic region (green oval)[10]. In the first region, the nanowire is in the superconducting state as confirmed by the curve slope. Indeed, for this voltage interval, the slope of the curve, which is inversely proportional to the wire resistance, is ideally infinite. The non-zero resistance is due to the resistance of the external circuit (~ 18Ω). As far as the nanowire SSPD is in the superconducting region, it can detect photons. When the voltage bias is increased up to the point that the critical current Ic is reached, the nanowire leaves the superconducting region. At this point, a section of the wire becomes resistive and the current flowing through the device drops. The detector is in an unstable regime, the oscillation-relaxation region[11], where the normal section oscillates between the

superconducting and normal state, causing an oscillation in the current. Since the current oscillations are faster than the readout circuit, the recorder current appearing in the graph is the average value of the current in the relaxation-oscillation regime. When the voltage bias in increased further, the nanowire is in the ohmic region. In this phase, the ohmic region becomes stable and it starts expanding. As the graph suggests (green oval), the resistive area grows such a way to keep the current nearly constant for increasing bias voltage.

The optical characterization is performed with the addition of several instruments. A chain of four 15dB amplifiers (Mini-Circuits ZX60-6013E-S+) is connected to the RF port of the bias-T. The amplified voltage signal coming from the amplifiers is then directed to the oscilloscope (LeCroy Waveace 234) or to a frequency counter (Agilent 53230a). In order to avoid electrical reflections, a 4dB attenuator (Mini-Circuits 15542) is inserted between the bias-T and the amplifier chain. The SSPD is illuminated via the optical window of the cryostat mainly with two continuous-wave diode lasers. The laser that emits at λ=635nm is used to align the laser beam to the device active area and adjust its focus. The second laser emits at 1300nm and it is employed to perform the device optical characterization. Before reaching the sample surface, the laser light is fed through a digital variable attenuator (OZ Optics DA-100) and a 50:50 fibre-coupled beam splitter. One branch of the beam splitter is fed to the SSPD, while the second one is connected to a power meter (Ophir Nova II) to monitor in real time the light power sent to the device. Once the previous configuration is established, the optical characterization is performed through the acquisition of the photon counts (PC) in presence of laser light and dark counts (DC) in its absence. The acquisition is performed while varying the bias voltage and, for the PC case, at a fixed light power. Thus, while the bias voltage is swept, the counts and the current I_b flowing through the device are recorded. The device quantum efficiency (DQE) is calculated dividing the counts by the number of photons falling within the device active area. The counts are obtained by subtracting the DCR to the PC, while the number of photons reaching the active area per unit time is estimated from the light power and the ratio between the device active area and the beam spot.

2.4.2 Waveguide probe station

The waveguide probe station (w-PS) was designed by Dr. J. P. Sprengers at the TU/e using a commercial cryostat from Janis Research Co. Inc. There are several similarities between the w-PS and the μ-PS whilst some characteristic properties of this setup makes it unique (Fig. 2.11).

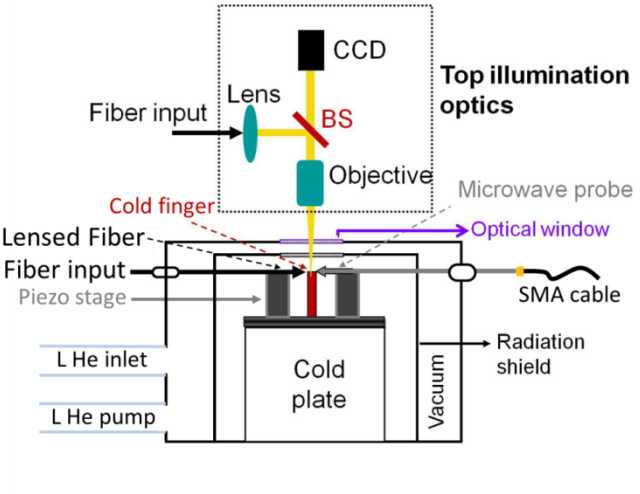

Fig. 2.11 Sketch of the w-PS

The sample mounting procedure is similar to the one used for the μ-PS; however it has to be noted that the sample holder has dimension only of 3x6mm^2, meaning that only a small piece of a full chip can be mounted in one cooling run. Moreover there is no space to insert copper clamps reducing in this way the thermal contact capability and making the mounting procedure even more critical. However the approach taken in this particular cryogenic setup is that both electrical connections and optical coupling to the waveguide photon detectors are manipulated in-situ and so since there are less interfaces to room temperature (less thermal load), it is possible to reach to a base temperature of 2.3K. In this way also for this setup a temperature on the sample lower than 4K is guaranteed. Probably the main distinctive difference between the w-PS and the μ-PS setup is the possibility of having lateral optical access to the sample thanks to fibres mounted on piezo stages.

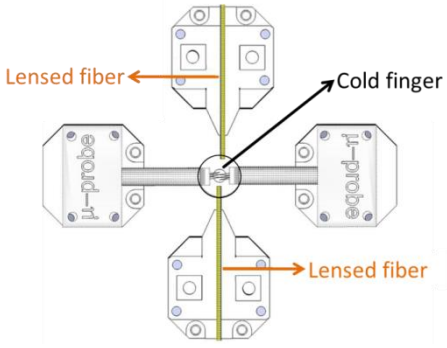

Fig. 2.12 Sketch of the inside of the cryostat, showing the configuration of probes and fibres used for this work

There are four independent nano-manipulated X, Y, Z piezo stages (ANP(x&z)101/ LT type) from Attocube systems with a maximum travelling range of 5 mm. They are mounted on the cold plate and anchored to its temperature. Their manipulation is done by two base positioning controllers (ANC300, attocube systems). The configuration is flexible to change according to the design of the chip but at maximum four different movable parts can be hosted in the cryostat. Usually a configuration with two μ-probes (customized Janis Research Co. Inc. (ST-500)) and two fibres (Oz Optics, spot size of 2.5 ± 0.5 μm) facing each other is mainly used during this work (Fig. 2.12).

The electrical connections of the piezos inside the cryostat are provided by Attocube and the probes are wired by the user by using low resistance and low thermal conducting LakeShore miniature coaxial cables (type-C). Finally, all the room-temperature and interface cabling is provided by Janis. The room-temperature cables are anchored first to the radiation shield and then to the cold plate with bobbins in order to decrease the thermal load to the setup. The optics in the top part of this setup is very similar to the one employed on the μ-PS system, however an extra arm that collects the emitted light from the top and sends it to the spectrometer (Horiba Jobin Yvon FHR 1000) through fibre coupling is added.

The cooling is controlled with the adjustable cryogenic flow control needle valve integrated on the transfer line. After the temperature on the radiation shield reaches below 20K, the flow is decreased in few steps in order to further reduce the temperature on the cold finger below 2.3K. The temperatures both at cold finger and the radiation shield are measured by Si-diodes through a temperature controller, LakeShore 331. After the base temperature is reached the μ-probes are put in contact with the metal pads of the device, in order to make them thermalize at the sample temperature, before starting the measurement.

This setup has not been used for a systematic electrical characterization of the SSPDs. The small dimension of the sample holder, the limitation at few millimetres in the movement of the piezo and the relative short length of the μ-probes arm, allow one to reach only between 2 and 4 devices for each cooling run. In those conditions the pre-characterization phase on the μ-PS is fundamental to select and mount on the w-PS only the devices that have shown good IV curve. An external electrical circuit, like the one used for the μ-PS system, is employed to check that the devices reached the base temperature and are superconductive.

One of the main characteristics of this setup is the flexibility of configurations in which is possible to do optical characterization. Several of them have been employed for the characterization of SSPDs and PhCs filters. In particular the optical characterization of the SSPDs has been performed sending the laser light through a polarization-maintaining lensed fibre into the waveguides, and collecting the detector output at the counter (Agilent 53230a).

In this setup the signal coming out directly from the μ-probes is sent to a control box (SCONTEL Superconducting Nanotechnology) containing all the electrical components,

current source included, and the amplification system. The control box has two inputs such that two probes can be used simultaneously and two outputs to send the amplified signal either to the counter or other instruments, like for example a correlation card (PicoHarp 300). The main reason why this control box has been employed, instead of the amplifier chain used on the μ-PS, it is related to the electrical noise and grounding issues that are present on the w-PS system. During the mounting of the sample special precaution has to be taken in order to reduce the electrical noise produced from the piezo cables and other cables present inside the cryostat.

The QDs and the PhC filters are characterized through the use of a non-resonant pump laser (780 nm) that is focused by a microscope objective (NA 0.4) onto the sample to excite the QDs. The photoluminescence (PL) signal is collected either from the top with the same objective or from the end facet of the RWG through the lensed fibre. The signal is then sent through fibre to the spectrometer (Horiba Jobin Yvon FHR 1000). Optical transmission measurements have also been performed on this setup positioning the two lensed fibres face to face.

The procedure to align the fibre to the waveguide facet is carried out in two steps. A coarse alignment is done by coupling a laser with high power (980 nm diode laser) which is visible to the CCD camera and approaching the facet as well as possible with an alignment by eye. A fine alignment is done by pumping with the 980 nm diode laser from the top at the highest power, close to the edge of the ridge waveguide, and then trying to maximize the PL counts at fixed wavelength, collected through the lensed fibre.

References

[1] https://www.researchgate.net/figure/Figure-A1-Cross-sectional-technical drawing-of-the-MBE-growth-chamber-used-for-this_fig13_318359673

[2] https://www.k-space.com/products/bandit

[3] B. Alloing, C. Zinoni, V. Zwiller, L.H. Li, C. Monat, M. Gobet, G. Buchs, A. Fiore, E. Pelucchi, and E. Kapon. "Growth and characterization of single quantum dots emitting at 1300 nm" *Applied Physics Letters*, **86** pp.101908, 2005.

[4] R. Gaudio, K.P.M. op`t Hoog, Z. Zhou, D.Sahin and A. Fiore, "Inhomogeneous critical current in nanowire superconducting single-photon detectors", *Applied Physics Letters*, **105** pp. 222602, 2014.

[5] https://www.ntmdt-tips.com/products/view/nsg10

[6] https://gwyddion.net/

[7] G.N. Gol'tsman, O. Okunev, G. Chulkova, A. Lipatov, A. Semenov, K. Smirnov, B. Voronov, A. Dzardanov, C. Williams, R. Sobolewski. " Picosecond superconducting single-photon optical detector" *Applied Physics Letters*, **79** pp. 705–707, 2001.

[8] https://www.jawoollam.com/

[9] F. Marsili. "Single-photon and photon-number-resolving detectors based on superconducting nanowires - Chapter 2" PhD thesis, École Polytechnique Fédérale de Lausanne, 2009.

[10] F. Mattioli, R. Leoni, A. Gaggero, M.G. Castellano, P. Carelli, F. Marsili, A. Fiore. "Electrical characterization of superconducting single-photon detectors" *Journal of Applied Physics*, **101** pp. 054302, 2007.

[11] A.J. Kerman, J.K.W. Yang, R.J. Molnar, E.A. Dauler, K.K. Berggren, "Electrothermal feedback in superconducting nanowire single-photon detectors," *Physics Review B*, **79** pp. 100509, 2009.

Chapter 3

Superconducting single-photon detectors: film growth and fabrication

3.1 Introduction

The SSPDs used for this work are made of nanowires patterned on top of NbN film. The NbN films are grown by the reactive DC-magnetron sputtering (Chap. 2.2) in the NanoLab@TU/e cleanroom facility. The films have been sputtered on top of different substrates: single-sides polished GaAs (100) and different designs of GaAs/AlGaAs heterostructures grown by MBE (Chap.2.1) in the NanoLab@TU/e by Ing. F.W.M. van Otten. In order to keep the thickness uniformity of the NbN films during the sputtering, the specimens are cleaved into 1x1 cm^2 or up to 2.0x2.0 cm^2 pieces from the 2-inch wafer, after that cleaned in an ultrasonic bath first of acetone and then isopropanol, and finally dried. Special attention has been put on keeping track of the crystallographic orientation of the cleaved pieces for the wafers, as the RWGs have to be aligned to the [011] plane in order to create a trapezoidal support (Chap.4.2.6).
Traditionally, SSPDs were fabricated on sapphire (Al_2O_3)[1] or magnesium oxide (MgO)[2], lately mainly on silicon (Si)[3]. In this work, GaAs has been selected as substrate material due to its high suitability for integration with single photon sources and passive circuit elements (Chap.1.2.3). The technology of SSPD on GaAs has been previously studied[4] and is not very straightforward. The deposition of NbN films on other substrates is mostly performed at high growth temperatures (> 400°C). On the other hand, GaAs is known to start evaporating above 350°C[5], severely restricting the range of optimum growth conditions. The implementation of the NbN film technology in the NanoLab@TU/e cleanroom was started by Dr. D. Sahin. The sputtering conditions found during that research project[6] have been mainly used for this work. However the optimization of such growth parameters has been performed along this project, in order to always guarantee the best quality film, whatever the condition of the DC-magnetron sputtering would be in that specific moment.

In the first part of this chapter the growth conditions are discussed with a particular focus on the temperature and pressure. The consequences of different film properties on the SSPDs characteristics are discussed in the second part of this chapter. In the last part some

important parameters for the design the SSPD are examined and the best solutions selected in order to define the "standard" SSPD used in all the integrated detectors and circuits of the present work.

3.2 NbN film growth and characterization

As already discussed on Chap.2.2.2, the growth variables are numerous and every different combination could strongly affect the quality of the film. In the following are presented the optimum condition parameters found in ref.[6] and used also for the present one.

- NbN target angle: 11° with respect to the normal to the chimney
- Distance target - substrate: 6 cm
- Holder rotation: 50 rpm
- Target current supply: 250 mA
- Gas flux: Φ_{N2} = 1.4sccm, Φ_{Ar}= 12sccm
- Deposition rate: 0.5 Å/s

Two very significant parameters that define the microstructure of the film are the deposition pressure and temperature. According to the Thornton model[7] (Fig.3.1), it is possible to define four growth regimes (structure zone) as a function only of these two parameters. The first zone is formed by small and elongated grains that form a columnar structure with porous morphology. This kind of structure is produced by low diffusion and mobility of the adatoms, mainly due to the low temperature. The second zone shows the beginning of formation of crystalline grains and higher binding among the columns. In this case the temperature is higher, so the adatoms mobility. The third zone is characterized by high diffusion into the grains which results in a nice crystalline structure. A fourth transition zone (T zone) has to be added between the first and second. The T zone is constituted by grains with very low porosity, so the surface is denser and smoother.
According to this model, in order to obtain a crystalline structure, i.e. to fall in the third zone regime, the substrate temperature has to be as close as possible to the melting point of the Nb target (T = 2477°C). On the other hand, GaAs starts to evaporate above 350°C, so only the first zone and T zone are the ones that can be taken into account considering this specific substrate.

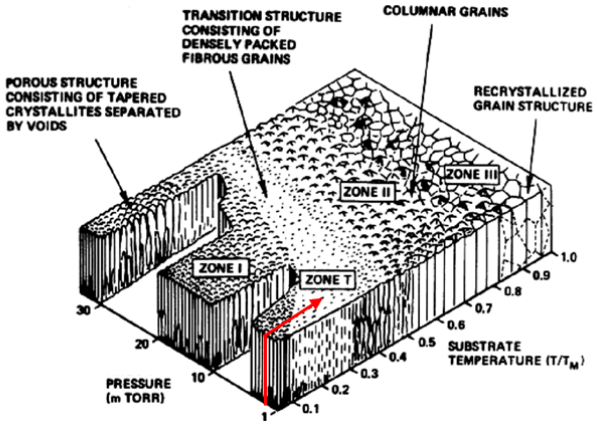

Fig. 3.1 Schematic rapresentaion of the Thornton model. The red arrow indicates the region of interest for sputtering on GaAs.

However the low pressure and low growth rate support the highly energetic particle bombardment. Indeed, the atoms are highly energetic when they are ejected from the target and with a very little collision rate, due to the low pressure, they can reach to the substrate by retaining most of their kinetic energy. Therefore, it has been proved[8] that it is possible to grow high quality NbN film even at relatively low temperatures, like the ones used for this work. Indeed, the high resolution TEM image of Fig. 3.2 clearly shows how the NbN film, growth under the above mentioned conditions, presents a poly-crystalline structure, rather than a porous structure (Zone 1) as expected for the used conditions of temperature and pressure.

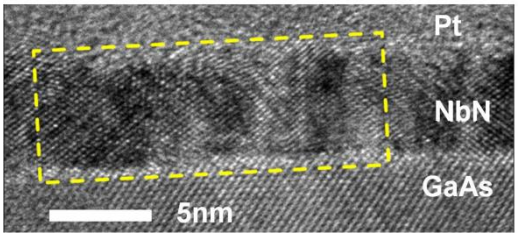

Fig. 3.2 HR-XTEM image of a NbN film deposited on GaAs at 410°C and 2 m Torr[6]

In the following are presented the characteristics of several films as a function of the above mentioned parameters. In particular every film has been characterized in term of thickness, roughness of the surface and critical temperature with the techniques described in Chap. 2.2.3.

3.2.1 Deposition temperature

It is possible to control this parameter either by changing the nominal set temperature (T_{set}) or by changing the heating time (t_{heat}). Indeed the deposition process starts with raising the temperature to T_{set}. Once the desired value of T_{set} is reached (this changes according to the condition of the infrared lamps) the holder is left inside the chamber to thermalize for a time t_{heat}, that can be controlled by the user. Only after this time the flow Φ of N_2 and Ar is let into the chamber and the Nb chimney supplied with a fixed current to ignite the plasma. The real deposition temperature strongly depends not only on T_{set} but also on t_{heat} and indirectly on the thickness of the holder (thicker holder require a longer t_{heat} to properly thermalize) and the amount of In used to glue the samples.
Firstly the impact of T_{set} on the film characteristics has been studied, fixing t_{heat} = 12min and the chamber pressure at 2 mTorr. Considering a starting value of 400°C [6], films have been grown within the range 370°C - 420°C with 10°C step. Once the thickness and roughness of the film have been found to match the required specifications (5nm thick, ρ_{rms} < 0.5 nm), R(T) measurements were performed. The calculated T_c as a function of T_{set} is shown in the following graph (Fig.3.3).

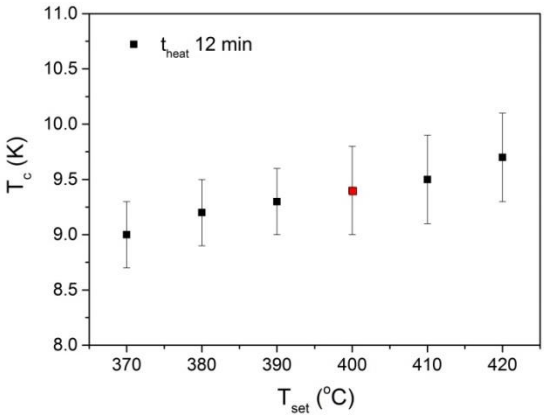

Fig. 3.3 Critical temperature as function of the set deposition temperature, at fixed heating time t_{heat} = 12min. The experimental point in red is the same as the one of the next figure.

From the graph a linear dependence of T_c with T_{set} is observed. The T_c increase with the deposition temperature up to T_c = 9.7K, however the increase of T_c is less than 1K within the 50°C considered temperatures range.
In previous work[6] this behaviour has been observed, over a smaller range of temperatures, but with a larger impact of T_{set} on T_c (1.1K increases over 30°C range). However a study on the dependence of T_c on the heating time t_{heat} was not been performed in that case.

In this work, it has been found that t_{heat} plays a much more significant role on the impact on the T_c compared to T_{set}. Fixing the chamber pressure at 2 mTorr and T_{set} = 400°C, films with different t_{heat} are grown and their T_c compared in Fig. 3.4.

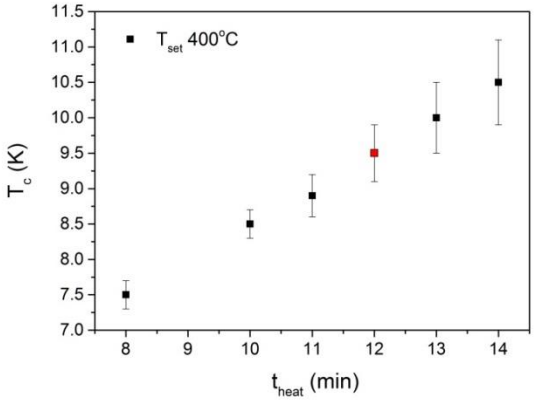

Fig. 3.4 Critical temperature as function of the heating time, at fixed set deposition temperature T_{set} = 400°C. The experimental point in red is the same as the one of the previous figure.

Also in this case a linear growth of T_c with t_{heat} is observed. However, it is clear how the T_c variation is much stronger in this case within the explored range of values. Indeed 3K have been gained on T_c within the explored range of 6 min (from 8min to 14min). For $t_{heat} \geq$ 14min, the quality of the film starts to degrade as indicated by the AFM images of Fig. 3.5. Therefore the range above 14min has not been explored.

The reason behind the strong influence of t_{heat} on T_{dep} is most probably due to the infrared lamps, together with other factors like the thickness of the holder. As said (Chap. 2.2.1), T_{set} is established by a thermocouple located between the two infrared lamps at the back side of the sample holder. The heating power that reaches the thermocouple is indeed stronger than the one that propagates through the INCONEL holder to reach the samples. The INCONEL material has a low thermal conductivity (15 W/m °K) that guarantees high uniformity of temperature in all the volume, but require long thermalization time. Therefore a longer t_{heat} can strongly affect more the real temperature at the surface of the samples.

The effect of higher T_{dep} does not only influence the T_c, but also the ΔT_c. As it can be noticed in the previous graphs, ΔT_c (error bar) increases as well with T_{dep}. In particular for high values of T_c (> 9.8K), $\Delta T_c \sim 0.6$K instead of the usually obtained $\Delta T_c \sim 0.3$K for lower T_c. A large value of the superconducting transition width indicates a degrading of the quality of the film, as it will be shown from a more detailed analysis of the film roughness.

So far, the roughness of the film as a function of the deposition temperature has not been particularly taken into account, due to the fact that the measured ρ_{rms} was always within

specification. However it is necessary to point out few aspects regarding the morphology of the samples surface in function of T_{dep}. In the following two AFM images (Fig 3.5) are shown, the left one of a film with T_c = 9.5K and ΔT_c = 0.3K and the right one with T_c = 10.5K and ΔT_c = 0.6K, the difference in growth has respectively been t_{heat} = 12min and t_{heat} = 14min.

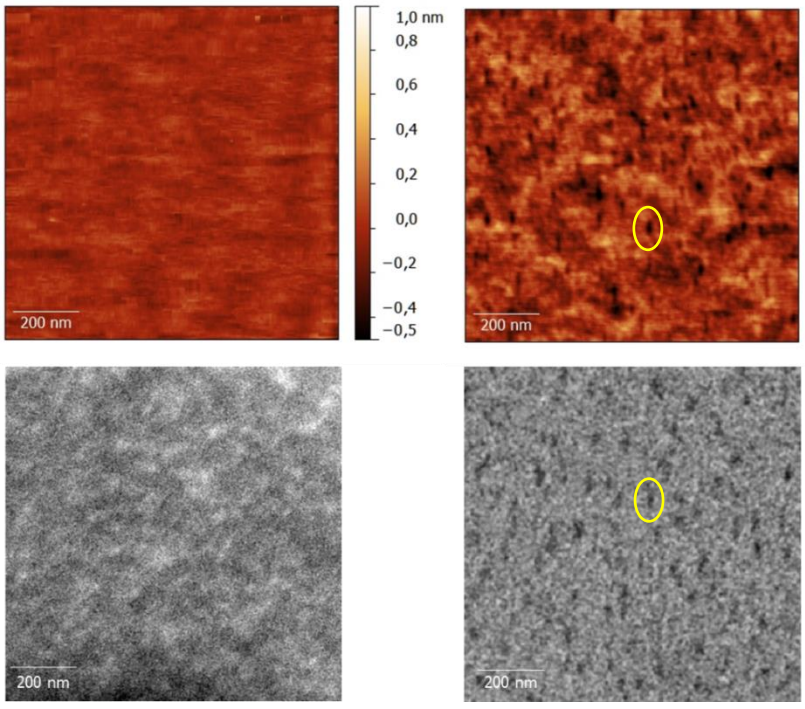

Fig. 3.5 AFM and SEM images of films growth with t_{heat} = 12min on the left and t_{heat} = 14min on the right. The yellow circles underline the craters on the film surface due to As evaporation.

The measured ρ_{rms} is well below 0.5nm for both films, specifically for the left ρ_{rms} = 0.15±0.05nm and for the right ρ_{rms} = 0.28±0.08nm. However darker spots of dimension < 100_nm are easily visible (yellow circle) both in the AFM and SEM images of the higher T_c sample. On the contrary the other sample does not show any particular surface feature. Similar behaviour has been verified for a majority of samples in which the T_c exceeds a certain threshold (~9.8°K). Those dark spot have been identified like craters due to desorption of As from the GaAs substrate. This phenomenon has been observed above a critical temperature of 350°C in ref.[5]. However in this work it has not been easy to establish a threshold temperature, due to the stronger dependence on t_{heat} rather than on T_{set}. Indeed above a certain T_{dep} (dependent both on t_{heat} and T_{set}) all the films present the following three properties: T_c > 9.8°K, ΔT_c > 0.5°K and craters. The consequence of such properties on the SSPD electro-optic characteristics will be shown in par 3.3.

3.2.2 Deposition pressure

The total pressure inside the deposition chamber is the other significant parameter that can influences the microstructure of the film according to the Thornton model[7]. As already mentioned, the limitation on the deposition temperature for this specific substrate requires very low pressures in order to obtain high quality films. While in the past the optimum pressure value found for this particular sputtering machine was 2 mTorr[6], during this work and considering the deteriorated condition of the sputtering machine, it has been necessary to experiment different solutions in order to obtain low enough pressure to grow good quality films.

Firstly, films have been growth using different pressure within a range of 2 mTorr < P_{dep} < 5 mTorr, keeping constant T_{set} = 400°C and t_{heat} = 12min. In the following the R(T) curves for all the examined pressure values are shown and in the inset the behaviour of T_c as a function of P_{dep}.

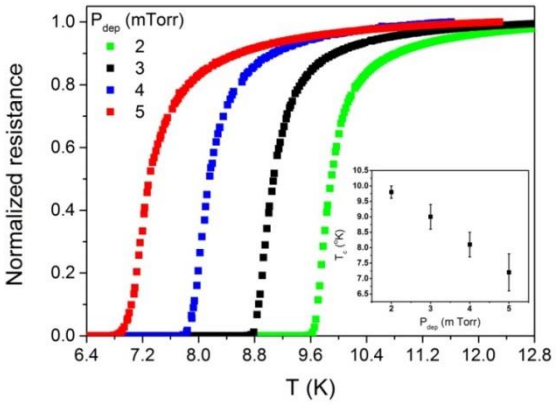

Fig. 3.6 R(T) measurments of NbN films for different deposition pressures. Inset: T_c values in function of P_{dep}.

As expected T_c increases and ΔT_c (error bar of T_c) decreases as P_{dep} decreases. Considering the very strict limitation on the deposition temperature, only P_{dep} = 2 mTorr can ensure an acceptable value of T_c. However the stability of the sputtering process for this specific value of pressure was not good enough to guarantee the reproducibility of the growth for several runs. This was mainly due to the unstable behaviour of the gate valve that is used to maintain a constant pressure inside the sputtering chamber. At P_{dep} = 2 mTorr the valve was not always able to keep the pressure stable and therefore a stable plasma, considering a flux of Ar Φ_{Ar}= 12sccm.

Usually the simplest way in order to maintain a plasma stable is to inject a flux of Ar. The amount of Ar flow used for optimum growth has been Φ_{Ar}= 12sccm, therefore the effect of small increases in Φ_{Ar} have been studied. Fig. 3.7 shows the R(T) curves and AFM

pictures for films grown with T_{set} = 400°C, t_{heat} = 12min, P_{dep} = 2 mTorr and using Φ_{Ar}= 12sccm (Fig. 3.7 b), Φ_{Ar}= 12.5sccm (Fig. 3.7 c) and Φ_{Ar}= 13sccm (Fig. 3.7 d).

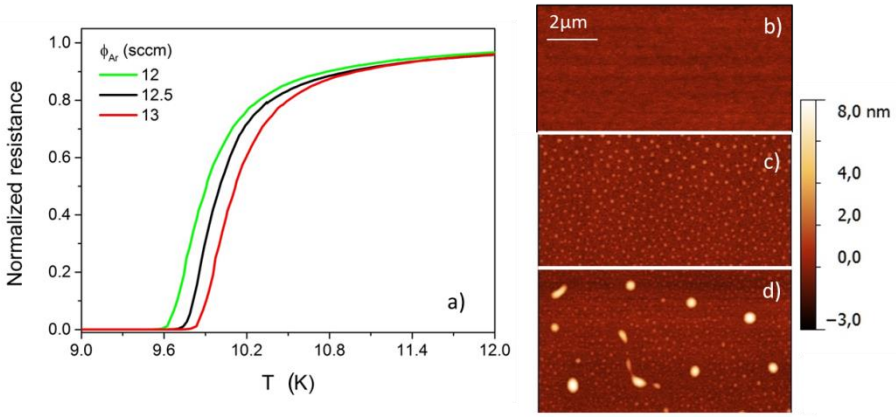

Fig. 3.7 a) R(T) measurments of NbN films for different Ar flux. AFM images for: b) Φ_{Ar} = 12sccm, c) Φ_{Ar} = 12.5sccm, d) Φ_{Ar} = 13sccm.

The R(T) curves do not present any particular feature with T_c= 9.8K and ΔT_c = 0.3K for the film grown at Φ_{Ar} = 12sccm (same curve as the green one in Fig, 3.6), T_c= 9.9K and ΔT_c = 0.4K for the film grown at Φ_{Ar} = 12.5sccm, T_c= 10K and ΔT_c = 0.4K for the one grown at Φ_{Ar} = 13sccm. Those obtained values are promising for a good film quality, however the AFM analysis reveal unexpected features on the film surface.

Structures similar to bubbles of a dimension ~150nm and with a very uniform density of ~500/μm^2 can be easily visualized in Fig. 3.7 (c). The other sample (Fig 3.7 d) shows similar structures as the previous one on the background, plus bigger bubbles (~500nm) but with not uniform distribution and much lower density ~1.2/μm^2.

The formation of bubbles on the surface of sputtered NbGe has been observed in the past[9] and is caused by Ar incorporation on the surface above a certain threshold of Φ_{Ar} injected on the system. Even if the considered material is different, a mechanism very similar to the one described for NbGe must be the reason for the behaviour observed in the AFM pictures. Moreover, this explanation could easily clarify why the sample growth with Φ_{Ar} = 13 sccm presents also bigger bubbles compared to the one with Φ_{Ar} = 12.5 sccm. Therefore increasing the Φ_{Ar} is not a feasible solution in order to keep the plasma stable.

Finally a different approach has been found and adopted to keep the pressure and therefore the plasma stable at P_{dep} = 2 mTorr. During the sputtering deposition process, after the time t_{heat} has passed, the flow Φ of N_2 and Ar is let into the chamber, but the Nb chimney is not supplied with current until the set pressure P_{dep} is reached. In order to maintain the valve stable, it is necessary to introduce intermediate steps in which, keeping the flow fixed, the pressure is gradually reduced until it reaches P_{dep}. Initially two intermediate steps were used to arrive at P_{dep}. The pressure was reduced from 5 mTorr to 3

mTorr and finally from 3 mTorr to 2 mTorr. Surprisingly adding two extra intermediate steps, 4 mTorr and 2.5 mTorr, was enough to ensure the valve stability at P_{dep} = 2 mTorr and so the reproducibility of the process also for low-pressure conditions.

3.3 Effect of film properties on the SSPD characteristics

As already discussed on the previous paragraph several films with different characteristics have been fabricated. Samples with important surface imperfections or ρ_{rms} > 0.5nm have been excluded from the fabrication process to avoid clear problems of constrictions[11] of the nanowires. Now considering two samples with the same thickness and very similar roughness but with very different T_c, normally the film with higher T_c would be the best choice to fabricate on. Indeed it is usually assumed that films with higher T_c would also provide higher current density (J_c)[12] and consequently higher efficiency[13]. However as it is shown following this assumption is not always correct.
In this section three films (NbN29, NbN41, NbN60) are examined. In the following table the main film parameters of those samples are shown for comparison:

Film	T_{set}(°C)	t_{heat} (min.)	Thickness (nm)	ρ_{rms} (nm)	T_c (K)
NbN29	420	12	5.11	0.28	9.3
NbN41	410	12	5.09	0.30	9.4
NbN60	400	14	5.10	0.33	10.2

Tab. 3.1 Main growth parameters and characteristics of three NbN films on which SSPDs have been fabricated

The three films are very similar in all the parameters except for the large difference in terms of T_c that distinguishes NbN60 from the others. Nanowires of 100nm width and 260nm pitch were fabricated on those films (Fig. 3.10) and electro-optically characterized. The electrical characterization is performed as explained in Chap. 2.4.1 over a set of 20 nominally identical devices for all the considered films. The optical characterization at λ=1300nm, described in Chap.2.4.1, has been performed over the devices with the highest values of I_C for the three films. From the optical characterization, the device quantum efficiency is calculated following Eq. 1.5 and Eq. 1.6 of Chap. 1.4.2. In this case, considering top coupling excitation, Eq. 1.5

$$N_{\Phi} = \frac{P\lambda}{hc}\eta_c \frac{A_d}{A_l}$$

has been multiplied by the ratio A_d/A_l , in order to take into account only the active area to photon absorption. The detectors area A_d has been estimated as the wire width plus the

pitch, multiplied by the wire length and the laser spot area A_l has been measured to be 314μm.
The coupling efficiency of the light to the device η_c considers the correction for the power loss between the laser source and detectors. For the optics currently mounted on the setup, the coupling efficiency has been calculated as 0.1%.
In the following the IV characteristics and DQE of the films of Tab. 3.1 are shown, together with a summary table for direct comparison:

Film	I_c (μA)	DQE (%)	T_c (K)
NbN29	8.2	~1	9.3
NbN41	5.9	~1	9.4
NbN60	6.0	~0.1	10.2

Tab. 3.2 Summary of avarage I_c and maximum of DQE of the nanowires fabricated on the films of Tab.3.1

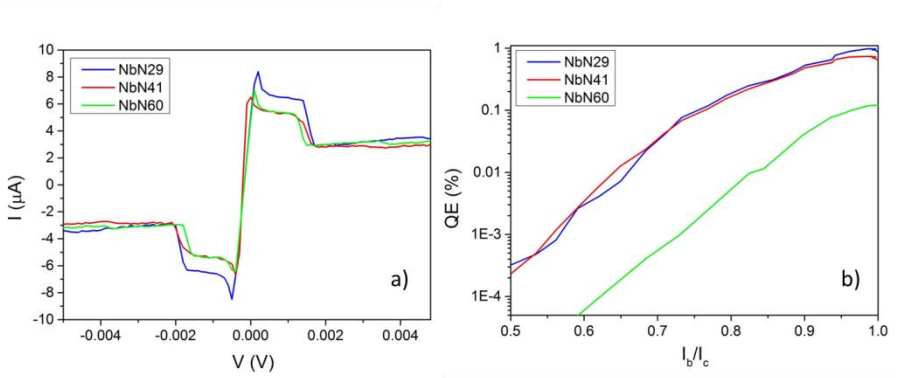

Fig. 3.9 a) IV characteristics and b) DQE curves of nanowires fabricated on different NbN films

The immediate results that come to the eye are the low value of DQE for the NbN60, that has the highest T_c. The two films (NbN29, NbN41) with lower T_c, despite the quite different values of I_c, show an optical response of the detectors that is the one expected considering the kind of device. The theoretical maximum for the DQE of NbN on GaAs when the detector is not integrated with a waveguide and other kind of optical cavities is only 10%[14].
Eventually it will be shown in Chap.5.3.1 that this value of 1%, measured at 4K, corresponds to 28% for a similar detector integrated on waveguide and measured at 2K.
However the value of DQE = 0.1%, for a film with high T_c and for devices with I_c comparable to the one of NbN41, it is very surprising. Further investigation on this film showed the presence of craters (<100nm) on the surface (Fig.3.10 b). The presence of holes is correlated to the higher value of T_c as already has been observed and explained in

the previous paragraph (par. 3.2.1). It also has to be noticed that the distribution on the average value of I_c is two times bigger than for the devices from other films, further implying the effect of constrictions[11] on the I_c.
Films with higher T_c are an advantage under a theoretical point of view[12,13] but also practical one, since the limitations related to a good thermalization of the samples inside the cryostat are a bit less restraining in the case of higher T_c. However as it has been shown in this chapter, it is crucial to work in a range of T_{dep} that is very far away from the threshold temperature of As evaporation. For this reason, as it is not always easy to clearly visualize the craters in the AFM pictures, it has been chosen to work only with films in which the measured T_c is below 10K, specifically in a range of 9.3-9.7K.

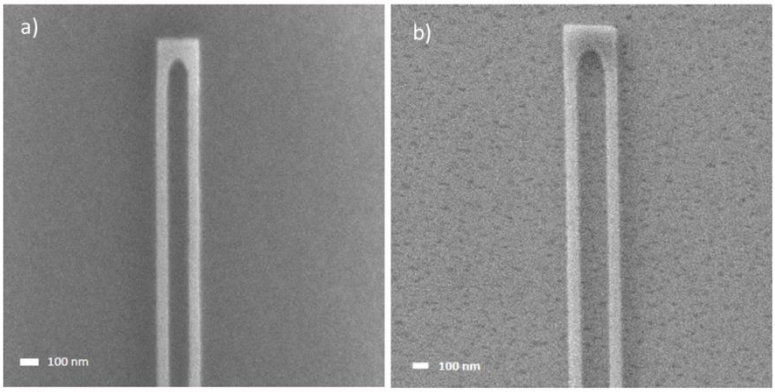

Fig. 3.10 SEM pictures of nanowires fabricated on top of NbN41 a) and NbN60 b)

3.4 SSPD design optimization

The requirement of placing the SSPD on top of a suspended nanobeam (SNB) calls for a compact design that diverges from the standard meander shape SSPD. This compact design is basically a single U-turn (Fig. 3.10) of a meander SSPD, connected to larger wires (300nm) that link the U-turn to the metal contact pads, used to bias the detectors. Placing the wires on top of a SNB guarantees higher absorptance of the photons requiring a shorter length in order to achieve the same efficiency. So for this work a length of the wire of 20µm has been chosen, as will be explained in Chap.5.2. All the other variables of the design of the SSPD (pitch, width, shape of the bending point, length and width of the contact wires) are going to be discussed in the following.

3.4.1 Pitch

The idea to see how the pitch influences the behaviour of the nanowires arose mainly because the first fabricated SSPDs didn't show any photon response, but had values of Ic that were way above (> 25µA) what could be expected for nanowires with such design (100nm width, 20µm long, 260nm pitch). The high values of Ic led to the belief that the etching in the middle of the U-shape of the wire might not have entirely work, creating a bridge between the two sides of the wire. A nanowire with a width bigger than 300nm, instead of the designed 100nm, could explain both the high I_c and the absence of responsivity to the excitation light (λ=1300nm). In order to verify this hypothesis, devices with larger pitch (290,320,350,380,420nm) were fabricated and electro-optically characterized. In the following the IV and DQE curves of one representative device (the one with higher I_c) for each pitch are shown.

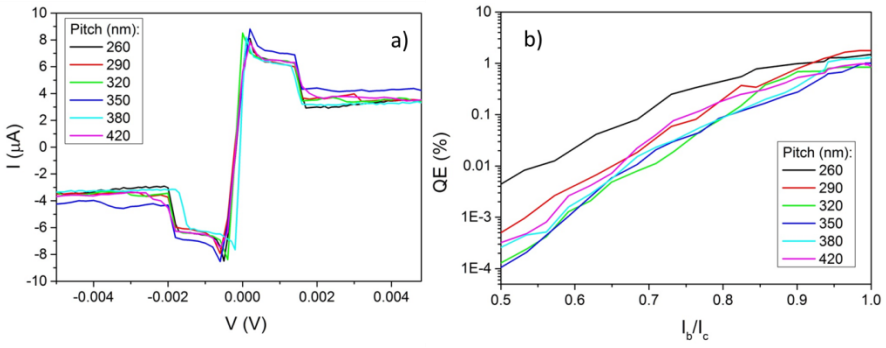

Fig. 3.11 a) IV characteristicts and b) DQE curves of nanowires fabricated with different pitches.

Pitch (nm)	260	290	320	350	380	420
I_c (µA)	8.1	8	8.3	8.6	7.6	8
DQE (%)	1.3	1.4	0.9	0.9	1.2	1

Tab. 3.3 Summary of avarage I_c and maximum of DQE of nanowires with different pitch

As expected the electrical properties of the SSPDs do not change if the pitch is being varied as this does not affect the cross section of the wire (Fig.3.11 a). A more detailed comparison between the I_c for different pitch is shown on Tab. 3.3, together with the maximum DQE values.

Clearly the hypothesis was verified, since for every considered pitch the value of I_c was within the expected range and also the photon responsivity was present. The devices with pitch of 260nm were also perfectly working. Actually, as shown in Fig.3.12 the supposed

bridge between the two parts of the wire was not covering the full space among them, but only the conjunction point with the contact wires. The contact wires were touching each other creating a short circuit, so the current was bypassing the nanowire altogether making them unresponsive to photons. This problem was easily solved by moving the contact wires further apart, without compromising any other sensitive part for the integrated SSPD design.

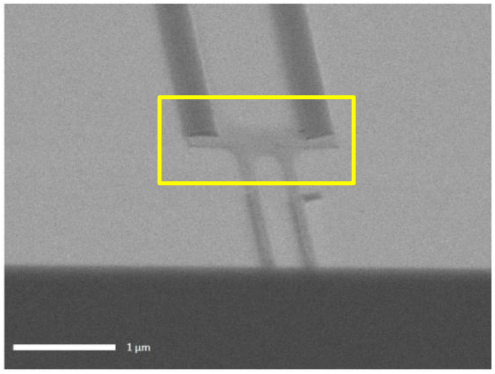

Fig. 3.12 SEM picture of the conjuction point between nanowire and contact wires, in which the NbN bridge, usually hidden underneath the HSQ mask, is exposed and visible (yellow rectangle).

As expected there is no sign of a significative difference between the different pitches[15]. The DQE curve of the device with 260 nm pitch (Fig. 3.11 right) reflects this behaviour as well, and actually shows the highest DQE at lower bias current. Since the low bias current is the best region to work with, due to very few dark counts, and also considering the convenience of positioning one or two SSPDs with a small pitch on top of a narrow nanobeam (1µm), the pitch for the final design has been set at 260nm.

3.4.2 Width

As mentioned previously (Chap1.4.2), the DQE can theoretically be enhanced by using narrower wires as this decreases the size of the section that has to be made resistive. To pursue the goal of high efficiency SSPDs on GaAs, nanowires with widths of 80 nm together with the standard width of 100 nm have been fabricated and electro-optically characterized.

Changing the width of the wires and therefore its cross section obviously has consequences on the electrical properties. More specifically, the value I_c is expected to decrease linearly with decreasing width, but, as can be seen in Fig.3.13 (a), the ratio of I_c between the two different designs is around 0.6, three times more than expected. Moreover the distribution around the average of I_c is much wider for the 80nm wires than

for the 100nm ones (Fig. 3.13 b, c). Both these facts lead to the conclusion that the nominally 80 nm width wires are narrower (~75nm) and much more affected than larger wires by variation in width due to fabrication imperfections or by inhomogeneities of the NbN film.

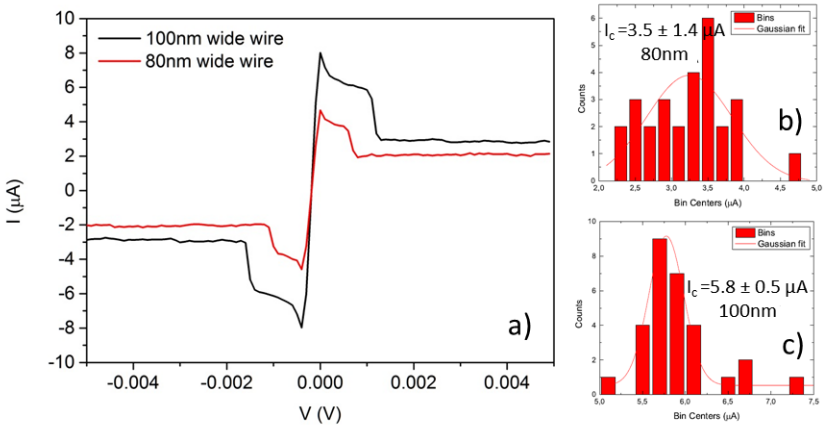

Fig. 3.13 a) IV characteristics for a 100nm and an 80nm wide wires. b) and c) I_c distribution of devices with width 80nm (b) and 100nm (c).

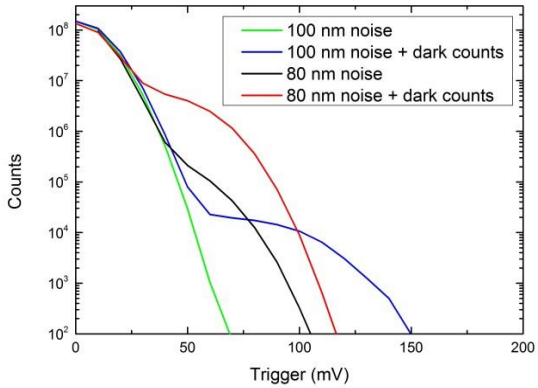

Fig. 3.14 Dependence of the counts on the trigger level for 100nm and 80nm wide devices and for the two configuration unbiased (noise) and biased (noise+dark counts).

Before every optical measurement it is important to set a trigger level on the counter that cuts out the electrical noise permitting only to dark and photon counts to be registered. The value of this trigger is easily found for SSPDs in which the I_c has a reasonably high value. However if the I_c is very low, like in the case of the 80nm wires, finding an adequate value for the trigger can be tricky. In Fig.14 the number of registered counts as a function of the trigger level is shown for an 80 nm and a 100 nm wire. These

measurements have been done for both unbiased detectors (noise), and biased detectors (noise + dark counts), in which the dark counts are measured together with the electrical noise. The 100 nm wire shows a clear difference between unbiased (green curve) and biased behaviour (blue curve) and for this wire the trigger level could be easily set between 70 and 100 mV, such that the electrical noise is completely cut out and the counts are all above trigger level. The 80 nm wire shows a less clear difference (black and red curves) and it is not immediately clear which trigger level will perform optimally. The plateau of the electrical noise plus dark counts line lays around 60 mV, but at this trigger value a lot of noise will also be registered. This leads to the conclusion that, due to the low value of I_c, finding an adequate trigger level for the 80nm wires is problematic, causing uncertainty on the reliability of the optical characterization of those wires.

Even in this condition in which it is difficult to find a proper trigger level, optical measurements of 80nm wide wires have been performed. In the following are shown the DQE curves for the 80nm and 100nm wide wires (Fig. 3.15). Unsurprisingly as theoretically expected, the 80nm detectors show higher DQE = 2.5% against the 1% that we already saw previously (par. 3.3) for the 100nm wires. Moreover for low bias current the DQE curve of the 80nm is way higher compared to the one of 100nm, and shows almost a saturation behaviour that has rarely been seen on standard NbN detectors on GaAs. However, even if the higher DQE would suggest to choose the 80nm design for the integrated SSPDs, lastly the standard 100nm one has been chosen. Indeed the very low average value of I_c together with a very broad distribution around it, meaning that a high percentage of the analysed devices could have I_c below 1µA, make the 80nm wide wires not suitable in term of scalability and integration. As it will be shown on the next chapter (Chap.4.2.2), the fabrication steps, that allow the integration of the SSPDs on quantum photonic circuits, damage the wires reducing step by step the initial value of I_c. So compromising on the efficiency in favour of a higher I_c was considered a safe choice.

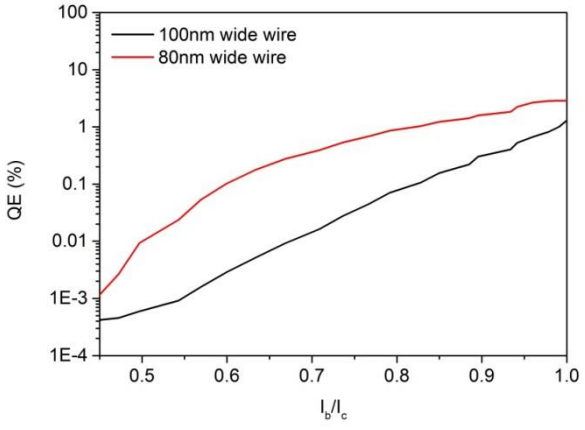

Fig. 3.15 DQE for an 80nm and a 100nm wide wires

3.4.3 Bending points

The geometry of the bending points has been designed following ref.[16], in order to avoid the problem of current crowding. When an electrical current travels through a 180° turn or around a sharp corner in a thin film, it tends to concentrate on the inner boundary of the curve. In a normal metal, this effect is known as current crowding, and results in an additional resistance around the bend area. In a superconductor the effect is analogous, except that it manifests itself primarily as an area with reduced critical current. A superconducting wire will become resistive as soon as the critical current for the inner corner is exceeded, even if the total current is lower than the critical current of the connecting straight-line segments. Basically those points could be considered the same as constriction points[11]. However, it has been proved that, a rounded shape for the inner corner can guarantee the same critical current on those points, as the one of the straight parts of the wire. The complex mathematical calculation reaches a model for an optimum design, in which the only important parameter to take into account is the width (w) of the nanowires. In the following are sketched the derived optimum designs for a 90° and 180° turn in function of w (Fig. 3.16 left). Both the 90° connection points between the nanowire and the contact wires and the 180° bending point of the nanowire, have been designed and fabricated following this method depending on w (Fig. 3.16 right).

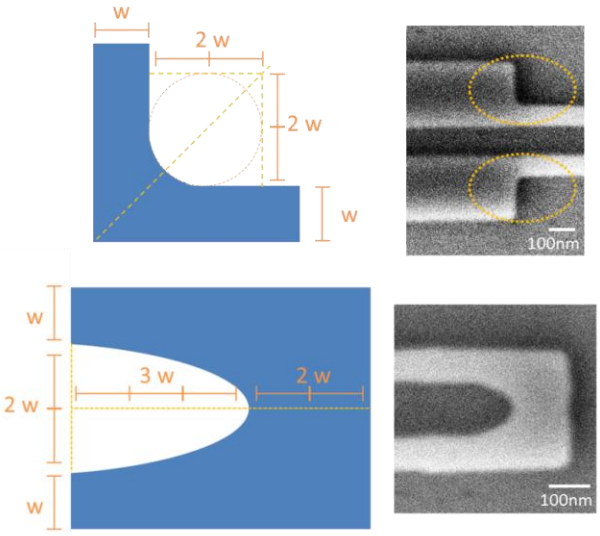

Fig. 3.16 On the left optimum design for 90° and 180° turn in function of nanowire width w. On the right SEM images of the fabricated nanowires following the designs on the left.

3.4.4 Contact wires

The contact wires do not constitute simply an electrical link among the nanowire and the metal pads, they play an important role in terms of recovery time of the SSPD. As already discussed in Chap1.4.2 the dead time ($3\tau_e$) is directly proportional to the kinetic inductance (L_k) of the nanowire divided by the load resistance (R_L), meaning that to obtain a fast SSPD either the L_k is decreased or the R_L is increased. However it has to be kept in mind that an excessive decrement of L_k and increment of R_L might lead to latching. In this case R_L =50Ω and $L_k/\square$=90pH are the used parameters[17] that guarantees the absence of latching. Indeed $L_k/\square = \mu_0\lambda^2/t$, where square (□) is the ratio of the length of the nanowire to its width, t the thickness of the film, μ_0 absolute permeability and λ penetration depth of the superconductor. So once the superconducting material and its thickness are established, it is possible to find the specific L_k per square. The number of squares, required for a NbN film, such that the proper value of L_k is obtained, are equal to 1600. This total number has to be reached considering all the squares of all the wires, so including both nanowire and contact wires. The already selected length of 20μm and width of 100nm for the nanowire represent 200□. The remaining 1400□ have been included by adjusting the length of the contact wires, considering a fixed width of 320nm (double the wire spacing).
The devices fabricated following this design did not show any latching and the measured recovery time is comparable with the one of a standard SSPD (Chap 5.3.2.).

3.5 Conclusion

Several NbN films have been analysed in terms of roughness and T_c in order to identify the best deposition conditions, specifically as a function of the deposition temperature. However, only the electro-optically characterization of devices, fabricated on films with slightly different characteristics, brought to a conclusive result. Indeed it has been found that even if it is advisable to work with films of higher T_c (>10K), it is safer to restrict the range to 9.3-9.7K, so that the deposition temperature is kept low and even small As evaporation is avoided. Films within such range of T_c have shown one order of magnitude higher DQE compared to films with higher T_c.
Once the sputtering deposition parameters have been found such to have a very smooth surface and T_c within the above mentioned range, the NbN is deposited on top of the heterostructured pieces grown by MBE.
After this step the contact pads and alignment markers, consisting of 14 nm Ti and 140 nm Au layers, are defined through optical or electron beam lithography (Chap.2.3.1), followed by electron beam evaporation (Chap2.3.2), and lift-off. The nanowires and the contact wires are patterned by electron beam lithography on a 100-nm-thick mask of HSQ (Chap.2.3.1). The nanowires are 20μm long with a pitch of 260nm and width of 100nm,

that has been preferred to 80nm due to the too low value of I_c that those last nanowires shown. All the bending points have been designed to avoid the current crowding and the contact wire (320nm wide) is long enough to provide the proper total kinetic inductance.
In the next step the design is transferred from the HSQ mask to the NbN film via reactive ion etching (RIE) in an Ar/SF_6 plasma (Chap2.3.4). The fabrication of the SSPDs is concluded with this step. From this point on all the rest of the fabrication is entirely dedicated to create the nanophotonic structures of the integrated circuit (see next chapter).

References

[1] S. Miki, Y. Uzawa, A. Kawakami, Z. Wang, “Fabrication and IF bandwidth measurements of NbN hot-electron bolometers”, *Electronics and Communications in Japan (Part II: Electronics)*, **7** pp.77–83, 2002.

[2] D. Bitauld, F. Marsili, A. Fiore, A. Gaggero, F. Mattioli, R. Leoni, M. Benkahoul, F. Lévy, “NbN nanowire superconducting single photon detectors fabricated on MgO substrates”, *Journal of Modern Optics*, **56** pp. 395-400, 2009.

[3] D. Rosenberg, A. J. Kerman, R. J. Molnar, E. A. Dauler, "High-speed and high-efficiency superconducting nanowire single photon detector array," *Optics Express*, **21** pp.1440, 2013.

[4] F. Marsili, A. Gaggero, L. H. Li, A. Surrente, R. Leoni, F. Lévy, A. Fiore, “High quality superconducting NbN thin films on GaAs”, *Superconductor Science and Technology*, **9** pp. 095013, 2009.

[5] A. Guillén-Cervantes, Z. Rivera-Alvarez, M. López-López, E. López-Luna, I. Hernández-Calderón, “GaAs surface oxide desorption by annealing in ultra-high vacuum”, *Thin Solid Films*, **1** pp. 159–163, 2000.

[6] D. Sahin “Waveguide Single-photon and photon-number-resolving detectors ” PhD thesis Chap.3, Technische Universiteit Eindhoven, 2014.

[7] J. A. Thornton, “High rate thick film growth”, *Annual Review of Materials Science*, **1** pp. 239–260, 1977.

[8] Z. Wang, A. Kawakami, Y. Uzawa, B. Komiyama, “Superconducting properties and crystal structures of single-crystal niobium nitride thin films deposited at ambient substrate
temperature”, *Journal of Applied Physics*, **10** pp. 7837–7842, 1996.

[9] A. Pruymboom, P. Berghuis, P. Kes, H. Zandbergen “Threshold for Argon Bubble-Growth in Sputtered Amorphous Nb3Ge”, *Applied Physics Letters*, **50** pp. 1645-1647, 1987.

[10] T. Karabacak, “Thin film-growth dynamics with shadowing and re-emission effect”, *Journal of Nanophotonics*, **5** pp.52501, 2011

[11] A.J. Kerman, E. A. Dauler, J. K.W. Yang, K. M. Rosfjord, V. Anant, K. K. Berggren, G. N. Goltsman, B. M. Voronov, “Constriction-limited detection efficiency of superconducting nanowire single-photon detectors”, *Applied Physics Letters*, **90** pp. 101110, 2007.

[12] G. Vidali, “Superconductivity: the next revolution?”, *Cambridge University Press*, 1993.

[13] R. Gaudio, K.P.M. op`t Hoog, Z. Zhou, D.Sahin and A. Fiore, "Inhomogeneous critical current in nanowire superconducting single-photon detectors", *Applied Physics Letters*, **105** pp. 222602, 2014.

[14] A. Gaggero, S. J. Nejad, F. Marsili, F. Mattioli, R. Leoni, D. Bitauld, D. Sahin, G. J. Hamhuis, R. Nötzel, R. Sanjines, A. Fiore, "Nanowire superconducting single-photon detectors on gaas for integrated quantum photonic applications", *Applied Physics Letters*, **15** pp. 151108-151108, 2010.

[15] V. Anant, A.J. Kerman, E.A. Dauler, J.K. Yang, K.M. Rosfjord, K.K. Berggren, "Optical properties of superconducting nanowire single-photon detectors"; *Optics Express*, **16** pp. 10750-10761, 2008.

[16] J.R. Clem, K.K. Berggren, "Geometry-dependent critical currents in superconducting nanocircuits", *Physics Review B*, **17** pp. 174510, 2011.

[17] F. Marsili, D. Bitauld, A. Gaggero, S. Jahanmirinejad, R. Leoni, F. Mattioli, A. Fiore "Physics and application of photon number resolving detectors based on superconducting parallel nanowires", *New Journal of Physics*, **11** pp. 45022-45043, 2009.

Chapter 4

Quantum Photonic Integrated Circuit fabrication processes

4.1 Introduction

The integration of SSPDs into nanophotonic circuits has been proved on different platforms: on GaAs with waveguides[1] and QDs[2], on Si with waveguides[3] and nanobeam cavities[4], on Si_3N_4 with waveguides and beam splitters[5] and Si LED[6] or carbon nanotube light emitters[7], on diamond with waveguides and beam splitters[8]. However the demonstrated circuits lacked of more complex structures (high-finesse cavities and electro-mechanical tunable cavities, tunable single photon sources), needed for photonic QIP. The integration of this kind of structures on a platform containing SSPDs presents significant technological challenges, as it will be shown in this chapter.

One of the main concerns, regarding the integration of NbN nanowires with other nanophotonic components on a GaAs platform, is related to the thermal degradation of the NbN film after its deposition. Indeed while for other platforms[6,8], it has been possible to operate at high (>250°C) temperature without compromising the SSPDs` characteristics. A degradation of the film for temperature above 210°C has been observed on GaAs. To systematically test this behaviour, test samples containing perfectly working SSPDs have been baked on hot plate for 2 min, exploring a temperature range between 210°C and 300°C. The baking time of 2 min has been chosen following the one used for the hardening of e-resists such as HSQ or ZEP. Afterwards the detectors have been electrically tested at 4.2K, and the average values of I_c are shown in Fig. 4.1 as function of the baking temperatures. The error bar represents the standard deviation considering 10 devices measured for each baking temperature.

The average I_c drops already to half (~4.5µA) of the value, measured before any baking and also at 210°C (~8µA), for an increase in temperature of only 20°C (at 230°C). The average I_c keeps decreasing as the baking temperature is increased, up to the point, at 300°C, for which the superconductive behaviour almost disappears and I_c ~0.5µA. This behaviour is most probably due to a fast oxidation of the NbN film, which has been proved to deteriorates the superconducting properties[9].

This temperature limitation, regarding the fabrication of nanophotonic structures on GaAs, has required the exploration of different solutions, in order to integrate such components

without damaging the superconductive wires. In this chapter a low-temperature (LT) fabrication process will be presented and compared to the "standard" temperature process normally used for the fabrication of nanophotonics components, such as photonic crystal cavities. The LT fabrication process, that in principle solves the temperature problem, will show the capability of producing high performances SSPDs integrated in the proposed QPIC. However the reproducibility of such result has been limited to few fabricated chips. The reasons behind the lack of reproducibility have been carefully analysed, for every fabrication step, in the present chapter.

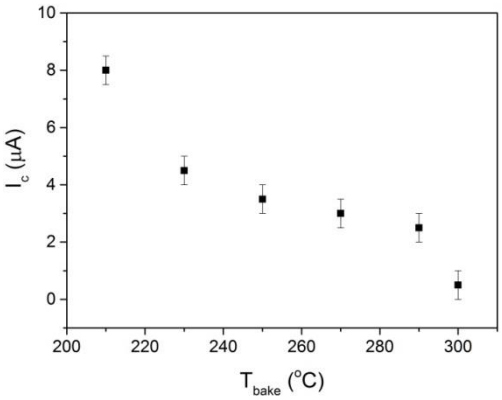

Fig. 4.1 Average SSPD critical current as function of the baking temperature for baking time of 2min.

In the first part of the chapter, the optimized process for integration on single membrane, of SSPDs with ridge waveguides, PhC cavities and waveguides and suspended nanobeams, will be shown. In the second part, the optimized process for the integration on double membrane and doped layers, with electro-mechanically tunable PhC cavities and Stark diodes will be presented.

4.2 Optimized process for integration on single membrane

The heterostructures used for the fabrication of these integrated devices, have been grown by MBE on an undoped GaAs substrate where a layer of GaAs with 320 nm thickness, embedding low-density InAs QDs, is grown on top of a 1.5 μm thick layer of $Al_{0.7}Ga_{0.3}As$, used as sacrificial layer (first two layers from the bottom of Fig. 4.2).
Once the NbN film is sputtered on top and the steps needed for the fabrication of the SSPDs (Chap. 3.5) are completed, the next steps required for the integration of RWGs, PhCCs and PhCWGs, SNBs, are the ones presented in the following.

4.2.1 Standard process flow on single membrane

Before presenting the optimized LT process, the standard temperature process flow, used for the fabrication of PhC structures and RWG, is shown in the following. This process has been developed inside the NanoLab@TU/e cleanroom facility by Dr. L. Midolo and Dr. T. Xia and later optimized by Dr. M. Petruzzella. The process flow for the fabrication of high quality factor photonic crystal can be summarized in the following 8 steps:

1. At the beginning of the process the sample is cleaned with O_2 plasma and deoxidized in a diluted solution of ammonium hydroxide.
2. A thick SiN layer (400 nm) is deposited by PECVD at 300°C for 30min to conformally cover the all surface and be used as hard mask.
3. On top a ZEP-520A e-beam resist is spinned, pre-baked from 100°C to 150°C in 4min and then at 200°C for other 2min. The PhCC patterns are then exposed in the EBL system and the ZEP developed.
4. The holes are then etched in the hard mask by a dedicated RIE machine at room temperature, using a pure CHF_3 recipe without oxygen for about 22min.
5. The residual resist is stripped-off from the SiN hard mask with O_2-plasma at 300 W for 20min.
6. The processing continues with the transfer of the PhCC from the SiN hard mask to the GaAs membrane. In order to obtain an optimized anisotropic vertical dry etching of the holes an ICP machine rather than a standard RIE has been employed. The chosen chemistry has been Cl_4/N_2 at 300°C for 4min.
7. To have the GaAs PhCC membrane surrounded by air, the AlGaAs sacrificial layer is removed below the PhC region. Two wet etching methods have been investigated. The first consists of a 1% HF dip for 10 sec and then cold concentrated 37% HCl acid for 8min at 1°C with a final water rinse. The second one consists of 10s etching in 10% HF and rinse in deionized water.
8. If metal contacts are present in the sample the SiN hard mask must be completely removed in order to clear the access to the μ-probes used during the experimental measurements to bias the devices. This is done by dry etching in a RIE machine at room temperature, using CF_4 plasma.

Clearly some steps of the standard temperature process (n. 2, 6) require higher temperatures than the one of thermal degradation of the NbN film (210°C). In the next paragraphs the alternative solutions to those steps are shown and an optimized LT process presented. Moreover, even if not directly related to temperature issues, some of the other steps (n. 1, 4, 7, 8) have been shown to be also critical in order to maintain high performances SSPDs and have been modified.

4.2.2 Optimized process flow

The optimized low-temperature process flow is the following (Fig. 4.2):

1. A SiN layer (230nm) is deposited by ICP PECVD at 70°C for 15 min.
2. Metal contacts are opened as follow:
   - 2.1 Optical lithography as described in Chap 2.3.1
   - 2.2 SiN etching by general purpose RIE machine at room temperature, using CHF_3 plus O_2 for 5 min (100nm of SiN etched).
   - 2.3 Optical resist removal by ultrasonic bath in acetone and then isopropanol.
3. The PhCC, PhCWG and RWG are patterned on top of the e-resist ZEP, following the same process as described in step 3 of the previous process flow.
4. SiN etching to transfer the pattern in the hard mask. Same recipe as n.2.2 but for a time of 12min (200nm of SiN etched). It has been found that this etching time is one of the most critical parameter in order to obtain high performances SSPDs (see par. 4.2.4).
5. The residual e-resist is removed by O_2-plasma at 300 W for 30min, using only quartz sample holder in order to partially thermally isolate the sample from the heating produced by the plasma.
6. The structures are transferred to the GaAs membrane by dry etching using a general purpose RIE machine at room temperature. The used chemistry is pure $SiCl_4$ for 4min (30nm SiN + 320nm GaAs + 350nm AlGaAs etched). The GaAs etching time is the other most critical parameter in terms of SSPD integration (see par 4.2.5).
7. Undercut of the AlGaAs sacrificial layer by wet etching at 1°C in 37% HCl solution for 8min. Ultrapure water rinsing and drying in warm isopropanol at 80°C temperature, to avoid membranes collapsing produced by the air pressure of a standard drying by pressured N_2.

Overall the process flow of the low-temperature process is not very dissimilar from the standard temperature one, except for the use of etching system that can work at low temperature. But it has to be underlined that the step 1 of pre cleaning of the sample surface, used for the standard temperature process, has been removed. Indeed it has been observed[10] that the HSQ is prone to damage when exposed to oxygen plasma. However some kind of cleaning is required. Indeed when the surface is not cleaned before the SiN deposition, there is a high risk of finding resist particles on the surface. Those particles could compromise the uniformity of the hard mask in certain areas of the chip damaging the fabrication final result on those areas. Even worse they could produce a completely cracked hard mask through which all the chemicals (especially acids for wet etching) can pass reaching directly the NbN nanowires.

When the fabrication part for the PhCC and RWG starts, the surface presents only the SSPDs metal contact pads and the HSQ nanowires covering the NbN film. The sample has been cleaned in the last step with acetone and isopropanol, but any other kind of cleaning (like oxidation-deoxidation, HF buffer (BHF), etc.) could potentially damage the covering layer of HSQ or worse the NbN film. However it has been observed, that, even with a simple acetone/isopropanol cleaning, without a special pre conditioning of the sample surface, the SiN hard mask maintains a good uniformity all over the chip and usually does not present cracking.

The other main difference of the optimized process flow is the presence of the metal contacts opening step (n. 2) and the elimination of the final SiN removal. Indeed the SiN has been used, not only as hard mask for transferring the PhC and RWG patterns on the GaAs membrane, but most importantly as protection of NbN nanowires during all the fabrication steps. A final SiN removal has disastrous consequences for the integrated SSPDs (par. 4.2.7), so in order to have access to the metal pads, an intermediate step of opening only of the contacts had been introduced.

All the other steps are discussed in the following in details, considering especially the effect of the fabrication parameters on the SSPDs performances.

Fig. 4.2 Schematic of the optimized process flow: the number indicates the corresponding process step.

4.2.3 SiN hard mask deposition

Since the deposition at 300°C of the SiN hard mask is not suitable for the SSPDs, one easy way of solving the problem would be trying to deposit the nitride in the same PECVD system, but at low temperature. However it has been observed[11] that films grown in this condition can contain significant amount of hydrogen, that compromises their structural and electronic properties. Therefore a different solution has been sought. An alternative deposition technique, to obtain high quality SiN film at low temperature, is the use of an ICP PECVD machine (Chap. 2.3.3). One way to judge the quality of a nitride films is to check the mechanical stress, the refractive index and the wet etching rate to acids such BHF. It has been found[12] that below a deposition temperature of 200°C, the ICP PECVD is capable of producing SiN films with comparable mechanical stress (200-800MPa) and refractive index (1.8-2.2) as the ones produced by PECVD at 300°C. Moreover the BHF etch rate is basically constant ($\leq$ 200nm/min) for deposition temperatures from 40°C to 300°C and comparable to the one of PECVD for deposition temperature above 200°C. The low BHF etch rate, verified also during this experimental work, is an indication for high density and low hydrogen content of the film.

The SiN films, used for this work, have been produced with the following system parameters:

RF frequency 13.56 MHz, ICP power 800W, RF power 100W, chamber pressure 10mTorr, SiH_4 flux 29sccm and NH_3 flux 24sccm, temperature deposition 70°C.

According to the relative gas flux ratio (0.82) and the RF power chosen, the produced SiN film should have: stress of 600MPa and refractive index of 2.0. Moreover a BHF etch rate of 20nm/min and deposition rate of 15.3 nm/min have been experimentally measured.

The thickness of the deposited SiN layer is a crucial parameter for the realization of the PhC structures. Indeed the ratio between SiN and ZEP thickness is fundamental for a proper transfer of the PhCC pattern to the SiN hard mask and then to the GaAs membrane. For example if the ZEP is too thin the SiN surface becomes uncovered before the holes are completely etched, with an increase of the holes dimensions and SiN roughness, that can worsen the later PhCC dry etching in GaAs. If the ZEP is too thick a trenching effect starts to arise inside the holes with the reacting ions of the RIE plasma that undergo spiral trajectories reducing their energies and therefore the etching rate in SiN, with poor results in depth and verticality of the holes.

On the other hand if the SiN is too thin, there is the risk that it will be completely etched away before all the fabrication steps are completed, leaving the sample surface uncovered. If it is too thick, an effect similar to the one for thick ZEP is expected. Moreover if the SiN and ZEP etching rate in the RIE are not balanced, it can happen that the ZEP is entirely consumed before the holes are completely etched up to the bottom of the SiN mask.

After several tests, a good balance has been found with a SiN layer of 230nm (15min deposition time) and ZEP thickness of 415nm (spinner 2700rpm). Compared to the

standard-temperature process the ZEP thickness has not been drastically changed (390nm vs 415nm). However the SiN thickness has been almost halved (400nm vs 230nm). As it will be discussed in the next paragraph, since the density of this new mask is higher than the one produced at high temperature, a new etching recipe had to be found. The new optimized etching recipe has an etching rate that is lower compared to the one for the standard-process SiN. This explains why a thickness of 230nm is required in order to obtain a reasonable layer of ZEP (~130nm) at the end of the SiN mask etching. Moreover, due to the very slow wet etching rate of the low-temperature SiN mask, its 230nm thickness is always enough to guarantee a thick (>50nm) covering layer above the full chip.

4.2.4 SiN hard mask etching

Commonly the dry etching of dielectric materials, such as SiO_2 or Si_3N_4, used as hard mask is performed by using either CF_4 or CHF_3. Both chemistries are employed in the standard PhC fabrication process, either to etch large (>1µm) structures (RWGs, vias or metal pads openings) with CF_4 or to etch PhCs structures with pure CHF_3. Pure CHF_3 guarantees high etching selectivity and directionality, therefore resulting more suitable for the etching of small and particularly fabrication sensitive structures such as PhCs.
Both chemistries have been tried in order to etch the LT SiN hard mask, but the results have been poor, in terms of etching rate (completely unbalanced comparing it with the one for the ZEP) but most importantly in the ability to completely remove every residual layers of the mask.
Indeed it is known[13] that, in CF_4 and CHF_3 plasmas, polymer-forming radicals can deposit on the substrate to form a barrier layer consisting of various bonds of carbon and fluorine. This protective layer acts as a diffusion barrier for the fluorine radicals to reach the surface of the material to be etched. The etch rates of dielectrics is inversely proportional to the thickness of this polymer layer and, eventually, for very thin layers of dielectric (<10nm) it has the ability to completely stop the etching. Moreover SiO_2 and Si_3N_4 have different abilities to consume carbon species during etching. The SiO_2 reacts stronger with fluorocarbon as compared to Si_3N_4. This is because oxygen in the oxide layer provides additional reaction channels with carbon in the polymer layer over nitrogen in the nitride layer. Therefore the addition of O_2 in the plasma could provide additional reaction paths that decrease the thickness of the polymer barrier layer on Si_3N_4.
Indeed, a study[14], about the dry etching of dielectrics by CHF_3/ O_2 chemistry, has proved how even a small amount of O_2 is helpful to reduce the polymer barrier, allowing a fast etching of the SiN mask.
This result has been confirmed in this work during the etching of the LT SiN hard mask. Indeed, without changing any other parameters (RF power 100W, process pressure 60 mTorr and total gas flow 60sccm) compared to the recipe with pure CHF_3 chemistry, a

small alteration on the stoichiometric ratio of the reactive chemicals has produced the sought result. Simply adding a flow of O_2 of 5 sccm to the 55 sccm of CHF_3 has been enough to both solve the inability to etch the last residual layers of SiN and achieve an etching rate (16.5 nm/min) which allows to work with the one for the ZEP (25 nm/min).
The high density and most importantly the low impurity content of the LT SiN hard mask are probably the reasons why the standard etching recipes, used for high-temperature PECVD SiN, have not worked in this case.
The room-temperature oxygen-enriched CHF_3 recipe has been used in this work for every etching of SiN layer, ensuring directionality and selectivity, as it is shown in the following SEM cross-section picture (Fig. 4.3) of a PhC structure after the SiN etching.

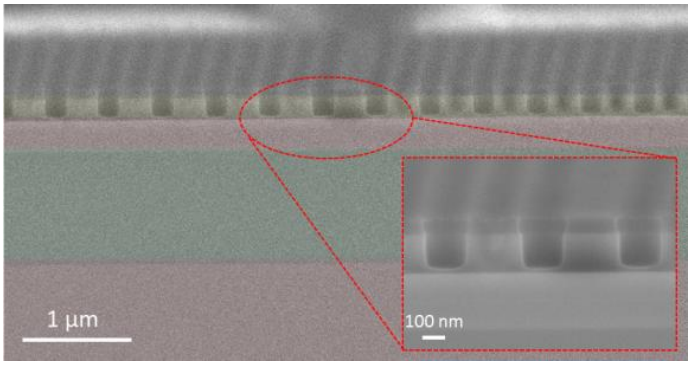

Fig. 4.3 SEM cross-section image of a PhCs structure after SiN etching. Colours have been added for clarity: in red the GaAs substrate and single membrane, in green the AlGaAs sacrificial layer, in yellow the SiN mask, on top the ZEP residual layer.

However, as already mentioned, even if in principle this etching procedure (room temperature process and NbN covered by several layers of materials for a total thickness of 400nm) should not produce any particular effect on the functionality of the SSPDs, it has been discovered as one of the most damaging in terms of detector integration. Indeed it has been observed often that after this etching step the average I_c of the SSPDs would drop from a standard ~8µA to half of it, with severe consequences on the detector efficiency. This behaviour has been noticed with an unpredictable dependence of the etching time and process chamber conditions. To try to understand and solve this unexpected behaviour, several tests have been performed.
To test the dependence on the etching time, test samples with working SSPDs have been covered with resist (~1µm thick and not etched by the SiN etching recipe) and inserted inside the process chamber, switching on the same plasma used for the etching of the SiN hard mask. For each test 4 pieces of similar dimensions have been inserted and left in plasma for 9 min, then, one piece has been removed for future electrical characterization, and other 3 pieces left inside for another extra 2 min in plasma, for a total time of 11min. A similar procedure has been repeated such to end up with a single piece, that has been

kept in plasma for a total time of 14min. Such step by step procedure has been chosen to exclude an overheating effect of the substrate due to a prolonged time in plasma. The minimum time of 9 min has been selected due to the fact that for such time a degradation of the NbN films during previous tests has never been observed. The maximum time of 14 min, has been chosen as the maximum time needed for SiN etching for all structures and machine conditions.

Moreover, during this experimental work, it has been noticed that the use of a general purpose RIE machine (used by several users to etch different kinds of materials) does not help in terms of reproducibility of the process. Different results have been obtained during different time periods of the machine use, without the possibility of finding a way to reset the system, such to guarantee the reproducibility of the fabrication process. For this reason two sets of data have been acquired during two different periods, corresponding to different machine conditions. The processing for the first data set (Set1) has been carried out inside a process chamber completely clean of every contamination of other materials, possible thanks to manual cleaning and polishing of every surface inside the chamber before the use. The second data set (Set2) has been acquired after 15 days of machine use by other users. It has to be underlined that before every use the process chamber has been cleaned using O_2 plasma for 45min and preconditioned for 20min by oxygen-enriched CHF_3 plasma. After the plasma treatment, the samples have been cleaned with acetone and isopropanol in order to remove the resist mask and electrically characterized at 4.2K.

One exemplary IV curve for each etching time is shown in Fig. 4.4 a, while the behaviour of the average I_c as function of the etching time is presented in Fig. 4.4 b, considering both Set1 and Set2 to see the difference according to the chamber conditions. The error bar is the standard deviation over the 10 devices measured for each etching time.

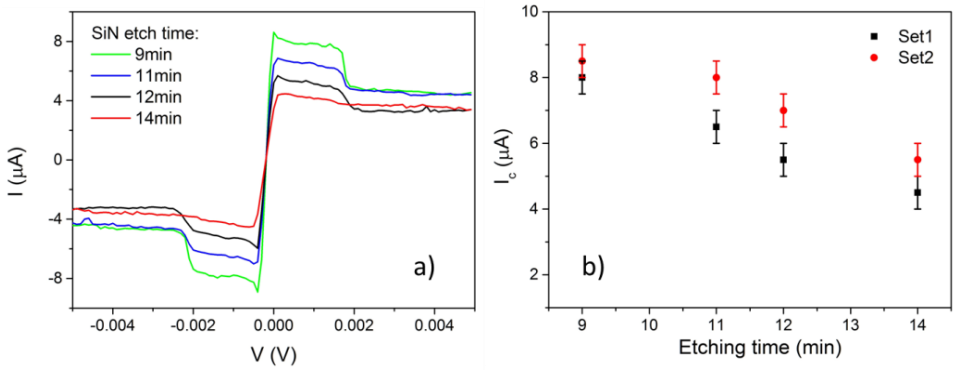

Fig. 4.4 a) Exemplary IV characteristics of SSPDs after SiN etching processing for different etching times. b) Average I_c as function of the SiN etching time for two different process chamber conditions: clean chamber (Se1), "used" chamber (Set2).

As expected for the minimum etching time of 9 min, the average I_c does not decrease compared to the standard one (~8.5μA) usually obtained at the end of the SSPDs

fabrication process. Moreover within the error there is no difference as function of the chamber conditions (first point of Fig. 4.4 b for Set1 and Set2). However a decrease of the I_c is observed for longer etching time as well as a different dependence as a function of the chamber conditions. The decrease is faster for Set1 (down to 4.6μA) rather than for Set2 (down to 5.3 μA). At the beginning it was assumed that different chamber conditions could be seen by monitoring the plasma voltage, and that a strong difference in voltage could explain the different results between Set1 and Set2 and for different etching time. However the monitoring of the voltage, during all the processes, has not underlined any particular variation and a constant 380±1V has always been observed for every chamber conditions and for every considered time.
Excluding a voltage dependence as well as an effect produced by substrate overheating, considering the step by step procedure followed for the sample processing, the observed behaviour of decreasing I_c for long etching time suggests that the exposure to the plasma is the reason for the progressive film degradation. However this does not explain the difference between Set1 and Set2.
Considering that usually the etching time required to etch the PhCs structures is around 11-12min, for a chamber not completely cleaned (Set2) the value of I_c is still acceptable (7μA) in order to have good working detectors. However often it can happen that according to the machine condition a longer etching time is required to etch through the PhCs holes, reducing even more the value of I_c.

4.2.5 GaAs etching

After the removal of the residual e-resist, the patterned structures are transferred to the GaAs membrane by using the same RIE system used for the SiN etching. The room temperature recipe has been implemented in the system by Dr. F. Pagliano and it uses a pure $SiCl_4$ chemistry. This recipe has shown good directionality as observed in the SEM cross-section picture of Fig. 4.3 of a PhCs structure.
The etching rate of the LT SiN hard mask (~37.5nm/min) has been monitored during this step to avoid excessive mask erosion with consequent increase in the hole diameter. Ensuring that about 100 nm of SiN would remain after dry etching of the GaAs membrane is a good rule of thumb for a proper PhCC processing.
Unfortunately, as already stated in the previous paragraph, the use of the general purpose RIE machine does not guarantee a good reproducibility of the process, especially in terms of etching rate. To etch through the residual SiN layer (~30nm) and the GaAs membrane (~320nm) to finally reach and partially etch (~350nm) into the AlGaAs layer, a time between 3 min 30s and 4 min 30 s has been used, according to the machine condition. While, once the etching rate is found for a particular run, the time can be tuned in order to completely open the PhCs structures without damaging the photonic components, the SSPDs functionality has been found, once again, strongly dependent on the used etching

time. Exactly the same procedure used in the previous paragraph has been used to try to understand and solve this unexpected behaviour. Two sets have been processed in two different periods either with the chamber completely clean (Set1) or after 15 days of use (Set2). The procedure has been made step by step considering etching time from 3min to 4.5min with step of 0.5min between each step, but of course this time the $SiCl_4$ plasma used for the etching of GaAs has been ignited.

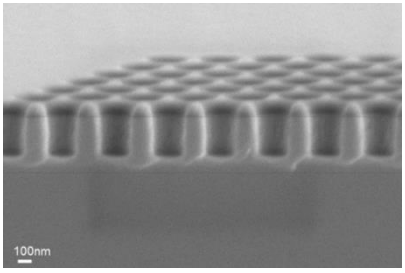

Fig. 4.3 SEM cross-section image of a PhCs structure after GaAs etching, the top darker layer is residual SiN

The samples have been electrically measured at 4.2K and one exemplary IV curve for each etching time is shown in Fig. 4.6 a. The behaviour of the average I_c as function of the etching time is presented in Fig. 4.4 b, both for Set1 and Set2.

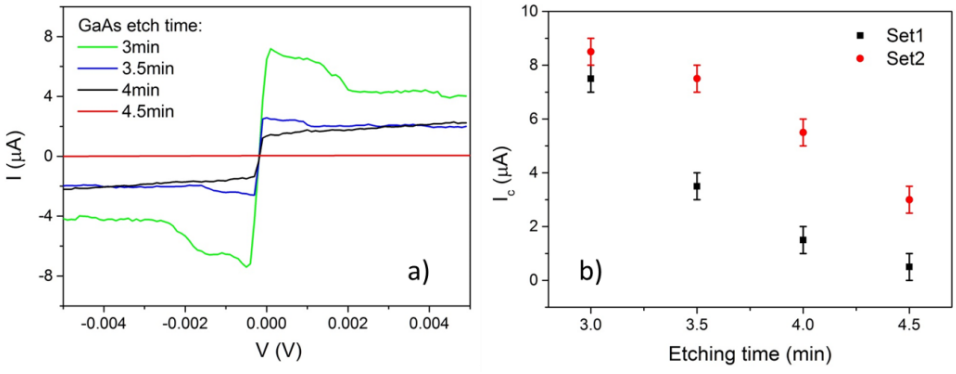

Fig. 4.4 a) Exemplary IV characteristics of SSPDs after GaAs etching processing for different etching times. b) Average I_c as function of the GaAs etching time for two different process chamber conditions: clean chamber (Se1), "used" chamber (Set2).

The minimum etching time of 3 min has been selected on purpose since no degradation of the detectors has been observed previously. However a small reduction of I_c (7.4μA) is already observed for 3min time in the case of Set1. Indeed a larger difference between Set1 and Set2 is observed in Fig. 4.6 b comparing it with the one of Fig. 4.4 b. The decrease of I_c as function of the etching time is much faster for Set1 leading to a value as

low as 0.5µA for a time of 4.5min. For Set2 instead the average I_c does not go below 3.6µA.
However, contrary to the SiN etching case previously analysed, in this one a relevant difference of ~10V in the plasma voltage has been observed, comparing Set1 (628±2V) and Set2 (618±2V).
Indeed, this voltage difference could explain the quite different behaviour of Set1 compared to Set2. However within one set, so within certain machine condition, no voltage difference has been observed for different etching times.
Also in this case, excluding the voltage dependence and the overheating of the substrate, the reduction of I_c as function of the etching time is due to the exposure of the nanowires to the plasma.
As previously stated, the appropriate time, required to etch through the PhCs holes such to obtain clean suspended structures, changes from time to time, according to the chamber condition, by an amount of around 1 min such that large differences in I_c can result. Therefore, finding a balanced etching time, such to preserve high-quality functioning detectors, but at the same time enough to etch all through the PhCs structures, has been a big challenge for each fabrication process.
Finally it has to be underlined, that if only structures of large dimension (>1µm) are fabricated, such as RWGs, the etching times required, in order to etch the SiN mask (8min) and the GaAs membrane (3min), are much less than the ones used for etching through the PhCs structures. Therefore the reproducibility of the LT fabrication process, such to obtain high-quality working detectors, is guaranteed in this last case.

4.2.6 Wet etching

In order to realize free-standing structures (PhCs membrane, SNBs), the $Al_{0.7}Ga_{0.3}As$ sacrificial layer has to be removed below them.
To do that, two wet methods have been considered in terms of etching capability and compatibility with the integrated detectors.
The first method consists of 10s dip in 10% HF and rinse in deionized water. This method is particularly efficient when the aluminium content in the AlGaAs layer is higher than 70%. This technique is very clean, reducing the probability to end up with Al-related hydrofluoric compounds underneath the suspended membrane. However this method does not give any geometrical control, contrary to the second one.
In the second method a wet etch in a cold (1°C) 37% HCl solution is performed. It has been experimentally found[15] that cold HCl can etch the AlGaAs layer with strong anisotropy. This anisotropy originating from different etching rates along different crystallographic orientations, results in a tilted profile which makes a 55° angle with the substrate. Using an appropriate orientation (waveguides aligned along the [011] crystallographic direction), this etching technique can be used to create a trapezoidal support for the RWGs (Fig. 4.7 a). Moreover the size of the trapezoidal base changes with

the width of the waveguide, until it disappears for width smaller than 1.5µm. This wet etching technique easily allows the fabrication of RWGs connected through adiabatic tapering to suspended nanobeams (see Chap. 6.1).
Even if the aluminium content in the AlGaAs is below 70%, with this last method is possible to obtain clean suspended PhCs structures like the one shown in Fig. 4.7 b. However if the etching through the GaAs has not been enough to properly reach the AlGaAs underneath, result like the one shown in Fig. 4.7 c is obtained. This kind of result has often been observed, due to the use of too short etching times employed in order to preserve the detector properties. In this situation the cavity is compromised and, in the µPL spectra, it is not possible to distinguish clear modes from the background created by the bulk material.

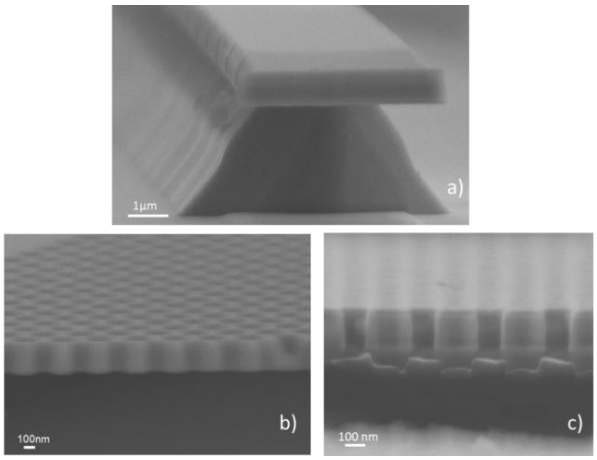

Fig. 4.7 SEM cross-section immages: a) Ridge waveguide with the trapezoidal support, b) suspended PhC membrane, c) suspended PhCs membrane with residual bulk material attached.

When this wet etching step is executed the NbN nanowires are covered by 100nm HSQ plus 80nm of SiN hard mask. However the side of the nanowires is less protected, due to the tight alignment on top of the nanobeam, and especially if the etching selectivity is not very high like in the case of 10% HF.
Indeed a strong reduction of the average I_c down to 1µA has been systematically observed, whenever 10% HF was used. This effect is due to a lateral nanowires etching, produced by small GaAs etching at the sides of the SNB (due to the limited etching selectivity of the HF) plus strong etching of the HSQ protecting the NbN film.
Instead the use of cold HCl did not produce any effect on the average starting value of I_c (~8µA) of the detectors. Therefore only this wet etching technique has been used to create the free-standing structures of the integrated chip.

4.2.7 SiN removal

A final step of dry etching to remove the residual SiN hard mask is usually required in order to open the metal contacts. However it was immediately noticed that this step is incompatible with the detectors integration. Indeed it has been observed several times that a complete removal of the SiN hard mask causes a strong damage to the detectors, due to a lateral etching that drastically reduces the width of the wire and correspondingly the value of the critical current.
The solution to this problem, in order to gain access to the contacts, was initially found introducing an intermediate step (step n.2 of par. 4.2.2) that would open only the metal pads. This technique was successful, however with poor reproducibility in maintaining always perfectly functional detectors. The reason for this poor reproducibility is related to two different effects that are depending on the amount of SiN left on top of the pads during their opening.
If the amount of removed SiN is too large (>50nm), during the GaAs etching the pads are going to be directly exposed to the plasma and a phenomenon, that could be compared to the antenna effect[16] in CMOS processing, is observed. The antenna effect is observed when the charges, produced in the plasma during the etching, create a strong passage of current in a MOSFET transistor, which is able to damage the oxide gate. In the case of SSPDs, a strong passage of current through the highly resistive nanowires could produce a large local heating of the NbN film, therefore damaging it.
This kind of effect has been proved checking the I_c of several SSPDs on a chip in which half has been completely protected by resist and the other half protected everywhere except above the metal pads. The chip has been exposed to the same plasma used for the SiN etching for a time of 8 min (well below the etching time for which damaging of the detectors is observed) and electrically measured at 4.2K.
For the covered devices an average I_c of 8.5μA with a standard deviation of 0.5μA has been observed. On the other hand the devices, in which the metal pads were uncovered, have shown ohmic behaviour or in few cases superconducting one, but with values of critical current around 0.5 μA. This result (Fig. 4.8 red point) implies that an effect comparable to the antenna effect is present whenever the SSPDs metal pads are directly exposed to the etching plasma for a time longer than few seconds.
On the other hand, if the thickness of the removed SiN is too small and a layer ~50nm is left on top of the metal pads, the detectors are protected from the antenna effect, but the thin layer creates problems both for the electrical and thermal contact with the μ-probe. Indeed it has been observed that even if the layer is thin enough to allow electrical measurements, the thickness of the layer has a strong effect on the thermalization of the μ-probe. Therefore the real value of I_c is masked by the poor thermalization of the μ-probe, and the effect is stronger for thicker SiN residual layers. A proof of that is presented in Fig. 4.8 where the average value of I_c is shown as function of the thickness of the SiN

layer remaining on top of the pads. The error bar is calculated as the standard deviation of the measured devices (10 for each SiN thickness).

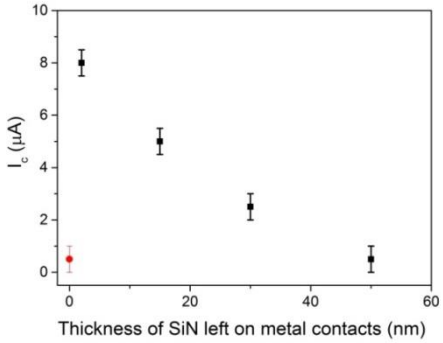

Fig. 4.8 Detectors avarage I_c as function of the thickness of the SiN layer left to cover the SSPDs contacts. The red point, obtained for 0nm covering layer, is correlated to antenna effect.

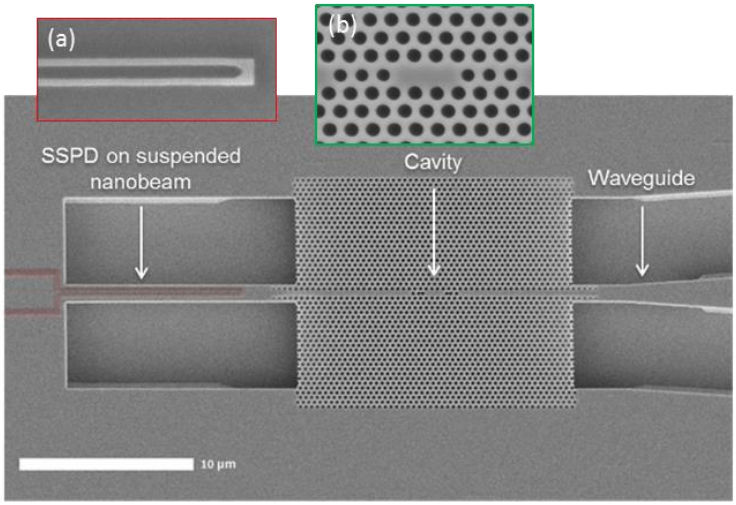

Fig. 4.9 SEM picture of the full QPIC. Zoomed pictures of SSPD (a) and PhCC (b)

From these observations, it is clear that it is not easy to find a balance for the right amount of SiN to leave on top of the metal pads, such to avoid the antenna effect, but also to obtain good electrical and thermal contact. Indeed from time to time the right SiN thickness has been found, but also in this case the precarious balance of such kind of effects creates big problems in terms of reproducibility of the integration process, particularly considering the detector performance.

On the other hand the SiN layer (~50nm) left on top of all the other components of the integrated chip does not seem to negatively impact them. Actually as it will be shown in

the next chapter (Chap. 5.2) the SiN layer helps in terms of SSPDs absorptance and polarization-independence.
Instead the optical properties of the PhC structures are not modified by the SiN layer. Indeed in Chap.6.2.2 it will be shown that the quality factors of the cavities are around 1000, as expected from the simulation, in which only the GaAs membrane has been considered.
An example of a complete QPIC at the end of the fabrication process is presented in Fig. 4.9. Its different components are enlighten: the nanowire (a) placed on top of a 15 µm-long, 1 µm-wide nanobeam, the two PhC waveguides with the PhC cavity (b) and the other SNB that is tapered to a RWG of 5 µm width at the cleaved facet.

4.3 Optimized process for integration on double membrane and doped layers

So far, the photonics components that have been considered for integration in the proposed QPIC do not allow any control of the resonances of QDs and/or cavities. However a reversible method to independently control such components is needed, in order to realize a scalable circuit. Indeed, the energy mismatch between the emitter and the cavity, due to growth and fabrication, is unavoidable. Therefore, without a control, the emission of single photons is purely based on probability. Several efforts have been made in order to produce scalable single-photon sources based on QDs emission, controlled post-fabrication by tuning systems[17,18]. However, due to the extensive fabrication know-how, implemented in the NanoLab@Tue cleanroom facility by Dr. L. Midolo first and by Dr. M. Petruzzella after, for this work, an electric field tuning of the QDs based on Stark effect[19] and a NOEMS approach for the cavity control[20,21] have been selected as tuning systems.
In order to implement such systems in the QPIC, the design of the heterostructure has been modified, including doped layers for the realization of Stark diodes and double GaAs membranes for the NOEMS implementation.
The layer stack is shown in Fig. 4.10. This time on top of the sacrificial layer of 1.5µm, not one but two membrane layers are grown, with thickness of 180nm for the one on top and 170nm for the one at the bottom. The upper membrane contains low density self-assembled InAs QDs and the two membranes are separated by an AlGaAs sacrificial layer 240nm thick.
In order to realize two p-i-n diodes, one for QDs tuning and the other for the cavity mechanical actuation, the top part (55nm thick) of the two membranes is p-doped, while the bottom part (55nm thick) of the top membrane is n-doped.

Fig. 4. 10 Layer stack of the heterostructure used for the implementation of Stark diodes and electro-tunable PhCs cavities.

Also for the fabrication of this more complex QPIC, the process flow can be separated in two parts: the first one in which the SSPDs are fabricated and the second one in which all the other photonic components (RWGs, Stark diodes, electro-mechanical tunable PhCs cavities, SNBs) are added.

4.3.1 Standard process flow on double membrane and for Stark tuning

Before presenting the optimized LT process, the standard process flow is shown in the following. The process for the fabrication of the electro-mechanically tunable PhC cavities has been developed by Dr. L. Midolo, while, further optimization of this process with integration of Stark diodes has been made by Dr. M. Petruzzella.
The process flow to realize such devices can be summarized in the following 7 main steps:

1. Cleaning of the sample with O_2 plasma and deoxidation in a diluted solution of ammonium hydroxide.
2. Realization of deep-etched alignment markers:
    - 2.1 Deposition of SiN layer (400nm) in PECVD at 300°C,
    - 2.2 Spinning, exposure and development of ZEP-520A,
    - 2.3 Transfer of the pattern by dry etching of the SiN using pure CHF_3 plasma,
    - 2.4 Stripping of the residual resist by O_2-plasma,
    - 2.5 Transfer of the pattern on the GaAs/AlGaAs layers by dry etching in RIE machine using pure $SiCl_4$ plasma,
    - 2.6 SiN removal by dry etching of the SiN using pure CF_4 plasma,
    - 2.7 Cleaning as step 1.
3. Opening of n-via:
    - 3.1 Deposition of SiN layer (50nm) in PECVD at 300°C,

3.2 Spinning, exposure and development of ZEP-520A,
3.3 Pattern transfer by dry etching of the SiN using CF_4 plasma,
3.4 Stripping of the residual resist by O_2-plasma,
3.5 Surface conditioning with 1% HF for 10s
3.6 Wet etch of GaAs with diluted citric acid solution until the n doped layer is reached,
3.7 Cleaning as step 1.

4. Opening of p-via:
   4.1 Spinning, exposure and development of ZEP-520A,
   4.2 Pattern transfer by dry etching of the SiN using pure CF_4 plasma,
   4.3 Then by dry etching of the GaAs/AlGaAs layers using pure $SiCl_4$ plasma,
   4.4 Stripping of the residual resist by O_2-plasma,
   4.5 Wet etch in 5% HF of the intermembranes AlGaAs, to expose the p doped layer
   4.6 Cleaning as step 1.
5. Metal contact deposition:
   5.1 In case of residual SiN, removal by dry etching,
   5.2 Spinning, exposure and development of the resist,
   5.3 Metal evaporation (Ti 50nm, Au 200nm),
   5.4 Lift-off in acetone vapour.
6. PhC structures and waveguides fabrication:
   6.1 Deposition of SiN layer (400nm) in PECVD at 300°C,
   6.2 Spinning, exposure and development of ZEP-520A,
   6.3 Transfer of the pattern by dry etching of the SiN using pure CHF_3 plasma,
   6.4 Stripping of the residual resist by O_2-plasma,
   6.5 Transfer of the pattern on the GaAs/AlGaAs layers by deep etching in ICP at 200°C by nitrogen enriched Cl_2 plasma,
   6.6 Undercut of the sacrificial layers by wet etch either in cold 37% HCl or 10% HF,
   6.7 Rinsing and drying in critical point dryer machine to avoid membranes collapsing or irreversible stitching,
7. SiN removal by dry etching of the SiN using pure CF_4 plasma.

Even at a first glance it is clear how several steps of this fabrication process are completely incompatible with the integration of the detectors. Excluding the ones incompatible for temperature limitations, that have already been discussed and solved for the fabrication process on single membrane, the main concern is related to the SiN removal and cleaning steps that are repeated several time during the process. Those steps are added in order to guarantee, in each etching step, an always fresh and good quality SiN hard mask, that does not crack, due to surface contamination.

As already discussed in the previous paragraph (4.2), it is of fundamental importance to cover the detectors with SiN in order to protect them during every fabrication step, therefore once the hard mask is deposited it should never be removed.
In order to make the two processes compatible different solutions have been explored.
The easiest way for an integrated process would be opening the vias to the doped layers at the very beginning and afterwards proceeding with the deposition of the superconducting film, SSPDs fabrication and integration of the other photonic components following the same process flow for single membrane described in par. 4.2.2. This solution has been experimentally tested, checking the IV characteristic at 4.2K of the SSPDs fabricated on a NbN film deposited after the opening of the vias. Unfortunately the average value of the I_c was below 0.5μA on 20 tested devices. Indeed, the roughness on the sample surface, produced by the vias opening, must have strongly compromised the quality of the 5nm NbN film.
The other solution, in which the detectors are first fabricated and afterwards all the other components are implemented, is presented in the next paragraph.

4.3.2 Optimized process flow on double membrane

The process flow presented in the following is a LT fabrication process, that excludes all the steps incompatible with the detector integration and that starts immediately after their fabrication.

1. Opening of n-via:
   - 1.1 Deposition of SiN layer (270nm) by ICP PECVD at 70°C,
   - 1.2 Spinning, exposure and development of ZEP-520A,
   - 1.3 Pattern transfer by dry etching of the SiN using oxygen enriched CHF_3 plasma in general purpose RIE at room temperature,
   - 1.4 Stripping of the residual resist by O_2-plasma,
   - 1.5 Surface conditioning with 1% HF for 10s,
   - 1.6 Wet etch of GaAs with diluted citric acid solution until the n-doped layer is reached.
2. Opening of p-via:
   - 2.1 Spinning, exposure and development of ZEP-520A,
   - 2.2 Pattern transfer by dry etching of the SiN using oxygen enriched CHF_3 plasma,
   - 2.3 Then by dry etching of the GaAs/AlGaAs layers using pure $SiCl_4$ plasma,
   - 2.4 Stripping of the residual resist by O_2-plasma,
   - 2.5 Wet etch in 5% HF of the intermembranes AlGaAs.
3. Metal contacts deposition for electrical tuning/actuation :
   - 3.1 Spinning, exposure and development of the resist,
   - 3.2 Metal evaporation (Ti 50nm, Au 200nm),

3.3 Lift-off in acetone vapour.

4. PhC structures and waveguides patterning and SSPDs metal contacts opening:
   - 4.1 Spinning, exposure and development of ZEP-520A,
   - 4.2 Pattern transfer by dry etching of the SiN using oxygen-enriched CHF_3 plasma,
   - 4.3 Stripping of the residual resist by O_2-plasma.
5. Definition of a protecting layer for the SSPDs including their contacts and vias, using the negative e-resist MaN2410.
6. Transfer of the PhCs and waveguides pattern from the SiN hard mask to the GaAs/AlGaAs layer by standard RIE etching at room temperature, using pure $SiCl_4$ plasma.
7. Removal of the e-resist MaN2410 by acetone
8. Undercut of the bottom sacrificial layer, and release of the two membranes by wet etching of the two AlGaAs layers at 1°C in 37% HCl solution for 8min. Ultrapure water rinsing and drying in warm isopropanol at 80°C, to avoid membrane collapse and stitching.

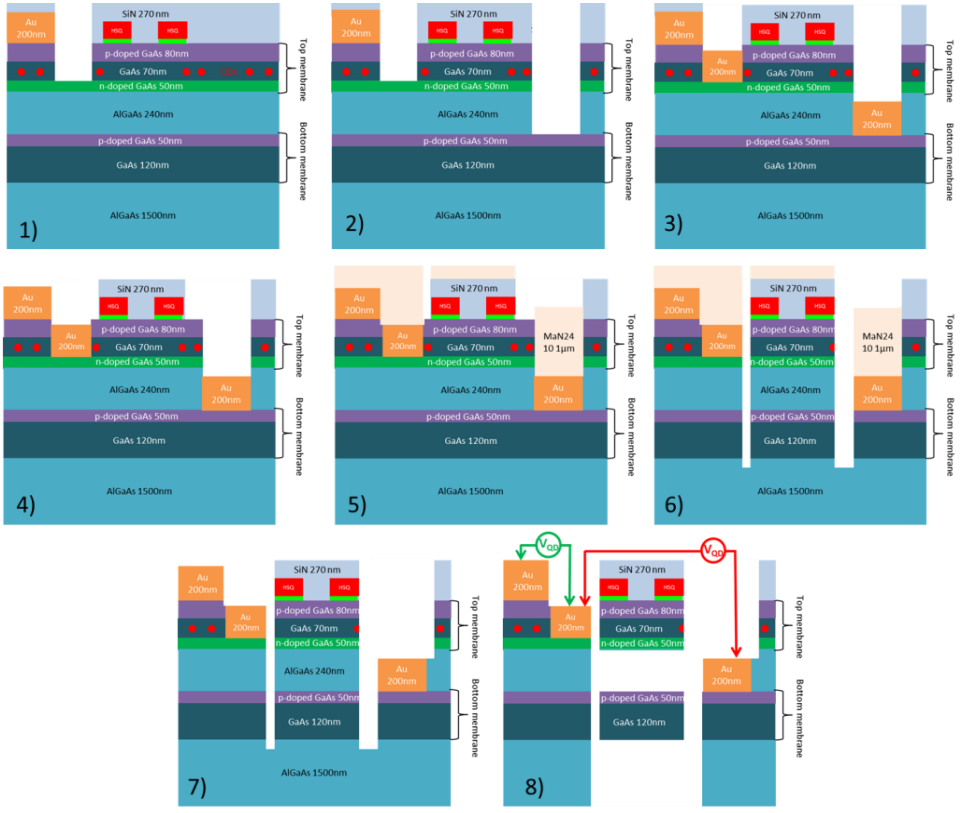

Fig. 4.11 Schematic of the optimized process flow: the number indicates the corresponding process step.

The optimized process flow for detector integration on double membranes and doped layers, differs from the standard process since the first step. The fabrication of alignment markers has been completely removed. Indeed, the metal markers, fabricated for the alignment of the SSPDs nanowires, can be also used for the alignment of all the other components, with better results than deep-etched markers.
The first step of the optimized process is the deposition of the SiN layer (270nm), used to protect the detectors and as hard mask to etch through the vias, PhCs holes and WGs trenches. The vias are created in similar way as for the standard process, however the SiN is never removed at the end of their fabrication.
The photonic structures are transferred from the resist to the SiN mask in the same way as made for the fabrication on single membrane. However the etching time required (13.5min), due to the use of a thicker mask compared to the one used for single membrane, is very close to point for which degradation of the NbN film is observed as shown in par. 4.2.4. Additionally the step 4 is used to create access to the SSPD metal pads.
At the end of step 4 the doped layers are unprotected, therefore the next GaAs etching would damage the Stark diode. The SSPDs metal contact needs to be protected in order to avoid the antenna effect during the GaAs etching and the nanowires need to be additionally covered as well. Indeed, the longer GaAs etching time, required in order to etch through the two membranes, produces a thinning of the SiN mask that may result in exposing the nanowires. For these reasons, it is fundamental to insert step 5 in between the etching through the photonic structures. It has been observed that inserting this step, while the PhCs holes and WGs trenches are already open in the SiN mask, does not compromise the verticality and smoothness of the side walls of the next etching step (Fig. 4.12).

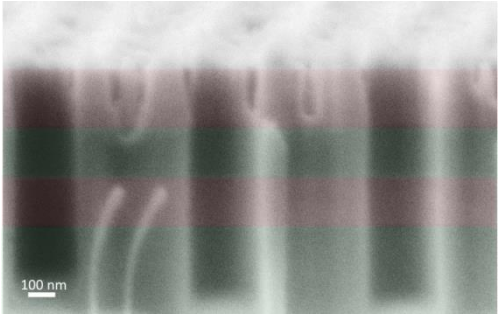

Fig. 4.12 SEM cross-section image of a PhCs structure on double membrane after GaAs etching. Colours have been added for clarity: in red the two GaAs membranes, in green the bottom AlGaAs sacrificial layer and intermembranes AlGaAs .

The step 6 is the most critical in terms of integration with the detectors. While good results have been observed in terms of deep etching (Fig. 4.12), using the standard RIE

rather than the ICP, the etching time required to etch all the way through the two GaAs membranes (170nm+180nm) plus the AlGaAs interlayer (240nm) is too long (6.5min) to avoid the superconducting film damaging observed in par. 4.2.5.
Therefore, while trying to keep the GaAs etching time as short as possible, the capacity of a clean release of the two membranes has been compromised with a poor final result (Fig. 4.13).
The characterization of all the components (electro-mechanical tunable cavity, Stark diode, SSPD) of the integrated QPIC is presented in the following.

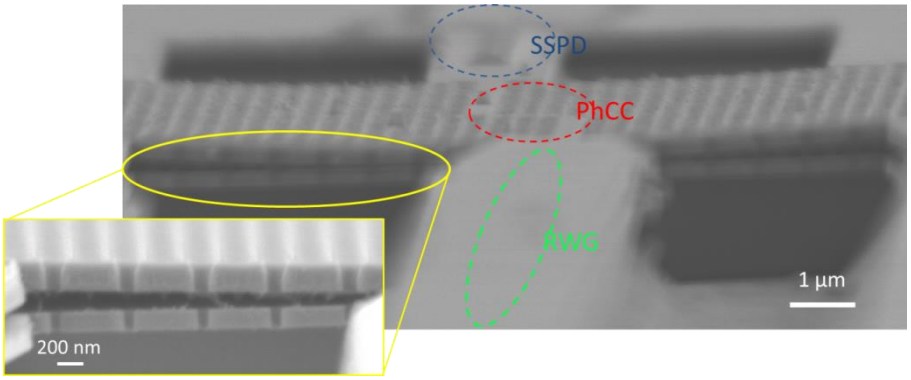

Fig. 4.13 SEM cross-section image of the full QPIC on double membrane at the end of the fabrication process. The main components are underlined for clarity: in blue the superconducting single-photon detector, in red the photonic crystal cavity shoulder coupled to the photonic crystal waveguides, in green the ridge waveguide. Inset: zoom of the intermembranes layer in which some residual AlGaAs is visble.

4.3.3 Results

As already mentioned above, the main concerns in terms of integration are expected to be observed after the etching steps of SiN and GaAs, due to the longer time required to etch through the double-membrane stack layer. Therefore, in order to monitor the process step by step, the detector functionality has been checked in different moments, with electrical characterization at 4.2K. Of particular relevance, it is the characterization after the fabrication of the diodes and of course the one at the end of the process.
During the diode fabrication (steps n. 1, 2, 3), due to the necessity of via opening, the detectors had to withstand a long SiN etching plasma, that could have compromised them. Instead the GaAs etching time required to access to the bottom p doped layer remains within the standard time used for single membrane processing (3.5min). Moreover the two wet etching steps (citric acid solution and 5% HF) could have produced other kind of damage to the detectors, like the one described in par. 4.2.6 for the use of 10% HF. The

IV characteristics of 8 SSPDs, measured after the diode fabrication, are shown in Fig. 4.14.

The average I_c of the detectors is 5.2μA with standard deviation 0.6μA. Considering the long SiN etching time (13.5min), this value of I_c is expected (see Fig. 4.4 a). Even though the I_c is not very high, it is still good enough to guarantee good detector functionality. Moreover it has to be underlined that, due to the presence of the doped layers especially the top p layer, the capability of observing the classic superconducting IV characteristic of the SSPDs was not easily foregone. As both the contact metal and NbN film rest on the p-doped GaAs layer, current conduction in this layer could potentially short-circuit the detector.

Instead, even a scan over a large range of applied voltage (Fig. 4.14 inset), shows the expected ohmic behaviour, observed for SSPDs fabricated on undoped substrates[22], proving that SSPDs can be fabricated on top of doped layers as well.

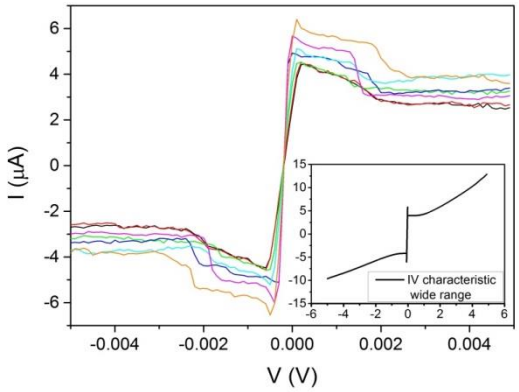

Fig. 4.14 SSPD IV characteristics after fabbrication of diodes. Inset: scan over a wide range of voltage and current for a typical detector.

The metal pads for the diodes of both QDs tuning and cavity actuation have been designed with a lateral configuration and facing the SSPDs pads (Fig. 4.15 a), in order to easily insert the waveguide in between. The diodes have been electrically isolated from the rest of the chip using 3μm wide trenches (blue thin lines in Fig. 4.15 a) etched down up to the bottom AlGaAs sacrificial layer. Two typical IV characteristics of Stark and cavity actuation diodes, measured at 4.2K, are shown in Fig. 4.15 b. For both, the reverse currents is very small (tens of nA), and the threshold (1.3 V for the Stark diodes and 1.5 V for the cavity actuation diodes) similar to the one observed in similar devices[23]. Due to the good IV characteristics of these diodes, good tunability is expected.

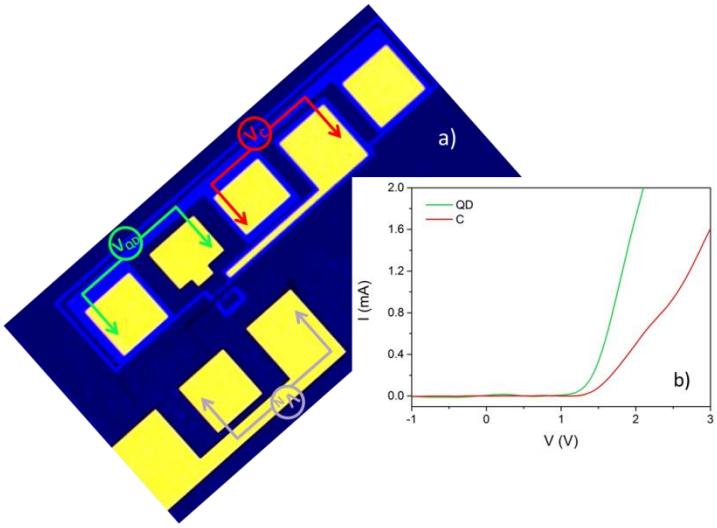

Fig. 4.15 a) optical microscope image of the device after diodes fabbrication. The green arrows indicate the pads used for QDs tuning, the red ones the pads used for cavity actuation and the brown the SSPDs pads. b) typical IV characteristics of Stark diode (green) and of cavity actuator diode (red).

At the end of the process the IV characteristics of both diodes and SSPDs have been tested again. The diodes showed exactly the same characteristics observed in Fig. 4.15 b. However, unfortunately, due to the very long GaAs etching time (6.5min), the I_c of the detectors dropped to values below 0.5μA (Fig. 4.16 a), making them optically unresponsive.

The fabricated double membrane cavities have been characterized at room temperature, acquiring μPL spectra by exciting the cavities from the top. For the main part of the devices was not possible to clearly distinguish a symmetric (S) and antisymmetric (AS) modes as expected[20]. However in few devices it was possible to observe several peaks in the μPL spectra. One example is shown in Fig. 4.16 b, where two peaks around 1168nm and other two around 1255nm are visible. Presumably they could be associated to the X and Y of the antisymmetric mode at 1168nm and to the X and Y of the symmetric mode at 1255nm. Indeed considering a large buckling of the top membrane, like the one shown in the SEM image of Fig. 4.13, the observed large distance (~90nm) between S and AS is what expected[20]. Moreover the large background underneath the peaks is another confirmation of the presence of residual AlGaAs between the membranes and unsuccessful openings of the holes of the bottom membrane, as observed in the SEM picture of Fig. 4.13.

Concluding, even though the optimized LT fabrication process for double membrane has been tailored on purpose for the SSPD integration, it does not serve to its objective, due to the fabrication obstacles presented in par. 4.2.4 and 4.2.5.

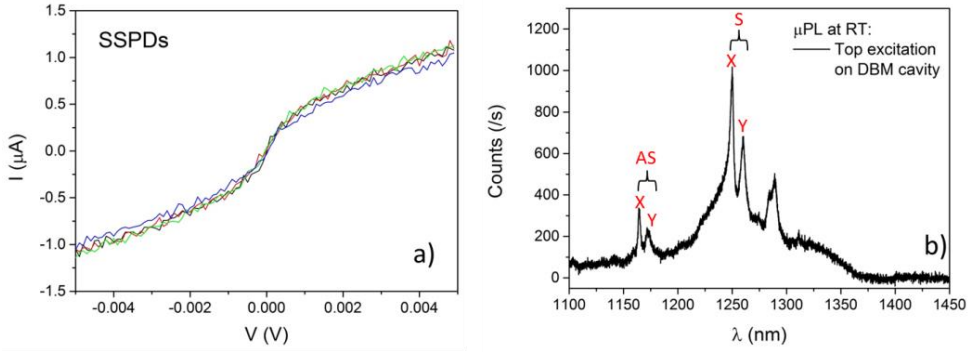

Fig. 4.16 a) SSPDs IV characteristics at the end of the LT fabbrication process on double membrane and doped layers. b) μPL spectrum acquired at room temperature with top excitation on a double membranes PhCs cavity, fabbricated with the optimized low-temperature process.

4.4 Conclusion

In this chapter two low-temperature fabrication processes, that allow the integration of the different components of QPICs, have been presented.

In the first part, the process for integration, on a single membrane, of SSPDs with RWGs, PhC cavities and SNB is analysed step by step. Even though nominally every step is perfectly compatible with the integration of the detectors, it has been observed that several steps together may degrade the NbN film. In particular, a dependence between the etching time and detector critical current has been found for both SiN and GaAs dry etching processes. The decrease of the I_c as the increase etching time does not seem connected to thermal heating of the substrate. The degradation is therefore likely related to the exposure to the plasma.

Due to the unstable RIE machine condition, the etching time, required to etch through the photonic structures and especially the PhCs holes, had to be tuned every time with strong consequences on the detector functionality. Indeed, finding a balanced etching time, such to preserve high-quality functioning detectors, but at the same time enough to etch all through the PhCs structures, has been a challenge for each fabrication process. Therefore the reproducibility of the LT fabrication process has been limited to few working chips and within a chip limited yield (20%) of fully functional devices has been obtained.

However, it has to be underlined that without the inclusion of PhC structures, the etching times required for other photonic components such RWGs and SNB, are much shorter. Therefore the reproducibility of the LT fabrication process, with high-quality detectors, is guaranteed in this case.

In the second part, the process for the integration of SSPDs on double membrane and doped layers, with electro-mechanically tunable PhC cavities and Stark diodes, has been presented.

Also in this case, even though every step appears perfectly compatible with the integration of the detectors, the results have not been completely positive. SSPDs have been integrated with diodes for QDs tuning and cavity actuation, which have also shown good potential for tunability. However due to the limitation in the etching time, already observed for the single membrane case, the detector functionality at the end of the process has been completely compromised. Indeed until the fabrication obstacles, presented in par. 4.2.4 and 4.2.5, are not understood and solved, the developed processes for the detector integration are not going to guarantee reproducibility and functional components.
In the next two chapters, the working devices, fabricated with the LT fabrication process presented in the first part of this chapter, are going to be characterized in every part of their components.

References

[1] J. Sprengers, A. Gaggero, D. Sahin, S. Jahanmirinejad, G. Frucci, F. Mattioli, R. Leoni, J. Beetz, M. Lermer, M. Kamp, S. Höfling, A. Fiore, "Waveguide superconducting single-photon detectors for integrated quantum photonic circuits", *Applied Physics Letters*, **99** pp. 181110, 2011.

[2] M. Kaniber, F. Flassig, G. Reithmaier, R. Gross, J. J Finley, "Integrated superconducting detectors on semiconductors for quantum optics application", *Applied Physics B*, **22** pp. 1-10, 2016.

[3] W.H.P. Pernice, C. Schuck, O. Minaeva, M. Li, G.N. Goltsman, A.V. Sergienko H.X. Thang, "High-speed and high-efficiency travelling wave single-photon detectors embedded in nanophotonic circuits", *Nature Communications*, **3** pp. 1325, 2012.

[4] M.K. Akhlaghi, E. Schelew, J.F. Young, "Waveguide integrated superconducting single photon detectors implemented as coherent perfect absorbers", *arXiv:1409.1962v1*, 2014.

[5] C. Schuck, W.H.P. Pernice, H.X. Thang, "Waveguide integrated low noise NbTiN nanowire single-photon detectors with milli-Hz dark count rate", *Scientific Reports*, **3** pp. 1893, 2013.

[6] S. Buckley, J. Chiles, A.N. McCaughan, G. Moody, K.L. Silverman, M.J. Stevens, R.P. Mirin, S.W. Nam, J.M. Shainline, "All-silicon light-emitting diodes waveguide-integrated with superconducting single-photon detectors", *Applied Physics Letters*, **111** pp. 141101, 2017.

[7] S. Khasminskaya, F. Pyatkov, K. Słowik, S. Ferrari, O. Kahl, V. Kovalyuk, P. Rath, A. Vetter, F. Hennrich, M.M. Kappes, G. Gol'tsman, A. Korneev, C. Rockstuhl, R. Krupke, W.H.P. Pernice, "Fully integrated quantum photonic circuit with an electrically driven light source", *Nature Photonics*, **10** pp. 727-732, 2016.

[8] P. Ratha, A. Vettera, V. Kovalyuka, S. Ferrari, O. Kahla, C. Nebele, G.N. Gol'tsman, A. Korneev, W.H.P. Pernice, "Travelling-wave single-photon detectors integrated with diamond photonic circuits - Operation at visible and telecom wavelengths with a timing jitter down to 23 ps", *arXiv:1603.01972v1*, 2016.

[9] J. Halbritter, "On the oxidation and on the superconductivity of niobium", *Applied Physics A*, **43** pp. 1-28, 1987.

[10] Y. Qianghua, Y. Guiqin, N. Zhaoyuan, "Effect of Oxygen Plasma on Low Dielectric Constant HSQ (Hydrogensilsesquioxane) Films", *Plasma Science and Technology*, **15** pp. 86-88, 2013.

[11] T. Domínguez Bucio, A.Z. Khokhar, C. Lacava, S. Stankovic, G.Z. Mashanovich, P. Petropoulos, F.Y. Gardes, "Material and optical properties of low-temperature NH_3-free

PECVD SiN_x layers for photonic applications", *Journal of Physics D: Applied Physics* **50** pp. 0250106-0250118, 2017.

[12] K.D. Mackenzie, J.W. Lee, D. Johnson, "Inductively-coupled plasma deposition of low temperature silicon dioxide and silicon nitride films for III-V applications*", Proceeding Symposium 30th State-of-the-Art Program on Compound Semiconductors*, **99** pp. 1-12, 1999.

[13] M. Schaepkens, T.E.F.M. Standaert, N.R. Rueger, P.G. M. Sebel, J.M. Cook, "Study of the SiO_2SiO_2-to-Si_3N_4 etch selectivity mechanism in inductively coupled fluorocarbon plasmas and a comparison with the SiO_2-to-Si mechanism", *Journal of Vacuum Science & Technology A*, **17** pp. 26, 1999.

[14] C. Gatzert, A.W. Blakers, N.K. Deenapanray, D. Macdonald, F.D. Auret, "Investigation of reactive ion etching of dielectrics and Si in CHF_3/O_2 or CHF_3 /Ar for photovoltaic applications", *Journal of Vacuum Science & Technology A*, **24** pp. 1857, 2006.

[15] S. Fattah poor, T. Hoang, L. Midolo, C. Dietrich, L. Li, E. Linfield, J. Schouwenberg, T. Xia, F. Pagliano, F. van Otten, A. Fiore, "Efficient coupling of single photons to ridge-waveguide photonic integrated circuits", *Applied Physics Letters*, **102** pp. 131105–131105, 2013.

[16] T. Watanabe, Y. Yoshida, "Dielectric breakdown of gate insulator due to reactive etching", *Solid State Technology*, **26** pp.263, 1984.

[17] S. Buckley, K. Rivoire, J. Vuckovic, "Engineered Quantum Dot Single Photon Sources", *arXiv:*1210.1234v1, 2012.

[18] P. Lodahl, S. Mahmoodian, S. Stobbe, "Interfacing single photons and single quantum dots with photonic nanostructures", *arXiv:*1312.1079v1, 2016.

[19] T.B. Hoang, J. Beetz, M. Lermer, L. Midolo, M. Kamp, S. Höfling, A. Fiore, "Widely tunable, efficient on-chip single photon sources at telecommunication wavelengths", *Optics Express*, **20** pp. 21758–21765, 2012.

[20] L. Midolo, F. Pagliano, T.B. Hoang, T. Xia, F.W.M. van Otten, L.H. Li, E.H. Linfield, M. Lermer, S. Hofling, A. Fiore, "Spontaneous emission control of single quantum dots by electromechanical tuning of a photonic crystal cavity", *Applied Physics Letters*, **101** pp. 091106, 2012.

[21] M. Petruzzella, T. Xia, F. Pagliano, S. Birindelli, L. Midolo, Z. Zobenica, L.H. Li, E.H. Linfield, A. Fiore, "Fully tuneable, Purcell-enhanced solid-state quantum emitters", *Applied Physics Letters*, **107** pp. 1411109, 2015.

[22] F. Mattioli, R. Leoni, A. Gaggero, M.G. Castellano, P. Carelli, F. Marsili, A. Fiore. "Electrical characterization of superconducting single-photon detectors", *Journal of Applied Physics*, **101** pp. 054302, 2007.

[23] M. Petruzzella “Tunable single-photon sources for integrated quantum photonics”, PhD thesis Chap.7, pp. 119-120, Technische Universiteit Eindhoven, 2017.

Chapter 5

Performance of suspended-nanobeam superconducting single-photon detector

5.1 Introduction

A key component of a quantum integrated photonic circuit is the single-photon detector. Superconducting single photon detectors based on NbN nanowires combine high detection efficiency, low dark count rates, and ultra-fast response, making them promising candidates for QIP [1]. The integration of such detectors into nanophotonic circuits has been proved on different platforms: on GaAs with waveguides [2] and QDs [3], and on Si with waveguides [4] and nanobeam cavities [5].

In this chapter superconducting nanowires integrated on top of suspended nanobeams (SNB SSPD) are presented together with other quantum photonic components such as QD photon sources, PhCs waveguides and cavities. The advantage of positioning the SSPDs on top of a waveguide is not only related to the possibility of integrating them with a photonic circuit, but it also increases the photon absorption. The quantum efficiency of an SSPD is absorption limited on a plain substrate, due to the very thin films. A substrate that presents nanophotonic structures (DBR, waveguides) will significatively increase the probability of photon absorption by the nanowires. For example a waveguide configuration provides above 90% absorption in superconducting wires after a few tens of micrometers [2]. As it will be shown in the following, the field confinement is higher in SNB compared to a RWG. The consequence is that shorter nanowires lengths are sufficient to reach high absorption. This is expected to reduce the role of wire inhomogeneities and increase efficiency. The effect on the field confinement of the SiN layer left on top of the nanowires is also investigated.

The characterization of the integrated SNB SSPDs is presented in the second part of this chapter, with all the main performance`s parameters: efficiency, jitter and dead time.

Finally the characterization of an autocorrelator system and its functionality are demonstrated. Indeed it has been proved[6], that two electrically independent detectors placed on top of the same waveguide probe the same guide mode. This system can be used for autocorrelation measurements. Here the proof that two SSPDs placed on top of a SNB behave as an autocorrelator system is shown.

5.2 Waveguide SSPD design

The chosen design for the detectors on top of a SNB is based on simulations in which the absorptances for nanowires on top of either GaAs waveguides or nanobeams are compared. In the first design (Fig. 5.1 a), an NbN meander (5-nm-thick, 100-nm-wide, and with a 250 nm pitch) was placed on top of a GaAs/$Al_{0.7}Ga_{0.3}As$ waveguide (1.85-µm-wide and 250-nm-deep). The electron beam resist (HSQ) of 100nm thickness is left on top of the nanowires for protection. This resist is a form of amorphous silicon oxide, therefore a 100nm layer of SiO_2 is considered in the simulation.
Using the complex refractive indices of Tab 5.1, a modal absorption coefficient of α_{TE} = 370 cm^{-1}, for the fundamental mode of TE, and α_{TM} = 347 cm^{-1}, for the fundamental mode of TM, are calculated at λ= 1310 nm, by using a finite element mode solver. Those absorption coefficients provide a total absorptance of 84% for TE and 82% for TM for a 50-µm-long waveguide[7] (Fig. 5.3). While the theoretical calculations suggest a high absorptance, the experimental device detection efficiency for this detector's design does not go above 20%[2], indicating that inhomogeneities could play a major role on limiting the detector's efficiency.

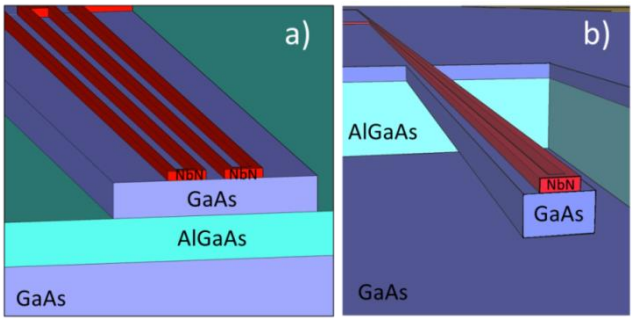

Fig. 5.1 Sketches of NbN superconducting nanowires on top of GaAs/AlGaAs ridge waveguide (a) and on top of suspended nanobeam (b). The NbN nanowires are indicated considering the HSQ mask rather than the thin film for visual clarity.

Therefore, a new design (Fig. 5.1 b), with a NbN meander on top of a GaAs SNB surrounded by air, has been proposed as a possible improvement[7]. As the index contrast between GaAs and the bottom cladding layer is higher as compared to the previous design, the field is pushed towards the top GaAs/NbN interface and the absorptance is improved. For the simulation, a NbN meander (5-nm-thick, 100-nm-wide nanowire with a 260 nm pitch), covered with 100nm thick SiO_2, on top of a 1-µm-wide and 320-nm-thick SNB, is considered. The dimensions of the SNB are chosen by considering those factors: the influence of the thickness on the supported guided modes, a width that would allow some space for alignment tolerance in the patterning of the wires on the SNB, while maintaining a good field confinement. Particularly regarding the thickness has been

observed[7] that for thinner waveguide (250nm) the quasi-TM mode presents a complex distribution of the electric field and as consequence the SSPDs have been observed to be polarization dependent. For a thickness of 350nm instead the complex distribution for the quasi-TM mode disappears and a polarization independent behaviour is observed. Moreover the coupling between the guided modes of the RWG and the SNB through a tapering adiabatic transition (Chap 6.1) have been simulated and optimized for a nanobeam thickness of 320nm[8].

Considering those nanobeam dimensions and using the complex index values in Tab. 5.1, the modal absorption coefficients for TE and TM polarizations at 1310nm are respectively α_{TE} = 847 cm^{-1} and α_{TM} = 2581 cm^{-1}. With those coefficients, 90% of the input light will be absorbed by the nanowires in a 15µm long nanobeam for TE polarization and 6µm long one for TM polarization (Fig 5.3). Neglecting the small perturbation to the guided mode produced by the NbN wires, the continuity conditions at the interface between the waveguide and the media above (SiO_2 wires + air) has as consequence an increase of the field for the TM mode in the top SiO_2 layer (Fig. 5.2 c). The higher field is also sensed by the NbN wires and this explains the big difference between the absorption coefficients for the TE and TM modes.

Medium	NbN	GaAs	AlGaAs	SiO_2	Si_3N_4
ñ (nm)	4.35 – i4.65	3.39	3.07	1.46	2.00

Tab. 5.1 Complex reflective indexes at λ=1310nm for all the media used for the simulations.

As already explained in Chap.4.2.7, at the end of the fabrication process, the residual SiN is not removed from the chip, in order not to damage the NbN nanowires. A residual layer of around 50nm is left on top and its effect on the field confinement has to be taken into account during the simulations. Using again the refractive indexes of Tab. 5.1, the absorption coefficients α_{TE} = 1166 cm^{-1} and α_{TM} = 1399 cm^{-1} are found for λ= 1310 nm. Differently than the previous case (without the SiN layer), in this one, the difference between the two polarizations is minor. Also in this condition there is an increase of the field for the TM mode at the interface between waveguide and SiN layer (Fig. 5.2 d). However, the refractive index contrast between the GaAs and the media above it is smaller in the case with the SiN layer. The impedance mismatch at the interface is smaller and so the field. Therefore the difference between the absorption coefficients for the TE and TM modes is much smaller compared to the case without SiN.

Indeed, in this case with the SiN layer, a 10µm long nanobeam is enough to guarantee, that 90% of the input light is absorbed regardless of the considered polarization (Fig. 5.3). In par.5.3.3 will be shown the dependence of the fabricated SNB SSPD efficiency on the input light polarization, but according to simulation they should present nearly polarization-independent behaviour. So after all, the SiN layer, included only to solve a

technological problem, shows also a useful purpose in terms of polarization and absorptance.

Actually it has to be underlined, that in terms of integration with the QD sources, only the fundamental TE mode has to be considered. But a polarization-independent device's behaviour will help to validate the result found in Chap. 6.3.3 regarding the interaction between SSPDs and PhCs filters.

The calculated electric field for the TE and TM mode is shown in Fig.5.2 for the case without (a,c) and with (b,d) 50nm thick SiN layer left on top of the nanowires.

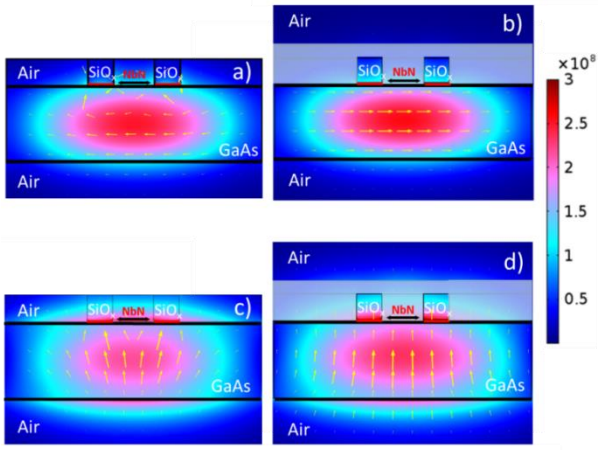

Fig. 5.2 Simulated electric field distribution of the TE mode (a,b) and TM mode (c,d) for NbN nanowires on top of SNB in the case without (a,c) and with (b,d) a cover layer of 50nm of SiN.

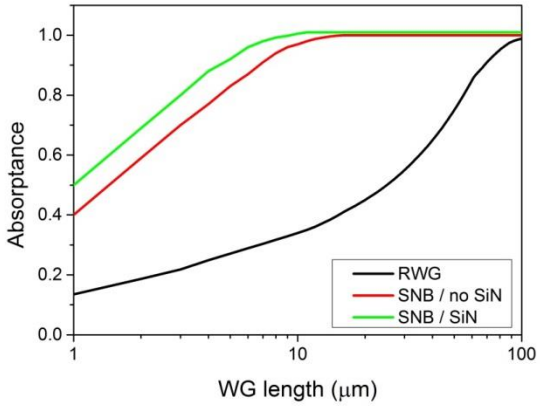

Fig. 5.3 Simulated absorptance of TE polarizated light at $\lambda = 1310$nm in function of the waveguide length. The three cases of: ridge waveguide (black), suspended nanobeam without SiN layer on top (red) and suspended nanobeam with SiN layer on top (green) are compared.

The absorptance of the fundamental TE mode in function of the waveguide length is presented in Fig. 5.3 for the three considered case: ridge waveguide, suspended nanobeam without SiN layer and suspended nanobeam with SiN layer. Clearly the design on suspended nanobeam with SiN layer is the one that guarantee the highest absorptance for short waveguide lengths. The use of shorter waveguides (10μm) and therefore nanowires (20μm) is expected to help to reduce the effect of film inhomogeneities and so increase the internal quantum efficiency η_i.

5.3 Performances

The integrated SNB SSPDs (Fig. 5.4), obtained using the fabrication process described in Chap 4.2.2, are here characterized.

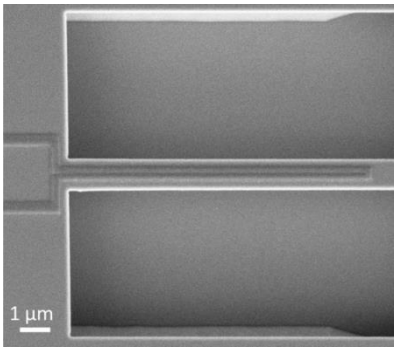

Fig. 5.4 SEM picture of a SSPD nanowire patterned on top of a SNB

The experimental setup used for the characterization has been the one described in Chap. 2.4.2. After an electrical pre-characterization made in the setup of Chap. 2.4.3, the chip is cleaved, so that only the SSPDs showing the highest I_c are going to be optically characterized. Indeed in this setup no more than 4-5 devices per time can be characterized, due to the reduced movement of the piezo and short length of the μ-probes arm. For the optical characterization of a single SNB SSPD, the configuration inside the cryostat is the one with one μ-probe and one lensed fibre at an angle of 90°. The μ-probe is connected to the control box and from there to the counter. The data from the counter are directly processed through a LabVIEW software. The laser light at 1310nm is coupled through the polarization-maintaining lensed fibre (nominal spot of 2.0±0.5μm) into the waveguides. A free-space setup, consisting of two mirrors, a half-wave plate and fibre-couplers, is used to control the polarization between the CW laser and the lensed fibre.
The measured performance`s parameters, defined in Chap 1.4.2 , are discussed in the following.

5.3.1 DQE and dark counts

The quality of an SSPD can be quickly judged by its I-V characteristic. As explained in Chap. 4.4, while the yield on a chip with tens of SSPDs is around 90%, before the integration with the other nano-photonics components, afterwards it drastically drops at 20% or even less. In the electrical pre-characterization only the devices showing a characteristic similar to the one of inset of Fig.5.5 are considered for the next step of optical characterization. In this particular device, with a 20-µm-long wire, the critical current is 8 µA.

For the optical characterization the procedure described at the end of Chap. 2.4.3 has been used, in order to optimally align the lensed fibre to the waveguide. However it has been observed, that the signal of the on-chip SSPDs is much stronger compared to the µ-PL signal collected in the external spectrometer (see Chap.6.3.3). Therefore a more precise alignment has been performed moving slowly the fibre until the SSPD counts rate was maximized.

The laser power has been constantly monitored, in order to guarantee single-photon regime operation. Fig. 5.5 shows the count rate in function of the laser power, a power law dependence of the kind $C \sim P^m$ is found as expected[9]. From the slope of the curves a value m=0.97 is found, proving the single-photon regime.

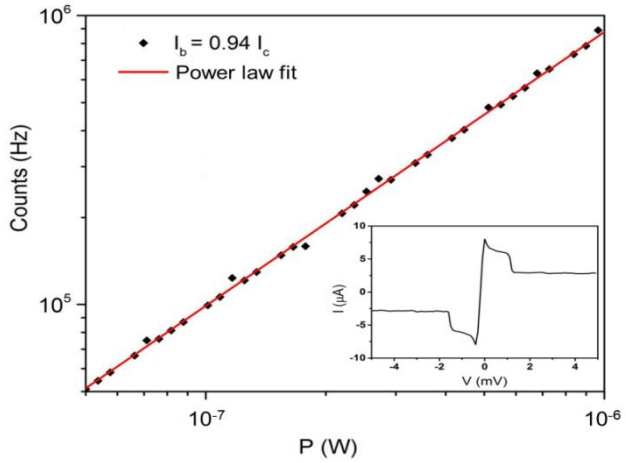

Fig.5.5 Counts with bias $I_b = 0.94\ I_c$ in function of the light power. The red line show the fit with slope m=0.97. Inset: I-V characteristic of a functioning SSPD (optical characteristic shown in the next Fig.)

The device quantum efficiency (DQE) for TE polarization is plotted in red of Fig. 5.6 as a function of the normalized bias current I_b/I_c, and it is defined as the number of counts minus the dark counts (in black) divided by the number of photons coupled to the waveguide. We note that the dark counts shown in Fig. 5.6 have been measured in a cryostat with an optical window. They are therefore mostly produced by the absorption of

infrared thermal photons and not indicative of the detector's performance in an optimized environment.

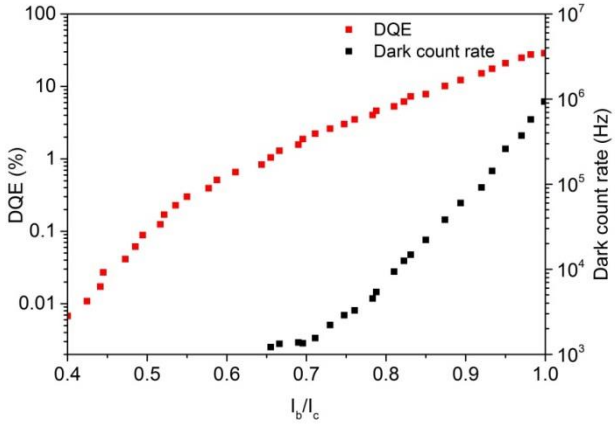

Fig.5.6 Device quantum efficiency (DQE) (red) of a 20 µm-long SSPD on top of SNB under TE polarized light at 1300 nm, and dark count rate (black) as a function of the normalized bias current.

The number of photons coupled into the system RWG-adiabatic tapering-SNB is determined by transmission measurements. The transmission is measured on a sample, covered with 50nm of SiN, in which the SNB (width 1µm, length 10µm) is coupled on both sides to RWG (width 5µm, length 1000µm) through tapering (width from 1 to 5µm, length 20µm). The experiment is performed at room temperature, with a configuration of the piezo stages in which the lensed fibres face each other. A tunable continuous wave laser is sent into one fibre and the transmission through the RWG-SNB-RWG system collected through the other fibre, then sent to the power-meter. The plot of the transmission as function of the wavelength is shown in Fig. 5.7, where the Fabry-Perot (FP) fringes due to the reflections at the two cleaved facets are evident. The period of the fringes can be calculated as $\Delta\lambda = \lambda^2/(2n_gL)$ where λ is the wavelength, n_g the effective group index of the RGW mode and L the length of the RWG. Considering $n_g \approx n_{eff} = 3.193$, extracted from the simulated fundamental TE mode, and L = 1030±20µm, the calculated fringe period is $\Delta\lambda = 0.16$nm. However from Fig. 5.7 is observed a period of ~0.13nm, the difference is attributed to uncertainty in the simulated index value.

From the FP fringes and particularly from the maximum and minimum transmission in TE polarization, the propagation loss over a 1 mm waveguide length is deduced using the equation[10]:

$$\alpha = \frac{-1}{L}\ln\left(\frac{1}{R}\frac{T+1}{T-1}\right) \qquad (5.1)$$

R is the reflectance at the facet and calculated by numerical simulations has a value around 0.27[8], and

$$T = \sqrt{\frac{T_{max}}{T_{min}}} \qquad (5.2)$$

is the visibility. The calculated value of the loss for unit length is $\alpha \approx 5$ cm^{-1}. Assuming symmetric input/output coupling and using the expression for the FP transmission[10]

$$\eta_C e^{-\alpha L/2} = \frac{2\sqrt{T_{max}T_{min}}}{\sqrt{T_{max}} + \sqrt{T_{min}}} \qquad (5.3)$$

the coupling efficiency is derived: η_C = 2.3%. Another way to calculate the coupling efficiency is using the spectrally averaged transmission (red line Fig. 5.7). From this calculation $\bar{T}$ = 0.065±0.001%, meaning that the coupling efficiency from the fibre to the centre of the nanobeam is $\eta_C = \sqrt{\bar{T}} = 2.5 \pm 0.3\%$, including the loss. The two values are in close agreement and the value η_C = 2.4% is used in the following.

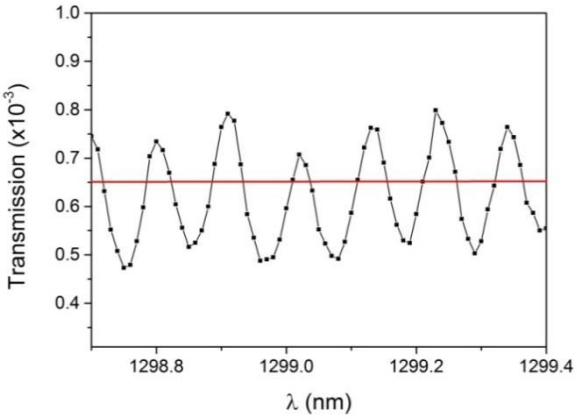

Fig. 5.7 Experimental trasmission of the system RWG-tapering-SNB in function of the excitation wavelength. The red line is the spectrally averaged trasmission.

Finally taking this η_c into account, the maximum value obtained for the DQE is ~28%. While the coupling efficiency is relatively low, due to the unoptimized modal matching between the lensed fibre and the waveguide, the DQE is the relevant figure of merit for integrated experiments where the photons are produced within the chip.

This kind of optical characterization has been performed on 5 different devices showing similar value of I_c. The average of the maximum DQE over the considered devices is 28% with a standard deviation of 2%. Indeed the yield of efficient devices can be considered

very high (above 90%) whenever the value of I_c ~ 8μA. However, as already mentioned, the yield of devices with good I_c drops to less than 20%, after the integration process with the nano-photonics components.
In conclusion this DQE value represents a record for waveguide SSPDs on the GaAs platform. The SNB SSPDs provide higher efficiency than RWG SSPDs in a smaller footprint. Moreover their reduced cross-section and higher mode confinement makes them suitable for integration with suspended PhC structures.
However this DQE is still lower than the calculated absorptance. Assuming that the simulations on the absorptance are correct, this DQE result implies that significantly shortening the length did not help as much as expected in term of internal quantum efficiency. Indeed, it has been observed[11], that the η_i dependence on the nanowire length tends to saturate for lengths much longer than 100nm. Therefore, even with a difference in the nanowires length of an order of magnitude (20μm rather than 200μm), the considered lengths range is still far away from the one in which a strong effect on η_i is expected.

5.3.2 Dead time and jitter

As already discussed in Chap.1.4.1, to quantify the speed of the device it is necessary to estimate the time constant (τ_e) of the exponential decay of the output voltage pulse. Indeed the decay part τ_e of the pulse corresponds to the recovery of the current in the nanowire. The dead time, during which the device is blind to photon arrival, can be estimated as $\tau_D = 3\ \tau_e$. Moreover τ_e can be used for an estimation of the kinetic inductance L_k using the equation $\tau_e = L_k/R_L$. As already mentioned in Chap. 3.4.4, the external load resistance R_L is equal to 50Ω and a kinetic inductance of 90 pH/□ is expected.
Fig. 5.8 a) shows a typical voltage response of an SSPD after amplification measured with the digital oscilloscope (LeCroy Waveace 234). The features present in the tail of the pulse are caused by reflections, probably due to a small mismatch in the nominal 50Ω load resistance. From the fittings of the pulse of Fig. 5.8 a) it is possible to derive a pulse duration of 3.4ns (FWHM) and a decay time of 2.8ns (τ_e). From this value of τ_e, a wire kinetic inductance of L_k = 150nH is derived, and considering a design with 1600□, an excellent agreement with the expected value of 144nH is found.
Finally the estimated dead time $\tau_D = 3\tau_e$ = 8.4ns implies a frequency $f = 1 / \tau_D$ = 119 MHz, that quantify the maximum counting rate.
The timing accuracy of registering a photon is the jitter (Chap.1.4.2). The jitter of a detector can be determined illuminating the detector with a pulsed laser (λ = 965 nm, 100 ps pulse width) and sending the output pulse to a correlation card, together with the laser trigger signal to record the coincidences counts.
Fig. 5.8 b) shows the coincidence peak using a bias current of 94% I_c. The fit with a Gaussian distribution gives FWHM = 127±8 ps. Indeed the jitter is the convolution of all the jitters in the measurement set-up. While the one of the correlation card is completely negligible, the laser pulse width (100ps) is comparable with the measured total jitter. This

means that it is not possible to establish a definitive value for the intrinsic detector jitter, because it is limited by the laser jitter. However considering that commonly SSPDs have jitter < 60ps[1], the total jitter value is indeed within the order of magnitude for what expected in a standard SSPD.
Low jitter is a fundamental requirement for time-correlated single-photon counting experiment since the temporal resolution is determined by this value. The QD carrier lifetime is of the order of 1 ns, much longer than the calculated total jitter, so correlation measurements are not going to be significantly affected by the detector jitter (see Chap. 6.3.1).
The fast response (few ns) and low jitter (<60ps) are maybe the most important characteristics, that distinguish the SSPDs from other types of single-photon detectors working in the near-infrared, and makes them very appealing for high-speed quantum photonic information processing.

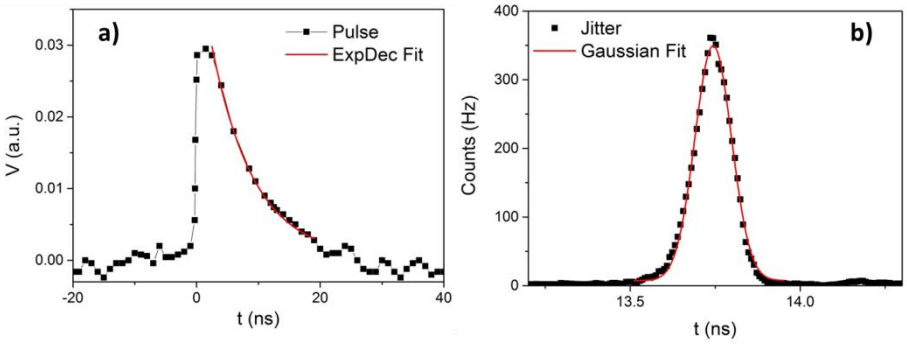

Fig. 5.8 a) Output pulse after 48dB amplification, the red line indicate the exponential decay fit. b) Histogram of the jitter time of the detector biased 94% Ic, the red line indicate the gaussian fit.

5.3.3 Polarization dependence

From the simulation shown above (par. 5.2), the SNB SSPDs covered with the SiN layer should not present a polarization-dependence. Indeed, for a nanowire length l = 20μm and λ= 1310 nm, the two polarization modes have very similar absorptance, above the 90%.
However this does not necessarily means that the DQE of the two modes have to be similar. One example of that has been presented in ref.[7], where despite very similar absorptance a DQE reduction of the TM mode of more than three times compared to the DQE of the TE mode was reported. The reasons for a polarization dependence could be related to a poor coupling, meaning that a design change could solve the problem. However the simulation images of Fig. 5.2 present a well confined field and also a good uniformity of the field polarization over the cross-section, especially in the case with SiN on top, making them promising for polarization independency.

Measurements of SQE in TE and TM polarization have been performed on the same device as Fig. 5.6 and are shown in Fig. 5.9.
Clearly the difference between the two polarizations is very small, although the maximum SQE value for TM reaches 0.75% while the one for TE it is 0.67%. This small difference could be related to the slightly higher absorption coefficient for TM, but could also be only a statistical fluctuation. Indeed an estimation of the error on the SQE of a single device is not reliable, especially considering the points at higher I_b/I_c where the contribution of dark counts is the most significant.
However from Fig. 5.9, it can be fairly concluded that for this particular design of SNB SSPD there is no significant dependence on polarization.

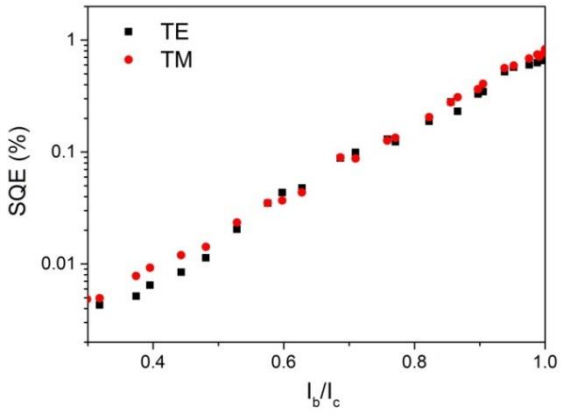

Fig. 5.9 System quantum efficiency of a 20 µm-long SSPD on top of SNB with cover layer of SiN under illumination at 1300 nm, in the case of TE (black) and TM (red) polarization, as a function of the normalized bias current.

5.4 Autocorrelators

5.4.1 Introduction

As already mentioned in Chap.1.5, the objective of this experimental work is to create a multi-functional quantum photonic integrated circuit. The measurement of the second-order correlation function $g^{(2)}(\tau)$ is a key functionality for a QPIC, since it allows the characterization of single- and entangled- photon states[12]. The second-order autocorrelation
function is usually measured in free space or fibre-optics with a Hanbury-Brown and Twiss (HBT) interferometer[13]. Fig. 5.10 shows the configuration of a free-space HBT interferometer for the characterisation of a single-photon source that is based on a 50:50

beamsplitter and two distinct detectors on the two output arms. $g^{(2)}(\tau)$ is measured by combining the electrical output of the two detectors in a correlation card.
A novel configuration of SSPDs has been introduced[6], in order to realize a similar functionality in an integrated platform. This configuration is based on two electrically independent SSPDs patterned on top of ridge waveguides. These devices are called integrated autocorrelators and enable the measurement of $g^{(2)}(\tau)$ in a compact integrated system.

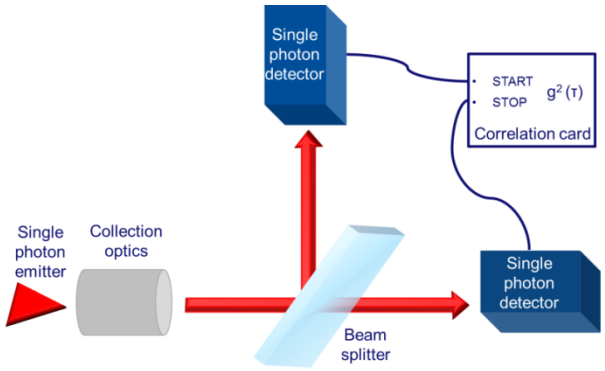

Fig. 5.10 Sketch of a free space HBT interferometer used to measure $g^2(\tau)$

Two different approaches have been pursued to realize the integrated autocorrelator system.
A first design (Fig. 5.11 a), exactly replicating the HBT interferometer in free space, in which the two SSPDs are patterned on each output arm of a multi-mode interference coupler (MMI), where the MMI is optimised for 50:50 splitting ratio, in order to operate as a 50:50 beamsplitter. A second design (Fig. 5.11 b), that simplifies and compacts even more the system, uses two SSPDs defined on a single waveguide and therefore sensing the same waveguide mode.

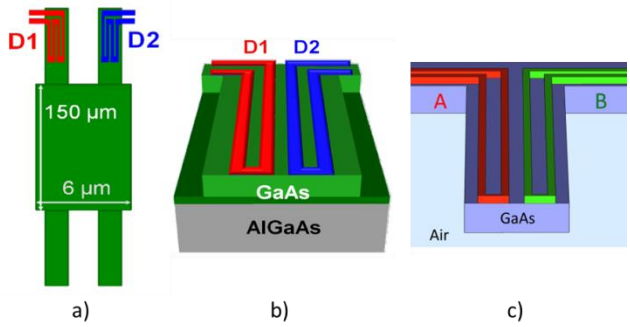

Fig. 5.11 Sketch of integrated autocorrelators systems. a) the two SSPDs are on two different arms and connected to a MMI acting as 50:50 beam splitter[6] b) the two SSPDs are on top of the same RWG[6] c) the two SSPDs are on top of the SNB.

The autocorrelator functionality of both designs has been proved[6], however the second design (waveguide autocorrelators) is more promising in term of integration in a QPIC, due to its very simple and compact structure. Following the waveguide autocorrelators design, in this work two electrically independent SSPDs have been patterned on top of the same SNB (Fig. 5.11 c).

5.4.2 Design and setup configuration

The nanowires design follows exactly the one used for a single nanowire on SNB (par. 5.2). The distance between the two independent nanowires is equal to the pitch (260nm) and the SNB has been enlarged by 0.5µm for a total width of 1.5µm. The SNB is directly tapered to a RWG, rather than going through a PhCs cavity as for the devices of the Chap 6.
The SNB autocorrelators (Fig. 5.12) have been fabricated following the same fabrication process described in Chap 4.2.2., and characterized.

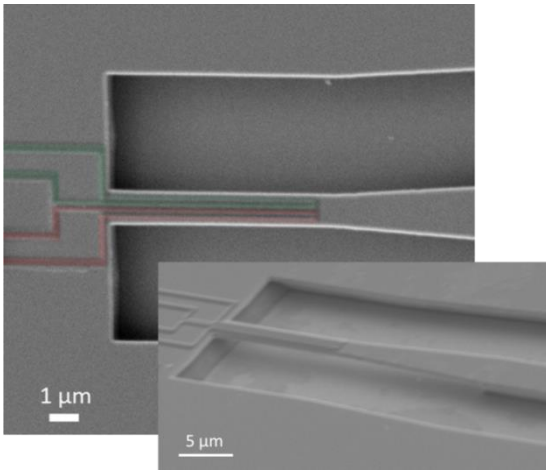

Fig. 5.12 SEM picture of a SNB autocorrelator. The two different colours underline the nanowires of the two electrically independent SSPDs. Inset: cross-section SEM picture of the same device.

As for the SNB SSPD, an electrical pre-characterization has been made in the setup of Chap. 2.4.1 and an optical characterization in the setup of Chap. 2.4.2. For this experiment the configuration inside the cryostat is the one with two µ-probes facing each other, one for every SSPD of the set composing an autocorrelator, and one lensed fibre at an angle of 90°.The signal of the two µ-probes is sent to the control box. This box presents two independent input/output channels and for each one is possible to control the bias current on the corresponding wire. The signals of the two output channels are sent either to a counter for efficiency measurements or to the correlation card for the autocorrelation

measurements and processed through LabVIEW software. It is important to notice, that in order to perform the autocorrelation measurements, a coaxial cable between the output of the amplifier and the correlation card, with a known time delay, has been used. The laser light, either CW at 1310nm or pulsed at 965nm, is coupled through the polarization-maintaining lensed fibre into the waveguides. The free-space setup, described previously, is used to control the polarization.
The performance of the two independent detectors composing an autocorrelators is shown in the following. Afterwards, the characterization of a possible crosstalk between the two components is presented. Finally the proof of principle of the autocorrelator functionality is demonstrated.

5.4.3 Single device performance

The detectors are first characterised in terms of their current-voltage characteristic curves. The IV curves of two detectors forming a SNB autocorrelator are shown in the inset of Fig. 5.13. The two detectors show similar IV behaviour, although a difference of 2.7µA in terms of critical current (I_c^A=13.9µA, I_c^B=11.2µA) is observed. Such difference in I_c of two nominally identical detectors is another indication that, for 20-µm-long wires, the inhomogeneities still play a role.

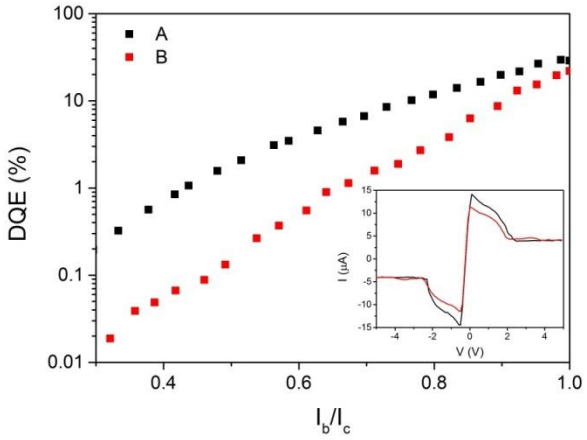

Fig. 5.13 Device quantum efficiency (DQE) of the two SSPDs (A in black and B in red) of an autocorrelator device on top of a SNB under illumination at 1300 nm, as a function of the normalized bias current. Inset: IV characteristics of A in black and B in red.

Fig. 5.13 shows the device quantum efficiency of both detectors measured using a CW laser at 1310 nm in the TE polarization. As expected, the difference in I_c between the two detectors has an impact also on the DQE. Indeed detector A, that presents higher I_c, also has higher DQE compared to detector B. The maximum values of DQE are respectively

27% for A and 23% for B. Those values have been derived by dividing the number of counts (after subtracting the dark counts) by the number of photons coupled to the waveguide, taking into account the measured coupling efficiency $\eta_c = 2.4\%$.
This difference in DQE between the two detectors is considered during the $g^{(2)}(\tau)$ measurements. Indeed the bias current, for each one of the two detectors, has been chosen such that both of them had comparable values of DQE.

5.4.4 Crosstalk

The close packing of the nanowires could in principle produce electrical, magnetic, or thermal coupling between the two detectors[14]. That potentially leads to either a false detection or a decreased detection probability in one wire after the other has fired. Such coupling, referred to as crosstalk, would introduce spurious correlations at and around zero delays and affect the measurement of the second-order correlation function.
Two different tests are performed in order to investigate the possible crosstalk between two adjacent detectors on a SNB. A first series of tests is performed in static conditions, to determine whether the bias condition of one detector has an influence on the electrical response of the other. The second series is in dynamic conditions in order to investigate any temporal variation of the detection probability of one detector due to the firing of the other detector. The dynamic crosstalk is measured through the analysis of the $g^{(2)}(\tau)$ of a pulsed laser coupled to the waveguide.
This experiment establishes also the proof of principle that the SNB autocorrelator system is suitable for on-chip $g^{(2)}(\tau)$ measurements.
In the following, the absence of any crosstalk, either static or dynamic, between the two detectors, is proved.

Static

To study the static crosstalk the electrical response of one detector is studied as a function of the bias of the adjacent detector. Fig. 5.14 shows the I-V characteristic of one detector (A) when the other one (B) is biased above the I_c or when it is not biased at all, and vice versa. Biasing the other detector in the resistive region is a stringent test to prove the absence of static crosstalk. Indeed, the heat dissipated due to Joule effect could thermally affect the other detector. For example in sapphire a 10 % decrease in the critical current of one detector has been observed, whenever the other one was in its resistive state[14]. This effect is not present in this case, as can be seen in Fig. 5.14. Indeed the I-V curves are completely superposed in every electrical regime of the devices. The difference between the behaviour of the two substrates could be related to the higher thermal conductivity of GaAs with respect to sapphire, leading to an efficient heat transport to the substrate.
In conclusion no static coupling between the SNB SSPDs is evidenced in this measurement.

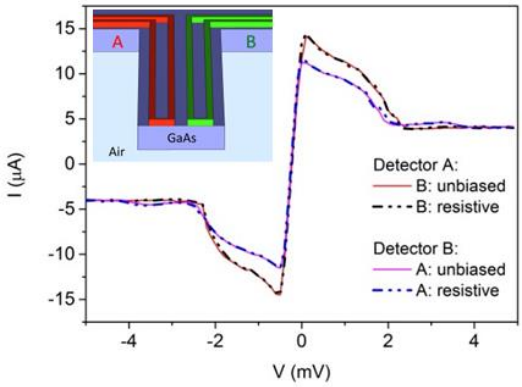

Fig. 5.14 IV curve of Detector A while Detector B is unbiased or in resistive state; IV curve of Detector B while Detector A is unbiased or in resistive state. Inset: sketch of the two independent SSPDs on top of SNB.

Dynamic

The idea behind this test on the dynamic crosstalk is the following. Since a coherent beam has a constant $g^{(2)}(\tau)$, if the probability to click, after a detection event on the other wire, was increased or decreased, $g^{(2)}(\tau)$ would show a peak or a dip at $\tau = 0$.

The expected time range for crosstalk is within a few ns delay because the relevant timescales are the recovery time of the detector (few ns), the electromagnetic wave travelling time along the waveguide (<1 ps) and the propagation time of phonons across the detector and between the two nanowires components of the autocorrelator (up to a few ps). The zero delay has been calibrated in a different experiment with a single-photon source and using the same delay line.

The test on the dynamic crosstalk has been realized measuring the intensity correlation function $g^{(2)}(\tau)$ of a pulsed laser (λ = 965 nm, 80 MHz repetition rate) coupled to the waveguide. As mentioned before the detectors were biased such to have similar values of DQE in the chosen working region, in particular $I_b^A = 0.86\ I_c$ and $I_b^B = 0.92\ I_c$.

In Fig. 5.15, the coincidence counts are shown as a function of the delay time between the start and stop channels, and as expected coincidences are observed only at delays multiple of the repetition period of the laser (12.5 ns). The coincidence counts are normalized to the average of the peak's maximum presented in Fig. 5.15 and show a standard deviation of 0.03 due to statistical fluctuation. Considering that the peak at zero delay has 1.00 normalized coincidences, it is fair to conclude that no dynamic crosstalk was observed, within the error margin related to the observed standard deviation.

Moreover it has been proved as the autocorrelator system on top of a SNB can be used for on-chip $g^{(2)}(\tau)$ measurements, with a limitation in time resolution related to detector`s jitter. This value, as shown in par.5.3.2, is well below the ns scale, meaning that this

autocorrelator system could be used for on-chip characterization of single-photon emitters (decay time of ns).

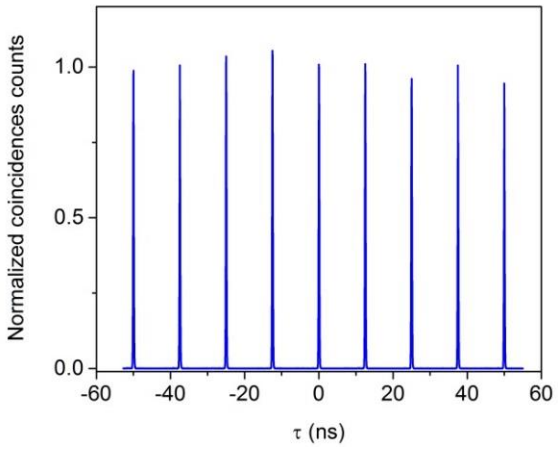

Fig. 5.15 Coincidence rate of the SNB autocorrelator system under illumination with 80MHz pulsed laser at 965nm.

5.5 Conclusion

It has been shown that the low-temperature fabrication process (Chap.4), developed in order to integrate single-photon sources and detectors on a GaAs platform, enables the fabrication of high performance SNB SSPDs. In particular they present maximum DQE = 28% at λ=1310nm in TE polarization, dead time τ_D = 9ns and jitter = 127±8ps.

The simulation of the electric field mode guided inside the SNB has shown the possibility to use shorter wires (20μm instead of 200μm long) preserving high absorptance (90%) and so reducing the inhomogeneities problem. The DQE = 28% is still lower than anticipated, considering the reduction of the nanowires length. However, even if the experimental DQE did not improve as much as estimated, a new record for the DQE on GaAs platform has been established. Moreover from the simulation of the TE and TM modes, a polarization-independent behaviour of the SNB SSPDs was expected and it has been experimentally confirmed.

A SNB autocorrelator system, composed of two electrically-independent SSPDs on top of a suspended nanobeam, has been realized and characterized. The system did not present any static or dynamic crosstalk, allowing the demonstration of the proof of principle that is it possible to perform an HBT experiment on chip. This result, combined with a jitter of the order of tens ps, shows how the SNB autocorrelator system is suitable for completely on chip characterization of single-photon emitters.

References

[1] C.M. Natarajan, M.G. Tanner, R.H. Hadfield, “Superconducting nanowire single-photon detectors: Physics and applications.”, *Superconductor science and Technology*, **25** pp. 063001, 2012.

[2] J. Sprengers, A. Gaggero, D. Sahin, S. Jahanmirinejad, G. Frucci, F. Mattioli, R. Leoni, J. Beetz, M. Lermer, M. Kamp, S. Hofling, A. Fiore, “Waveguide superconducting single-photon detectors for integrated quantum photonic circuits”, *Applied Physics Letters*, **99** pp. 181110, 2011.

[3] M. Kaniber, F. Flassig, G. Reithmaier, R. Gross, J.J. Finley, “Integrated superconducting detectors on semiconductors for quantum optics application”, *Applied Physics B*, **22** pp. 1–10, 2016.

[4] W.H.P. Pernice, C. Schuck, O. Minaeva, M. Li, G.N. Goltsman, A.V. Sergienko, H.X. Than, “High-speed and high-efficiency travelling wave single-photon detectors embedded in nanophotonic circuits”, *Nature Communications*, **3** pp. 1325, 2012.

[5] M.K. Akhlaghi E. Schelew, J.F. Young, “Waveguide integrated superconducting single photon detectors implemented as coherent perfect absorbers”, *Nature Communications*, **6** pp. 8233, 2015.

[6] D. Sahin, A. Gaggero, T. Ba Hoang, G. Frucci, F. Mattioli, R. Leoni, J. Beetz, M. Lermer, M. Kamp, S. Höfling, A. Fiore, “Integrated autocorrelator based on superconducting nanowires”, *Optics Express*, **21** pp. 11162–11170, 2013.

[7] D. Sahin, A. Gaggero, J.W. Weber, I. Agafonov, M. A. Verheijen, F. Mattioli, J. Beetz, M. Kamp, S. Höfling, M.C.M. van de Sanden, R. Leoni, A. Fiore, “Waveguide nanowire superconducting single-photon detectors fabricated on GaAs and the study of their optical properties”, *IEEE Journal of Selected Topics in Quantum Electronics*, **2** pp. 1-10, 2015.

[8] S. Fattah poor, T. Hoang, L. Midolo, C. Dietrich, L. Li, E. Linfield, J. Schouwenberg, T. Xia, F. Pagliano, F. van Otten, A. Fiore, “Efficient coupling of single photons to ridge-waveguide photonic integrated circuits”, *Applied Physics Letters*, **102** pp. 131105–131105, 2013.

[9] **A**. Verevkin, J. Zhang, R. Sobolewski, A. Lipatov, O. Okunev, G. Chulkova, A. Korneev, K. Smirnov, G.N. Gol`tsman, **“**Detection efficiency of large-active-area NbN single-photon superconducting detectors in the ultraviolet to near-infrared range”, *Applied Physics Letters*, **80** pp. 4687, 2002

[10] A. De Rossi, V. Ortiz, M. Calligaro, L. Lanco, S. Ducci, V. Berger, I. Sagnes, “Measuring propagation loss in a multimode semiconductor waveguide”, *Journal of Applied Physics*, **97** pp. 073105, 2005.

[11] R. Gaudio, K.P.M. op`t Hoog, Z. Zhou, D.Sahin and A. Fiore, “Inhomogeneous critical current in nanowire superconducting single-photon detectors”, *Applied Physics Letters*, **105** pp. 222602, 2014.

[12] A. J. Shields, “Semiconductor quantum light sources”, *Nature Photonics*, **4** pp. 215-223, 2007.

[13] R.H. Brown and R. Twiss, “A test of a new type of stellar interferometer on sirius”, *Nature*, **4541** pp. 1046–1048, 1956.

[14] E.A. Dauler, B.S. Robinson, A.J. Kerman, J.K. Yang, E. Rosfjord, V. Anant, B. Voronov, G. Gol’tsman, K.K. Berggren, “Multi-element superconducting nanowire single-photon detector”, *IEEE Transactions on Applied Superconductivity*, **17** pp. 279–284, 2007.

Chapter 6

Performance of the quantum photonic components

6.1 Introduction

As already discussed in Chap.1.5, a prototype architecture of a quantum photonic integrated circuit on GaAs platform is presented in this work. The integrated circuit consists of InAs QDs, photonic crystal waveguides and cavities, and SSPDs patterned on top of suspended nanobeams (Fig.6.1).
The advantages of using SSPDs over other kinds of single-photon detectors have already been discussed in the previous chapter (Chap.5.5).
This chapter, instead, starts with a focus on the photonic crystal units of the proposed QPIC. The addition of PhCCs and PhCWGs is required in order to filter the emission from one or several QDs, so that single photons originating from a single excitonic line are funnelled to the circuit and then measured. Photonic crystals are one of the best candidates for the control of the emission from single-photon emitters and realization of processing units in a QPIC, but they typically suffer from high propagation losses.
For the successful realization of the QPIC efficient coupling of light into the circuit and among its different units is required. For this reason the coupling between PhC structures and conventional low-loss waveguides has been realized employing an adiabatic taper[1]. Direct coupling of the two structures will result in considerable loss due to scattering and reflection at the interface. This is due to the spatial mode profile mismatch related to the difference in the width. In order to reduce this mismatch and consequently the losses, a design based on the adiabatic theorem[2] has been proposed. The theorem states that a system remains in its eigenstate in the presence of a perturbation only if the perturbation is introduced gradually. Based on this strategy the width of the nanobeam is gradually increased along the propagation direction until it reaches the same width of the RWG (Fig. 6.1 inset) After a critical width of 1.65µm, a supporting post of AlGaAs is created to sustain the membrane and the width of the trapezoidal AlGaAs pedestal increase accordingly to the width of the taper (see Chap.4.2.6 for the fabrication details). The longer the taper, the lower the losses associated to the transition. However the taper cannot be arbitrary long, due to the presence of buckling, as observed for structures longer

than 10µm. In this work a linear taper of a length L = 8µm and angle θ = 6.7° has been employed.
At the beginning of this chapter different designs of PhCCs are compared in order to select the one that presents the best filtering. Afterwards the cavities fabricated following the selected designs are tested and the one that shows better performance chosen as part of the QPIC.
In the second part of this chapter, the QPIC, realized following the low-temperature fabrication process (Chap.4.2.2) and including all the optimized devices, is tested in terms of functionality and interactions between the different components.

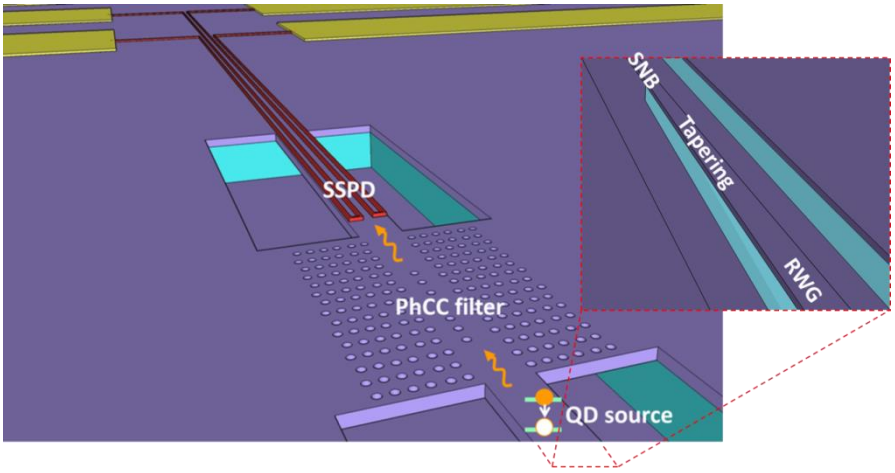

Fig. 6.1 Sketch of the proposed approach for the QPIC. Single photons are produced via spontaneous emission of excitons in QDs, efficiently funnelled in waveguides, filtered by a PhCC and detected by waveguide SSPDs. Inset: sketch of the adiabatic taper used as interface between the SNB and the RWG.

6.2 Filters

In order to detect single-photon emission from QDs, a single excitonic line must be filtered out of the complex emission spectrum of one or more QDs.
A coupled PhCC-PhCWG system has been theoretically and experimentally investigated and proposed as a system capable of realizing the filtering functionality[3,4]. Basically when the wavelength of the input light matches the wavelength of the cavity, light can pass through the cavity by resonant tunnelling.
The performance of this filter can be described by coupled-mode theory[5]. The coupling of the cavity to the PhCWG and to the leaky radiation modes can be characterized by quality-factors Q_{WG} and Q_R , where the total quality factor Q_T is obtained as

$$\frac{1}{Q_T} = \frac{1}{Q_{WG}} + \frac{1}{Q_R} \qquad (6.1)$$

and the transmission is calculated as

$$T = \left(\frac{Q_T}{Q_{WG}}\right)^2 = \left(\frac{1}{1 + {Q_{WG}}/{Q_R}}\right)^2 \qquad (6.2)$$

This means that for a fixed Q_R (~5000 considering the design and fabrication of the cavity), increasing the transmission requires a decrease of the Q_{WG}, which will increase the bandwidth of the filter thus deteriorating the filtering functionality. So to achieve good filtering performances a trade-off between the transmission and the bandwidth is required, limiting Q_T to a value of around 1000.
The free spectral range (FSR) is another important parameter of a filter and relates the spectral distance between two consecutive modes. In this application of PhCCs as filters, it is essential to have a FSR as large as possible, such that all the QDs with a wavelength different from the one interest are filtered out. A reasonable FSR around the transmission peak is at least 40nm, given the QD emission spectrum.

6.2.1 Design

In this paragraph different designs for the coupling between PhCC and the PhCWG are compared. The evanescent coupling of the cavity to the PhC waveguide is realized by removing a single row of holes from the hexagonal lattice of the photonic crystal. To achieve high coupling efficiency, the cavity modes must be matched spatially and in energy with a guided mode supported by the PhC waveguide. For this work only L3 PhC cavities, obtained by removing the first three holes from the centre of the PhC, have been considered. It is possible to modify the coupling efficiency playing with few parameters, such as manipulating *r* (holes radius) and *a* (lattice period) of the holes around the cavity or using different number of holes as barriers between the PhCC and the PhCWG or even aligning the waveguide to a certain angle respect to the cavity axis.
For this work three different designs have been first simulated and then experimentally tested (Fig. 6.2). The first two designs consist of a direct coupling (in-line) between a L3 PhCC and a PhCWG. The difference between the two stands in the number of holes that have been used as barriers between the PhCC and the PhCWG, either three holes (design A) or two holes (design B). Moreover the diameter (2*r*) of external hole of the barrier for the design B has been reduced of the 10% compared to the others holes such that higher Q is expected[6].

In the third design the cavity axis in not in-line with the waveguide axis but it is tilted with an angle of 60° (shoulder coupling) and the barrier is realized with two holes (design C). This last design has been realized following a proposal[7] which suggests that as the spatial profile of the fundamental mode of an L3 cavity is tilted by 30° with respect to the axis of the cavity, aligning the waveguide to the cavity at an angle of 60° should maximize the mode field overlap.

The simulated transmission spectra of a PhCWG (Fig. 6.2 top-left) and of the three considered designs for the filters are shown in following (Fig. 6.2).The design with the simulated amplitude of the electric field is shown close to the transmission spectrum. In the table the calculated values of FSR, transmission T and quality factor Q for the fundamental mode Y_1 and the first-order mode Y_2 are presented.

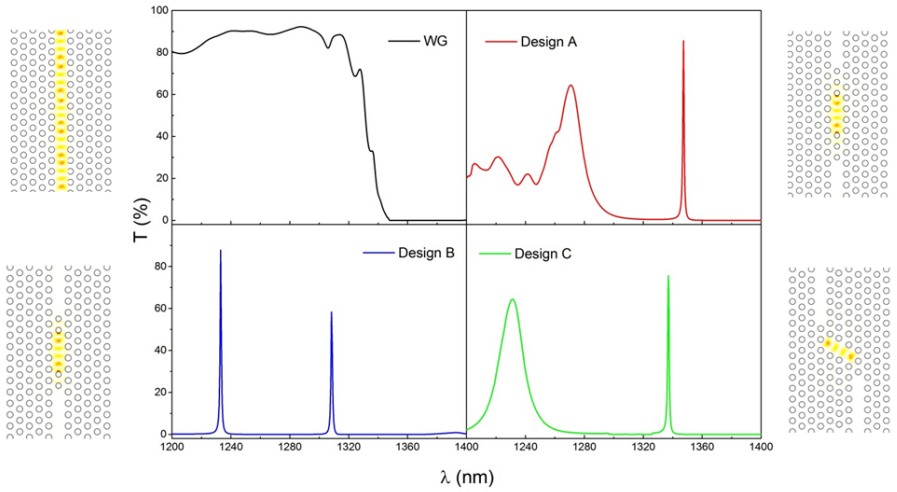

Fig. 6.2 Simulated spectra of a PhCWG (WG) and of the three different PhCC-PhCWG designs: A in-line 3 holes barrier, B in-line 2 holes barrier, C shoulder coupling 2 holes barrier. Inset: sketches of all the considered designs. The simulated amplitude of the electric field is shown in yellow.

Design	Q_{Y1}	Q_{Y2}	T_{Y1} (%)	T_{Y2} (%)	FSR (nm)
A	1250	-	87	-	60
B	1170	1230	58	78	75
C	1145	65	75	64	70

Tab. 6.1 PhCC calculated parameters of the three simulated designs.

The spectrum for the PhCWG, considering a ratio *r/a* = 0.28, presents more than 80% of transmission until a cut-off at the wavelength λ = 1350nm.

The spectra for the design A presents a very promising fundamental mode peak with Q = 1250, FSR = 60nm and the 87% of transmission, indeed it fulfil all the wanted requirements.

However it has to be noticed that the wavelength of the fundamental mode (λ = 1348nm) is very close to the cut-off wavelength of PhCWG and this could create problems for the mode propagation.

In the spectra for the design B both the fundamental and first-order mode peaks are quite narrow (Q_{Y1} = 1170, Q_{Y2} = 1230) and well separated with a FSR=75nm. The transmission for both modes is high especially for the excited mode (T_{Y1} = 78%) , meaning that also the design B satisfies the requirements.

The design C has a simulated spectrum that presents both modes with a FSR=70nm, however the Q_{Y2} of the first-order mode is very low. The fundamental mode (λ = 1338nm) has Q and T comparable with the ones of the other two designs, so overall the design C satisfies as well all the requirements.

Filters following those three different designs have been fabricated (Fig. 6.3), including RWGs coupled on both sides of the crystal to allow direct transmission measurements. In the next paragraph the experimental results are presented.

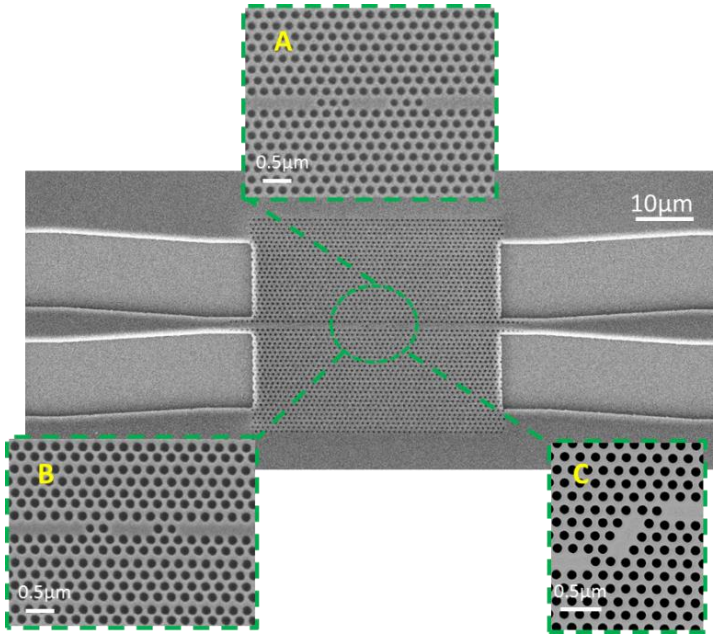

Fig. 6.3 SEM picture of a photonic crystal membrane coupled to both side to RWGs through adibatic taper. Inset: SEM pictures zoomed on the cavity for all the considered designs: A (in-line 3 holes barrier), B (in-line 2 holes barrier), C (shoulder coupling 2 holes barrier).

6.2.2 Performance

Based on simulations the three designs should work properly for the filtering purpose, but actually the experimental transmission measurements show that only the design in-line with 2 holes in the barrier (design B) fulfils the required specifications.
As mentioned the filters are coupled on both sides with RWGs such that fibre-in fibre-out measurements can be performed to directly evaluate the transmission. For those measurements the transmission is calculated as the power-out power-in ratio over all the scanned wavelengths, considering a fibre-RWG-SNB coupling efficiency of $\eta c = 2.4\%$ (Chap. 5.3.1). However the transmission scan over a large range of wavelengths requires quite a long time, meaning that usually measurements are performed on a smaller wavelength range (~30nm) around the transmission peak.
On the other hand an indirect method can be used to measure the transmission allowing fast measurements over a large range of wavelengths. With this method the transmission spectra are calculated as the ratio between the PL spectra acquired from the two sides of the cavity, therefore before and after filtering. To obtain these spectra a non-resonant laser (780nm) is applied from the top on the two sides of the cavity. The PL is collected through the lensed fibre from one side only, using the RWG coupled to the PhCC-PhCWG system.
Ten devices for each design have been measured, in order to check the reproducibility of the result. In the following the transmission spectra of an exemplary device for each design are shown. The ones obtained with direct fibre-in fibre-out measurements (Fig. 6.4 direct) are compared with the ones obtained as ratio between the PL spectra before and after filtering (Fig. 6.4 indirect).
It is easily seen that the peaks are modulated by fringes. It has been verified that those are Fabry-Perot fringes due to reflections at the cleaved facet and at the interface between RWG and SNB.
The comparison between two spectra, coming from the same filter's design, but measured with either the direct or indirect method, shows no significant differences, meaning that the indirect method can be employed as systematic technique to measure the transmission.
From Fig.6.4 it is obvious how the spectrum for the design A does not present any clear transmission peak, rather it shows a broadband transmission over the considered wavelength range. As already mentioned, the calculated wavelength for the fundamental peak ($\lambda = 1348$nm) is very close to the PhCWG cut-off wavelength ($\lambda = 1348$nm). Indeed in the wavelength region close to the cut-off, PhCWG are known to present high losses, which could have masked the observation of the cavity peak. Moreover from the simulated spectra of Fig.6.3 (design A) a high broadband transmission is expected for wavelength below 1285nm. Therefore a wavelength shift due to fabrication imperfection could partially explain what observed in the experimental spectra of Fig.6.4 (design A).

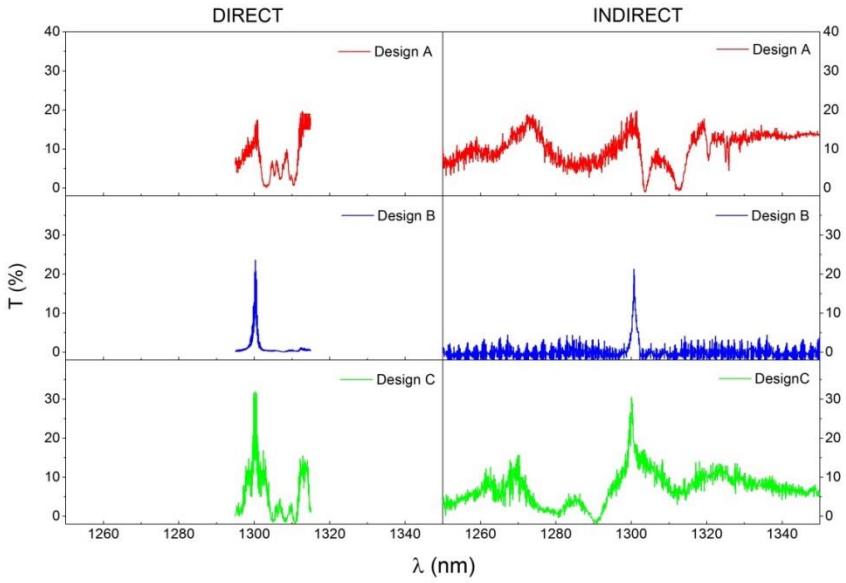

Fig. 6.4 Experimental transmission spectra calculated by direct and indirect measurements for the three studied filters` designs: in-line 3 holes barrier (A), in-line 2 holes barrier (B), shoulder coupling 2 holes barrier (C).

Design B is the only one, that provides a clear and isolated transmission peak (1300nm) with a very large FSR = 60nm. The wavelength of the peak suggests that is the one related to the fundamental mode, however the first-order mode peak is not clearly visible in the range of wavelengths below 1250nm (not shown in Fig. 6.4). In that wavelength region the transmission is not suppressed and similar spectrum as the one for the design A is present. The value for the FSR in this case is calculated as the distance between the peak and the area of broadband transmission and is smaller compared to the simulated one (FSR = 75nm).

The peak transmission obtained with the direct measurement is equal to 24±2%, while the one calculated by ratio of the two spectra before and after filtering is 23±2%. The two values, differently calculated, are in good agreement, meaning that a consistent value for the transmission peak of the design B can be considered ~23%. This experimental result is far from the simulated transmission for the fundamental mode peak of 58%. From the experimental transmission (T ~23%) and total quality factor (Q_T ~1000) and using the formulas of par. 6.2, a value of Q_R ~ 2000 is calculated. This value, much lower than what expected for this fabrication process (Q_R ~ 5000), explains the difference between the simulated and experimental transmission.

Finally the spectrum for the design C shows the presence of a peak at λ = 1300nm, with a percentage of transmission ~28%. However, contrary to the design B, the transmission for other wavelengths is not well suppressed and a strong transmission background is present over the considered wavelength range. So in this last case even if a transmission peak is

present and with a percentage of transmission comparable to the one found for design B, the background is so strong that design C cannot be used for an efficient filtering action.

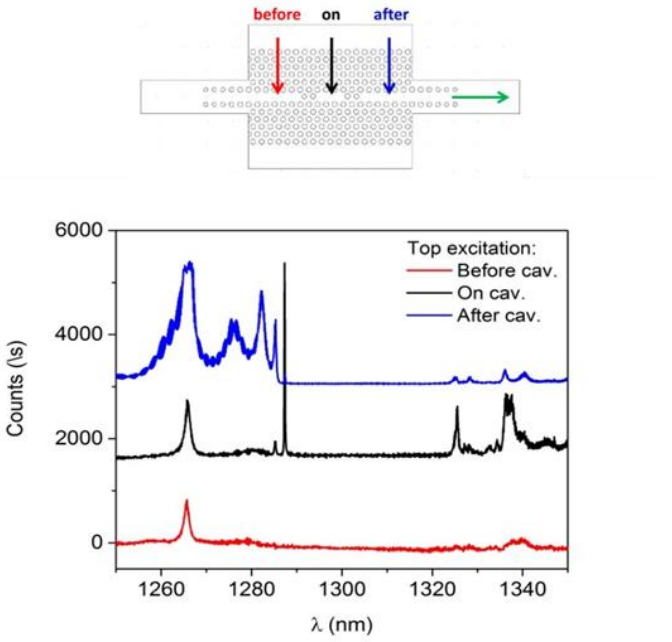

Fig. 6.5 Top: sketch of the design B filter: the red (before cavity), black (on cavity) and blue (after cavity) arrows indicate the different position of the top excitation, while the green the direction of the side collection. Bottom: μPL spectra for the three different excitation positions with corresponding colour coding, the blue spectra has been reduced of a factor 5 to greater clarity.

To better clarify the indirect method and especially to clearly visualize the filtering action of the PhCC-PhCWG system, PL measurements of a device with design B are presented (Fig. 6.5 bottom). They are obtained, as previously explained, applying a non-resonant laser from the top on the two sides of the cavity (Fig. 6.5 top, red and blue arrows) and directly on top of it (black arrow). The PL coupled to the PhCWG (green arrow) is collected from the RWG through a lensed fibre. The PL spectra and the arrows indicating the position on PhCC-PhCWG system are correspondingly colour coded.

The blue curve (after cavity) shows a broad emission with several peaks in the slow-light part of the dispersion curve of the PhCWG mode[8], while in the other two it is possible to observe the filtered cavity mode (1266nm) located around 20nm away from the slow-light dispersion edge. When the pump is applied on top of the PhCC, some additional peaks are observed compared to the case where the laser is applied before the PhCC, due to the excitation of PhCWG section around the cavity (since the laser spot is bigger than the area of the cavity). From the Lorentzian fit of the cavity mode a Q = 1000 is obtained, a value close to the one predicted from the simulation (Q_{Y1} = 1170). From the spectra before

cavity (red curve) for the full range of wavelengths (1200nm-1350nm not shown) no other cavity peak was observed, indicating that a FSR of at least 66nm or bigger has been obtained for this particular device

In conclusion, among the three simulated designs of PhC-PhCWG systems, only the one with in-line coupling and 2 holes in the barrier presents all the required parameters for an efficient filtering action. The experimental transmission of the cavity mode (~23%) is not as high as expected, presumably due to disorder-induced optical losses, however the suppression for all the other wavelengths outside the cavity mode is pretty strong. This will help to obtain a higher ratio between the filtered single QD excitonic line and the background emission of all the other QDs.

6.3 Coupling between QPIC components

The low-temperature fabrication process, developed in order to integrate single-photon sources, detectors and passive circuitry, has shown the capability to preserve high performance for each component of the proposed QPIC. In particular the SSPD patterned on top of a SNB presented DQE = 28% and jitter = 127±8ps, and two electrically independent SNB SSPDs have been used to perform on-chip $g^{(2)}(\tau)$ measurements. The PhCC-PhCWG system showed the expected filtering functionality, with a FSR $\geq$ 60nm and transmission ~23%.

To finally demonstrate that a working multi-functional QPIC has been fabricated, it is necessary to prove that all the involved components, not only work independently, but can also be coupled with each other. In the following the integration of two functionalities per time will be presented.

The conclusive proof of principle of the integration of all the three functionalities would have been a fully on-chip $g^{(2)}(\tau)$ measurement of the filtered single QD excitonic line emission. This experiment has been performed several times during this project, however the perfect condition, in which every device was working as expected, has been very rare. Indeed, as already mentioned, the yield of the integrated SSPDs is quite low. Additionally for the autocorrelator system to perform the $g^{(2)}(\tau)$ measurement two working SSPDs on the same SNB are needed. On the other hand, without any electro-mechanical control, the filtering of a single QD excitonic line emission is purely based on the probability of finding a QD emitting in resonance with the mode of the PhC filter. Even though for very few devices all those conditions have been realized, it has not been possible to distinguish a clear deep for $\tau = 0$, as expected for a single-photon source. This has been mainly due to technical problems related to electrical noise that produced spurious counts in the SSPDs, especially considering the long acquisition time (2-3h) required in order to distinguish a dip at zero delay.

Even though this last conclusive proof has not been demonstrated, the working capability of the multi-functional QPIC has been proved and it will be presented in the following.

6.3.1 SSPDs and QDs

In order to demonstrate a fully-functional QPIC it is necessary to prove that the SSPDs are able to detect only light coming from the QDs and not from other sources like for example the direct or scattered light of the laser pump. In order to test that, fully on-chip time resolved measurements, using the integrated detectors, have been performed at low-temperature (2.2K). The devices used for this test did not present a PhC filter in between the QDs embedded in the RWG and the SNB SSPD (Fig. 6.6 inset).

For these measurements, a technique very similar to the one used to measure the SSPD`s jitter (Chap. 5.3.2) is used. However in this case, a gain switched diode laser at $\lambda = 750$nm and with a repetition rate of 80MHz is used to excite the QDs and use them as an internal light source. The SSPD on SNB is biased at $0.94I_c$ and the output is send to the correlation card together with the laser trigger to record the coincidences counts.

In a first measurement the instrument response function (IRF) of the SSPD under direct laser illumination at normal incidence with 30nW of power is measured. The IRF (Fig.6.6 blue curve) shows a main peak and a shoulder, which may be due to a relaxation oscillation of the laser. A Gaussian fit to the main peak has a FWHM of 134±4ps, that corresponds very well with the value of jitter previously measured for the SSPD on a sample without QDs. At long delay it is possible to recognize a shoulder due to the response to QD emission. The exponential decay fit of the shoulder (green curve) gives a decay time value $\tau_d = 0.94 \pm 0.01$ns that corresponds to the typical spontaneous emission lifetime of these InAs quantum dots[9].

In the second measurement an ensemble of QDs at the edge of the ridge waveguide (0.5mm away from the SSPD) is excited non-resonantly with the same power and the on-chip time resolved photoluminescence (TR PL) data are recorded (Fig. 6.6 black curve). The exponential fit of the decay time gives a value $\tau_d = 0.92 \pm 0.01$ns, in good agreement with the decay time observed in the shoulder on the IRF curve. And most importantly the temporal profile of the excitation laser pulse is not observed anymore at $t \sim 37.5$ns. This proves that, whenever the excitation spot is far enough from the detector, the laser is completely absorbed in the GaAs so that only the QD emission is detected.

In the QD TR PL of Fig 6.6, a relatively long rise time (τ_r) of the luminescence signal is observed. The same behaviour has been observed in ref. [10], where the rise time has been studied as function of the excitation energy level, finding a strong dependence. Indeed, the ultrafast response and high detection efficiency of the integrated SSPDs permit to probe the PL dynamics at low excitation levels.

Actually for a fully discrete electronic structure such as QDs, efficient relaxation is expected to be limited by phonon bottleneck phenomena[11], caused by the large energetic spacing of QD energy levels that inhibits single-phonon mediated scattering processes[12]. Thanks to the fast intrinsic timing resolution of the SSPDs, the charge carrier capture and relaxation dynamics of the excited QDs can be studied such to observe the relaxation bottleneck.

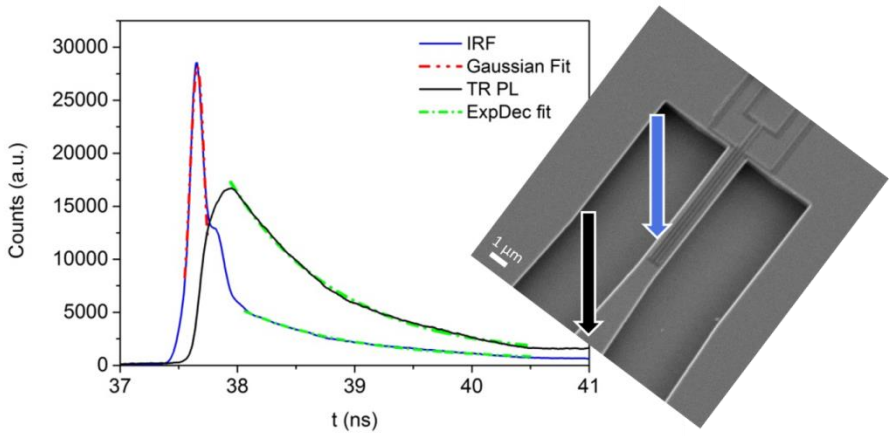

Fig. 6.6 IRF of the SSPD (blue) and on-chip time resolved QD photoluminescence measurement (black). The red line represents the Gaussian fit of the IRF and the green lines the exponential fit of the decay time of the QD emission. Inset: SEM picture of the device. The arrows indicate the excitation points and are colour coded according to the graph.

The non-resonant laser, used to excite the low-density ensemble of QDs at the edge of the ridge waveguide, is set with different powers and on-chip TR PL data are acquired.
In the following, the on-chip TR PL curves for different excitation energies are shown (Fig. 6.7 a).

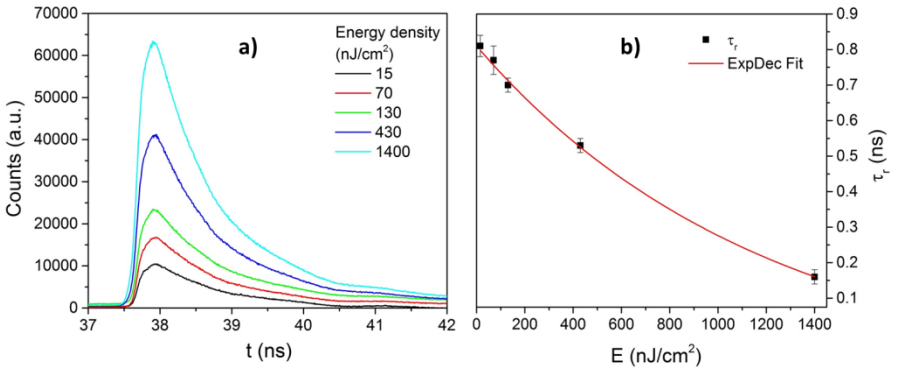

Fig. 6.7 a) On-chip time-resolved QD photoluminescence measurements for different excitation energy densities. b) carrier relaxation time (black square), obtained from the exponential fit of the rising component of the TR PL curves shown on the left, as a function of the excitation energy density. The red curve fits the points with an exponential decay function.

For the lowest energy density used E = 15 nJ/cm^2 the curve (in black in Fig. 6.6 a) follows an exponential increase and immediately after a mono-exponential decay at longer

timescale. Same behaviour is observed for the other two energy densities E = 70 nJ/cm^2 (in red) and E = 130 nJ/cm^2 (in green). Instead for E = 430 nJ/cm^2 and above the decay became multi-exponential, as light emitted by the faster decays of multi-excitonic transitions[13] is detected by the SSPD. Moreover from the exponential decay fits a small dependence of τ_d as a function of the energy density is observed. From a τ_d = 1.01 ns for the highest energy to a τ_d = 0.88 ns for the lowest energy, this excitation energy dependence and the found values are in agreement with ref. [10].
From the fit of the exponential PL rise the rise times τ_r are calculated and a strong dependence on the energy density is found. As shown in Fig 6.6 right as the energy is increased the relaxation time reduces, specifically from τ_r = 0.81ns for E = 0.3 nJ/cm^2 to τ_r = 0.16ns for E = 1400 nJ/cm^2. This trend, that can be fitted with an exponential decay (red curve), reach almost a saturation close to the limit resolution of the SSPDs (jitter = 0.13ns).
The slow relaxation time τ_r = 0.81ns, found for the lowest excitation level, indicates the presence of the phonon bottleneck, which for stronger excitation levels is masked by much faster carrier capture and relaxation via Auger-like processes with other charge carriers[14].
In the case of off-chip TR PL experiments, typically a relaxation time < 100ps is found[13], indicating that the experimental conditions are not adapt to show the presence of the phonon bottleneck. Indeed in the case of on-chip experiments, not only the detectors have an excellent timing resolution, but being placed directly on-chip permit to use ultra-low excitation energy, without losing too many counts.
The trend of the relaxation time in function of the energy density is in good agreement with what found on ref.[10].

6.3.2 QDs and filters

The capability of the on-chip filter to isolate a single QD excitonic line is presented here. In par. 6.2 it has been demonstrated that the coupled PhCC-PhCWG system has filtering functionality. Indeed it has been shown how only light resonant with the cavity mode can pass through the filter, while all the other peaks are completely suppressed (Fig. 6.5).
To prove that those filters are able to isolate a single QD excitonic line, it is necessary to work at low temperature (2.2K) in order to find a device in which there is a dot emitting in resonance with the mode of the PhC filter. Without any possibility of tuning either the cavity mode or the QD emission or both, the only way to find such a device is scanning through several ones until the one satisfying this condition is found. A quick way to individuate such kind of devices is by pumping the non-resonant laser on top of the cavity, collecting the PL emission from the top optics and sending the signal to the spectrometer (see Chap. 2.4.2). Fig. 6.8 blue curve shows a typical PL spectrum (divided by a factor 100 for direct comparison) acquired by top-excitation top-collection, in which the

presence of a QD excitonic line in resonance with the cavity mode is clearly visible at λ = 1185nm (yellow arrow).

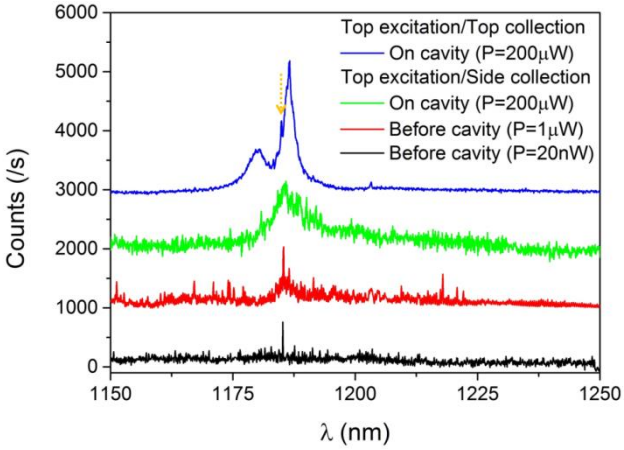

Fig. 6.8 μPL spectra at 2K of top excitation on cavity (P=200μW) and top collection (blue) or side collection (green). Top excitation before cavity with P= 1μW (red) or P = 20nW (black) and side collection. The yellow arrow indicates the wavelength of the single QD excitonic line.

This technique to scan the devices is faster because avoid the necessity to align the lensed fibre to every single device of the chip. However once few devices with the required condition have been found, the PL signal has to be collected from the side through the lensed fibre, in order to see the filtering action. The green curve in Fig. 6.8 shows the resonant emission of the cavity, measured by top pumping on cavity and collecting from the side. Three main features differentiate the two curves: the absence of Fabry-Perot fringes for the top collection, the absence of a second peak (λ= 1180nm) close to the cavity mode (λ= 1186nm) and a strong PL intensity reduction for the side collection. The absence of Fabry-Perot fringes is expected as well as a reduction of the side collection signal due to the not so high coupling efficiency of the RWG-SNB (η_C = 2.4%), even considering the same pump power (~200μW) for both configurations. On the other hand, the absence of a second peak, in the side collection spectrum, is probably due to a poor coupling of certain cavity modes to the RWG modes, which does not allow their propagation.

The other two spectra of Fig. 6.8 are acquired for side collection with the laser focusing on top of the SNB before the cavity. The red curve clearly shows the presence of a single excitonic line perfectly in resonance the cavity mode, however the pumping power is quite strong (1μW) and also other excitonic lines are presents in the background, as well as the signature shape of the cavity mode. To be able to better discriminate the single QD excitonic emission line, the pump laser power was strongly attenuated (20 nW) and the spectrometer was left to acquire for long time (60s instead of the standard 10s) in order to get enough signal. In the black curve, the QD emitting at λ = 1185nm is isolated while all

the other QDs emission lines at different wavelengths are suppressed. However due to the lower Q = 300 of this specific cavity some residual QD emissions close to the filtered line are not yet well suppressed. Indeed the filtered QD line is three times higher than the average off-resonance background, but only two times higher than other lines within the bandwidth of the cavity mode.
However it has been proved that whenever a QD is emitting exactly within the bandwidth of the cavity mode, only a single excitonic line is passing through the filter while all the other lines are suppressed. Moreover cavity mode with higher Q (~1000) will help to obtain a higher ratio of the filtered QD`s signal to background.

6.3.3 Filters and SSPDs

In this paragraph the integration of a SSPD with a filter is presented, which is a key requirement for the application of SSPDs within the QPIC. It will be shown how the SSPDs respond only to TE polarized photons passing through the PhCs filter, while photons with different polarization are not detected (Fig. 6.9).
In this case it is important to mention that the polarization-independent behaviour of the SSPDs (Chap. 5.3.3) helps to validate the result found in this paragraph. Indeed if the SSPDs would be polarization dependent, it could not be excluded, that the different responses to the polarized light, passing through the filter, is an effect of difference in efficiency between the TE and TM mode. Instead polarization-independent SSPDs guarantee the same sensitivity to the two modes, so that the only discriminant is the polarization of the light passing through the filter.
For this experiment, firstly the wavelength range around the transmission peak has to be located, this is done by exciting non-resonantly the cavity from the top and collecting from the side with the off-chip spectrometer (dotted curve of Fig. 6.9). A tunable laser, with a wavelengths range of tunability comparable to the wavelengths range around the transmission peak of the selected device, is fibre-coupled to the free-space setup for the polarization control and sent to the lensed fibre. A laser scan over the considered wavelengths range is performed and its signal collected by the on-chip SNB SSPD, after passing through the system RWG-PhC filter (Fig. 6.9 inset).
In Fig. 6.9 the on-chip SSPD counts as a function of the laser emission wavelength are shown and the curves for TE and TM polarized light are compared, together with the off-chip µPL signal. For the TM polarized detection curve (green) there is no sign of transmission peak but only background counts. This is expected since TM polarized light is not guided in the PhC WG as there is no gap in TM. On the other hand the TE polarized detection curve (blue) present a peak right where the transmission peak is expected, considering the off-chip µPL signal (dotted black). Moreover FP fringes are observed on the transmission peak and they match well the fringes observed in the off-chip µPL signal.

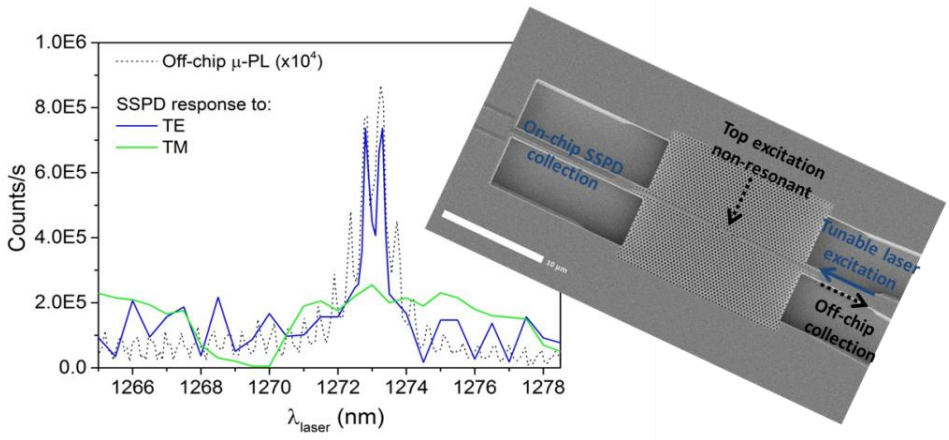

Fig. 6.9 Off-chip μPL signal of top non-resonant excitation on PhC cavity (dotted black). On-chip SSPD counts of the tunable laser excitation, passing through the PhC filter, for TM (green) and TE (blue) polarized light. Inset: SEM picture of the device, the arrows indicate excitation and collection points for the off-chip (dotted black) and on-chip (blue) measurments.

6.4 Conclusion

In this chapter different designs of the PhCC-PhCWG system have been theoretically and experimentally tested. The design with in-line coupling and 2 holes in the barrier presents all the required parameters for an efficient filtering action. From the experimental transmission spectra a FSR $\geq$ 60nm and Q = 1000, as estimated from simulation, were found, however the transmission 23% was lower than expected.

Moreover it has been proved that the three main components of the QPIC (SSPDs, QDs, PhC filters), not only independently work as they are supposed to, but also interact between each other.

The study of the interaction between SSPDs and QDs has been performed through an on-chip time-resolved PL measurement and it has been verified that the SSPDs detect only the QDs emission, whenever the laser is focused at a sufficiently long distance from the detector. From the fits of the TR PL spectra a QDs spontaneous emission lifetime τ_d = 0.94ns has been calculated and a study on the PL dynamics at low excitation levels has been shown. From this study a strong dependence of the rise time τ_r in function of the excitation power level has been observed and attributed to an Auger-mediated interband relaxation process [10].

The interaction between the QDs and filters have been proved, showing, that even with relatively low filter transmission, it is possible to isolate the single excitonic line and transmit it through the filter. The ratio of the excitonic line over the background is

dependent on the Q of the considered cavity (~300) and a higher ratio is expected for higher Q (~1000).
From the interaction between SSPDs and filters it has been concluded that the SSPDs respond only to TE polarized photons passing through the PhCs filter, while photons with different polarization are not detected.
In conclusion a number of key components of a QPIC, including QD sources, filters and detectors, have been developed and successfully tested, opening the way for numerous QIP applications.

References

[1] S. Fattah poor, T. Hoang, L. Midolo, C. Dietrich, L. Li, E. Linfield, J. Schouwenberg, T. Xia, F. Pagliano, F. van Otten, A. Fiore, "Efficient coupling of single photons to ridge-waveguide photonic integrated circuits", *Applied Physics Letters*, **102** pp. 131105–131105, 2013.

[2] S. G. Johnson, P. Bienstman, M. A. Skorobogatiy, M. Ibanescu, E. Lidorikis, J. D. Joannopoulos, "Adiabatic theorem and continuous coupled-mode theory for efficient taper transitions in photonic crystals", *Physical Review E*, **66** pp. 066608, 2002.

[3] H. Takano, Y. Akahane, T. Asano, S. Noda, "In plan-type channel drop filter in a two-dimensional photonic crystal slab", *Applied Physics Letters*, **24** pp. 2226, 2004.

[4] J. Moosburger, M. Kamp, A. Forchel, U. Oesterle, R. Houdre, "Transmission spectroscopy of photonic crystal based waveguides with resonant cavities", *Journal of Applied Physics*, **91** pp. 4791, 2009.

[5] J.D. Joannopoulos, S.G. Johnson, J.N. Winn, R.D. Meade, "Photonic crystals molding the flow of light", 3rd Ed. *Princeton University Press*, 2008.

[6] A.R.A. Chalcraft, S. Lam, D. O'Brien, T.F. Krauss, M. Sahin, D. Szymanski, D. Sanvitto, R. Oulton, M.S. Skolnick, M.A. Fox, D.M. Whittaker, H.Y. Liu, M. Hopkinson, "Mode structure of the L3 photonic crystal cavity", *Applied Physics Letters*, **90** pp. 241117, 2007.

[7] A. Faraon, E. Waks, D. Englund, I. Fushman, J. Vuckovic, "Efficient photonic crystal cavity-waveguide couplers", *Applied Physics Letters*, **90** pp. 073102, 2007.

[8] T.B. Hoang, J. Beetz, M. Lermer, L. Midolo, M. Kamp, S. Höfling, A. Fiore, "Widely tunable, efficient on-chip single photon sources at telecommunication wavelengths," *Optics Express*, **20** pp. 21758–21765, 2012.

[9] C. Zinoni, B Alloing, C Monat, V Zwiller, LH Li, A Fiore, L Lunghi, A Gerardino, Hugues De Riedmatten, Hugo Zbinden, Nicolas Gisin, "time-resolved and antibunching experiment on single quantum dots at 1300nm," *Applied Physics Letters*, **88** pp. 131102, 2006.

[10] G. Reithmaier, F. Flassing, P. Hasch, S. Lichtmannecker, K. Muller, J. Vuckovic, R. Gross, M. Kaniber, J.J. Finley, "A carrier relaxation bottleneck probed in single InGaAs quantum dots using integrated superconducting single photon detectors", *Applied Physics Letters*, **105** pp. 081107, 2014.

[11] J. Urayama, T.B. Norris, J. Singh, P. Bhattacharya, "Observation of Phonon Bottleneck in Quantum Dot Electronic Relaxation", *Physical Review Letters*, **86** pp. 4930, 2001.

[12] H. Benisty, C. M. Sotomayor-Torrès, C. Weisbuch, "Intrinsic mechanism for the poor luminescence properties of quantum-box systems", *Physical Review B*, **44** pp. 10945, 1991.

[13] S. Raymond, S. Fafard, P.J. Poole, A. Wojs, P. Hawrylak, S. Charbonneau, "State filling and time-resolved photoluminescence of excited states in $In_xGa_{1-x}As/GaAs$ self-assembled quantum dots", *Physical Review B*, **54** pp. 11548-11554, 1996.

[14] R. M'ghaïeth, H. Maâref, I. Mihalcescu, J.C. Vial, "Auger effect as the origin of the fast-luminescent band of freshly anodized porous silicon", *Physical Review B*, **60** pp. 4450, 1999.

Chapter 7

Conclusion and outlook

Photonic quantum information processing (QIP) is very promising and interesting results have already been achieved, especially in the cryptography field. However, in order to scale photonic QIP to more complex functionalities, quantum photonic integrated circuits (QPICs) are required. QPICs promise many key advantages, however some stringent criteria on the performance of each component are required. Despite the impressive progress made in the development of each component at the single unit level, to date a fully-functional QPIC has not been demonstrated.

GaAs is a favourable material in order to integrate many QPIC elements, from excellent single-photon sources to high-performance single-photon detectors. In this work the prototype architectures of two slightly different QPIC demonstrators have been investigated.

The first kind of QPIC is realized on a GaAs single-membrane with embedded InAs QDs used as single-photon sources and on which photonic crystal waveguides (PhCWGs) and cavities (PhCCs) are fabricated, in order to filter a single excitonic line, and superconducting single-photon detectors (SSPDs) are patterned on top of suspended nanobeams (SNBs). The second kind of QPIC comprises all the components of the previous one, but it is realized on GaAs double-membranes and includes doped-layers. This allows the fabrication of p-i-n diodes for Stark control of the QDs emission and the realization of a nano-opto-electro-mechanical photonic crystal cavity which can be electrically actuated in order to bring it in resonance with the QD emission and so have an on-demand highly efficient single-photon source. The results on the realization of the proposed QPICs are the following:

- SSPDs have been fabricated using NbN as superconducting film. The deposition process via DC-magnetron sputtering has been optimized, comparing films grown with different deposition parameters (temperature, pressure). SSPDs fabricated on different films have been electro-optically characterized and the best results in terms of efficiency have been obtained for films with critical temperature (T_c) in the range of 9.3-9.7K. The optimized deposition parameters have been used to sputter NbN thin films on top of heterostructure wafers growth by MBE.
- The design of the detectors has been carefully chosen in order to realize the SNB-SSPDs. Different pitches and widths have been compared, and a design

with 260nm pitch and 100nm width has been selected. Moreover the design of the bending points has been optimized in order to reduce the current crowding and the length of the contact wires carefully chosen to avoid latching of the detectors.

- Once the optimized SSPDs are fabricated, they are integrated with the other photonic components. A low-temperature (LT) fabrication process, developed in order to preserve the SSPDs performance, is used. Even though nominally every step of the process is perfectly compatible with the integration of the detectors, it has been observed that several steps together may degrade the NbN film. In particular, a dependence between the etching time and detector critical current has been found for both SiN and GaAs dry etching processes.
- The SSPDs patterned on top of a 10μm-long SNB and integrated with QDs, PhC structures and RWGs are characterized and they present maximum DQE = 28% at λ=1310nm in TE polarization, polarization-independent behaviour, dead time τ_D = 9ns and jitter = 127±8ps. The DQE = 28% is lower than anticipated, considering the numerical simulation and the reduction of the nanowires length to 20 μm, that should have reduced the inhomogeneities problem. However, even if the experimental DQE did not improve as much as estimated, a new record for the DQE on GaAs platform has been established.
- A SNB autocorrelator system, composed of two electrically-independent SSPDs on top of a suspended nanobeam, has been realized and characterized. The system did not present any static or dynamic crosstalk, showing that it is possible to perform a HBT experiment on chip. This result, combined with a jitter of the order of tens ps, shows how the SNB autocorrelator system is suitable for completely on-chip characterization of single-photon emitters.
- Different designs of PhCC-PhCWG systems, used as filters of single excitonic QDs lines, have been tested. The design with in-line coupling and 2 holes in the barrier presents all the required parameters for an efficient filtering action. From the experimental transmission spectra a FSR ≥ 60nm and Q = 1000, as estimated from simulation, were found, however the transmission 23% was lower than expected.
- The realization of the first kind of QPIC has been proved, testing the interaction between the three main components (SSPDs, QDs, PhC filters). The SSPDs have been used for on-chip time-resolved PL measurements of the QDs emission, finding a spontaneous emission lifetime τ_d = 0.94ns. Moreover the PL dynamics at low excitation levels have been studied, finding a strong dependence of the rise time τ_r in function of the excitation power level, attributed to an Auger-mediated interband relaxation process. The integration of QDs and filters have been proved, showing, that even with relatively low filter transmission, it is possible to isolate the single excitonic line and transmit it through the filter. From the coupling between SSPDs and filters it has been concluded that the SSPDs

respond only to TE polarized photons passing through the PhCs filter, while photons with different polarization are not detected. It should be noted that the reproducibility of this process has been observed to be limited due to problems related to degradation during subsequent etching steps.

- The second kind of QPICs, including the p-i-n diodes for QDs control and cavity actuation, have been realized using a LT process with a different process flow compared to the one used for the QPICs on single-membrane. The diodes for QDs tuning and cavity actuation have shown good potential for tunability, and in few devices the signatures antisymmetric and symmetric modes of the double-membrane cavity have been identified in the μ-PL spectra. However, due to the long time required to etch PhC structures through the double-membranes, the functionality of the SSPDs has been completely compromised, therefore not allowing the demonstration of this second kind of QPIC.

Even though few key components of a QPIC (QDs sources, filters, detectors and autocorrelators) have been successfully integrated on the same chip, some problems must be addressed before the realization of a fully-integrated QPIC able to perform complex QIP functionalities.

First of all, each component can be further improved, for example increasing the quality factor of the cavity in order to improve the filtering action, or trying to use superconducting amorphous material (WSi, MoSi) for the SSPD in order to enhance the efficiency.

In what concerns the integration, the main problem is related to the understanding and solving of the etching time fabrication issue. Indeed, until this obstacle is overcome the optimized LT fabrication process will not be able to guarantee reproducibility or the realization of more complex QPICs like the second one proposed.

On the other hand, once this issue is solved, the GaAs platform can be considered the one in which the realization of a fully-integrated QPIC can be done in a relatively short term. Indeed the second proposed platform on GaAs double-membrane and with doped layers would allow the integration on the same chip of all the key components necessary for linear quantum information protocols, namely electrically-driven on-demand single-photon sources[1], electro-optic phase shifters[2], passive circuitry such as waveguides or directional couplers, and detectors.

References

[1] M. Petruzzella, F.M. Pagliano, Ž. Zobenica, S. Birindelli, M. Cotrufo, F.W.M. van Otten, R.W. van der Heijden, A. Fiore "Electrically driven quantum light emission in electromechanically tuneable photonic crystal cavities", *Applied Physics Letters*, **111** pp. 251101, 2017.

[2] L. Midolo, S.L. Hansen, W. Zhang, C. Papon, R. Schott, A. Ludwig, A.D. Wieck, P. Lodahl, S. Stobbe, "Electro-optic routing of photons from single quantum dots in photonic integrated circuits", arXiv:1707.06522v1, 2017.

List of publication

Peer-reviewed journals

G.E. Digeronimo, M. Petruzzella, S. Birindelli, R. Gaudio, S. Fattah Poor, F.W.M. van Otten and A.Fiore, “Integration of single-photon sources and detectors on GaAs”, Photonics, 3, 55 (2016)

Conference contributions

G.E. Digeronimo, M. Petruzzella, S. Birindelli, R. Gaudio, S. Fattah Poor, F.W.M. van Otten and A.Fiore, "On-chip integration of single-photon sources and detectors" Scientific school architectures for quantum photonic circuits, 8-10 February 2017, Nice, France (**oral contribution**)

G.E. Digeronimo, M. Petruzzella, S. Birindelli, R. Gaudio, S. Fattah Poor, F.W.M. van Otten and A.Fiore, “Integration of single-photon sources and detectors on GaAs platform” International Conference on Integrated Quantum Photonics, 26-29 September 2017, Rome, Italy (**oral contribution**)

G.E. Digeronimo, M. Petruzzella, S. Birindelli, R. Gaudio, S. Fattah Poor, F.W.M. van Otten and A.Fiore, “Toward the on-chip integration of single-photon sources and detectors” PICQUE Integrated Quantum Photonics Workshop, 7-9 January 2015, Oxford, UK. (**poster**)

G.E. Digeronimo, M. Petruzzella, S. Birindelli, R. Gaudio, S. Fattah Poor, F.W.M. van Otten and A.Fiore, “Integration of superconducting single-photon detectors in a quantum photonic integrated circuit” Physics @ FOM Veldhoven 2015, 20-21 January 2015, Veldhoven, The Netherlands (**poster**)

G.E. Digeronimo, M. Petruzzella, S. Birindelli, R. Gaudio, S. Fattah Poor, F.W.M. van Otten and A.Fiore, “Toward the on-chip integration of single-photon sources and detectors” for “Women in Optics: The Castle Meeting 2015” conference, 3-6 August 2015, Marburg, Germany (**poster**)

G.E. Digeronimo, M. Petruzzella, S. Birindelli, R. Gaudio, S. Fattah Poor, F.W.M. van Otten and A.Fiore, “Quantum photonic integrated circuits on GaAs” Physics @ FOM Veldhoven 2016, 19-20 January 2016, Veldhoven, The Netherlands (**poster**)

G.E. Digeronimo, M. Petruzzella, S. Birindelli, R. Gaudio, S. Fattah Poor, F.W.M. van Otten and A.Fiore, “Quantum photonic integrated circuits on GaAs” PICQUE Young Scientist Conference, 4-6 April 2016, Bristol, UK (**poster**)

G.E. Digeronimo, M. Petruzzella, S. Birindelli, R. Gaudio, S. Fattah Poor, F.W.M. van Otten and A.Fiore, "SSPD integrated on a multi-functional quantum photonic circuit" Lorentz Center Nanowire superconducting single photon detectors workshop, 28 November -1 December 2016, Leiden, The Netherlands (**poster**)

G.E. Digeronimo, M. Petruzzella, S. Birindelli, R. Gaudio, S. Fattah Poor, F.W.M. van Otten and A.Fiore, "SSPD integrated on a multi-functional quantum photonic circuit" Physics @ Veldhoven 2017, 17-18 January 2017, Veldhoven, The Netherlands (**poster**)

G.E. Digeronimo, M. Petruzzella, S. Birindelli, R. Gaudio, S. Fattah Poor, F.W.M. van Otten and A.Fiore, “Integration of single-photon sources and detectors on GaAs” International Superconductive Electronic Conference 2017, 12-16 June 2017, Sorrento, Italy (**poster**)

Acknowledgments

The work presented in this thesis would have not been possible without the contribution of many people who kindly provided me with technical and moral support. In the following, I want to express all my gratitude to them.

First I would like to thank my first promotor and daily supervisor prof. dr. Andrea Fiore, for offering me the opportunity of working on an interesting and challenging project. I am grateful for his scientific and professional guidance.

I wish to express my gratitude to the members of the defense committee: prof. dr. ir. Gerrit Kroesen, dr. Roberto Leoni, prof. dr. Robert Hadfield, dr. Jos van der Tol, prof. dr. Dries van Thourhout and dr. Rob van der Heijden, for the time that they spent reading my thesis and for the valuable comments they provided. In particular, I would like to thank dr. Roberto Leoni for being the co-promotor and for the useful discussions about the SSPDs fabrication and working mechanism. For the same reason I would also like to thank his collaborators of the Italian Council of Research (CNR) in Rome, dr. Alessandro Gaggero and dr. Francesco Mattioli, thanks to them I felt less alone on my never-ending quest for the fabrication of the perfectly working integrated SSPD.

I would like to thank the scientific staff of the PSN-AND group: prof. dr. Paul Koenraad, prof. dr. Erik Bakkers, dr. Rob van der Hejiden, dr. Jos Havenkort, dr. Andrei Silov, dr. Gonzalez Curto, and the secretaries: Therese-Anne Botman-van Amelsvoort and Simone Krooswijk.

During those five years, I spent the main part of my working life inside what I like to call "a cage of glasses filled with gasses", the "detention time" would have been longer and for sure even more stressful without the support of the NanoLab@TU/e staff: Erik Jan Geluk, Barry Smalbrugge, Tjibbe de Vries, Robert van der Laar, Martijn Dijstelbloem, Nando Harmesen and Huub Hambrosius. Particularly I want to thank Huub and Tjibbe for the understanding on my critical situation related to the GP RIE and their help on finding a way to please all the involved users. Tjibbe, I also want to thank you for bearing with me all the time I messed up the ICP PECVD and the help when the machine messed up itself. Erik Jan, thanks for your help with the EBL, for teaching us the machine tricks, making the transition, from one machine to the other, a very smooth process and for being available at all the time, every day. Your passion and dedication to the work is admirable. Barry, thanks for your indispensable help with the sputtering machine, but most of all thank you for being the "in pectore" father of the clean room, I always felt taken care and in a safe environment even if the place is full of hazards. A big thanks to Frank van Otten for the effort made on finding the best growing conditions required for my specific wafers and for teaching me few tricks for the AFM measurements. Thanks to Henny Manders for the helpful hand in the Lab and to Herman Leijssen for providing the Helium.

I am grateful to former and present members of Andrea`s sub-group for sharing their knowledge and contributed to build a pleasant working environment: Dondu, Zili, Tian, Francesco, Sartoon, Ivan, Bruno, Tianran, Federico, Pierre, Ivana, Kaylee. A particular mention to ’mpare Daniele from Sicily, my messy ex-desk mate Michele and my dear first office mate Zarko always ready to cheer you up with a big hug and supportive words or to fix a LabVIEW problem while discussing about the meaning of life. I thank Simone Biro for all the help in the Lab and for all the fun nights spent clubbing in Stratum. I am deeply grateful to my colleagues and paranymphs Rosalinda and Maurangelo. Particularly I would like to thank Rosalinda for giving me the necessary instruments to work with the SSPD from the sputtering deposition to the nanowires fabrication and finally their characterization in the Lab, for being always supportive and also for the fun and cultural time spent outside of the university. Maurangelo for being always available for any simulation, design, clean room and lab work, I will always remember our crazy clean room nights as well as the crazy nights hanging out in the center of Eindhoven. I also want to thank my Bachelor student Ruben for the time spent in the lab and data analysis.

PSN is a big group and luckily during those years I had the opportunity to share my time inside and outside of the university with many people of the group: Alain, Alessandro, Ang, Anthony, Armando, Christian, Claudiu, Daniël, Diana, Douglas, Elham, Ghada, Hans, Ikaros, Ilaria, Johannes, Philipp, Roy, Ruben, Sasa, Sebastian, Simone A., Tuy, Yizhen. A special mention to Milo and Rianne, my bridge to Dutch culture and to Davide and Luca my bridge to Northern Italy culture.

I also would like to thank other former and present TU/e members: Maria, Katarina and Okan for sharing a great time discovering Eindhoven and beyond. Leonardo and Katia, you guys are like an encyclopaedia, always something to learn from and deep interesting topic to discuss. A big shout-out to my Campanian family: Antonella, Simona, Fabio, Rosaria and Jessica, thank you for the funniest evenings, for being always there for a laugh, a trip, sharing a meal and a drink, I know that wherever we are or we will end up, the connection will not be cut. Also thanks to them for introducing me to the people of the Polymer technology group: Koen, Javier, Prakhyat (the Queen`s guardian), Siavash and Tarek.

This manuscript is not the only product of my PhD time. The stress, craziness, creativity desperation, happiness, collateral to such life, have been of great inspiration, so that I managed to write and compose eight original songs. Thanks a lot to my band mates: Fabio, Giovanni, Javier and Michele for allowing me to transform in real (dare to say good) music my crazy ideas.

My PhD project was born as part of a Marie Curie initial training network called PICQUE, a great experience both professionally and personally. I would like to thank the coordinator Prof. Dr. Fabio Sciarrino and the project manager Giuliana Pensa for the organization of the network events during those years and the fellows: Chiara, Diego, Imad, Ioannis, Joelle, Marcello, Maxime, Panagiotis, Thomas for being supportive and a very good company during the intense weeks of conferences and schools.

At last but not least, I would like to thank some people that have borne with me way more than a PhD life time. My favourite “colleagues” of all time, Crì and Frà and the other half of the Cooper pair Marzia. I know that wherever I am and no matter the distance I can always count on you.

I am deeply grateful to my family and particularly to the ones that are not with me anymore, your way of life helped to forge my personality, so that I will always have a part of you within me. Il ringraziamento piu grande va ai miei genitori, le rocce che mi hanno supportato dal mio primo istante di vita e che continuano a farlo nonostante a volte io vada a schiantarci contro, vi adoro.

Finally, my biggest acknowledgement goes to my hard head and determination. Doing a PhD is not an easy task for anyone, but some projects require an extra dose of perseverance, resilience and patience, so I would like to thank my crazy self for never giving up.

Curriculum Vitae

Giulia Enrica Digeronimo was born on August 29th, 1987, in Catania, Italy.

After finishing high school in 2006 at "E. Majorana" Scientific High School in Caltagirone (Italy), she studied Physics at University of Catania (Italy), where she received her Bachelor degree in 2010. She carried out her Master's studies in Condensed Matter Physics at the same University, where she graduated summa cum laude in 2013, with a thesis on "Synthesis in plasma and characterization of silicon nanocrystals and their application on photovoltaic cells". In September 2013 she started a PhD project at Eindhoven University of Technology (The Netherlands) of which the results are presented in this dissertation.